

Synthesis, Structural Studies, Spectroscopic Investigations and Oxidation state variation in Corrole metal complexes

By

**BRATATI PATRA
CHEM 11201404003**

**National Institute of Science Education and Research (NISER),
Bhubaneswar**

*A thesis submitted to the
Board of Studies in Chemical Sciences
In partial fulfilment of requirements
for the Degree of*

**DOCTOR OF PHILOSOPHY
of
HOMI BHABHA NATIONAL INSTITUTE**



November, 2019

Homi Bhabha National Institute

Recommendations of the Viva Voce Committee

As members of the Viva Voce Committee, we certify that we have read the dissertation prepared by **Bratati Patra** entitled "Synthesis, Structural Studies, Spectroscopic Investigations and Oxidation state variation in Corrole metal complexes" and recommend that it may be accepted as fulfilling the thesis requirement for the award of Degree of Doctor of Philosophy.

Chairman – Dr. Moloy Sarkar		Date: 11/11/2019
Guide / Convener – Dr. Sanjib Kar		Date: 11/11/2019
Examiner – Prof. M. Ravikanth		Date: 11/11/19
Member 1- Dr. Nagendra K Sharma		Date: 11/11/19
Member 2- Prof. A. Srinivasan		Date: 11.11.19
Member 3- Dr. Abdur Rahaman		Date: 11.11.19

Final approval and acceptance of this thesis is contingent upon the candidate's submission of the final copies of the thesis to HBNI.

I/We hereby certify that I/we have read this thesis prepared under my/our direction and recommend that it may be accepted as fulfilling the thesis requirement.

Date: 11/11/2019

Place: NISER, Jatni

Guide


11/11/2019

STATEMENT BY AUTHOR

This dissertation has been submitted in partial fulfillment of requirements for an advanced degree at Homi Bhabha National Institute (HBNI) and is deposited in the Library to be made available to borrowers under rules of the HBNI.

Brief quotations from this dissertation are allowable without special permission, provided that accurate acknowledgement of source is made. Requests for permission for extended quotation from or reproduction of this manuscript in whole or in part may be granted by the Competent Authority of HBNI when in his or her judgment the proposed use of the material is in the interests of scholarship. In all other instances, however, permission must be obtained from the author.



BRATATI PATRA

DECLARATION

I, hereby declare that the investigation presented in the thesis has been carried out by me. The work is original and has not been submitted earlier as a whole or in part for a degree / diploma at this or any other Institution / University.

Bratati Patra

BRATATI PATRA

LIST OF PUBLICATIONS

Journal:

1. *"Grignard reagents mediated demetallation of silver corrole complexes", **Bratati Patra**, Sajal Kumar Patra, Payel Mukherjee, Yogesh Kumar Maurya, Woormileela Sinha, and Sanjib Kar*, *Eur.J. Inorg. Chem.* **2017**, 2363–2368.
2. *"Metal coordination induced ring contraction of porphyrin derivatives", **Bratati Patra**, Sebastian Sobottka, Sruti Mondal, Biprajit Sarkar* and Sanjib Kar*, *Chem. Commun.* **2018**, 54, 9945-9948.
3. *"Ruthenium-Ruthenium Bonded [Bis{corrolato-ruthenium(III)}]ⁿ (n = 0, +1, 1) Complexes: Model Compounds for the Photosynthetic Special Pair", Woormileela Sinha, Michael G. Sommer, Lara Hettmanczyk, **Bratati Patra**, Vasileios Filippou, Biprajit Sarkar* and Sanjib Kar*, *Chem. Eur. J.* **2017**, 23, 2396 – 2404.
4. *"Isovalent Ag^{III}/Ag^{III}, Ag^{II}/Ag^{II}, Mixed-Valent Ag^{II}/Ag^{III}, and Corrolato Based Mixed-Valency in β,β'-Linked [Bis{corrolato-silver}]ⁿ Complexes", **Bratati Patra**, Sebastian Sobottka, Woormileela Sinha, Biprajit Sarkar* and Sanjib Kar*, *Chem. Eur. J.* **2017**, 23, 13858 –1386.
5. "Synthesis of urea derivatives via reductive carbon dioxide fixation into contracted porphyrin analogues", Sajal Kumar Patra, Kasturi Sahu, **Bratati Patra**, Dipak Kumar Sahoo, Sruti Mondal, Payel Mukherjee, Himansu S. Biswal* and Sanjib Kar*, *Green Chem.*, **2017**, 19, 5772–5776.
6. "An N,N'-Bridged Corrole: First Example of a N²¹,N²²-Methylene Bridged Corrole Derivative", Sajal Kumar Patra, Kasturi Sahu, **Bratati Patra**, Sruti Mondal, and Sanjib Kar*, *Eur. J. Org. Chem.* **2018**, 6764–6767.

7. “Regioselective substitution of Corroles and the synthesis of Corrol assemblies”, Kasturi Sahu, Sruti Mondal, **Bratati Patra**, Tanmoy Pain, Sajal Kumar Patra, Carsten Dosche, and Sanjib Kar* *Nanoscale Adv.* (under revision).
8. “Manganese(IV)-dihydroxide as a catalyst for porphyrin synthesis: a new synthesis of porphyrin”, Sruti Mondal, Kasturi Sahu, **Bratati Patra**, Subhrakant Jena, Himansu S. Biswal, and Sanjib Kar* *Dalton Trans.* (under revision).

Chapters in books:

“Corroles”, **Bratati Patra**, Sruti Mondal, Sanjib Kar*, *Encyclopaedia of Inorganic and Bioinorganic Chemistry: eibc2729*, Invited Book Chapter, 2020. (under revision)

* Pertaining to this thesis


BRATATI PATRA

Conferences:

1. Ruthenium-Ruthenium Bonded [Bis{corrolato-ruthenium (III)}] n ($n = 0, +1, -1$) Complexes: Model Compounds for the Photosynthetic Special Pair. **Bratati Patra**, Woormileela Sinha, Sanjib Kar*. MTIC-XVII, 17th International Symposium on ‘Modern Trends in Inorganic Chemistry’ 2017 held at CSIR-NCL, Pune and IISER, Pune during 11-14th December 2017. **(Poster Presentation)**
2. Isovalent $\text{Ag}^{\text{III}}/\text{Ag}^{\text{III}}$, $\text{Ag}^{\text{II}}/\text{Ag}^{\text{II}}$, Mixed-Valent $\text{Ag}^{\text{II}}/\text{Ag}^{\text{III}}$, and Corrolato Based Mixed-Valency in β, β' -Linked [Bis{corrolato-silver}] n Complexes. **Bratati Patra**, Sanjib Kar*. Inter IISER & NISER Chemistry Meet (IINCM-2017) held between December 22-24, 2017 at NISER, Bhubaneswar. **(Poster Presentation)**
3. Grignard reagents mediated demetallation of silver corrole complexes. **Bratati Patra**, Sajal Kumar Patra, Sanjib Kar*. ‘ACS on Campus’ held at NISER Bhubaneswar on July 23, 2018. **(Poster Presentation)**
4. Synthesis of urea derivatives via reductive carbon dioxide fixation into contracted porphyrin analogues. Sajal Kumar Patra, **Bratati Patra**, Sanjib Kar*. ‘ACS on Campus’ held at NISER Bhubaneswar on July 23, 2018. **(Poster Presentation)**
5. Metal coordination induced ring contraction of porphyrin derivatives. **Bratati Patra**, Sanjib Kar*. National Bioorganic Chemistry Conference (NBCC-2018) organised by School of Chemical Sciences, NISER, Bhubaneswar during 22-24th December 2018. **(Poster Presentation)**

Bratati Patra

BRATATI PATRA

DEDICATIONS

I want to dedicate this thesis to my beloved parents and sister.

ACKNOWLEDGEMENTS

*In the first place, I want to express my sincere gratitude to my supervisor **Dr. Sanjib Kar**, Assoc. Prof, NISER, for his guidance throughout my PhD work. His continuous support, inspirational words, knowledge and patience help me to continue and successfully complete my research work.*

*I would like to thank **Prof. Sudhakar Panda**, Director of NISER for providing the laboratory and instrumentation facilities. I also like to express my gratitude to **Prof. V. Chandrasekhar**, **Prof. T. K. Chandrashekar** Ex-Directors, NISER and **Prof. A. Srinivasan**, Head of the Chemistry Dept. I would like to acknowledge **NISER** for providing fellowship.*

*My sincere thanks go to my doctoral committee members **Dr. Moloy Sarkar**, Chairman, **Dr. Nagendra K Sharma**, **Prof. A. Srinivasan** and **Dr. Abdur Rahaman** for sharing expertise and valuable guidance.*

*Besides that, I want to thank my collaborator **Prof. Biprajit Sarkar** for all the instrumentation facilities which help me to extend my research into various levels.*

*I also want to thank NISER operators **Mr. Deepak**, **Mr. Sanjaya**, **Mr. Mriganka**, **Mr. Amit** and **Mr. Prakash**, for the measurements of all my compounds.*

*I thank my fellow lab members, friends, juniors and seniors for all the fun times I had during my stint at NISER. Specially, I am grateful to my lab members **Kasturi**, **Sruti**, **Tanmay**, **Panisha**, **Manisha**, **Sajal** and my good friends **Mainak**, **Sangya**, **Pankaj** and **Dipak** for their help and support.*

*My special regards to **all my teachers** for their guidance at different stages of education which has helped me to reach here.*

*I am highly grateful to my loving **parents** and **sister** for their selfless love, care and support which is the key strength for all my achievements in my life. I also want to thank my fiancé*

Argha Mondal for his unfailing support and continuous encouragement throughout my PhD years.

Last but not the least, I want to thank the **almighty god**, for his showers of blessings throughout my whole life.

Bratati Patra

BRATATI PATRA

CONTENTS

	<i>Page No.</i>
<i>SUMMARY</i>	xv-xvi
<i>LIST OF FIGURES</i>	xviii-xxxi
<i>LIST OF TABLES</i>	xxxii-xxxiv
<i>LIST OF SCHEMES</i>	xxxv
<i>LIST OF ACRONYMS</i>	xxxvi-xxxvii
<i>CHAPTER ONE</i>	1-30
<i>CHAPTER TWO</i>	32-54
<i>CHAPTER THREE</i>	56-87
<i>CHAPTER FOUR</i>	89-129
<i>CHAPTER FIVE</i>	131-200
<i>REFERENCES</i>	202-219
<i>SUMMARY OF THE THESIS</i>	221

Summary

Corrole is a core modified porphyrin which has one carbon less than regular porphyrin macrocycle. It is a tetrapyrrolic, trianionic unit and it contains direct pyrrole pyrrole bond which is almost similar to the corrin ring of vitamin B₁₂, but it is an 18 π electrons aromatic system like the porphyrin ring. As it has much more contracted core than porphyrin thus it can stabilize higher oxidation state of metals. In recent years, it has been receiving major attention because of its superiority over porphyrin in many applications. Various research group has already synthesized different corrole and metallocorrole complexes and explored their interesting properties in different fields like catalysis, sensing, medicinal chemistry specially cancer diagnosis and treatment, dye sensitized solar cell and many more. Despite all these major contributions by various scientists worldwide, still there are deficits in some areas which are not yet explored. Several challenging corrole based systems are currently under intense investigation like corrole dimers. This thesis contains some of the less explored area in corrole field. The first chapter is about the origin, various synthetic protocols and the important applications of one of the most important porphyrin derivatives, corrole. The interesting coordination chemistry of corrole including the synthesis of metal chelated corrole complexes, spectral characterization and their applications in various fields for instance catalysis, sensing, medicinal chemistry are also extensively discussed. In the second chapter, the reactivity of various Grignard reagents with differently substituted A₃– and *trans*-A₂B-corrolato Ag (III) complexes have been discussed. A series of reactions have been performed to establish the new demetalation protocol for a range of different corrolato silver (III) complexes using three different Grignard reagents, methyl magnesium chloride, methyl magnesium bromide and phenyl magnesium bromide. In case of methyl magnesium chloride, complete conversion from corrolato silver (III) complex to free base corrole occurs with 80% isolated yield. In the next chapter, we have discussed about the synthesis and characterization of two A₂B₂-type ferrocenyl porphyrins (one new and other previously reported), their novel copper complexes and silver complexes. During the silver complexation, corrolato Ag

(III) complex is formed instead of silver porphyrin via ring contraction method and the yield is very satisfactory (>80%). Composition and purity of the complexes are confirmed by elemental analyses, ^1H NMR and ^{13}C NMR spectroscopy, ESI mass spectrometry and X-ray crystallography. In-situ NMR experiments clearly demonstrate the ring contraction and silver chelation process. GC-EIMS experiments suggests the course of the reaction through identification of a key ferrocenyl moiety from the starting FB porphyrin ligand. In another chapter, we have synthesized and characterized three new bis(corrolato-ruthenium(III)) complexes containing metal metal triple bonds. To establish the redox state distribution a series of UV-Vis-NIR/EPR Spectroelectrochemical study and DFT calculations have been performed. The mean plane separation between two corrole units of this dimer is $\sim 3.543\text{\AA}$ (from X-ray data) and this distance is in close agreement with that of the ‘special pairs’ in chlorophyll. The one-electron oxidized forms of these dimers show charge transfer transition between the Ru metal centre and the corrole ligands, which appear in the NIR region. The appearance of two NIR bands at 1064 nm (LMCT type) and 2315 nm (ILCT type) on oxidation resembles nicely with the original bands of the radical cations of the photosynthetic ‘special pair’ (1250 nm and 3846 nm). In the last chapter, a new β,β' -(3,3')-linked bis{corrolato-silver(III)} complex is synthesized by following the silver metalation method. Corresponding FB corrole dimer was reported previously by Osuka et al. The desired silver complex is confirmed by elemental analyses, $^1\text{H}/^{19}\text{F}$ -NMR spectroscopy, ESI mass spectrometry and X-ray crystallography. We have characterized this dimeric silver corrole in five different oxidation states by using combined electrochemistry, spectroelectrochemistry and DFT calculations.

List of Figures

		<i>Page No</i>
1.	Figure 1.1: Structures of biological pigments containing porphyrin macrocycles.	3
2.	Figure 1.2: Parent structure of porphyrin, porphin	4
3.	Figure 1.3: Ring modifications of Porphyrin	6
4.	Figure 1.4: Structures of Vitamin B ₁₂	7
5.	Figure 1.5 Representative contracted porphyrins	9
6.	Figure 1.6: Comparative view of porphyrin, corrole and corrin	11
7.	Figure 1.7: Periodic table of elements inserted into corroles Macrocycle	21
8.	Figure 1.8: Coordination modes in Corrole metal complexes	22
9.	Figure 1.9: a) Amphiphilic Fe and Mn metallocorroles. b) Equations of peroxynitrite decomposition reaction catalysed by Mn-corrole complex. c) Catalytic cycle for peroxynitrite decomposition reaction catalysed by Mn-corrole complex	24
10.	Figure 1.10: a) Manganese corrole complex used for the activation of O ₂ and formation of O–O bond. b) Reaction scheme of the formation of manganese–oxygen intermediates c) Proposed mechanisms for the formation of Mn(V)-Oxo and Mn (IV)-Peroxo species through O ₂ -activation and O–O bond formation reactions	26
11.	Figure 1.11: Structures of Ga(III) Corroles complex.	27
12.	Figure 1.12: Conjugation of Metallocorroles and Tumor-Targeting Cell-Penetrating Protein (HerPBK10)	27

13.	Figure 1.13: Structures of all the cobalt (III) corroles examined for CO sensing	29
14.	Figure 2.1: Structures of the FB corroles, 1A–2A , and the corresponding corrolato–Ag ^{III} complexes, 1B–2B	35
15.	Figure 2.2: Structures of the FB corroles, 3A–6A , and the corresponding corrolato–Ag ^{III} complexes, 3B–6B .	36
16.	Figure 2.3: Electronic absorption spectrum of a) 3B in CH ₂ Cl ₂ solution (——), (b) 3B in CH ₂ Cl ₂ solution + 50 equivalents of CH ₃ MgCl (-----) and c) 3A in CH ₂ Cl ₂ solution + 50 equivalents of CH ₃ MgCl (·····)	40
17.	Figure 2.4: ESI- MS spectrum of 5,10,15-tris(2-bromo-5-fluorophenyl)corrole, 1A in CH ₃ CN.	41
18.	Figure 2.5: ESI-MS spectrum of 5,10,15-tris(2-bromo-5-fluorophenyl)corrolato-silver(III), 1B in CH ₃ OH	42
19.	Figure 2.6: ESI- MS spectrum of 10-(pyrene-1-yl)-5,15-bis(4-cyanophenyl)corrole, 6A in CH ₃ CN	42
20.	Figure 2.7: ESI- MS spectrum of 10-(pyrene-1-yl)-5,15-bis(4-cyanophenyl)corrolato silver(III), 6B in CH ₃ OH	43
21.	Figure 2.8: Electronic absorption spectrum of 5,10,15-tris(2-bromo-5-fluorophenyl)corrole, 1A in CH ₂ Cl ₂	43
22.	Figure 2.9: Electronic absorption spectrum of 5,10,15-tris(2-bromo-5-fluorophenyl)corrolato-silver(III), 1B in CH ₂ Cl ₂	44
23.	Figure 2.10: ¹ H NMR spectrum of 5,10,15-tris(2-bromo-5-fluorophenyl)corrole, 1A in CDCl ₃	45
24.	Figure 2.11: ¹ H NMR spectrum of 5,10,15-tris(2-bromo-5-	45

	fluorophenyl)corrolato-silver(III), 1B in CDCl ₃	
25.	Figure 2.12: ¹ H NMR spectrum of 10-(pyrene-1-yl)-5,15-bis (4-cyanophenyl) corrole, 6A in CDCl ₃	46
26.	Figure 2.13: ¹ H NMR spectrum of 10-(pyrene-1-yl)- 5,15-bis(4-cyanophenyl)corrolato-silver(III), 6B in CDCl ₃	47
27.	Figure 2.14: ORTEP diagram of 3B . Ellipsoids are drawn at 50% probability	47
28.	Figure 2.15: ORTEP diagram of 6B . Ellipsoids are drawn at 50% probability	48
29.	Figure 3.1: Ultraviolet-Visible spectral diagram for porphyrin 1 measured in DCM solvent	61
30.	Figure 3.2: Ultraviolet-Visible spectroscopic diagram for complex 3 in DCM solvent	62
31.	Figure 3.3: Ultraviolet-Visible spectroscopic diagram for complex 5 in DCM solvent	62
32.	Figure 3.4: Electronic absorption spectrum of 5 in dichloromethane	62
33.	Figure 3.5: Electronic absorption spectrum of 6 in DCM solvent	62
34.	Figure 3.6: CV diagram (——) and DPV diagram (----) of complex 3 in DCM solvent. The potentials are vs. ferrocene/ferrocinium	63
35.	Figure 3.7: CV diagram (——) and DPV diagram (----) of complex 5 measured in DCM solvent. The potentials are vs. ferrocene/ferricenium	64
36.	Figure 3.8: ¹ H NMR spectrum of 5,15-diferrocenyl-10,20-bis (4-cyanophenyl)porphyrin, 1 in CDCl ₃	65
37.	Figure 3.9: ¹³ C NMR spectrum of 5,15-diferrocenyl-10,20-bis (4-cyanophenyl)porphyrin, 1 in CDCl ₃	66

38.	Figure 3.10: ^1H NMR spectrum of 10-ferrocenyl-5,15-bis(4-cyanophenyl)corrolato-Ag(III), 5 in CDCl_3	66
39.	Figure 3.11: ^{13}C NMR spectrum of 10-ferrocenyl-5,15-bis(4-cyanophenyl)corrolato-Ag(III), 5 in CDCl_3	67
40.	Figure 3.12: ^1H NMR spectrum of 10-ferrocenyl-5,15-bis(4-nitrophenyl)corrolato-Ag(III), 6 in CDCl_3	67
41.	Figure 3.13: ^{13}C NMR spectrum of 10-ferrocenyl-5,15-bis(4-nitrophenyl)corrolato-Ag(III), 6 in CDCl_3	68
42.	Figure 3.14: ESI-MS spectrum of 5,15-diferrocenyl-10,20-bis(4-cyanophenyl)porphyrin, 1 in CH_3CN shows (a) the recorded spectrum and (b) with isotopic distribution pattern.	68
43.	Figure 3.15: ESI-MS spectrum of 5,15-diferrocenyl-10,20-bis(4-cyanophenyl)porphyrinato Cu(II), 3 in CH_3CN shows (a) the measured spectrum and (b) with isotopic distribution pattern.	69
44.	Figure 3.16: ESI-MS spectrum of 5,15-diferrocenyl-10,20-bis(4-nitrophenyl)porphyrinato-Cu(II), 4 in CH_3CN shows (a) the measured spectrum and (b) with isotopic distribution pattern.	69
45.	Figure 3.17: ESI-MS spectrum of 10-ferrocenyl-5,15-bis(4-cyanophenyl)corrolato-Ag(III), 5 in CH_3CN shows (a) the measured spectrum and (b) with isotopic distribution pattern	70
46.	Figure 3.18: ESI-MS spectrum of 10-ferrocenyl-5,15-bis(4-nitrophenyl)corrolato-Ag(III), 6 in CH_3CN shows (a) the measured spectrum and (b) with isotopic distribution pattern.	71
47.	Figure 3.19: Experimentally observed and simulated EPR spectrum of 3 measured in dichloromethane solvent at room temperature	71

48.	Figure 3.20: Experimentally observed and simulated EPR spectrum of 4 measured in dichloromethane solvent at room temperature	71
49.	Figure 3.21: X-ray crystallographic structure of complex 3 . All the hydrogen atoms are excluded for clarity	72
50.	Figure 3.22: X-ray crystallographic structure of complex 5 . All the H atoms are excluded for clarity	73
51.	Figure 3.23: ^1H NMR spectra of (a) pure 1 in CDCl_3 , (b) the sample prepared via treatment of 1 (equimolar amount) with $\text{Ag}(\text{CH}_3\text{COO})$ and trimethylamine in DCM, stirred at RT for 30 mins, followed by filtration of the silver residues and the evaporation of the residual solvent containing triethylamine and dissolution in CDCl_3 , and (c) pure 5 in CDCl_3	75
52.	Figure 3.24: 5,15-diferrocenyl-10,20-bis(4-cyanophenyl)porphyrin, 1 was dissolved in DCM and subsequently silver acetate was added followed by the addition of triethylamine solvent into the reaction mixture and it was stirred continuously at room temperature. Aliquots of this reaction mixture was taken after 2 minutes and were monitored by GC-EIMS analysis	76
53.	Figure 3.25: Mass spectrum (GC-EIMS) of ferrocenyl derivatives detected by GC of the reaction mixture	76
54.	Figure 3.26: Mass spectrum (GC-EIMS) of ferrocenyl derivatives detected by GC of the reaction mixture	77
55.	Figure 3.27: 5,15-diferrocenyl-10,20-bis(4-cyanophenyl)porphyrin, 1 was dissolved in DCM and subsequently silver acetate was added followed by the addition of triethylamine solvent into the reaction mixture. It was stirred continuously at room temperature. Aliquots of	77

	this reaction mixture was taken after 30 minutes and were monitored by GC-EIMS analysis	
56.	Figure 3.28: Mass spectrum (GC-EIMS) of ferrocenyl derivatives detected by GC of the reaction mixture	78
57.	Figure 3.29: Mass spectrum (GC-EIMS) of ferrocenyl derivatives detected by GC of the reaction mixture	78
58.	Figure 3.30: Ferrocene was dissolved in dichloromethane and were monitored by GC-EIMS analysis	79
59.	Figure 3.31: Mass spectrum (GC-EIMS) of ferrocene detected by GC of the reaction mixture	79
60.	Figure 3.32: Ferrocenecarboxaldehyde was dissolved in dichloromethane and were monitored by GC-EIMS analysis	80
61.	Figure 3.33: Mass spectrum (GC-EIMS) of ferrocenecarboxaldehyde detected by GC of the reaction mixture	80
62.	Figure 3.34: 5,15-diferrocenyl-10,20-bis(4-cyanophenyl)porphyrin, 1 was dissolved in DCM solvent followed by the addition of triethylamine solvent into the reaction mixture and it was stirred continuously at room temperature. Aliquots of this reaction mixture were taken after 15 minutes and were monitored by GC-EIMS analysis.	81
63.	Figure 4.1: Structures of the ruthenium corrole complexes: 1) bis(5,10,15-tris(4-cyanophenyl)corrolato-ruthenium(III)), 2) bis(10-(2,4,5-trimethoxyphenyl)-5,15-bis(4-cyanophenyl)corrolato-ruthenium(III)), and 3) bis(10-(4,7-dimethoxynaphthalen-1-yl)-5,15-bis(4-cyanophenyl)corrolato-ruthenium(III))	92
64.	Figure 4.2: Electrospray mass spectrum of complex 1 using CH ₃ CN	93

	solvent showing the isotopic distribution pattern	
65.	Figure 4.3: Electrospray mass spectrum of 2 in CH ₃ CN shows the isotopic distribution pattern	94
66.	Figure 4.4: Proton NMR spectrum of 1 in CD ₂ Cl ₂ at 298 K	94
67.	Figure 4.5: Proton NMR spectrum of 2 in CDCl ₃ at 273 K	95
68.	Figure 4.6: ¹ H NMR spectra of 2 in CDCl ₃ at variable temperatures	96
69.	Figure 4.7: ¹ H NMR spectrum of 3 in CD ₂ Cl ₂ at 253 K	96
70.	Figure 4.8: ¹ H NMR spectra of 3 in CD ₂ Cl ₂ at variable temperatures	97
71.	Figure 4.9: X-ray crystal structure of 2 (top view)	98
72.	Figure 4.10: DFT optimized structures of a) 1 , b) 1 ⁺ , c) 1 ⁻ , d) 2 , e) 2 ⁺ , and f) 2 ⁻	99
73.	Figure 4.11: X-ray structure analysis of 2 , revealing the π- π stacking interactions [4.150 Å]. The entry in square brackets is the distance	100
74.	Figure 4.12: X-ray single crystal structure analysis of 2 , having a zig-zag arrangement when viewed along <i>c</i> -axis	100
75.	Figure 4.13: X-ray single crystal structure analysis of 2 , showing C-H... π interactions, [2.776-3.094Å] between neighbouring molecules. The entry in square brackets is the distance	101
76.	Figure 4.14: X-ray single crystal structure analysis of, 2 , showing (a) C-H...π interactions, [2.950 Å] and (b) parallel displaced π-π stacking interactions [5.142 Å] between neighbouring molecules. The entries (b) in square brackets are the distances	101
77.	Figure 4.15: Cyclic voltammograms (—) and differential pulse voltammograms (-----) of a) 1 , b) 2 and c) 3 . The potentials are	103

	vs. ferrocene/ferrocenium	
78.	Figure 4.16: Spin density calculations for a) $(1)^{+\bullet}$, b) $(2)^{+\bullet}$, c) $(1)^{-\bullet}$ and d) $(2)^{-\bullet}$ (iso-value 0.005). Blue colour shows positive, red colour negative sign	106
79.	Figure 4.17: X-band Electron paramagnetic resonance spectrum spectrum of $1^{+\bullet}$ at 151 K in DCM/0.1M Bu ₄ NPF ₆ ; $1^{+\bullet}$ was generated by in-situ electrolysis at room temperature	107
80.	Figure 4.18: X-band Electron paramagnetic resonance spectrum of $(2)^{+\bullet}$ at 115 K generated by AgBF ₄ in DCM solvent	108
81.	Figure 4.19: X-Band Electron paramagnetic resonance spectrum of $(3)^{+\bullet}$ at 134 K generated by AgBF ₄ in DCM solvent	108
82.	Figure 4.20: Change in the Ultraviolet-Visible -NIR spectrum of a) 1 and b) 2 during first reduction. Results from OTTLE spectroelectrochemistry in CH ₂ Cl ₂ /0.1 M Bu ₄ NPF ₆	109
83.	Figure 4.21: Change in the UV-Vis-NIR spectrum of a) 1 , and b) 2 during first oxidation. Results from OTTLE spectroelectrochemistry in CH ₂ Cl ₂ /0.1 M Bu ₄ NPF ₆	110
84.	Figure 4.22: Change in the UV-Vis-NIR spectrum of a) $[1]^+ \rightarrow [1]^{2+}$ and b) $[2]^+ \rightarrow [2]^{2+}$. Results from OTTLE spectroelectrochemistry in CH ₂ Cl ₂ /0.1 M Bu ₄ NPF ₆	111
85.	Figure 4.23: Variation in the Ultraviolet-visible-NIR spectra of complex 3 during a) $[3] \rightarrow [3]^+$ b) $[3]^+ \rightarrow [3]^{2+}$ and c) $[3] \rightarrow [3]^-$. Results from OTTLE spectroelectrochemistry in DCM solvent/0.1 M Bu ₄ NPF ₆ .	112
86.	Figure 4.24: All the selected Molecular Orbitals of 1	119
87.	Figure 4.25: All the selected Molecular Orbitals of 1^+	120

88.	Figure 4.26: All the selected Molecular Orbitals of 1^-	122
89.	Figure 4.27: All the selected Molecular Orbitals of 2	124
90.	Figure 4.28: All the selected Molecular Orbitals of 2^+	126
91.	Figure 4.29: All the selected Molecular Orbitals of 2^-	128
92.	Figure 5.1: Structure of compound 1 and 1A	134
93.	Figure 5.2: Perspective view of 1 . Hydrogen atoms are omitted for clarity	135
94.	Figure 5.3: DFT-optimized structure for 1	136
95.	Figure 5.4: Proton NMR spectrum of 3,3'-Bis(5,10,15-tris(pentafluorophenyl) corrole, 1A in $CDCl_3$	138
96.	Figure 5.5: ^{19}F NMR spectrum of 3,3'-Bis(5,10,15-tris(pentafluorophenyl) corrole, 1A in $CDCl_3$	138
97.	Figure 5.6: 1H NMR spectrum of 3,3'-Bis{(5,10,15-tris(pentafluorophenyl) corrolato-silver(III))}, 1 in $CDCl_3$	139
98.	Figure 5.7: ^{19}F NMR spectrum of 3,3'-Bis{(5,10,15-tris(pentafluorophenyl) corrolato-silver(III))}, 1 in $CDCl_3$	139
99.	Figure 5.8: ESI-MS spectrum of 3,3'-Bis(5,10,15-tris(pentafluorophenyl) corrole, 1A in CH_3CN display the studied spectrum with isotopic distribution pattern	140
100.	Figure 5.9: ESI-MS spectrum of 3,3'-Bis{(5,10,15-tris(pentafluorophenyl) corrolato-silver(III))}, 1 in CH_3CN display the studied spectrum with isotopic distribution pattern	140
101.	Figure 5.10: CV of 1 in DCM solvent/0.1 M NBu_4BArF_{24} studied using glassy carbon as working electrode using 100 mVs^{-1} scan rates	141
102.	Figure 5.11: CV of 1 in DCM solvent/0.1 M NBu_4BArF_{24} studied using a platinum working electrode with scan rate 100 mVs^{-1}	141

103.	Figure 5.12: CV of 1 in DCM solvent/0.1 M NBu ₄ BPF ₆ measured using glassy carbon working electrode using 100 mVs ⁻¹ scan rate	142
104.	Figure 5.13: Comparison of CV of 1 measured with different electrolytes. For comparative reasons the current has been normalized to unity	142
105.	Figure 5.14: Cyclic voltammograms (black) and differential pulse voltammogram (red)_of 1 in dichloromethane. The potentials are vs. Ag/AgCl	143
106.	Figure 5.15: DPV of 1 in CH ₂ Cl ₂ /0.1 M NBu ₄ BArF ₂₄ measured with a glassy carbon working electrode	144
107.	Figure 5.16: X-band EPR spectrum of a) (1) ^{•-} and b) (1) ²⁻ generated by <i>in-situ</i> electrolysis at 298 K in CH ₂ Cl ₂ /0.1 M NBu ₄ BArF ₂₄	144
108.	Figure 5.17: Electron paramagnetic resonance spectrum of electro-chemically generated 1 ^{•-} recorded in CH ₂ Cl ₂ /0.1 M NBu ₄ BArF ₂₄ at -0.65 V vs Ag-wire pseudoreference electrode. Experimental details: Accumulation of 16 scans, 20 s sweep time, 0.2 mT modulation, 100 kHz modulation frequency, 10 mW microwave power, 298 K, microwave frequency: 9.46 GHz. Experiment: black, simulation: red	145
109.	Figure 5.18: Electron paramagnetic resonance spectrum of electro-chemically generated 1 ²⁻ recorded in CH ₂ Cl ₂ /0.1 M NBu ₄ BArF ₂₄ at -1.5 V vs Ag-wire pseudoreference electrode. Experimental details: Accumulation of 16 scans, 20 s sweep time, 0.2 mT modulation, 100 kHz modulation frequency, 10 mW microwave power, 298 K, microwave frequency: 9.46 GHz	147
110.	Figure 5.19: Electron paramagnetic resonance spectrum of electro-chemically generated 1 ⁺ recorded in CH ₂ Cl ₂ /0.1 M NBu ₄ BArF ₂₄ at	148

	+0.50 V vs Ag-wire pseudoreference electrode. Experimental details: 20 s sweep time, 0.8 mT modulation, 100 kHz modulation frequency, 5 mW microwave power, 298 K, microwave frequency: 9.46 GHz	
111.	Figure 5.20: EPR spectrum of electrochemically generated $\mathbf{1}^{2+}$ recorded in $\text{CH}_2\text{Cl}_2/0.1 \text{ M NBu}_4\text{BArF}_{24}$ at +1.48 V vs Ag-wire pseudoreference electrode. Experimental details: 40 s sweep time, 0.1 mT modulation, 100 kHz modulation frequency, 5 mW microwave power, 298 K, microwave frequency: 9.46 GHz	148
112.	Figure 5.21: Spin density from DFT calculation of $\mathbf{1}^+$	149
113.	Figure 5.22: Spin density from DFT calculation of $\mathbf{1}^{2+}$	149
114.	Figure 5.23: Spin density from DFT calculation of $\mathbf{1}^-$	149
115.	Figure 5.24: Spin density from DFT calculation of $\mathbf{1}^{2-}$	149
116.	Figure 5.25: UV-vis-NIR spectra of the three redox states of $\mathbf{1}$ from OTTLE spectroelectrochemistry in $\text{CH}_2\text{Cl}_2/0.1 \text{ M NBu}_4\text{BArF}_{24}$. Inset shows the weak NIR band for $(\mathbf{1})^{\bullet-}$	150
117.	Figure 5.26: Variations in the Ultraviolet-visible-NIR spectrum for $\mathbf{1}$ throughout the OTTLE spectroelectrochemistry experiment measured in DCM solvent/ $0.1 \text{ M NBu}_4\text{BArF}_{24}$	151
118.	Figure 5.27: Variations in the Ultraviolet-visible-NIR spectrum for $\mathbf{1}$ throughout the OTTLE spectroelectrochemistry experiment measured in DCM solvent/ $0.1 \text{ M NBu}_4\text{BArF}_{24}$	151
119.	Figure 5.28: UV-vis-NIR spectra of $\mathbf{1}$ in three different redox states from OTTLE spectroelectrochemistry in $\text{CH}_2\text{Cl}_2/0.1 \text{ M NBu}_4\text{BArF}_{24}$. Inset shows the NIR band for $(\mathbf{1})^{\bullet+}$	152

120.	Figure 5.29: Changes in the Ultraviolet-visible -NIR spectrum of 1 during OTTLE spectroelectrochemistry experiment measured in DCM solvent /0.1 M NBu ₄ BArF ₂₄	152
121.	Figure 5.30: Variations in the Ultraviolet-visible-NIR spectrum of 1 throughout the OTTLE spectroelectrochemistry experiment measured in DCM solvent/0.1 M NBu ₄ BArF ₂₄	153
122.	Figure 5.31: Variations in the Ultraviolet-visible-NIR spectrum of 1 throughout the OTTLE spectroelectrochemistry experiment measured in DCM solvent/0.1 M NBu ₄ BArF ₂₄	153
123.	Figure 5.32: Variations in the Ultraviolet-visible-NIR spectrum of 1 throughout the OTTLE spectroelectrochemistry experiment measured in DCM solvent/0.1 M NBu ₄ BArF ₂₄	154
124.	Figure 5.33: Comparison of the Ultraviolet-visible -NIR spectrum of 1 before and after reductive OTTLE spectroelectrochemistry	155
125.	Figure 5.34: Comparison of the Ultraviolet-visible -NIR spectrum of 1 before and after oxidative OTTLE spectroelectrochemistry	155
126.	Figure 5.35: Comparison between experimental (black) and TD-DFT (red) UV/Vis-NIR spectrum	161
127.	Figure 5.36: Calculated spectrum with TD-DFT and discrete transitions. Line width 1500 cm ⁻¹	161
128.	Figure 5.37: Comparison of the experimental and calculated spectrum	166
129.	Figure 5.38: Comparison of discrete transitions and the experimental spectrum	166
130.	Figure 5.39: Calculated spectrum with TD-DFT and discrete transitions. Line width 1500 cm ⁻¹	167
131.	Figure 5.40: Zoom-In of the calculated spectrum with TD-DFT and discrete	167

	transitions. Line width 1500 cm ⁻¹	
132.	Figure 5.41: Calculated spectrum with TD-DFT and discrete transitions. Line width 1500 cm ⁻¹	175
133.	Figure 5.42: Zoom- in of the calculated spectrum with TD-DFT and discrete transitions. Line width 1500 cm ⁻¹	175
134.	Figure 5.43: Comparison of discrete transitions with the experimental spectrum	176
135.	Figure 5.44: Comparison between experimental (black) and TD-DFT (red) UV/Vis-NIR spectrum	182
136.	Figure 5.45: Calculated spectrum with TD-DFT and discrete transitions. Line width 1500 cm ⁻¹	182
137.	Figure 5.46: Experimental spectrum and discrete calculated transitions	183
138.	Figure 5.47: Comparison between experimental (black) and TD-DFT (red) UV/Vis-NIR spectrum	188
139.	Figure 5.48: Calculated spectrum with TD-DFT and discrete transitions. Line width 1500 cm ⁻¹	189
140.	Figure 5.49: Optimized structure for the monomer (BP86/def2-TZVP, final single point energy B3LYP/def2-TZVP)	195
141.	Figure 5.50: Monomer with distorted pyrrole ring, geometry taken directly from the optimized dimer from the dimer (final single point energy B3LYP/def2-TZVP)	196
142.	Figure 5.51: Comparison of the Gouterman orbitals for the dimer 1 and the corresponding monomer	199
143.	Figure 5.52: Comparison of the Gouterman orbitals for the dimer 1 and the corresponding monomer	200

- 144.** Figure 5.53: Energy diagram for the Gouterman orbitals of dimer **1** and the monomer **200**

List of Tables

	<i>Page No</i>
1. Table 2.1: Scope of the demetallation reaction	38
2. Table 2.2: Optimization of the demetallation reactions 4B to 4A	39
3. Table 2.3: Crystallographic Data for Compounds 3B and 6B	48-49
4. Table 3.1: UV–Vis. and electrochemical data	64
5. Table 3.2: Overview of g values and hyperfine coupling constants obtained from simulation	72
6. Table 3.3: Crystallographic Data for 3 and 5	73-74
7. Table 4.1: X-Ray Crystallographic data	102
8. Table 4.2: Electrochemical data	104
9. Table 4.3: Electron paramagnetic resonance data of paramagnetic states	105
10. Table 4.4: (B3LYP/TZVPP-ZORA) calculated Löwdin spin densities on each Ru and on each Corrole	106
11. Table 4.5: Ultraviolet-Visible -NIR Data of 1ⁿ , 2ⁿ and 3ⁿ [$n = -1, +1,$ $+2, 0$] from Spectroelectrochemistry	113
12. Table 4.6: Time-dependent density functional theory Calculated Electronic Transitions for 1	118
13. Table 4.7: Time-dependent density functional theory Calculated Electronic Transitions for 1⁺	119-120
14. Table 4.8: Time-dependent density functional theory Calculated Electronic Transitions for 1⁻	121-122
15. Table 4.9: Time-dependent density functional theory Calculated	122-123

Electronic Transitions for **2**

16.	Table 4.10: Time-dependent density functional theory Calculated Electronic Transitions for 2⁺	124-125
17.	Table 4.11: Time-dependent density functional theory Calculated Electronic Transitions for 2⁻	126-127
18.	Table 4.12: Gibbs free enthalpies used for calculation of redox potentials	129
19.	Table 5.1: X-Ray Crystallographic data for complex 1	137
20.	Table 5.2: Electrochemical data for 1	143
21.	Table 5.3: Electron paramagnetic resonance data of paramagnetic states	146
22.	Table 5.4: Löwdin spin population analysis from DFT calculation (B3LYP/TZVPP-ZORA) for the various paramagnetic species	149
23.	Table 5.5: Data from UV-Vis-NIR spectroelectrochemical measurements	154
24.	Table 5.6: TD-DFT calculated electronic transitions of 1	162
25.	Table 5.7: Composition of selected molecular orbitals of 1	163-164
26.	Table 5.8: Orbital energies of 1 from DFT-calculation	165
27.	Table 5.9: TD-DFT calculated electronic transitions of 1^{•+}	168
28.	Table 5.10: Orbital energies of (1) ^{•+} from DFT-calculation	169
29.	Table 5.11: Composition of all specific molecular orbitals with alpha spin for (1) ^{•+}	169-171
30.	Table 5.12: Composition of selected molecular orbitals with beta spin of (1) ^{•+}	172-174
31.	Table 5.13: TD-DFT calculated electronic transitions of (1) ²⁺	176-177
32.	Table 5.14: Composition of selected molecular orbitals with alpha spin of (1) ²⁺	177-178

33.	Table 5.15: Composition of selected molecular orbitals with beta spin of $(\mathbf{1})^{2+}$	179-180
34.	Table 5.16: Orbital energies of $(\mathbf{1})^{2+}$ from DFT-calculation	181
35.	Table 5.17: TD-DFT calculated electronic transitions of $(\mathbf{1})^{\bullet-}$	183
36.	Table 5.18: Composition of selected molecular orbitals with alpha spin of $(\mathbf{1})^{\bullet-}$	184-185
37.	Table 5.19: Composition of selected molecular orbitals with beta spin of $(\mathbf{1})^{\bullet-}$	186-187
38.	Table 5.20: Orbital energies of $(\mathbf{1})^{\bullet-}$ from DFT-calculation	187-188
39.	Table 5.21: TD-DFT calculated electronic transitions for $(\mathbf{1})^{2-}$	189-190
40.	Table 5.22: Orbital energies of $(\mathbf{1})^{2-}$ from DFT-calculation	191
41.	Table 5.23: Composition of selected molecular orbitals with alpha spin of $(\mathbf{1})^{2-}$	192-193
42.	Table 5.24: Composition of selected molecular orbitals with beta spin of $(\mathbf{1})^{2-}$	194-195
43.	Table 5.25: Gouterman orbitals for the optimized monomer	196
44.	Table 5.26: Gouterman orbitals for the distorted monomer	197
45.	Table 5.27: Gouterman orbitals for the dimer 1	197

List of Scheme

	<i>Page No</i>
1. Scheme 1.1: Cyclization of α,γ -biladienes	14
2. Scheme 1.2: Direct tetramerization of pyrrole	15
3. Scheme 1.3: Generation of the β -Substituted Corroles through Dipyrroles and Bipyrrrole Condensation	16
4. Scheme 1.4: Retrosynthetic study of Meso-Substituted Corroles	17
5. Scheme 1.5: A ₃ -Corroles synthesis from Pyrrole	18
6. Scheme 1.6: Synthetic protocol for 5,10,15-Triphenylcorrole by a revised Rothmund reaction	18
7. Scheme 1.7: A ₃ -corrole synthesis from pyrrole and aldehyde	19
8. Scheme 1.8: Synthesis of a trans A ₂ B-corrole from dipyrromethane and aldehyde	20
9. Scheme 2.1: Reactivity of silver (III)-corrole complexes with methylmagnesium Chloride	34
10. Scheme 2.2: Proposed mechanism	40
11. Scheme 3.1: Literature review of the previously reported cases of ring contraction	59
12. Scheme 3.2: Comparative reactivities of ferrocenyl-porphyrin with copper acetate and silver acetate	60
13. Scheme 5.1. The species characterized in this work	156

LIST OF ACRONYMS

<i>Acronyms</i>	<i>Full Name</i>
^1H NMR	Proton Nuclear Magnetic Resonance
DDQ	2,3-Dichloro-5,6-dicyano-1,4-benzoquinone
CH_2Cl_2	Dichloromethane
CHCl_3	Chloroform
^{13}C NMR	Carbon-13 Nuclear Magnetic Resonance
^{19}F NMR	Fluorine-19 Nuclear Magnetic Resonance
EPR	Electron Paramagnetic Resonance
UV-Vis	Ultraviolet–Visible
NIR	Near-Infrared
DFT	Density Functional Theory
cor	corrole
TD-DFT	Time-Dependent Density Functional Theory
HCl	Hydrogen chloride
TFA	Trifluoroacetic acid
NaNO_2	Sodium nitrite
GOF	Goodness of Fit
CCDC	Cambridge Crystallographic Data Centre
TBAP	Tetrabutylammonium perchlorate
OTTLE	Optically Transparent Thin Layer
HOMO	Highest Occupied Molecular Orbital
SOMO	Singly Occupied Molecular Orbital

LUMO	Lowest Unoccupied Molecular Orbital
Anal. Calcd	Analytically Calculated
CH ₃ CN	Acetonitrile
FB	Free-Base
TLC	Thin Layer Chromatography
ESI	Electrospray Ionization
CH ₃ OH	Methanol
KOH	Potassium hydroxide
CaH ₂	Calcium hydride
HPLC	High-Performance Liquid Chromatography
ILCT	Intra-Ligand Charge Transfer
MLCT	Metal to Ligand Charge Transfer
LMCT	Ligand to Metal Charge Transfer
Na ₂ SO ₄	Sodium sulphate
CD ₂ Cl ₂	Dideuteromethylenechloride
Cu(OAc) ₂ .H ₂ O	Copper acetate monohydrate
Ag(OAc)	Silver acetate
Bu ₄ NPF ₆	Tetrabutylammonium hexafluorophosphate
GC-EIMS	Gas Chromatography Electron Ionization Mass Spectroscopy
ORTEP	Oak Ridge Thermal Ellipsoid Plot Program
DBU	1,8-Diazabicyclo[5.4.0]undec-7-ene
IVCT	Intervalence Charge Transfer
THF	Tetrahydrofuran



Chapter One

Introduction of Corrole

1.1 Introduction

1.2 Structure and Nomenclature of Porphyrin

1.3 Spectral characterization of porphyrin

1.4 Structural variation

1.4.1 Contracted Porphyrins

1.4.1.1. Subphthalocyanines

1.4.1.2. Isocorrole

1.4.1.3. Norcorrole

1.4.1.4. Subporphyrins

1.4.1.5. Synthetic Protocols of all the above-mentioned Contracted Porphyrins

1.4.1.6 What is Corrole

1.4.1.6.1 Properties of Corrole

1.4.1.6.2 Synthesis of corrole

1.4.1.6.3 Corrole Metal complexes

1.4.1.6.4 Coordination mode of corroles

1.4.1.6.5 Application of Corrole and

Metallocorroles in various fields

1.5 Lacunae

1.6 Scope and Objectives of the Present Thesis

1.1 Introduction:

Ever since the origin of civilization, human being has wondered about the life on earth and always tried to decode and imitate the naturally occurring systems and processes. Due to these continuous searching, several discoveries have enhanced our knowledge about the natural elements. Life on earth mostly depends on one of the most important natural occurring process named photosynthesis. For this process, chlorophyll, **1** (Figure 1.1)¹ is the primary pigment. It is a green coloured pigment which gives leaves their green colour. Through photosynthesis light energy is converted into chemical energy with the help of carbon dioxide (CO_2) and water (H_2O). As a by-product, glucose ($\text{C}_6\text{H}_{12}\text{O}_6$) is formed and oxygen (O_2) gas is liberated. Photosynthesis produce and conserve the oxygen quantity in the atmosphere and provide all the necessary minerals and most of the energy necessary for life on Earth. Basic structure of the chlorophyll molecule contain porphyrin ring, **4** (Figure 1.1)² as the core moiety coordinating with a magnesium atom in centre. This core structure is almost identical with heme group found in haemoglobin, **2** (Figure 1.1)¹ which is an oxygen carrying pigment in red blood cell. But in case of heme, porphyrin ring coordinate with an iron metal. Another porphyrin containing natural ingredient is cytochrome P450, **3** (Figure 1.1)¹. It consists of the similar structure like heme with one cysteine thiolate ligand attached to the iron centre. It helps to metabolize potentially toxic compounds from the food and drugs which is a very essential process to protect our body. This porphyrin ring can bind with different metal ions and each combination provide different biological functions.³ The name ‘porphyrin’ originates from the twentieth century Greek word ‘porphura’ which means purple and all porphyrins are intensely coloured. Because of the bright colour and biological applicability in nature, porphyrins are named as “pigments of life”.¹

1.2 Structure and Nomenclature of Porphyrin:

The parent ring of porphyrins is called porphin, **5** (Figure 1.2) which comprise of four pyrrole rings attached with each other via methine bridges ($=\text{CH}-$) at the α carbons with an extensive delocalization.

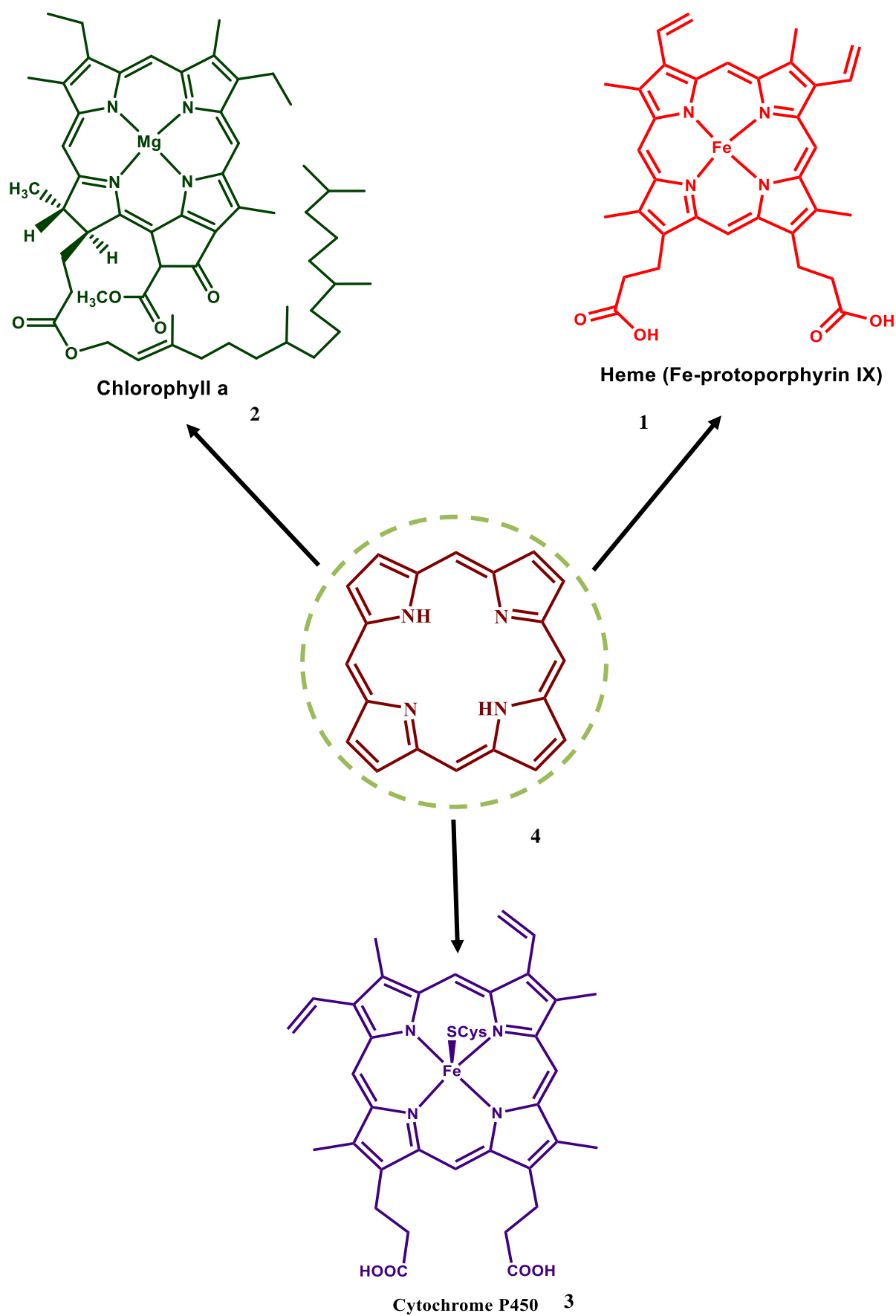
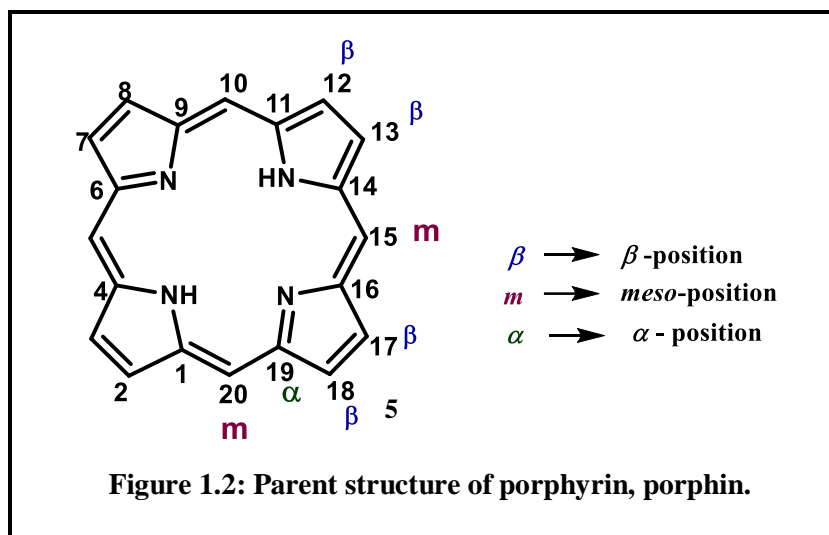


Figure 1.1: Structures of biological pigments containing porphyrin macrocycles.³

In the inner core it has two amino ($-NH$) and two imino ($=N$) like N atom². It is a planar macrocycle, with π - π conjugation and with several possible conformational arrangements. In the year of 1912, W. Küster recommended this cyclic tetrapyrrole structure.⁴ All porphyrins consist of this similar basic structure, but they can exist in various form containing different substituents at the β positions (2, 3, 7, 8, 12, 13, 17 and 18) or on the meso positions (5, 10, 15 and 20).²



In earlier days, all these porphyrinoids were given trivial names derived from their colour and other features of the macrocycles by their concerned discoverer to avoid the complexity of usual IUPAC nomenclature. Those names were followed by the suffix “phyrin” or “rin” from porphyrin.⁵ R.B. Woodward first assigned a pentapyrrolic porphyrinoid as “sapphyrin” after it was found as dark blue solid crystal.⁶ Following that trend, later bright red coloured six-pyrrole-containing macrocycles were named as rubyrin and large “Texas-sized” system as “texaphyrin”. Gossauer established other less colourful names like “pentaphyrin” and “hexaphyrin” for five and six pyrroles containing porphyrinoids respectively.⁷ A while later a generalized schematic approach had been proposed by Franck and Nonn.⁸ As stated by him, hexaphyrin is represented as [26]hexaphyrin-(1.1.1.1.1.1). This naming process has three important steps: a) all the π -electrons involve in the conjugation is mentioned within the square-brackets b) general name denote the number of existing pyrrolic rings in the macrocycles c) at last the number of connecting carbon atoms in the middle of the heterocyclic rings are written within first brackets separated by dots.²

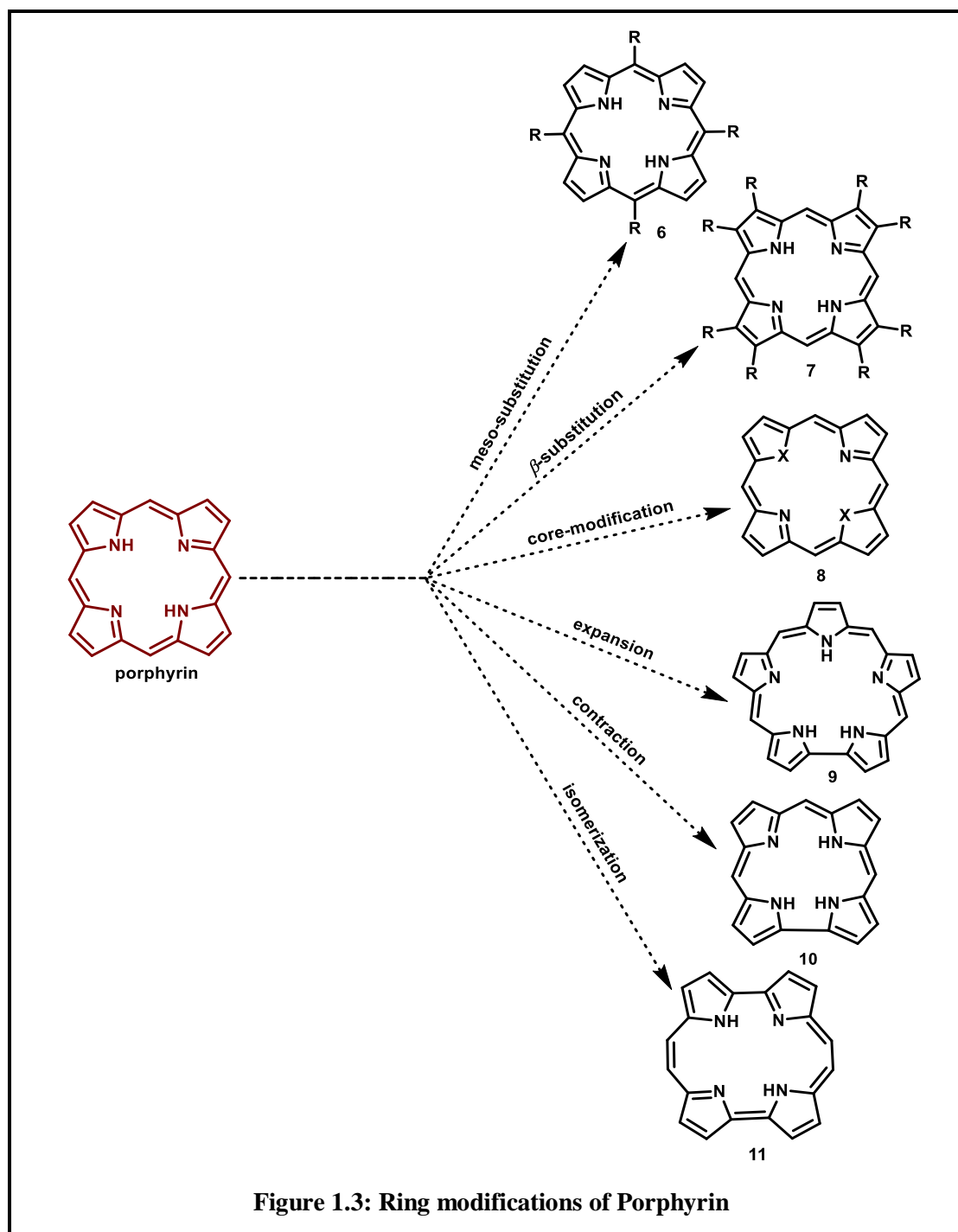
1.3 Spectral characterization of porphyrin:

Porphyrins are one of the strongest lights absorbing substance in nature and due to that property, they display intense colour. UV-Visible spectroscopy is the most fundamental technique for the explanation of the electronic structure of porphyrin even at very low concentration. Porphyrin have characteristics absorption spectra due to their fourfold symmetry. They show intense band at 400 nm which is called Soret band (molar extinction coefficients $\sim 10^5 \text{ M}^{-1}\text{cm}^{-1}$) and another weak bands within 500-650nm which called Q band.^{9,10} Sometime this characteristic bands perturb because of change in electronic factor, structural variation etc. This spectroscopy is also effective in differentiating between the porphyrin and their metal complexes.

^1H NMR spectra of porphyrins confirm its aromatic nature. Spectrum of free-base porphyrin disclose that the inner N-H protons resonate in the shielded region of δ -2 ppm to -4 ppm. Both the *meso*- and β -pyrrolic protons resonate at deshielded region. For *meso*-protons it appears at $\delta \sim 8$ ppm to 9 ppm and the β -pyrrolic protons appear at $\delta \sim 10$ ppm.^{11,12}

1.4 Structural variation:

Field of porphyrins has been expanded into a subject of multidisciplinary research because of their importance and applicability in a wide range of areas such as chemistry, biology and medicine. Researchers are trying hard to synthesize various porphyrinoids using different substituents and some structural changes in the ring (Fig 1.3). These syntheses lead to attune the electronic structure and function of the porphyrin which shows different applications in various field. Most used technique for this purpose is *meso* and β - substitution at the porphyrin ring.² Through these techniques both symmetrical and unsymmetrical *meso*- substituted porphyrinoid, **6** (Figure 1.3) and β -substituted porphyrinoid, **7** (Figure 1.3) derivatives have been synthesized. β -substituted porphyrinoids are widely available in natural elements like chlorophyll, haem, cytochrome P450 etc. The *meso*-substituted porphyrins are not structurally identical to the naturally existing one, but they can be used as models for the biological cofactors and also in material science.¹³ Apart from substitutions at the

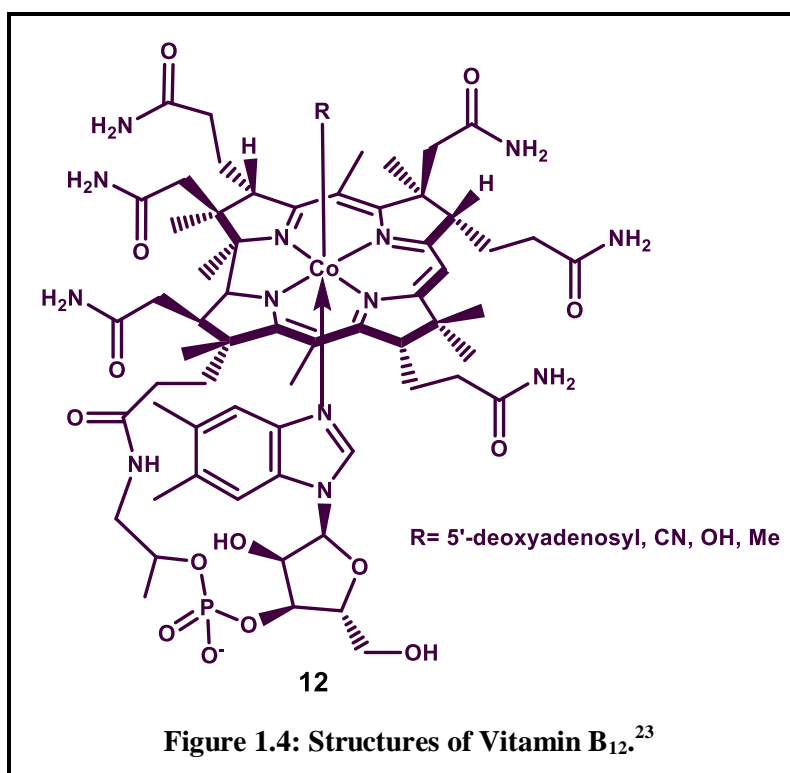


ring, structural changes at the porphyrin core has also been performed which can vary its reactivity in various reactions.² As for example inner ring N atoms can be exchanged by other heteroatoms like oxygen, sulphur, selenium, tellurium or carbon, **8**.² Other forms are because of expansion, contraction and isomerisation of the ring. Structure **9** denotes expanded porphyrin. This derivative composed of more than four pyrrole rings which are arranged through either direct bonding with each other or by one or more connecting atoms. The inner core moiety consists of a at least 17 atoms.² Innumerable

studies on expanded porphyrins show that it can acquire different type of conformations with Möbius and twisted-Hückel topologies.¹⁴ Recent studies reveal its application in numerous fields like photodynamic therapy, medicinal chemistry, sensing, nonlinear optics (NLO) etc.^{15,16} These expanded porphyrins also stabilize higher coordination number of some metals specially for lanthanides and actinides.^{17,18} Another form of structural change is isomerization of the ring. Isomeric porphyrin, **11** can be explained as the structural modification of the main $C_{20}H_{14}N_4$ unit by jumbling of the position of four pyrrole ring and four bridging carbon atoms.² Contracted porphyrin analogues, **10** comprise of at least three pyrrole ring or pyrrole like units organized in a conjugated skeleton and there will be minimum one *meso*-carbon or one pyrrole-ring less than the parent porphyrin structure.^{2,5}

1.4.1. Contracted Porphyrins:

Origin of contracted porphyrin is an outcome of the structural discovery of vitamin B₁₂, **12** (Figure 1.4). This vitamin has a direct relation with pernicious anaemia (PA) which was a fatal illness before the 1920s. But the discovery of vitamin B₁₂ has changed the situation which finally cure the pernicious anaemia and leads to Nobel Prize in Medicine in the year of 1934. The structural clarification of



vitamin B₁₂ reveals that it has corrin ring as a core moiety which is similar to porphyrin macrocycle with one less meso carbon atom.¹⁹⁻²² This corrin ring can be classified as contracted porphyrin because of its structural similarity. Soon after the structural explanation, researchers devoted their efforts towards the progress of suitable synthetic protocols for Vitamin B₁₂. In the year of 1960, Johnson and Price planned to synthesize a series of metallic derivatives of pentadehydrocorrin and from that they suggested the name corrole.²⁴ Later in the year of 1965, Johnson and Kay first reported the synthesis of corrole and proposed that the term corrole can be classified as a macrocycle containing ten double bonds hence a “tetrahydrocorrins”.²⁵ Following that report, later researchers started to develop several other contracted porphyrinoid systems (Figure 1.5). Some of the well-explored contracted porphyrins have been discussed in below:

1.4.1.1. Subphthalocyanines:

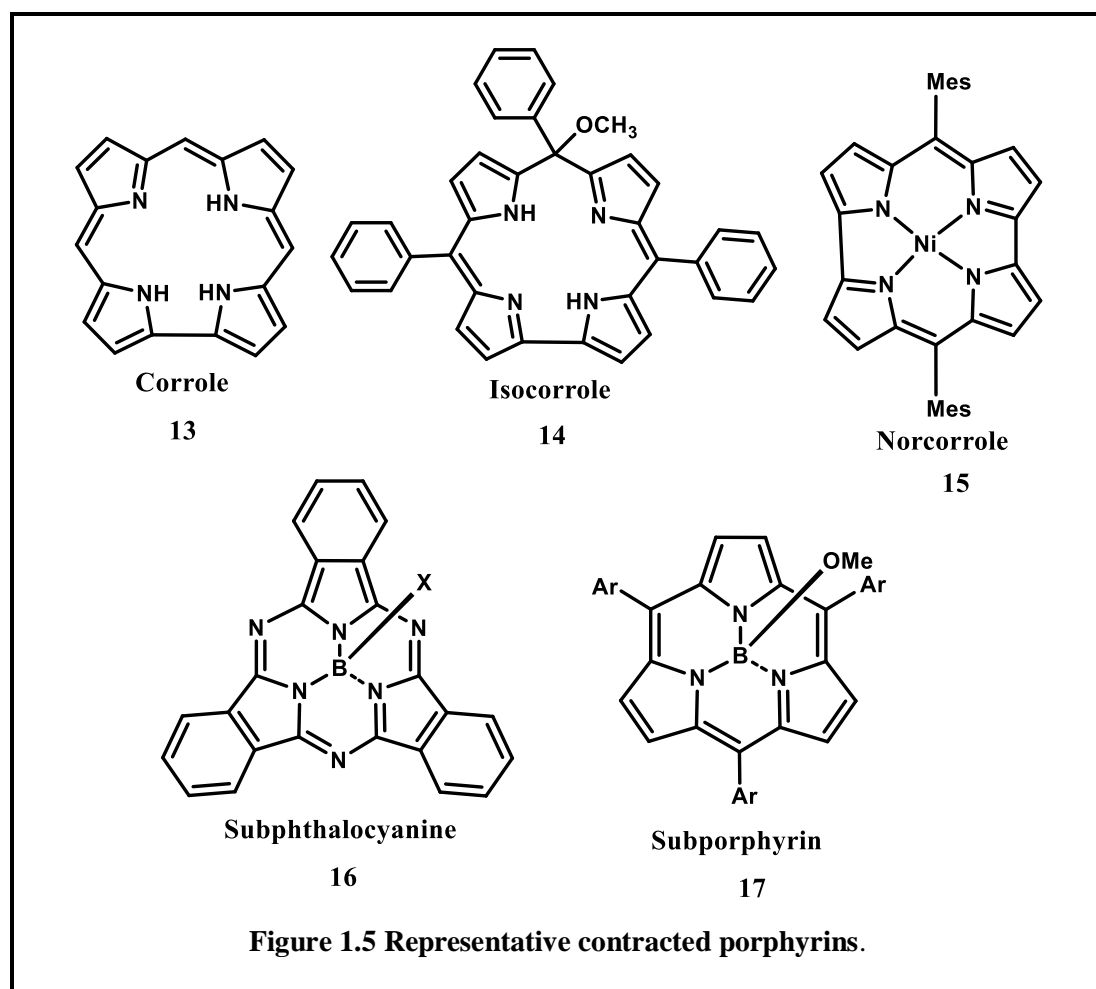
Subphthalocyanines, **16** (Figure 1.6) are 14 π -electron containing aromatic macrocycles with a boron atom within the central cavity. It is considered as the lower homologues of phthalocyanines. Subphthalocyanine consist of three N-fused diiminoisoindoline units surrounding the boron centre.²⁶ This unusual structure of Subphthalocyanine makes its chemical and physical properties very interesting. In recent times, subphthalocyanine derivatives have been appeared as a very useful material in various applications like: optical data storage, organic electronic devices such as nonlinear optics, chemical sensors, organic photovoltaics (OPVs), photodynamic therapy etc.^{27,28}

1.4.1.2. Isocorrole:

Isocorrole, **14** (Figure 1.5) is a stable isomer of corrole. Some of the tetrapyrrolic macrocycle isocorrole contain one sp³ hybridized meso carbon atom and two inner NH protons which arrange opposite to each other. The name isocorrole has been used to indicate that it is a corrole analogue.²⁹

1.4.1.3. Norcorrole:

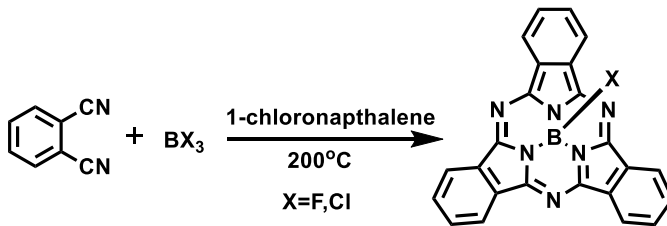
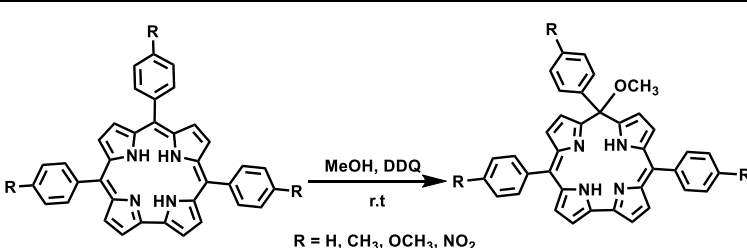
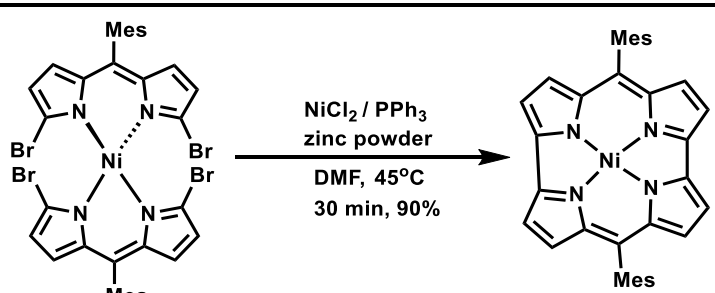
Norcorrole, **15** (Figure 1.5) is another ring-contracted version of porphyrin. It has a shortage of two meso carbons than porphyrin. The ring structure has 16π electron and according to the Hückel rule it is antiaromatic system. In the year of 2008, Bröring et al. first developed the synthesis of a norcorrole–iron (III) complex, but it was almost impossible to isolate because of the rapid dimerization.³⁰ Also, later in the year of 2012, another synthesis of norcorrole has been reported. Synthesis of antiaromatic norcorrole–nickel(II) has been performed through metal-templated procedure. Due to the unstable nature of this antiaromatic porphyrinoid, norcorrole–nickel(II), this efficient synthetic protocol is a remarkable development. Moreover, this synthetic accessibility makes it possible to study those antiaromatic norcorroles for various applications like organic opto-electronic materials.³¹

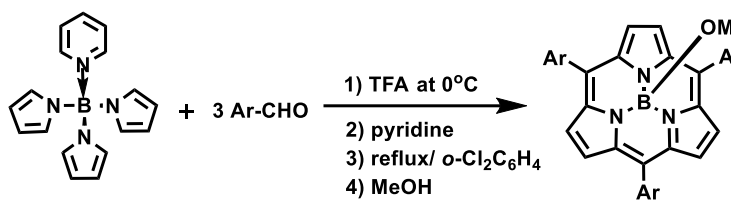


1.4.1.4. Subporphyrins:

Subporphyrins, **17** (Figure 1.5) is equivalent to subphthalocyanine in structure. This category is the proper ring-contraction form of porphyrin containing three pyrrole rings attached through methine bridges (=CH–). It is a bowl-shaped macrocycle with 14π electron aromatic circuit. First ever synthesized subporphyrin is tribenzosubporphine in 2008 by Osuka et al. It exhibits some peculiar characteristics like green coloured fluorescence, well-defined aromaticity appeared from proper conjugation with 14π -electron.³²

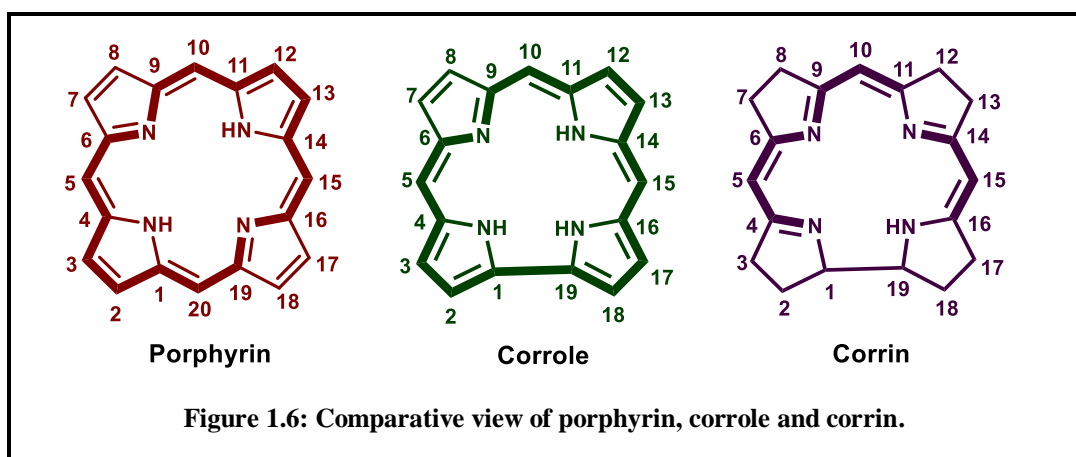
1.4.1.5. Synthetic Protocols of all the above-mentioned Contracted Porphyrins:

Contracted Porphyrin	Synthetic Report	Reaction Scheme
1. Subphthalocyanine	A. Meller and A. Ossko in 1972 ²⁶	 <p>1,2-dicyanobenzene + BX_3 $\xrightarrow[200^\circ C]{\text{1-chloronaphthalene}}$ Subphthalocyanine derivative (X = F, Cl)</p>
2. Isocorrole	Paolesse <i>et al</i> in 2007 ²⁹	 <p>Macrocycle precursor $\xrightarrow[r.t.]{\text{MeOH, DDQ}}$ Isocorrole derivative (R = H, CH₃, OCH₃, NO₂)</p>
3. Norcorrole	Shinokubo <i>et al</i> in 2012 ³¹	 <p>Nickel complex $\xrightarrow[30 \text{ min, } 90\%]{\text{NiCl}_2 / \text{PPh}_3, \text{zinc powder, DMF, } 45^\circ C}$ Norcorrole derivative</p>

4. Subporphyrin	A.Osuka and Y. Inokuma in 2008 ³²	 <p>Ar = Ph, 4-<i>tert</i>-BuPh, 4-BrPh, 4-CNPh, 4-NO₂Ph, 3,4,5-(OMe)₃Ph, 2,4,6-(OMe)₃Ph</p>
-----------------	--	---

1.4.1.6. What is Corrole:

Corroles, **13** (Figure 1.5) have structural similarity with the cobalt-chelating corrin ring in vitamin B₁₂ and this similarity is the main driving force behind the discovery of corrole ring.²³ In the year of 1971, Hodgkin *et al* resolved the crystal structure of free base corrole ring for the first time.³³ It has 18 π electron aromatic system which is also closely related to porphyrin. So, basically corrole should be described as the intermediate of porphyrin and corrin. Despite of all the structural similarities between porphyrin and corrole, there are some major structural differences between porphyrin and corrole.^{2,5} In case of corrole, one of the *meso*-carbons, C-20 is missing and because of that two pyrrole rings at that position are directly connected by a bond between C-1 and C-19. Numbering of corrole macrocycle is derived from the porphyrin ring. Inner core of corrole ring contain three amino nitrogens and one imino nitrogen and these NH protons tautomerize very rapidly in the free-base corrole.



Because of the absence of C-20 position, the inner N₄ coordination core become much more contracted than porphyrin which make it suitable for stabilizing the higher oxidation states of metal ions.^{2,34}

1.4.1.6.1 Properties of Corrole:

Due to the presence of three NH protons, corrole can behave as trianionic instead of dianionic and it also has lower symmetry than porphyrin. The meso-carbon positions are extremely reactive for substitution reactions, specially to oxidation. Corrole π cloud system is way more electron-rich than porphyrins. As the inner core already accommodate three NH, there is apparently no such steric enhancement after the addition of another proton to the imine nitrogen. However, on elimination of one proton from the inner core, a significant amount of energy is released because of steric relaxation which finally leads to surprisingly high NH acidity of corroles.²

In the year of 1971, Hodgkin and co-workers have published the first crystal structure of the corrole macrocycle during their project on the structural investigation of vitamin B₁₂.³³ Much accurate structures were reported in 1999 from the structural examination of 5,10,15-tris(pentafluorophenyl)corrole which were studied at 116 K.³⁵ This result showed a notable displacement from the ring planarity to reduce the steric crowding within the contracted N₄ coordination core because of the three NH protons. The pyrrole rings are slightly twisted from the mean plane with angles of 4.4-19.58°. As a result of the saddling type structure, two NH protons in the core shifted to above and below the mean plane while another NH proton remain in the mean plane.^{35,36}

Corroles are intensely coloured compound. Electronic absorption spectra of corrole is almost like corresponding porphyrin ligand. They display an intense band at around 400 nm (soret band) and weaker bands within the range of 500-600 nm (Q bands). They show strong fluorescence in the range of 600-700 nm. Fluorescence intensity increases upon deprotonation of inner NH proton which are facilitated by the steric release.³⁷

^1H NMR spectra of corroles exhibit similar characteristics like porphyrin. The *meso*- and the β -protons resonate in the deshielding region and the peaks for meso proton appear at ~8 to ~9 ppm and β -protons appear at ~10ppm. This kind of diatropic ring current clearly points out the aromatic character of the macrocycle. The inner ring NH protons appear in the shielding zone of -2.00 to -3.00 ppm, as a broad singlet and this broadness is because of the highly acidic character of those NH protons and the non-identical tautomers.³⁸

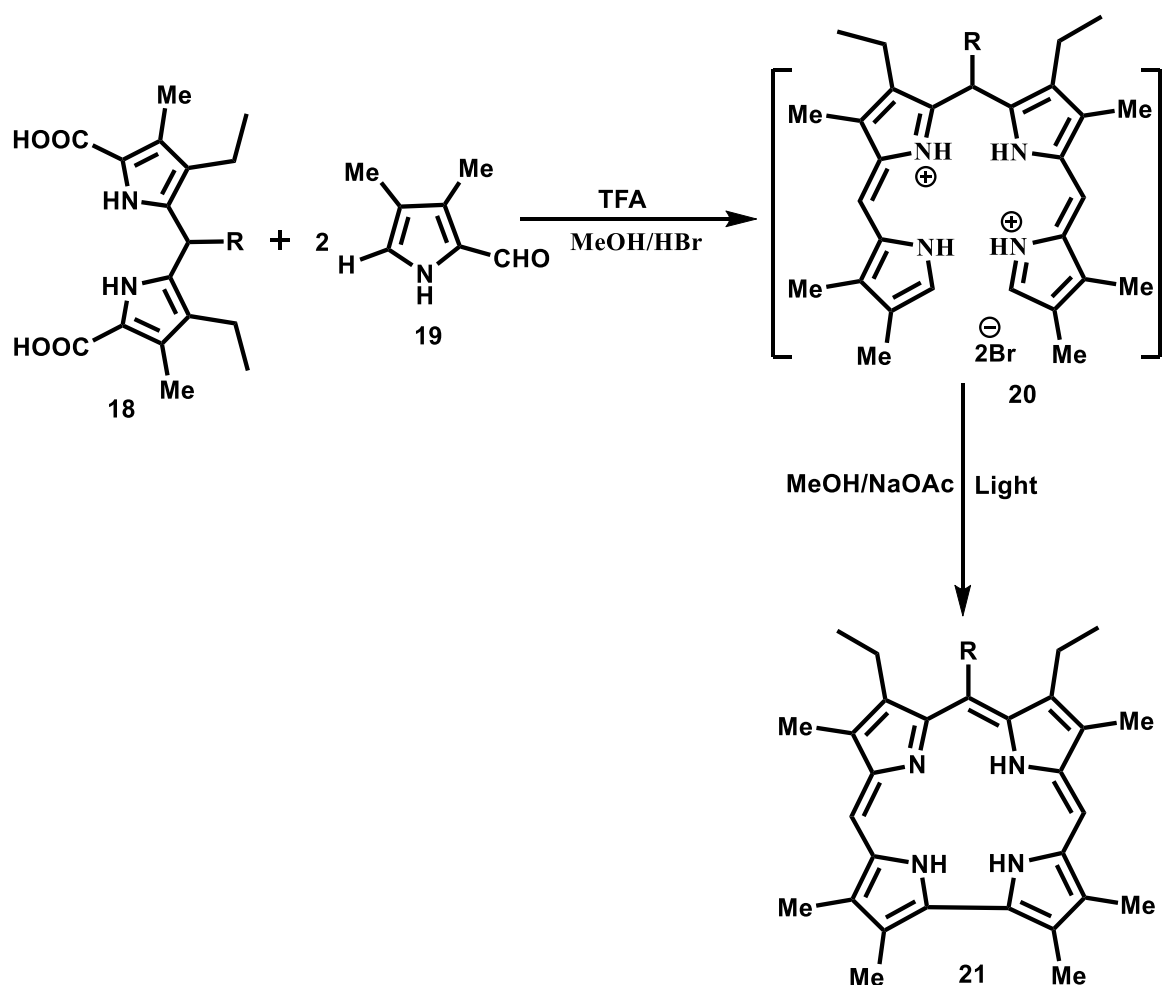
1.4.1.6.2 Synthesis of corrole:

First corrole synthesis has been reported by Johnson and Kay in 1965 during the synthesis of vitamin B₁₂. Their plan was to synthesize corrin ring which is the core skeleton of vitamin B₁₂ and they finally leads to the synthesis of corrole macrocycles through cyclization of a,c-biladienes.²⁵ From then many researchers started to develop numerous procedures to simplify the synthetic procedure and increase the yield. In this section, some of the important synthetic procedures have been discussed.

a) Synthesis of β -substituted corrole:

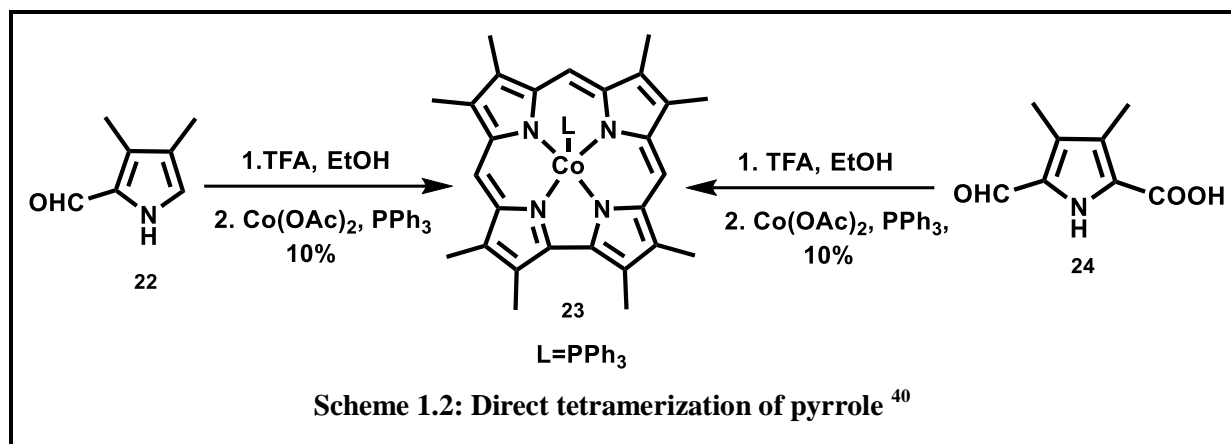
1) From a,c-biladienes:

Johnson and Kay in 1965 first time synthesize corrole, **21** (Scheme 1.1) via photochemical cyclization of a,c-biladienes, **20**.²⁵ The methanolic solution of a,c-biladienes were treated with slight excess of ammonium hydroxide or sodium acetate (Scheme 1.1). After that the solution is illuminated under 200w bulb at a distance of 5 cm and the colour of the solutions changed from yellow to green. On cooling the solution, the crystalline corroles were obtained with 20-60% yield. They readily formed purple crystalline monohydrobromides (porphyrins give dihydrobromides) The yield of these reactions varied from 20-60%. The necessary a,c-biladienes is a tetrapyrrolic compound which has been synthesized by the condensation between two equivalents of 2-formylpyrrole, **19** and one equivalent of dipyrromethanedicarboxylic acid, **18**. The desired a,c-biladienes has been isolated as the crystalline hydrobromides with 80% yield. In 1994 Vogel *et al* have reported the use of *p*-chloranil as a versatile oxidant which improve the cyclization step.³⁹

Scheme 1.1: Cyclization of a,c-biladienes⁴⁰

2) Direct pyrrole tetramerization:

For the synthesis of β -substituted corrole, **23** (Scheme 1.2) most of the reports include those methodologies which leads to stepwise formation of the tetrapyrrolic intermediates. Regardless of a series of research for decades, there is only one suitable procedure for synthesizing β -substituted corrole in one single step. In the year of 1996, Paolesse *et al.* have published another synthetic protocol for corrole from substituted pyrroles, **22**, **24**.⁴¹ Meso-free β -substituted corroles has been synthesized using 3,4-dimethyl-pyrrole-2-carbaldehyde, **22** which results into the emergence of β -substituted corrole via tetramerization with 10% yield. While using 3,4-dimethyl-2-formylpyrrole-5-carboxylic acid, **24** as the starting material, corrole, **23** has been formed with similar yield because of the rapid decarboxylation in acidic media. This reaction scheme goes via Friedel–Crafts reaction



mechanism succeeding by dehydration, emergence of a cobalt complex, then formation of the cobalt complex through cyclization, and at last one of the meso carbon atoms eliminate from the system.⁴⁰

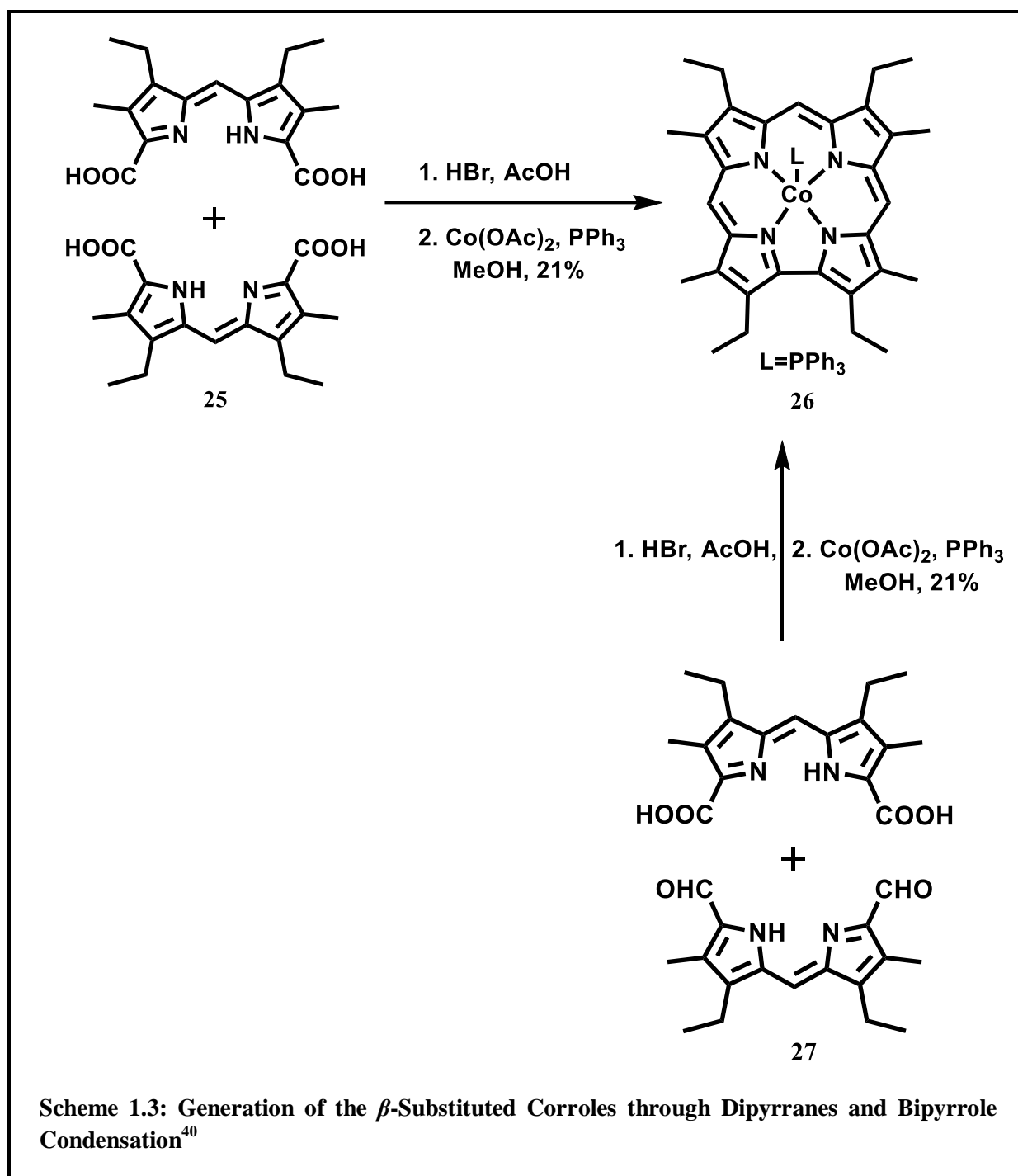
3) From the 2,2'-Bipyrrole and Dipyrroles derivatives:

Another suitable corrole synthetic protocol can be recommended from the structure of corrole macrocycle which is by the addition of substituted dipyrane with 2,2'-bipyrrole, **25** (Scheme 1.3). In the year of 1973 Conlon et al have first reported this procedure.⁴² Mixture of substituted dipyrane and bipyrrole under acidic condition lead to the formation of a red precipitate which after addition of triphenylphosphine and cobalt (II) acetate convert into cobalt (III)corrole, **26** complexes with moderate yield. In this reaction cobalt (II) acetate facilitate corrole formation by stabilizing the tetrapyrrolic intermediate. But the absence of metal in the reaction leads to the generation of another complex named octapyrrolic macrocycles.⁴⁰

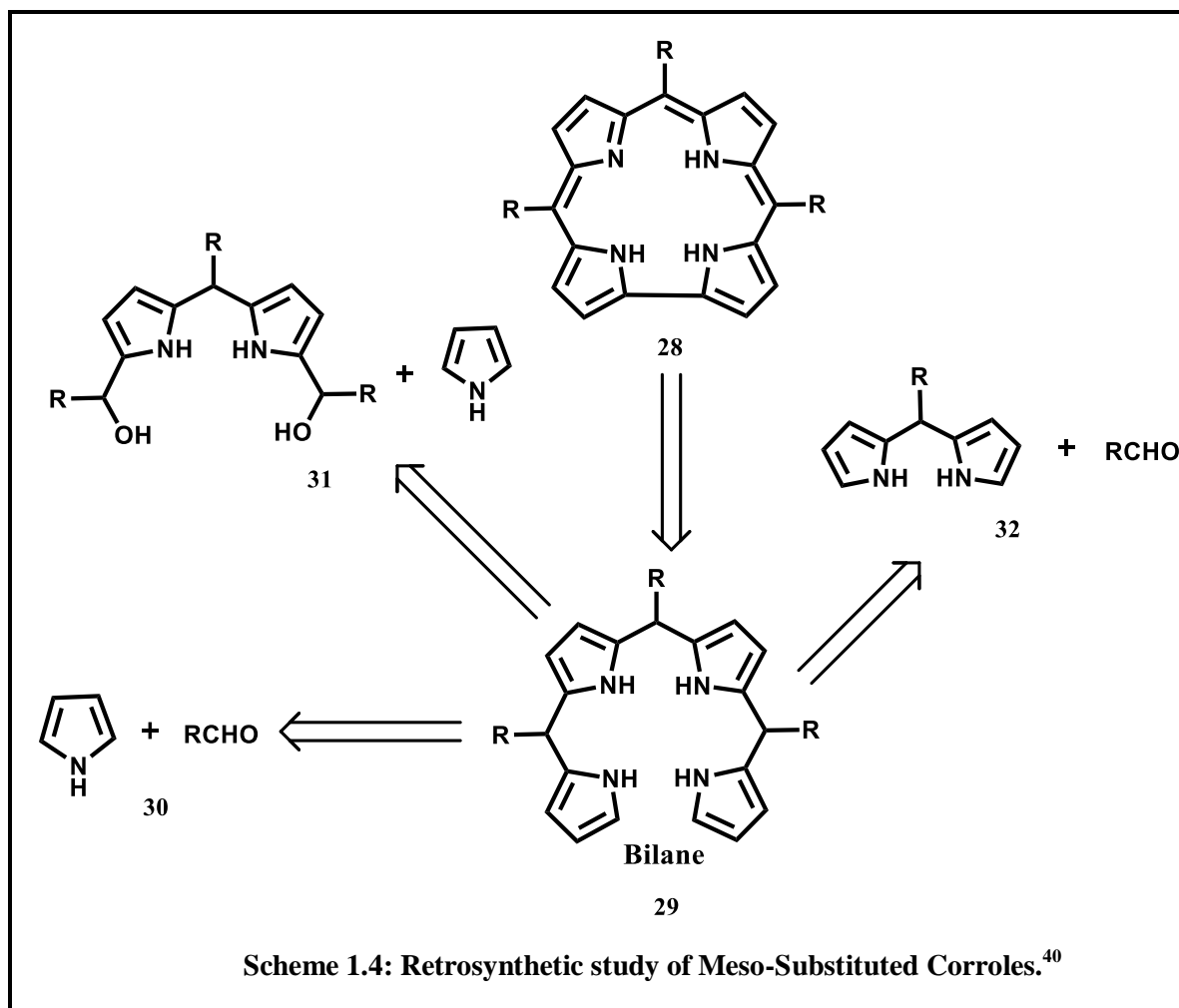
b) Meso Substituted Corrole:

There are several synthetic protocols for the *meso*-substituted corroles. Retrosynthetic study of *meso*-substituted corroles, **28** (Scheme 1.4) reveals that it goes via bilane, **29** formation which is a tetrapyrane derivative. Different procedures are there for synthesizing bilane, **29**:

a) directly from pyrrole and aldehydes, **30** (scheme 1.4); b) from dipyrane–diols and pyrrole, **31**; and c) from dipyranes (dipyrromethanes) and aldehydes, **32**.⁴⁰ There are different types of corroles depending on the substitutions at meso positions.

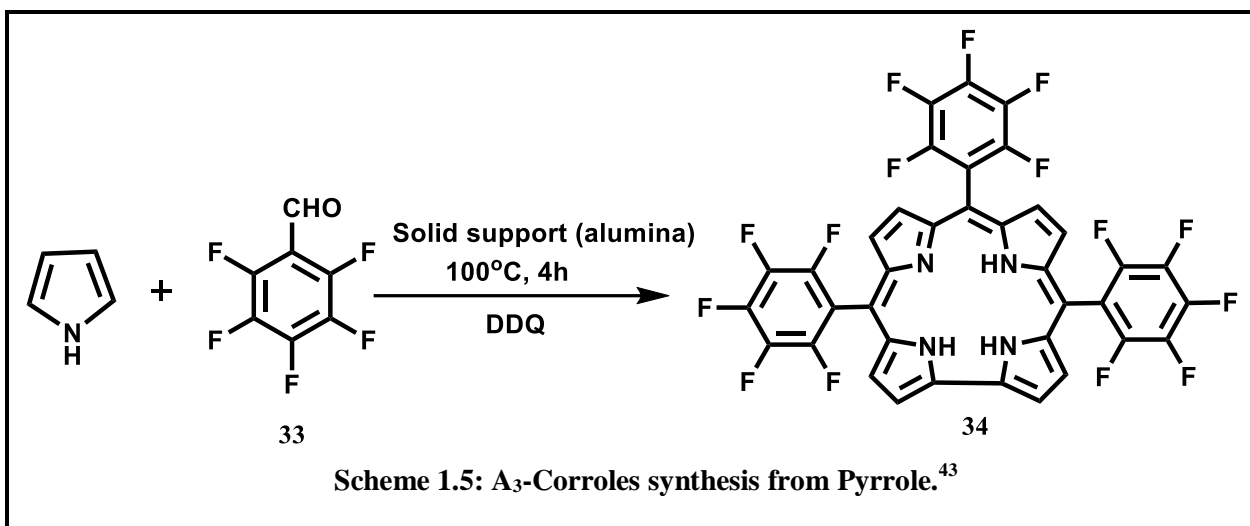


a) A_3 corroles: All the three meso positions (5, 10 and 15) consist of three similar substituents. b) A_2B corroles: Types of Corroles which bear identical substituents at 5 and 15 positions, and the 10 position contain different substituent are called trans- A_2B -corroles. Cis- A_2B corroles can also exist but the trans patterns are much more favoured due to synthetic approachability.⁴⁰

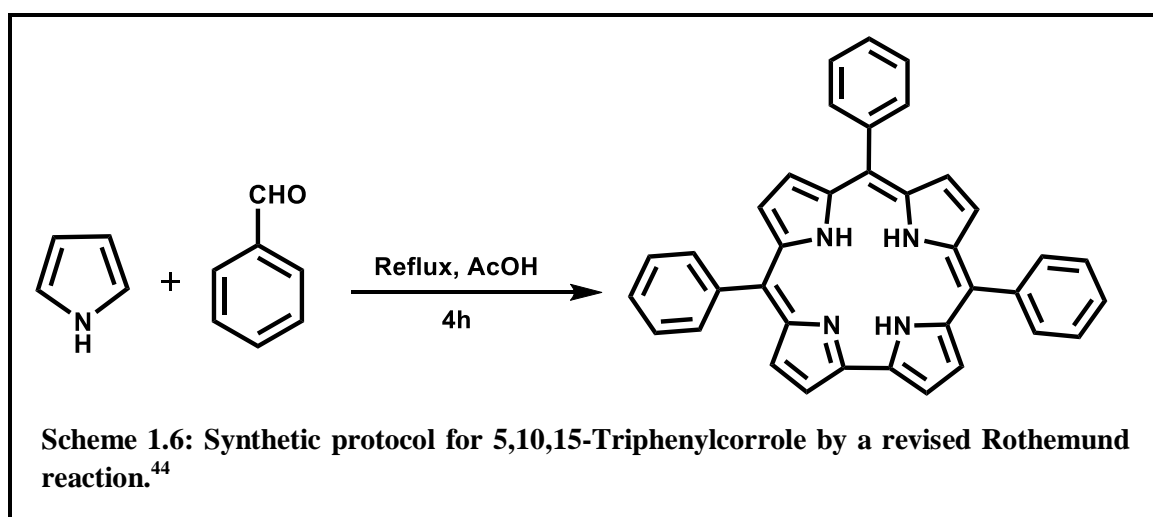


Synthesis of A₃ Corrole:

In the year of 1999 Gross and co-workers have reported this one pot corrole synthesis for the first time which include the condensation of pyrrole and aldehydes without using any solvent. They have started with two aldehydes: benzaldehyde and pentafluorobenzaldehyde. The mixer of equimolar amount of pyrrole and those aldehydes are heated to 100°C for four hours in open atmosphere and after that the solution is oxidised with 2,3-dichloro-5,6-dicyano-1,4-benzoquinone (DDQ). In case of pentafluorobenzaldehyde, **33** (scheme 1.5) 5,10,15-tri(2,3,4,5,6-pentafluorophenyl), **34** corrole is formed with 11% yield. But in case of benzaldehyde, corresponding porphyrin is formed with $5 \pm 8\%$ yield. In this case, reactivity of the carbonyl carbon depends on its positive charge density which mainly influenced by the substituents attached to it. The highly electron-withdrawing property of pentafluorophenyl (C₆F₅) group facilitate the reaction.⁴³

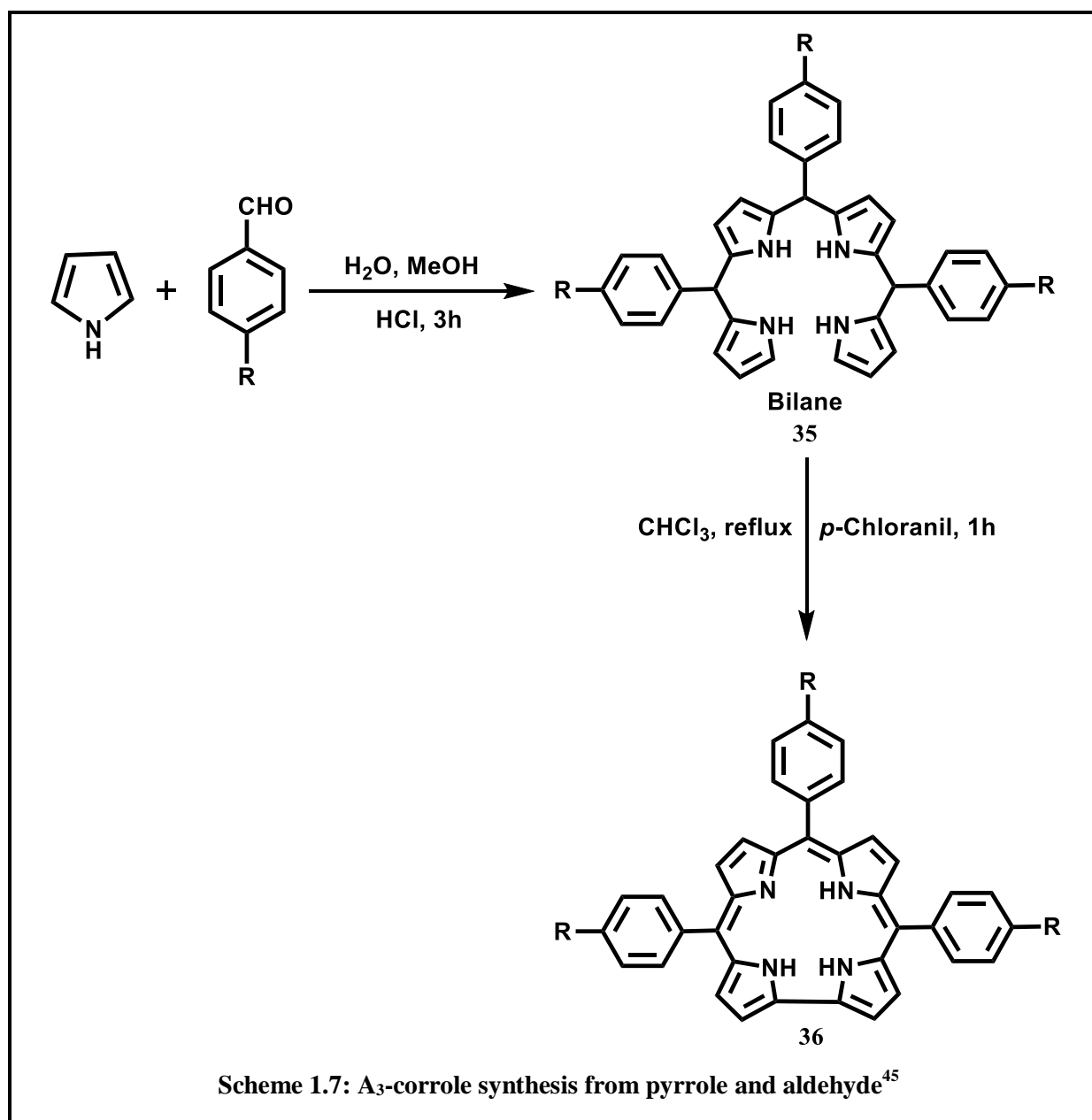


Another accomplished synthetic method for corrole is modified Rothmund reaction. Paolesse *et al* has reported this procedure in 1999 using different type of aldehydes. Mixture of pyrrole and aldehydes are dissolved in acetic acid and the solution is refluxed for 4h. Yield of the product is mainly controlled by the pyrrole and aldehydes molar ratio and the highest yields of corrole is obtained while using 3:1 pyrrole/benzaldehyde (scheme 1.6). While synthesizing A₃ corrole, always a certain amount of A₄ porphyrin has been formed as a side product. Separation of this porphyrin from corrole is sometime really challenging.⁴⁴



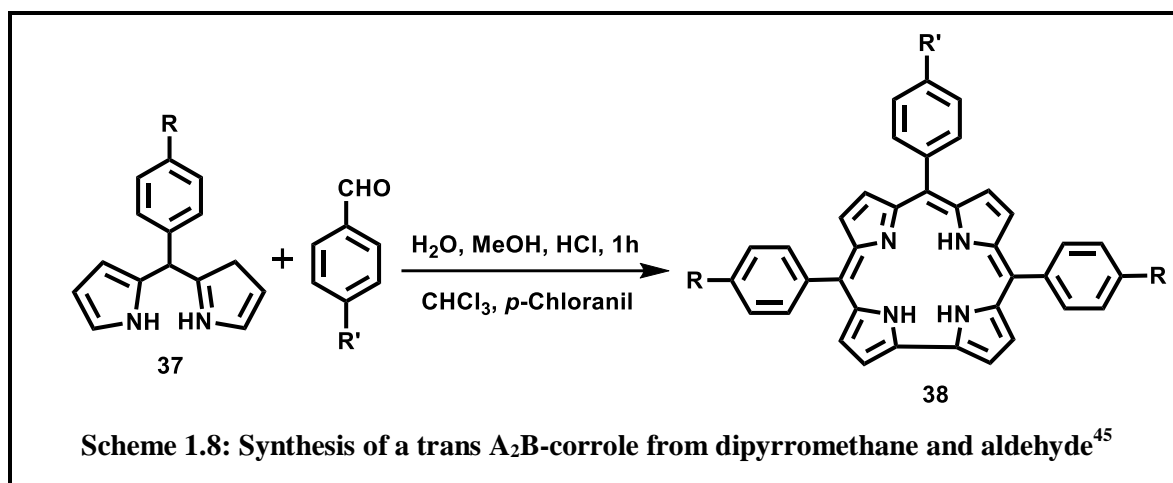
As a solution of this problem later in 2006, Gryko and Koszarna⁴⁵ have proposed one advanced synthetic protocol for corrole encouraged by Král's dipyrroles synthesis⁴⁶. For synthesizing A₃

corrole, the mixture of pyrrole and corresponding aldehyde are stirred in methanol and water mixture (1:1) in presence of conc. HCl as catalyst. First step of this reaction is carried out in a water and methanol mixture which is catalysed by HCl. Ratio of both the solvents are optimized in such a way that lipophilic tetrapyrane, **35** (scheme 1.7) precipitated from the solution and both the dipyrane and tripyrane left in the mixture as a by-product. This procedure leads to a certain increase of the corrole, **36** yield (~30%) and the side product porphyrin decreased to only ~1%.



Synthesis of trans-A₂B Corrole:

Gryko and Koszarna have also utilize their water methanol procedure for trans-A₂B corrole, **38** (scheme 1.8) synthesis. In case of A₂B corrole, they have used unhindered dipyrromethene, **37** instead of pyrrole in the first step. Rest of the procedures are almost same as A₃ corrole. Yield of the desired trans-A₂B corrole is almost 55%. For hindered dipyrroles, they have used MeOH-H₂O in 2:1 ratio which affords 27–31% yield of the desired corrole. The main advantages for this procedure are that the desired corrole is very easy to purify and there no scrambling in the reaction although concentrated HCl has been used.⁴⁵



1.4.1.6.3 Corrole Metal complexes:

Exploration of corrole metal complexes has started right after the successful synthesis of corrole ligand. In previous section, we have already discussed that the inner core NH protons of corroles are highly acidic in nature. So, they can be easily deprotonated, and the inner N atoms can be easily coordinated to a metal ion. As per previous discussion, corrole core is much more contracted than porphyrin and it contain three NH protons in the inner core, so it can stabilize higher oxidation state of metals. The area of corroles and metallocorroles are growing very rapidly due to their diversity in synthesis and applications in various fields. Metalation of corrole can be categorized in two ways: a) cyclization of metallated tetrapyrane and b) by incorporating a metal into the corrole cavity.²

Each year scientists are chelating new elements with corrole from the periodic table. Figure 1.8 highlights all those elements from periodic table which has successfully inserted into the corrole cavity. A large variety of metallocorroles have already been explored because of their vital roles in different fields. In earlier time, only few transition elements were coordinated into the corrole cavity. But through recent developments insertion of various heavy metals like rare transition elements, lanthanides and actinides, main group elements become feasible.

From all the group 1 metals only, lithium corrole complex is reported in the literature which normally use for the synthesis of group 4 metallocorroles (titanium, zirconium, and hafnium), lanthanide (gadolinium) and actinide (thorium and uranium).⁴⁷

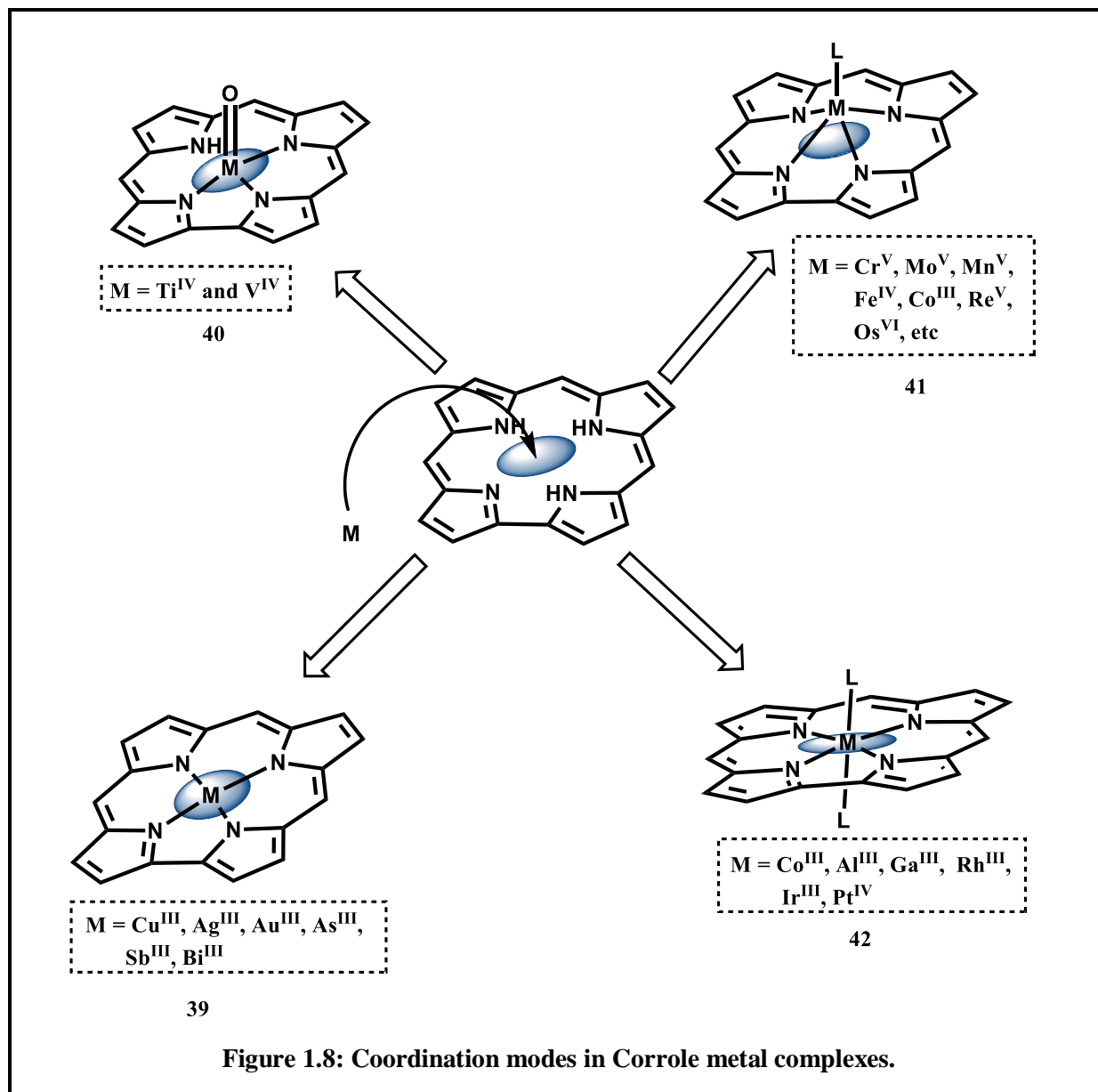
1.4.1.6.4 Coordination mode of corroles:

Usually corrole act as tetradentate and trianionic (Figure 1.8) ligands and this pattern is mainly detected in case of Cu(III), Ag(III), Au(III), As(III), Sb(III), Bi(III), **39** etc.⁴⁸⁻⁵¹ In this coordination

Figure 1.7: Periodic table of elements inserted into corroles macrocycle.⁴⁷

mode complex adopts square planar geometry. Still there are some exceptions in coordination mode. During metalation with $[\text{Ti}(\text{O})]^{2+}$ and $[\text{V}(\text{O})]^{2+}$ corrole can act as tridentate and dianionic ligand, **40**. In this case one of the NH does not participate in metal binding.⁵²

Another exceptional coordination mode is penta-coordination, **41**. It adopts square pyramidal geometry around the metal centre which form a domed like conformation. In this arrangement the central atom is axially displaced from the N₄ coordination core. Mainly trivalent Cr, Mo, Mn, Fe, Co, Re, Os, Ge, Sn or P show this kind of geometry containing oxo, halides (F⁻, Cl⁻, Br⁻, I⁻), nitride, nitrosyl, triphenylphosphine, pyridine as axial ligands.⁵³⁻⁵⁵



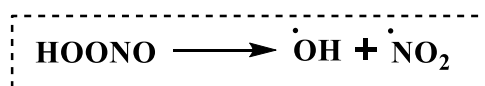
In some cases, corrole can also form six coordinated complexes with octahedral geometry, **42**. Few examples are there like Al(III), Co (III), Ga(III), Rh(III), Pt(IV), Ir(III), coordinating with pyridine, trimethylamine as axial ligands.⁵⁶⁻⁵⁹

1.4.1.6.5 Application of Corrole and Metalloporroles in various fields:

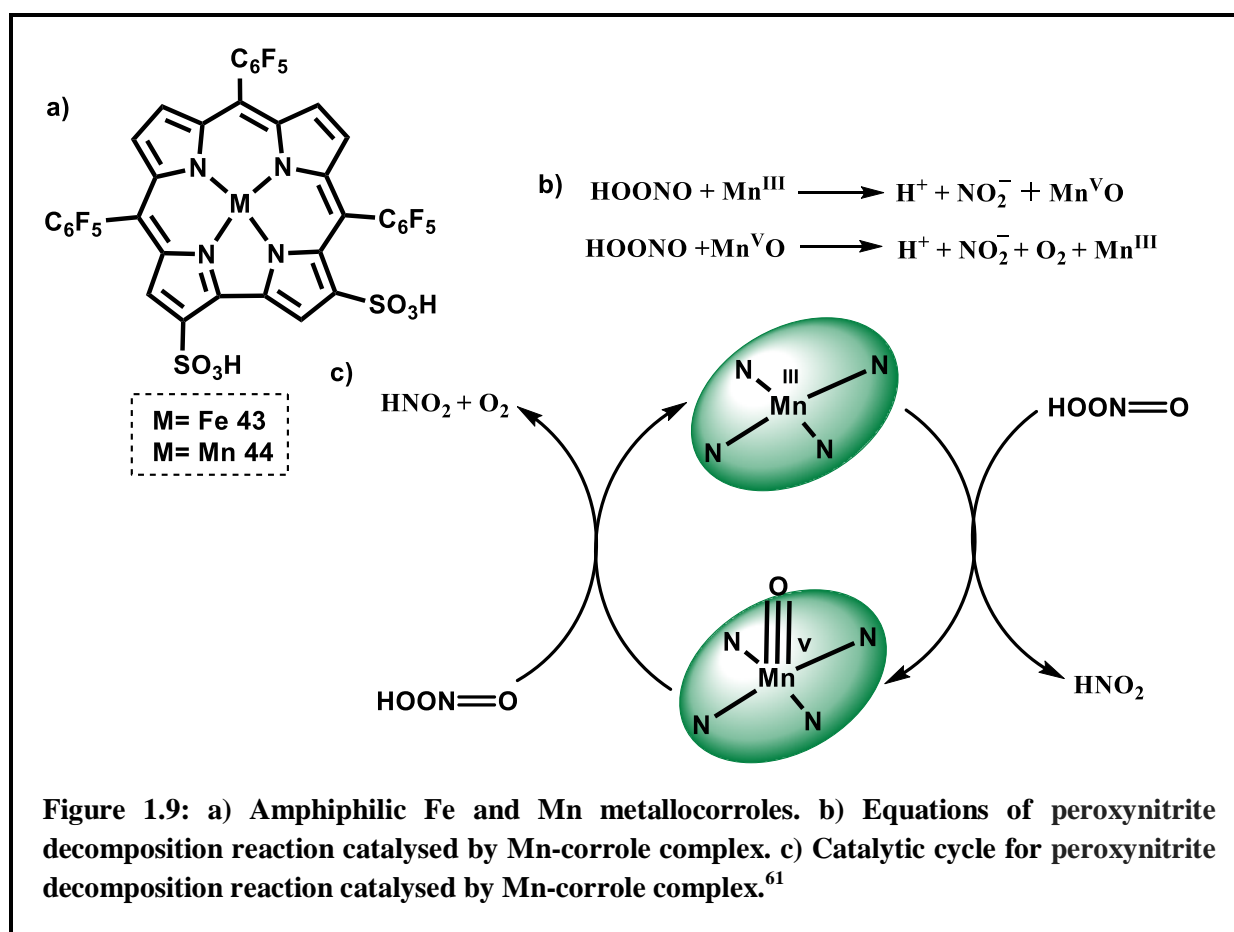
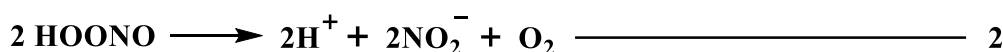
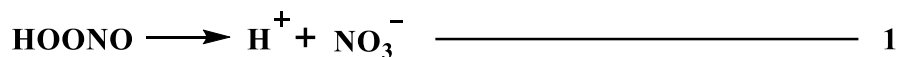
Due to the structural diversity and peculiar properties, this tetrapyrrolic macrocycle have attracted enormous interest over the last century. Synthetic developments make it very easy to synthesize a vast range of corroles, their metal complexes and various other derivatives. Various research group has already explored their interesting properties in different fields like catalysis, sensing, medicinal chemistry specially cancer diagnosis and treatment, dye sensitized solar cell and many more. In this section, very few important applications are discussed in brief.

1) Catalysts for the Decomposition of reactive oxygen species (ROS):

Reactive oxygen species (ROS) are highly chemically reactive species which must have an oxygen atom in the chemical formula e.g. peroxide, superoxide etc. Usually these species generate as by-products during mitochondrial electron transport. During the environmental stress, reactive oxygen species level can increase which leads to damage the cellular molecule like DNA, proteins, peptides, lipids and sugars which leads to various neurodestructive disease like Huntington's, Alzheimer's, and Parkinson's disease.⁶⁰ Unfortunately, there was no such enzyme available to hamper its destructive effects on living cells. Hence, in this crucial point it is very important to develop some remedies to prevent these damages. In the year of 2006, Z. Gross and A. Mahammed have first reported two amphiphilic metalloporroles.⁶¹ Due to their water solubility, they can easily associate with proteins. Complex **43** and **44** (Figure 1.9) can easily bind with human serum albumin (HSA) through noncovalent conjugation. These conjugated products can act as a very facile catalyst for the decomposition of peroxynitrite and H_2O_2 which are reactive oxygen species (ROS)⁶². Peroxynitrite is a highly reactive oxidant and nitrating anion with chemical formula ONOO^- . This can form by the in vivo reaction of NO and O_2 . It can also be described as an unstable structural isomer of NO_3^- . It has high oxidizing property. It can form two radicals OH^\bullet and NO_2^\bullet through homolytic cleavage which is the main reason for its destructive properties.⁶³⁻⁶⁵



Fe-corrole complex catalyses the decomposition process through isomerization (Equation 1) and it form nitrate anion and it shows more efficiency for this purpose than the corresponding porphyrin derivative. On the other side, Mn-corrole display the catalytic activity through disproportionation process (Equation 2) and it does not produce any radical species.



2) Activation of Dioxygen (O₂) and formation of O-O bond catalysed by Manganese Corrole complex:

Green plants produce Dioxygen (O₂) through photosynthesis which plays a significant role for all the living organisms. It is produced through photosynthesis in plants. Within the living cells, various

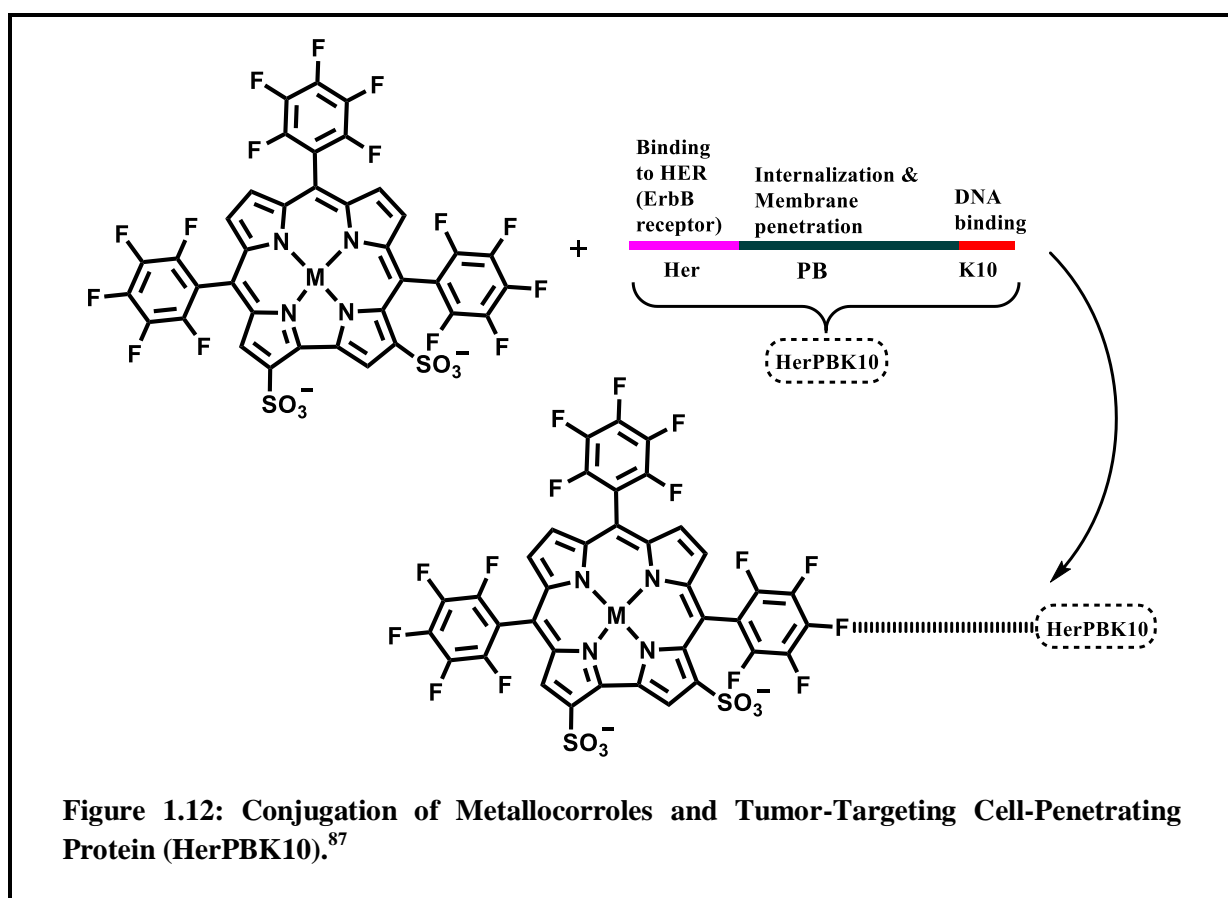
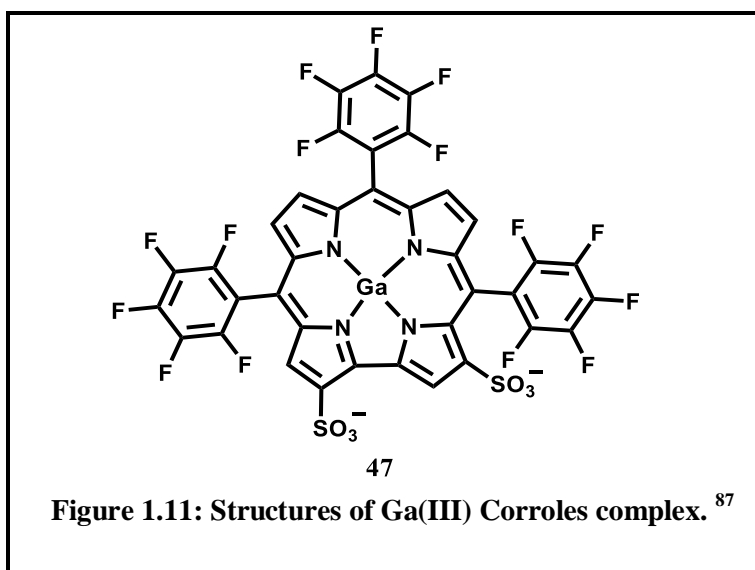
biological process is going on like binding and activation of O_2 through metalloenzymes and formation of oxygen binding metal intermediates (-peroxo, superoxo, -oxo, and -hydroperoxo, species).⁶⁶⁻⁶⁷ Iron containing heme and nonheme enzymes conduct O_2 activation and binding through formation of iron-oxygen intermediates which can be easily characterize through various spectroscopic techniques.⁶⁸ Earlier reports describe the synthesis of high valent manganese (IV or V)-oxo complex through oxidation by artificial oxidizing agent like PhIO, peracids, and NaOCl.⁶⁹⁻⁷² This manganese-oxo complex can act as the reactive intermediate in oxidizing various organic substances like water (OEC) in Photosystem II (PS II).⁷³⁻⁷⁵ Unlike these artificial oxidant inducing reactions, there are very less examples about the Mn(V)-oxo complexes synthesis using aerial O_2 as the oxidizing agents.⁷⁶⁻⁸⁰ In the year of 2017, Mn (III) corroles **45**, **46** (Figure 1.10) have been synthesized and shown their ability to active O_2 in presence of base.⁸¹ Formation of Mn(V)-oxo and Mn(IV)-peroxo species have also been established. This is the first report on manganese corrole which can act as a catalyst for the O_2 activation and O–O bond formation at the same time. In this process, Mn(III) corrole is treated with O_2 in the presence of base and hydrogen atom (H atom) donors. Amount of base in the reaction mixture controls the generation of the Mn(V)-oxo and Mn(IV)-peroxo species. In the following figure 1.10 formation of Mn(V)-oxo and Mn(IV)-peroxo intermediates during O_2 activation and O–O bond formation have been described through detailed reaction scheme and proposed mechanism.

3) Corrole in cancer treatment:

Since 1999, area of corrole has started growing and they have shown their property to act as both therapeutic and imaging agents. Corrole can easily bind with proteins like HerPBK10 in a noncovalent manner, **49** (Figure 1.12) for targeted delivery in the cell.⁸² One of the most important cancer treatments is photodynamic therapy (PDT) which include a drug called photosensitizer and a light. This photosensitizer generates oxygen after continuous light exposer which can kills nearby cells.⁸³ By incorporating different substituents and metals in the corrole macrocycles, their theranostic

property can be modulated. Various amphiphilic corroles have been synthesized for this purpose. This amphiphilic nature helps them to bind with many proteins. In 2000, first stable water soluble corrole has been synthesized and its ability to act as a powerful inhibitor of lung metastasis has been discovered.⁸⁴ It is almost 10 times more effective than tetrakis(4-methoxyphenyl)-porphyrin.⁸⁵ Most rigorously examined corroles and metallocorroles for therapeutic applications contain two sulfonic acid groups in the macrocycles. Sulfonated Ga(III) corrole, **47** (Figure 1.11) complex is intense red coloured fluorescent compound which can assemble with the most abundant protein in blood cell human serum albumin (HSA), **48**.^{86,87} In vivo image and therapeutic efficiency of protein binded

Ga(III) corrole complex aimed at the human epidermal growth factor receptor (HER) have been reported. This corrole-protein assembly can accumulate the tumour cells which can be easily



visualize because of its high red coloured fluorescence. This is a very effective opportunity to identify the tumour cells positions and targeted chemotherapy.

4) Metallocorrole as CO sensor:

Corrole has the ability to stabilize higher oxidation state of metals because of its contracted core and three NH atoms. In case of cobalt metal, porphyrin can stabilize +2 oxidation state while corrole can stabilize +3 oxidation state. Because of this high oxidation state, Co(III) corrole complex can bind with carbon monoxide (CO).⁸⁸⁻⁹⁰ At present time, carbon monoxide is a pollutant with a potential to harm all living things and detection of this CO is a very crucial point. In 2004, Guillard *et al* have first published the use of Co (III)corrole complexes (Figure 1.13) as CO sensors.⁹¹ They have also revealed that during the coordination of Co (III) corroles with CO, areal O₂ doesn't interfere. To determine the selectivity of these Co(III) corrole complexes, an equation is necessary.

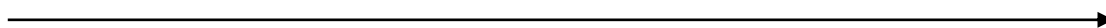
$$M = P_{1/2}^{O_2} / P_{1/2}^{CO}$$

where $P_{1/2}^{O_2}$ and $P_{1/2}^{CO}$ are the half-saturation pressures of O₂ and CO, respectively.

Higher M value represent the higher affinity for CO. M Value of a model compound, (To-PivPP) Fe(1,2-Me₂Im) is 4280⁹² but the cobalt (III) corroles show $M = \infty$ which means it doesn't interact with O₂.⁸⁸ This CO detection affinity is mainly dependent on the Lewis acidity of the cobalt (III) centre. The higher the Lewis acidic character, the higher the CO affinity. In figure 1.13 complex **50** shows lowest CO affinity as it has electron donating group on the macrocycle. Electron withdrawing substituents increase the Lewis acidity on the cobalt (III) centre. With the decreasing of d→π back bonding increases the CO stretching frequency.

$$\text{Corrole } \mathbf{50} < \text{Corrole } \mathbf{55} \approx \text{Corrole } \mathbf{52} \approx \text{Corrole } \mathbf{51} < \text{Corrole } \mathbf{53} < \text{Corrole } \mathbf{54}$$

Lewis acidity of the Cobalt(III) centre



CO stretching frequency, affinity for CO

Only corrole **51** shows exceptional CO affinity value which is higher than expected. The CO molecule can be removed from the cobalt (III) corroles **51**, **52** and **55** through degassing those complexes at

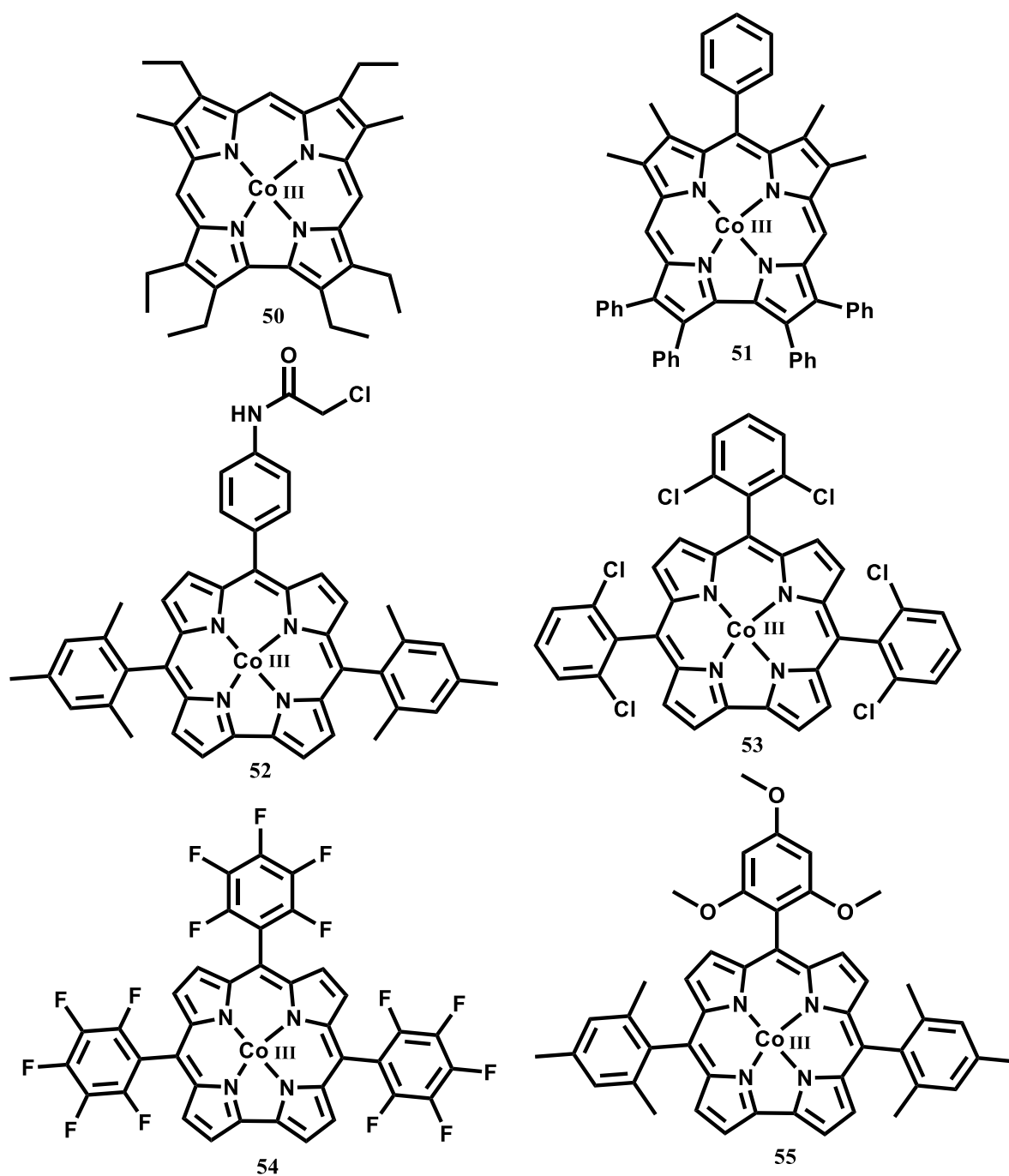


Figure 1.13: Structures of all the cobalt (III) corroles examined for CO sensing.⁹¹

room temperature for 2 h under 10^{-3} Torr and from complex **53** through degassing for 8 h under 10^{-3} Torr. As complex **54** shows the largest CO affinity, so it can be degassed at 50°C under 10^{-3} Torr for 12 h. So, from this report it has been well established that these six cobalt (III) corroles show infinite CO affinity and are perfect example for CO sensing purposes.⁹¹

1.5 Lacunae:

Despite of all these significant progresses in the corrole field, still there are deficits in some areas which are less explored. Most of the major research groups devote a good portion of their efforts towards monomeric corrole systems. Still there are no such generalized demetallation protocols for metallocorrole available in the literature. As metallocorrole is much more robust in nature than free base corrole ligands, so some structural variations within the corrole periphery or substitutions at *meso*- or β - positions of corrole will be more favourable in case of metallocorrole than free base corrole ligands. Several other challenging corrole based systems are currently under intense investigation like ring contraction reaction of porphyrins to corroles. Ring contraction reaction of porphyrin to corrole is rarely explored in the literature. There are very few previous reports on this conversion with poor yields like only 9%. So, no such synthetic reports are available in the literature with suitable yield of product. Unlike monomeric corroles, diversity in synthesis and applications in various fields for dimeric corrole is surprisingly less explored aspect of this fields. In case of porphyrin macrocycles β - β , *meso*-*meso*, triply linked porphyrin arrangements were extensively studied in the literature. Investigations of a diverse class of triply linked porphyrin derivatives have been disclosed their optical and electrochemical properties. But to the best of our knowledge, such multiple corrole based systems are comparatively less explored than porphyrin systems.

1.6 Scope and Objectives of the Present Thesis:

This thesis contains some of the less explored area in corrole field. Synthesis of metallated dimer, their spectroscopic nature and existence in mixed valence state is discussed here and also different types of synthetic methodology of corroles from other macrocycles like metallocorroles and porphyrins have been explored in detail. Additionally, synthesis of metal metal bonded rotationally ordered dimeric corrole complex and their existence in various accessible oxidation states which relevance its application as “photosynthetic special pair” is also discussed.



Chapter Two

Grignard Reagents Mediated Demetallation of Silver Corrole Complexes

2.1 Introduction

2.2 Results and Discussion

2.2.1 Demetallation strategy in detail

2.3 Spectral Characterization

2.3.1 Mass Spectroscopy

2.3.2 Electronic absorption spectrum and Emission spectrum

2.3.3 NMR Spectroscopy

2.3.4 Crystal Structure

2.4 Conclusions

2.5 Experimental Section

2.5.1 Materials

2.5.2 Physical measurements

2.5.3 Crystal Structure Determination

2.5.4 Syntheses

2.5.4.1 5,10,15-Tris(2-bromo-5-fluorophenyl)corrole, 1A

2.5.4.2 5,10,15-Tris(2-bromo-5-fluorophenyl)corrolato-silver(III), 1B

2.5.4.3 10-(pyrene-1-yl)-5,15-bis(4-cyanophenyl) corrole, 6A

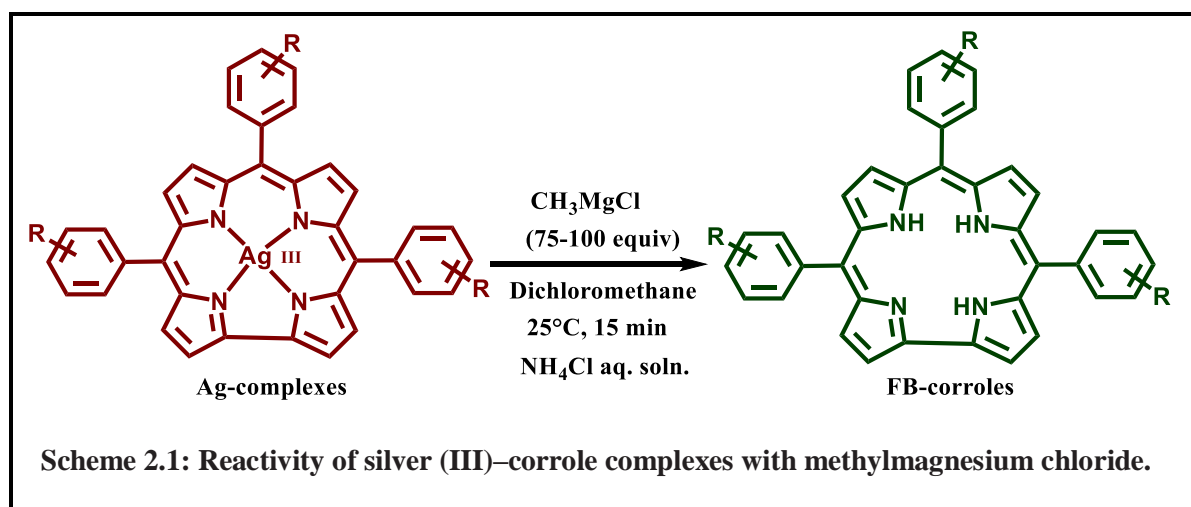
2.5.4.4 10-(pyrene-1-yl)-5,15-bis(4-cyanophenyl)corrolato silver(III),6B

2.5.4.5 Demetallation

2.1. Introduction:

In the previous chapter, superiority of corrole over porphyrin in many aspects have been discussed in detail. Extensive applications of corroles in different fields like catalysis, medicinal chemistry, material science have also been discussed. The chemical modification of corroles, by introducing a series of different functional groups, has been an active area of research in recent times. These systems have widespread applications in chemistry, biology, and in materials science. Structural modifications in the corrole macrocycles at the *meso*- and β -positions can lead to the development of newer varieties of corrole derivatives, which can play an important role in electron-transfer reactions,⁹³⁻¹⁰⁰ oxidation catalysis,¹⁰¹⁻¹⁰⁴ reduction catalysis,¹⁰⁵⁻¹⁰⁷ group transfer reactions,¹⁰⁸ sensors,¹⁰⁹ cancer diagnostics,¹¹⁰ and in treatment purposes.¹¹¹⁻¹¹⁴ In porphyrin chemistry, various functionalizations at the *meso*- and β -positions of the macrocycles are often carried out by selective metalation and demetallation reactions. One possible reason is that the metal–porphyrinoid systems are often more robust than the metal-free porphyrinoid systems. Contrary to the porphyrin-based systems, the development of suitable demetallation strategies for corrole chemistry is still in its infancy.¹¹⁵⁻¹²⁵ Only a few selected metals ions (Cu,¹²² Ag,¹²¹ Mn,¹²⁵ Bi,¹¹⁶ and Sn¹²⁶) can be demetallated from the corrole cavity. In addition to this, there is no generalized protocol for demetallation available in the literature of corrole chemistry. Out of the several methodologies described so far, the most intriguing method for the demetallation of corrolato–silver(III) complexes was reported by Paolesse *et al.*¹²¹ They have shown that DBU in THF solutions is an excellent reagent for the demetallation reactions of Ag–corroles with average yields of 45 % to 62 %. Furuta *et al.* have reported the demetallation of silver(III) complexes of N-confused porphyrin by using sodium borohydride.¹²⁴ Dehaen *et al.* have developed an interesting methodology for demetallation of Cu–corroles by using SnCl₂ (in acidic condition) as a reducing agent.¹²² Ghosh *et al.* have described the demetallation strategy of Mn–Corroles by using FeCl₂ and conc. H₂SO₄.¹¹⁵ Bröring *et al.* have performed the demetallation of Mn–Corroles by using HBr in acetic acid.¹²⁵ Osuka *et al.* have reported the use of Grignard reagents (4-methylphenylmagnesium bromide) for the first time for the facile demetallation reactions of Ni–porphyrin to FB (free-base)

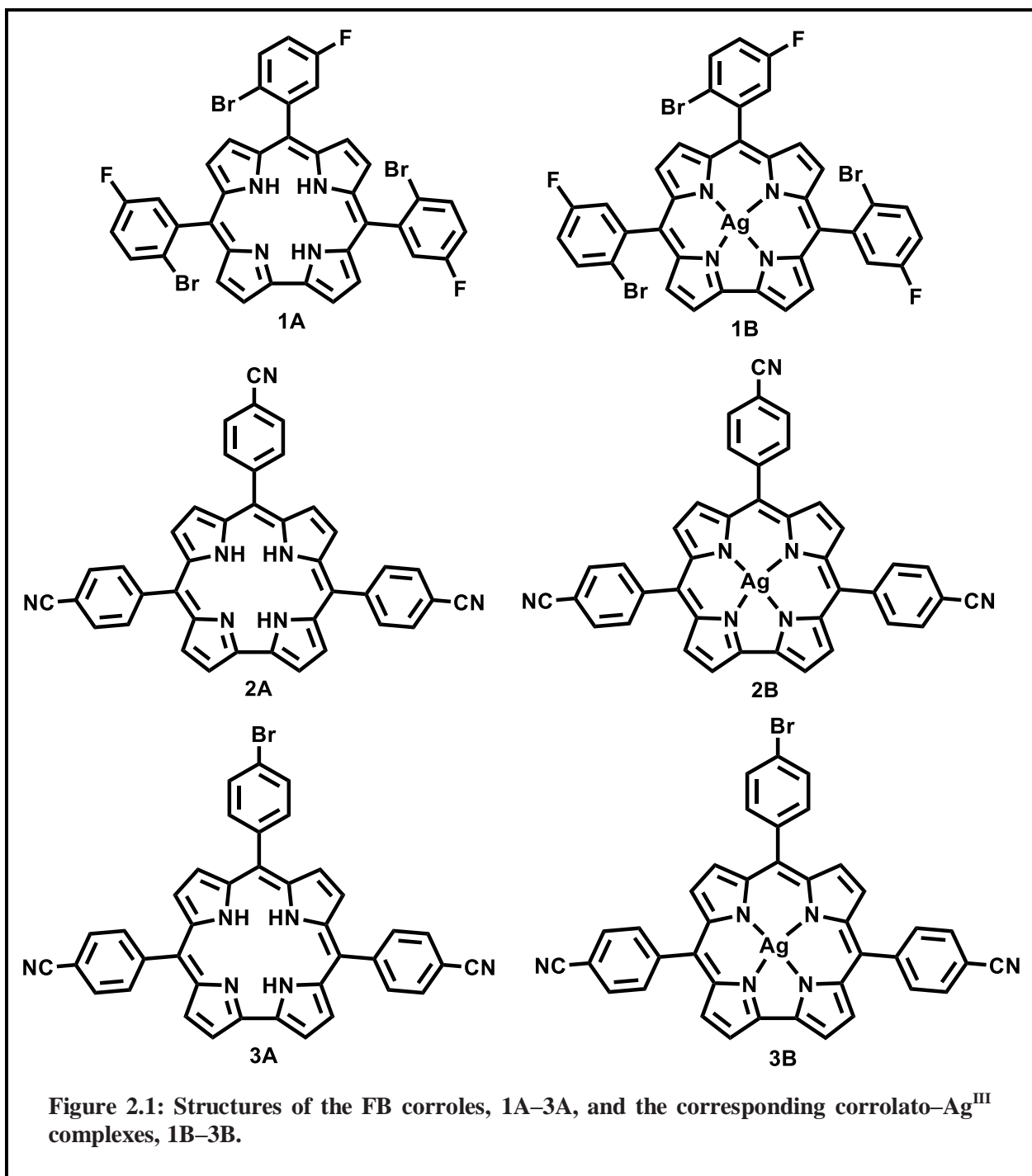
porphyrin via a Mg–porphyrin.¹²⁷ Our group has also reported the demetallation strategy of Sn^{IV} –corroles by using methyl magnesium chloride.¹²⁶ In search of a generalized protocol for the demetallation of metallo–corrole derivatives, we have chosen corrolato–silver(III) complexes for the present work. One reason for this choice is that the native state electronic configurations of corrolato–silver(III) complexes are square planar (d^8 configurations) and hence diamagnetic in nature. As a result, these complexes can be monitored by NMR spectroscopy very easily after suitable functionalization at their ligand periphery. A series of substituents having different electronic properties have been inserted into the corrole periphery. These substituents have been chosen keeping in mind that a series of post metalation organic transformation reactions can be conveniently performed on the metallo–corrole derivatives. In the present work, we have observed that a series of corrolato–silver(III) complexes, upon treatment with methylmagnesium chloride resulted in the formation of FB corroles in excellent yields (Scheme 2.1). Compared with the previously reported



results for other demetallation strategies of corrolato–silver(III) complexes, the present methodology delivers significantly improved isolated yields for the corresponding FB corroles.

A series of corrolato–silver(III) complexes have been synthesized for this purpose, namely, 5,10,15-tris(2-bromo-5-fluorophenyl) corrolato–silver(III) (**1B**); 5,10,15-tris(4-cyanophenyl)corrolato–silver(III) (**2B**);⁹⁶ 10-(4-Bromophenyl)-5,15-bis(4-cyanophenyl)corrolato–silver(III) (**3B**);⁹⁶ 10-(2,4,5-Trimethoxyphenyl)-5,15-bis(4-cyanophenyl)corrolato–silver(III) (**4B**);⁹⁶ 10-(4,7-

Dimethoxynaphthalen-1-yl)-5,15-bis(4-cyanophenyl)corrolato–silver(III) (**5B**);⁹⁶ and 10-(Pyrene-1-yl)-5,15-bis(4-cyanophenyl)-corrolato–silver(III) (**6B**). In addition to a new demetallation protocol, the present work also describes the synthesis of two novel corroles, **1A** and **6A** (Figure 2.1 and 2.2). Two novel corrolato–Ag^{III} complexes have also been synthesized, namely **1B** and **6B** (Figure 2.1 and 2.2).



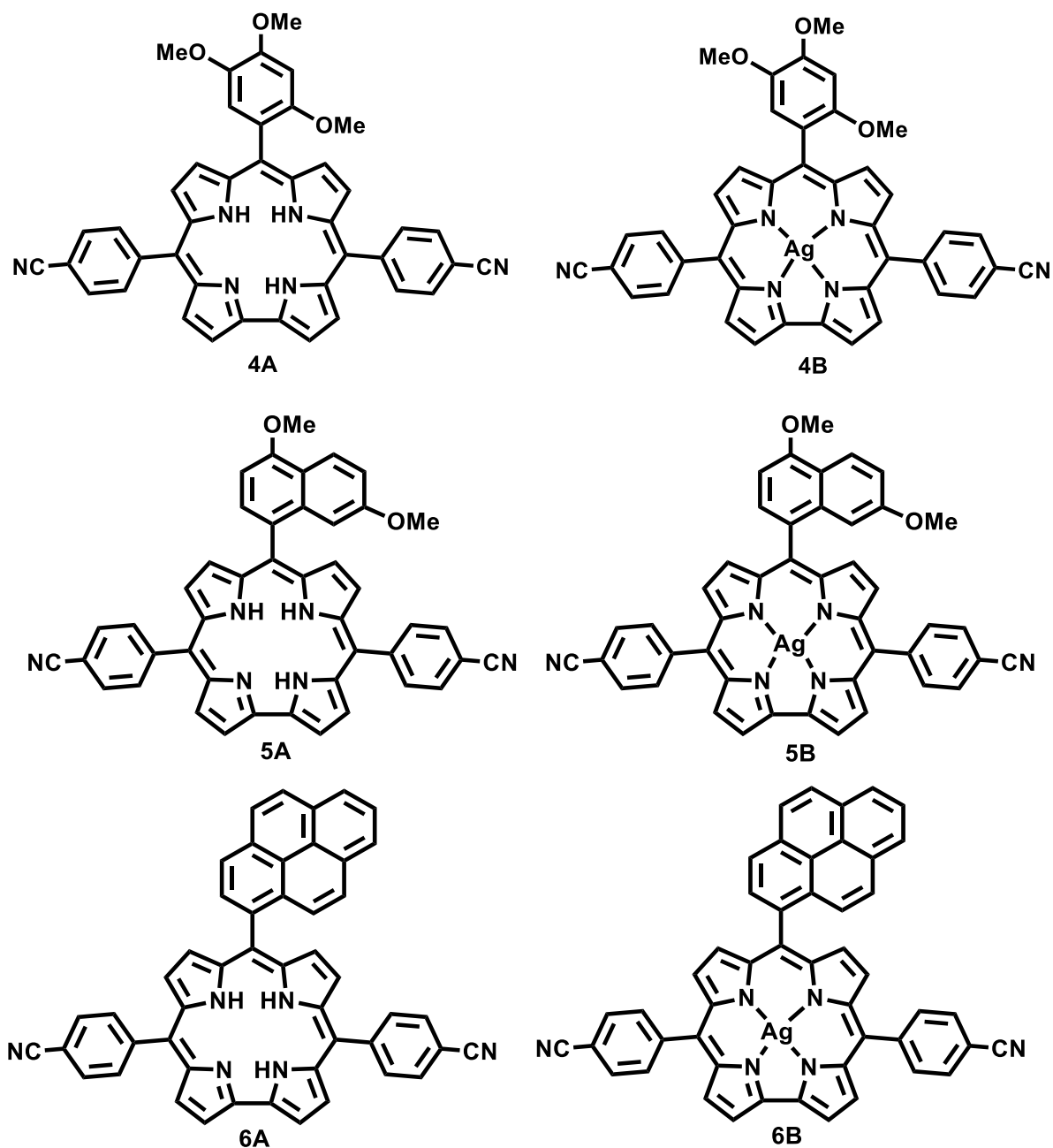


Figure 2.2: Structures of the FB corroles, 4A–6A, and the corresponding corrolato–Ag^{III} complexes, 4B–6B.

All these complexes have been thoroughly characterized by various spectroscopic techniques including single crystal X-ray structural analysis for the representative derivatives.

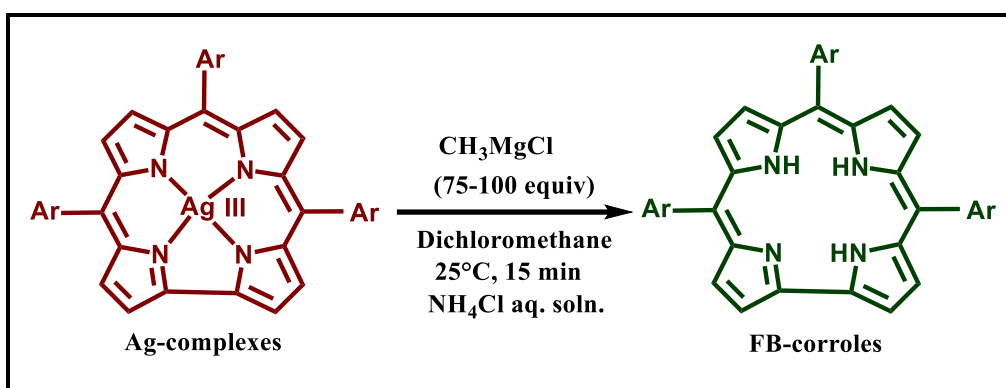
2.2 Results and Discussion:

2.2.1 Demetallation strategy in detail:

Corrolato–silver(III) complexes (**1B–6B**) were treated with a series of different Grignard reagents,

like phenylmagnesium bromide, methylmagnesium bromide, and methylmagnesium chloride. We have found that the Grignard reagents, phenylmagnesium bromide and methylmagnesium bromide, are responsible for the partial demetallation of Corrolato–silver(III) complexes (**1B–6B**). However, in the presence of methylmagnesium chloride, complete demetallation of the corrolato–silver(III) complexes (**1B–6B**) occurred. It was observed that upon treatment with methylmagnesium chloride in dichloromethane solvent at room temperature and under a nitrogen atmosphere, the corrolato–silver(III) complexes (**1B–6B**) were converted to corresponding free-base (FB) corroles (**1A–6A**) (Table 2.1) in excellent yields (isolated yields > 80 %). In order to understand the scope and applicability of this new demetallation strategy, we have screened a series of different reaction conditions. Our first observation is that the new reaction is fully dependent on the Grignard reagents used. The reaction is also highly solvent specific, e.g. no demetallated products were observed in other solvents like tetrahydrofuran, which is frequently used in the reactions related to Grignard reagents. The rate of the reaction is very fast and in most of the cases, the desired transformations to FB corroles occur within the first fifteen minutes. We have screened this reaction with a series of corrolato–silver(III) complexes having different functionalities in the corrole periphery based on their electron releasing and withdrawing capabilities. Our observations showed that the reaction is equally successful in all cases. One can easily observe the conversion of metalated corroles to the FB corroles by the simple visualization of the colour change of the reaction mixtures, after the complete addition of Grignard reagents. With the addition of the Grignard reagent, the colour of the solution changes rapidly from red [corrolato–silver(III) complexes] to green (FB corroles). In addition to this, the degree of completion of the reaction can be easily monitored by TLC and UV/Vis techniques. The desired transformation happens almost quantitatively and no traces of isocorrole¹²⁸⁻¹³⁰ derivatives were found in the reaction mixtures.

Table 2.1: Scope of the demetallation reaction.

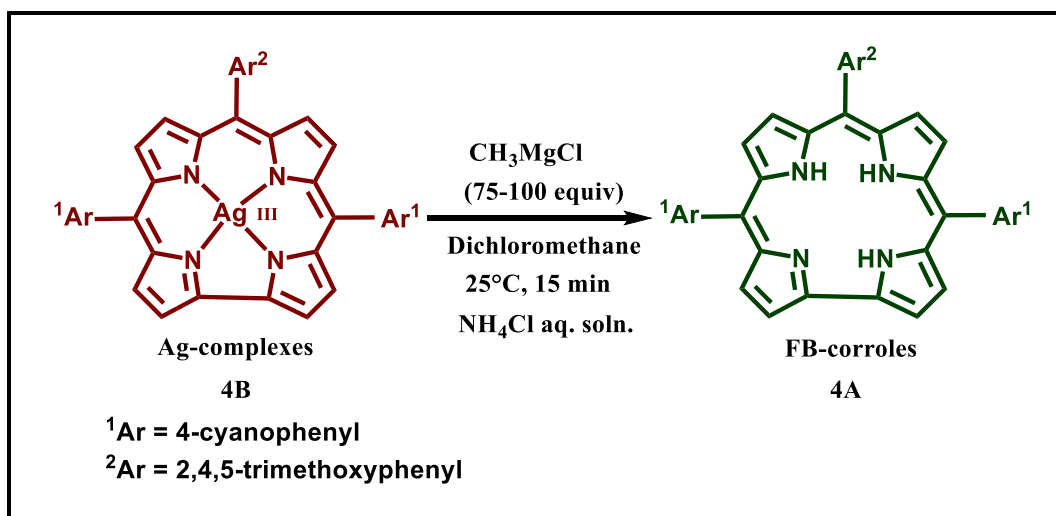


	Corrolato- Ag^{III} \rightarrow FB corroles	Isolated yield [%]
1	1B \rightarrow 1A	87
2	2B \rightarrow 2A	81
3	3B \rightarrow 3A	83
4	4B \rightarrow 4A	88
5	5B \rightarrow 5A	84
6	6B \rightarrow 6A	87

As already mentioned, the conversion of corrolato- Ag^{III} complexes to the FB corrole is highly dependent on the equivalents of the Grignard reagent used (Table 2.2), thus we have systematically varied the equivalents of the Grignard reagents in the reaction vessels. We observed that the effect of Grignard reagents is negligible, when used in amounts of less than 25 equiv. With the successive increase in the mol ratio of Grignard reagents, the concomitant conversion to FB corroles was observed (Table 2.2). After the addition of 75–100 equiv. of Grignard reagent, an almost complete conversion to FB corroles was observed. The conversion is almost quantitative and no traces of metalated corroles or isocorrole species were found at the end of the reaction (Table 2.2). However,

on further addition of Grignard reagents, the rate of the reaction increases with little to no change in the reaction yields. With the addition of 200 equiv. of Grignard reagent, the desired conversions occurred in a few seconds. Corrolato–Ag^{III} complexes bearing electron-withdrawing and electron-releasing substituents (*meso*-aryl) have proven to be highly efficient reactants and demetallation was observed almost quantitatively. A broad variety of substrates such as cyano, methoxy, halogen groups as well as polycyclic aromatic rings are tolerated (Table 2.1).

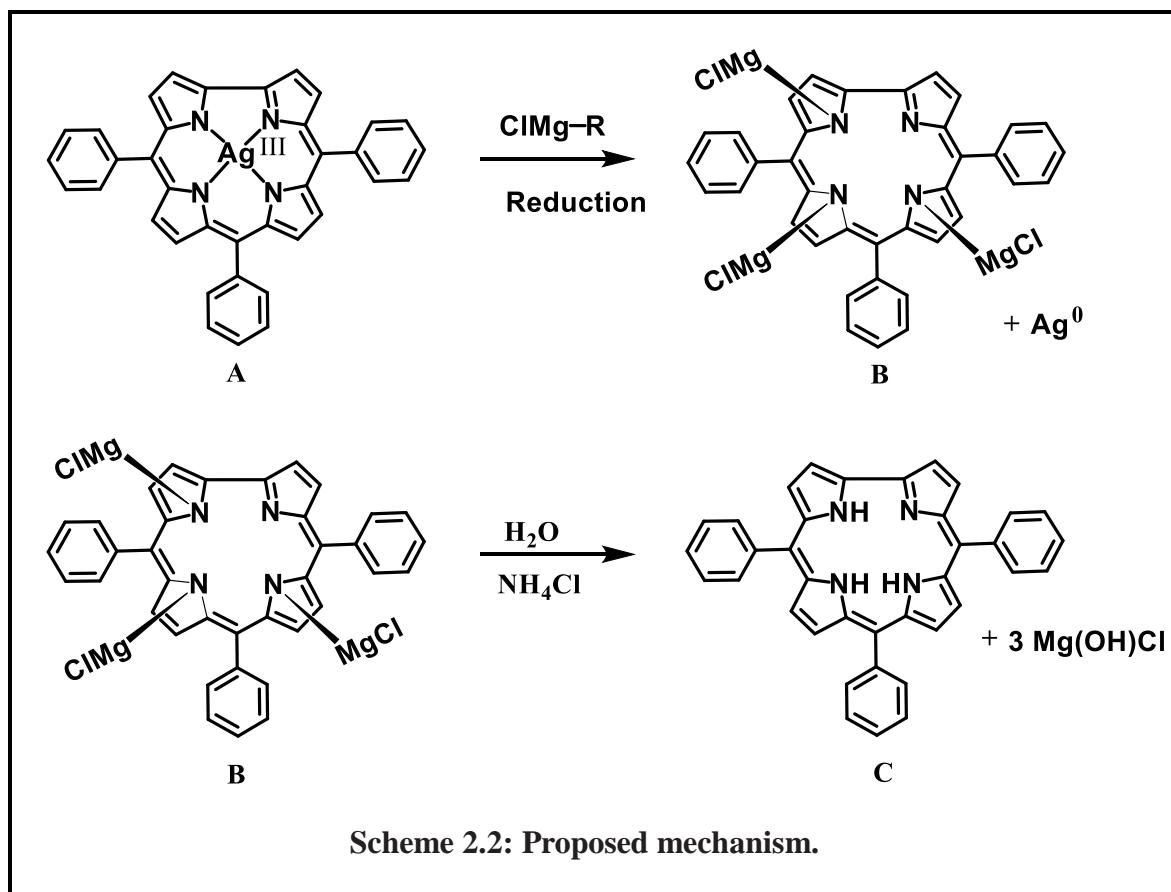
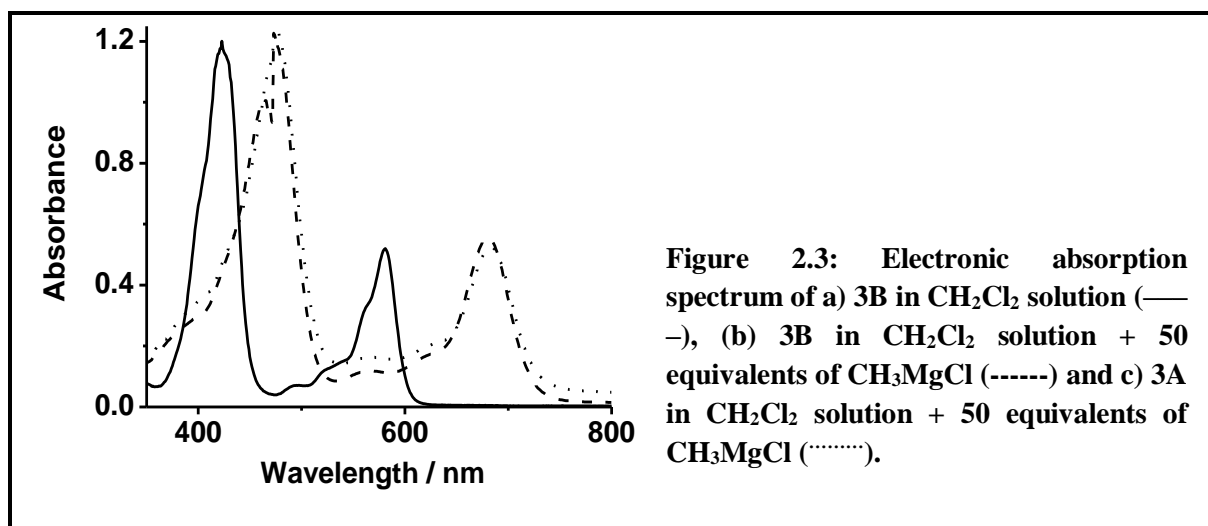
Table 2.2: Optimization of the demetallation reactions 4B to 4A.



Equiv. of CH ₃ MgCl	Yield (%) of 4A
25	10
50	50
75	82
100	88

A mechanism has also been proposed for the demetallation of corrolato–Ag^{III} complexes (Scheme 2.2). The mechanism has been formulated based on the earlier reports of Osuka et al.¹²⁷ and Kochi et al.¹³¹ A facile reduction of Ni^{II} to Ni⁰ by a Grignard reagent was reported earlier.¹²⁷ In line with the

previous reports, we assume that in the first step of the reaction, fast reduction of Ag^{III} to Ag^0 occurs. Thus, in the first step, the Grignard reagent in DCM solution reacts with the silver(III) center and it forms Ag^0 and the by-product MgCl is hypothesized to be associated with the inner ring nitrogen atoms. This fact is further supported by the UV/Vis spectra of the intermediates generated upon addition of Grignard reagents to the corrolato–silver(III) complexes (Figure 2.3).

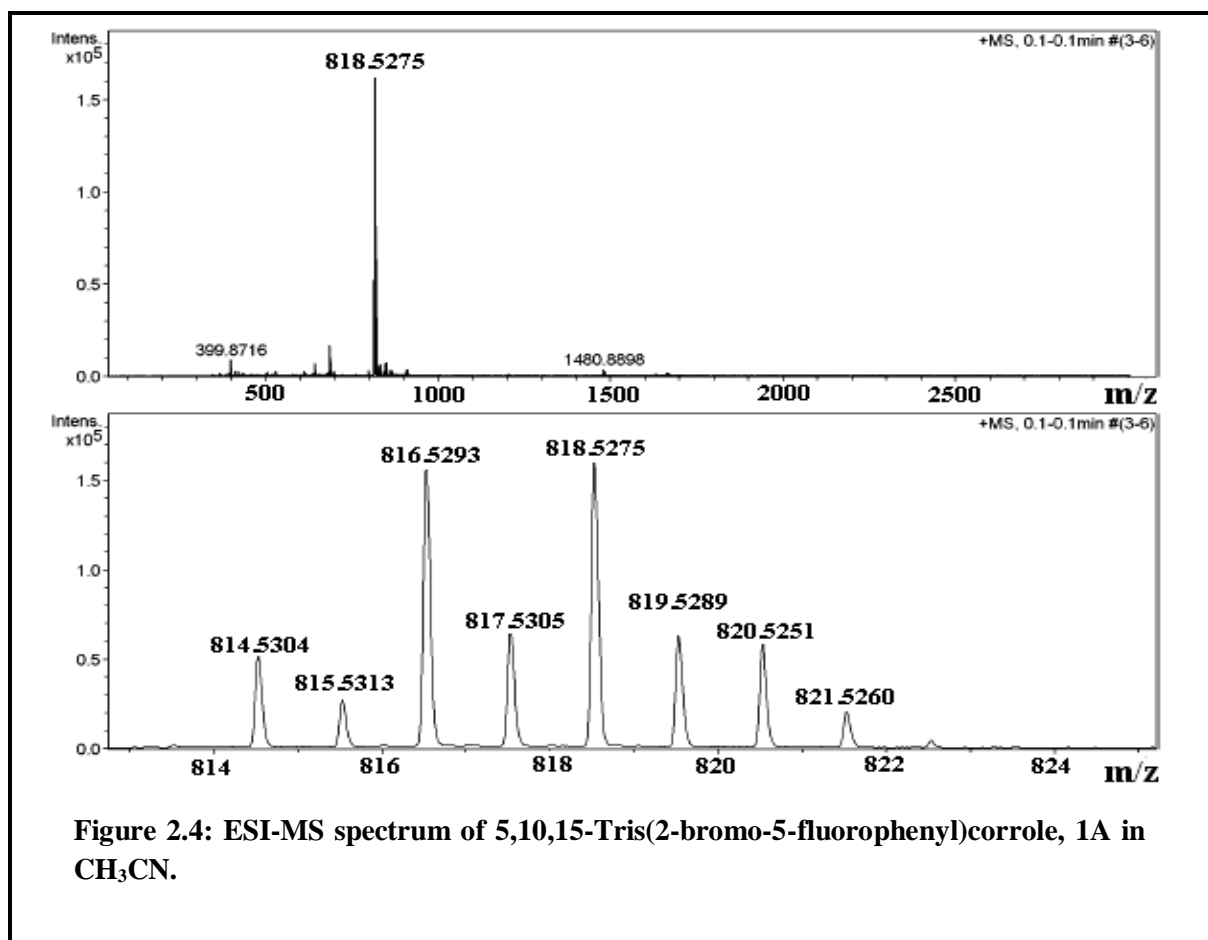


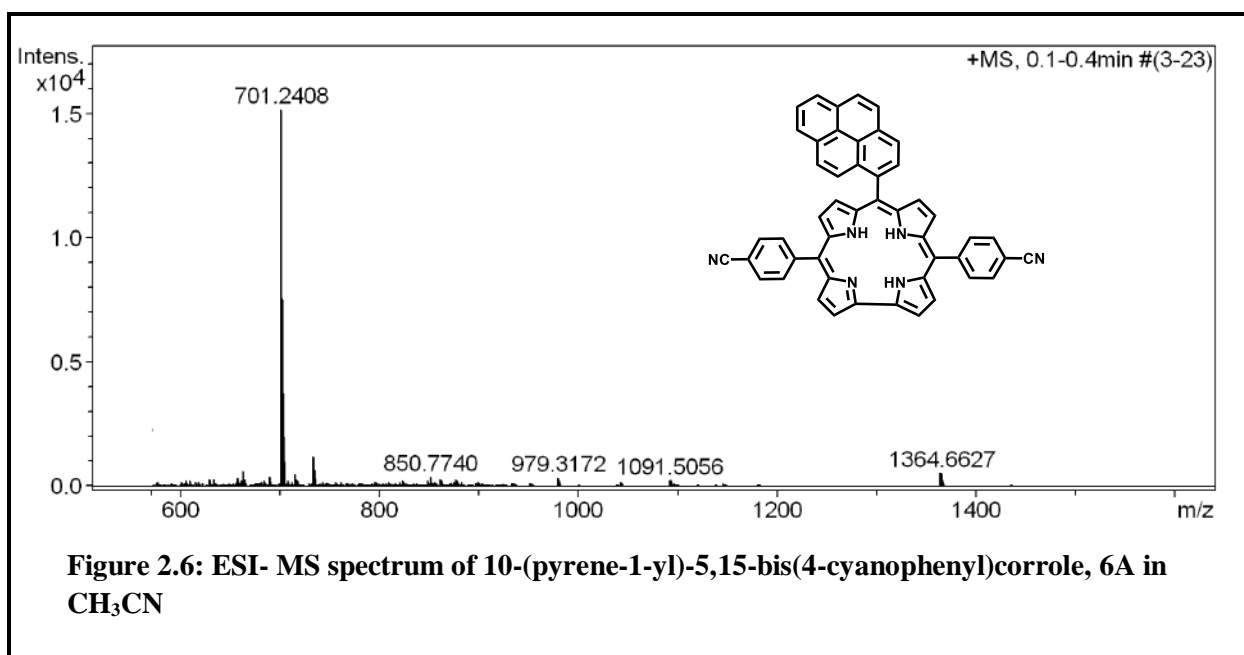
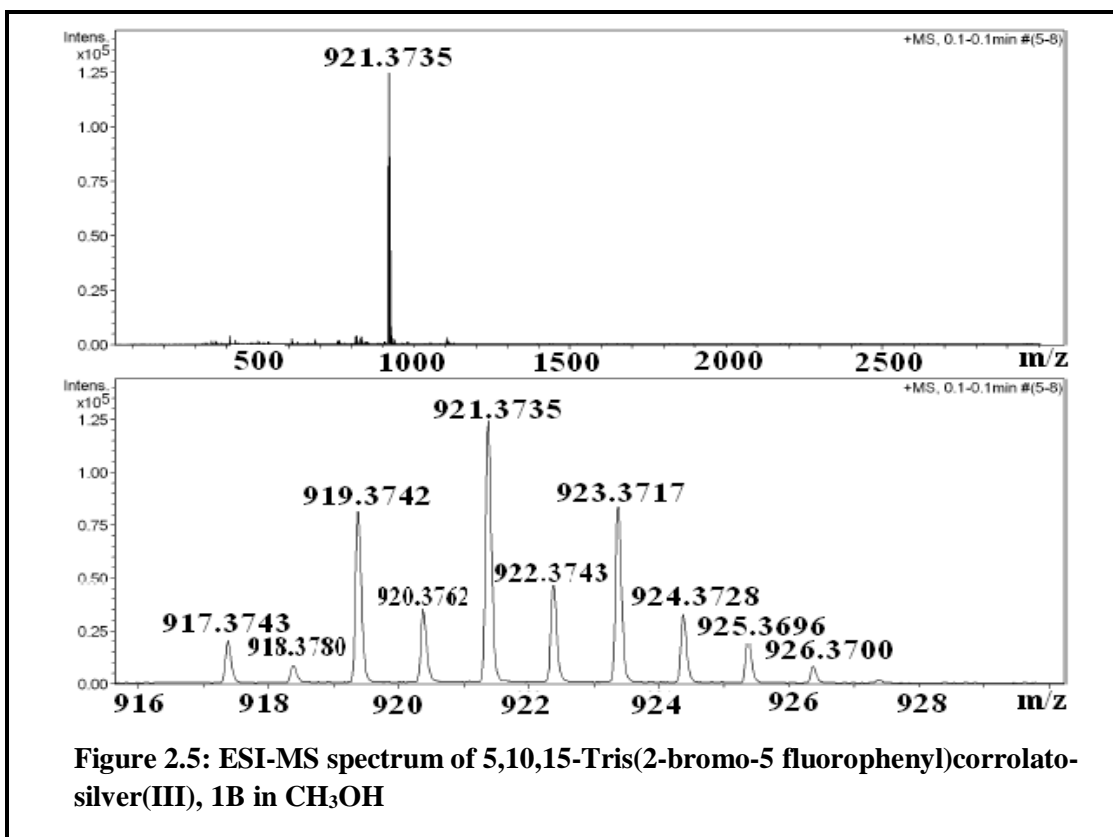
In the next step, in the presence of water and ammonium chloride as a proton source, all the magnesium–nitrogen bonds are cleaved and this generates the corresponding FB corroles and $\text{Mg}(\text{OH})\text{Cl}$.

2.3 Spectral Characterization:

2.3.1 Mass Spectroscopy:

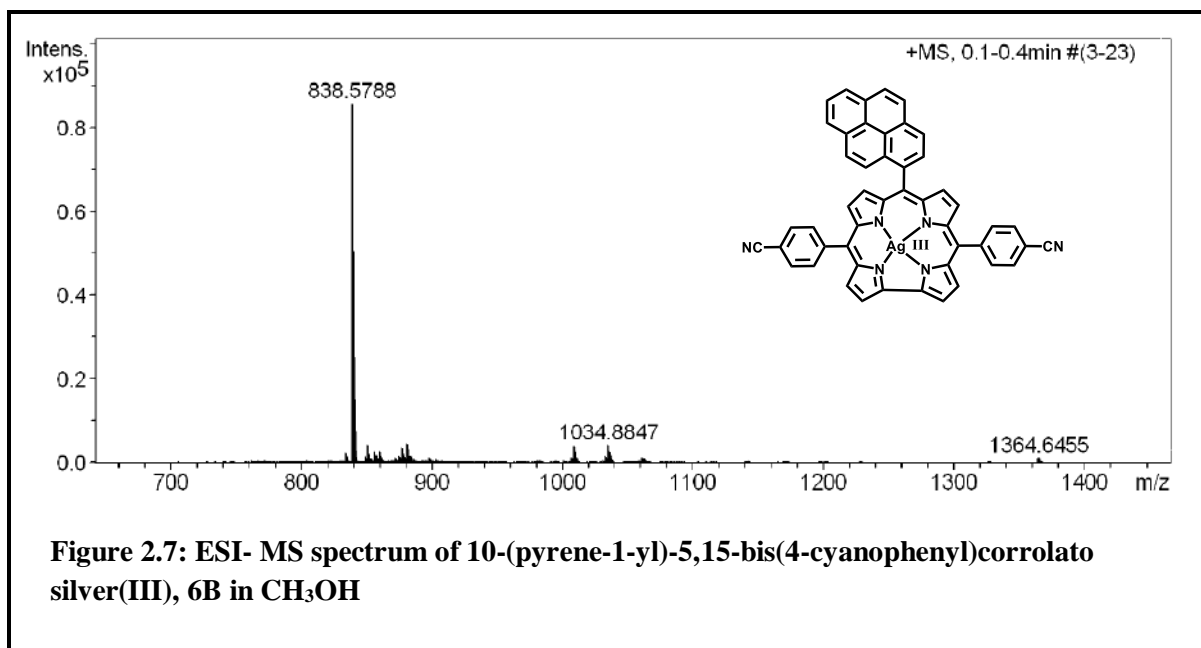
The electrospray mass spectrum of the corrole, **1A**, is reported which shows peaks centered at $m/z = 818.53$ corresponding to $[\text{M}+\text{H}]^+$ (817.29 calcd for $\text{C}_{37}\text{H}_{20}\text{Br}_3\text{F}_3\text{N}_4$) (Figure 2.4). The corresponding silver(III) corrole complex, **1B** shows the mass peak centered at $m/z = 921.37$ corresponding to $[\text{M}]^+$ (922.13 calcd for $\text{C}_{37}\text{H}_{17}\text{AgBr}_3\text{F}_3\text{N}_4$) (Figure 2.5). Another FB corrole **6A** exhibits strong peak at $m/z = 701.24$ corresponding to $[\text{M}+\text{H}]^+$ (700.24 calcd for $\text{C}_{49}\text{H}_{28}\text{N}_6$) (Figure 2.6). The corresponding silver(III) corrole complex, **6B** displays the intense peak centered at $m/z = 838.58$ $[\text{M}+\text{CH}_3\text{OH}+\text{H}]^+$ (calcd for $\text{C}_{50}\text{H}_{29}\text{AgN}_6\text{O}$: 837.67) (Figure 2.7).



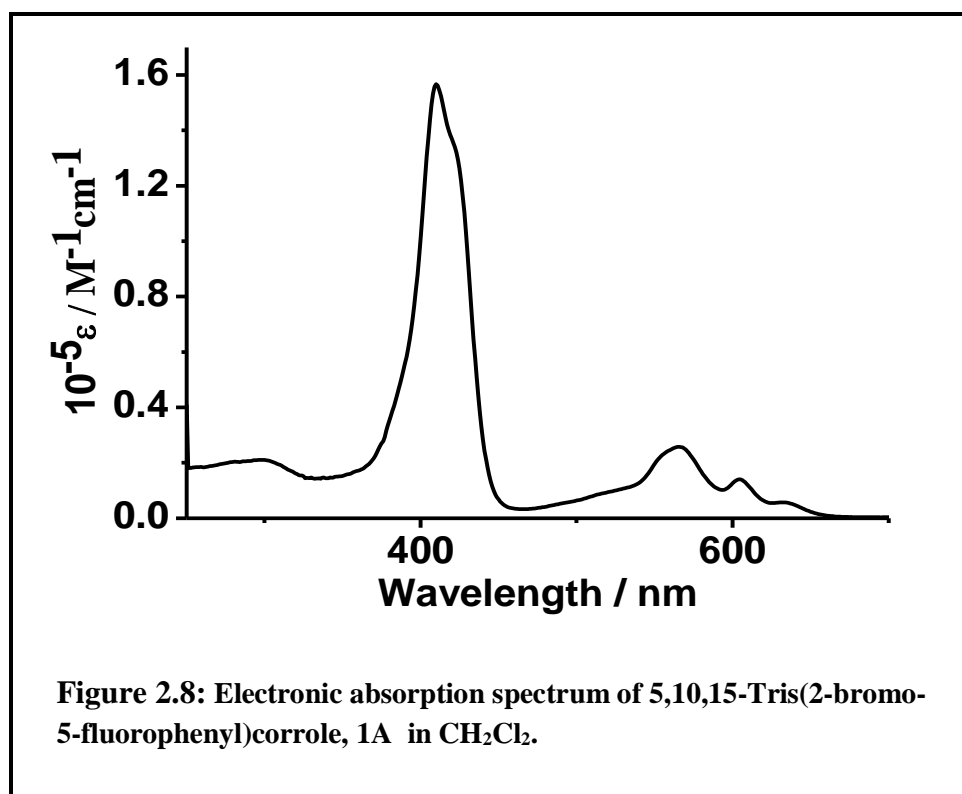


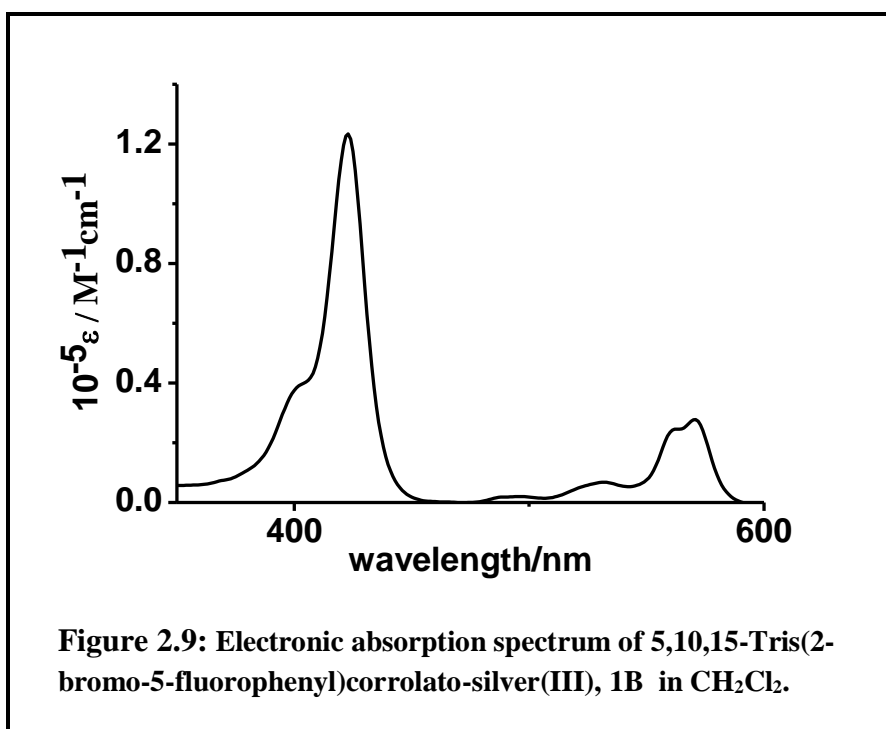
2.3.2 Electronic absorption spectrum and Emission spectrum:

Electronic absorption spectrum of the free-base ligands **1A**, **6A** and their silver(III) complexes **1B**, **6B** are reported in this chapter. Each compound shows one intense solet band at around 400 nm and Q bands within the range of 500-650nm (Figure 2.8 and 2.9).



Compound **1A** and **6A** display strong fluorescence at 646nm and 676nm respectively.



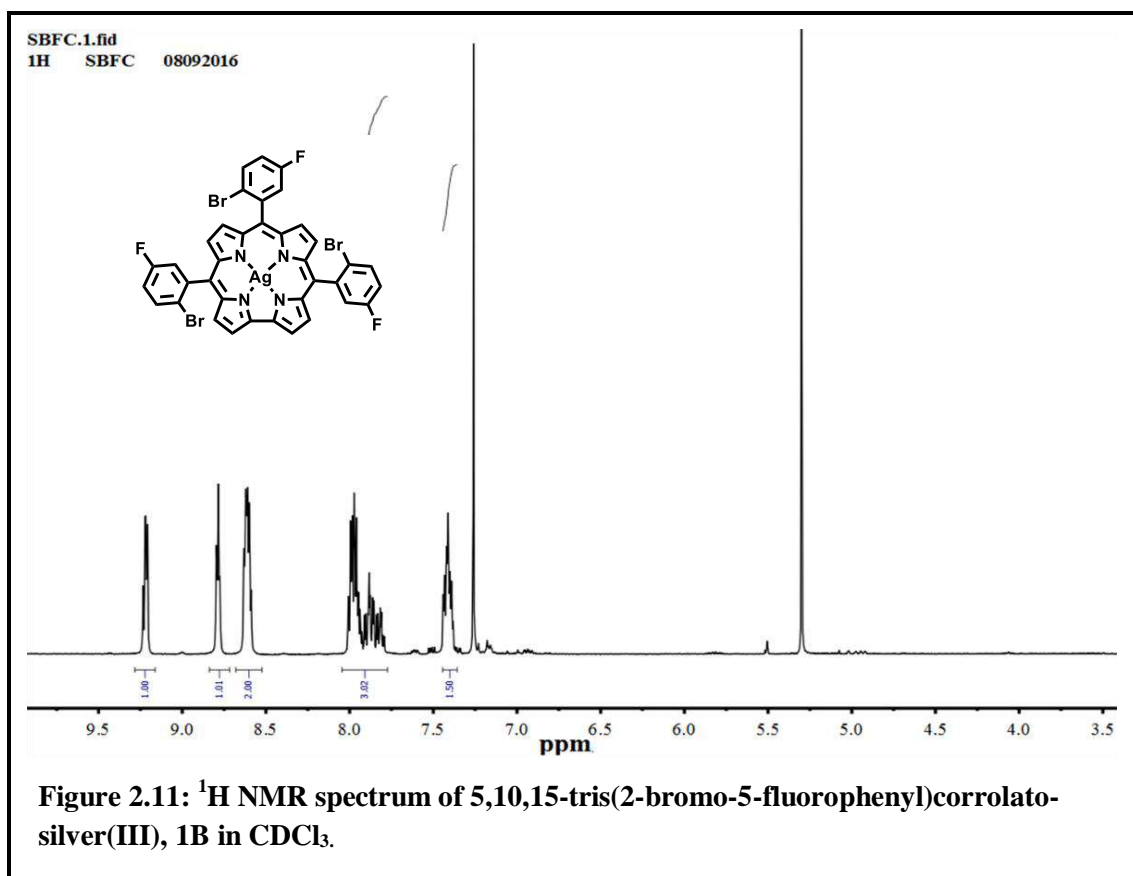
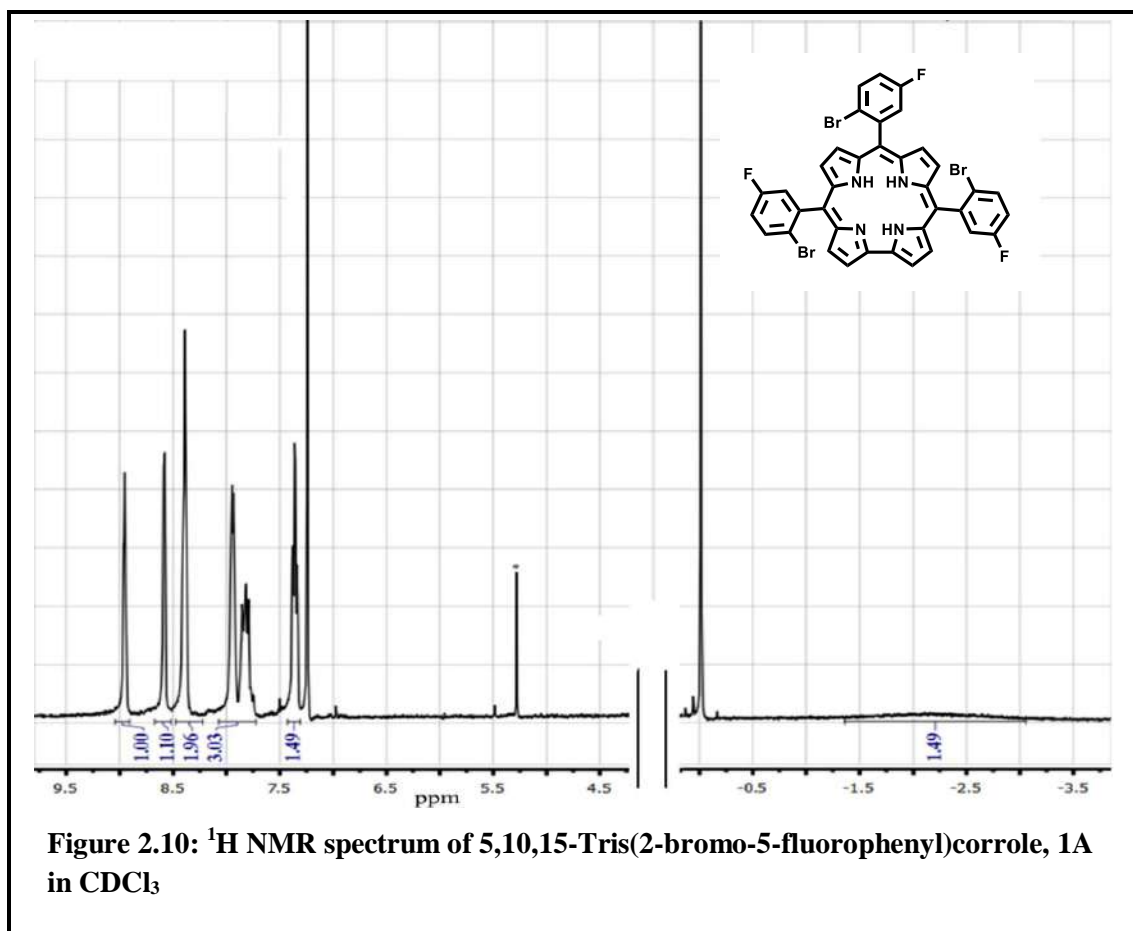


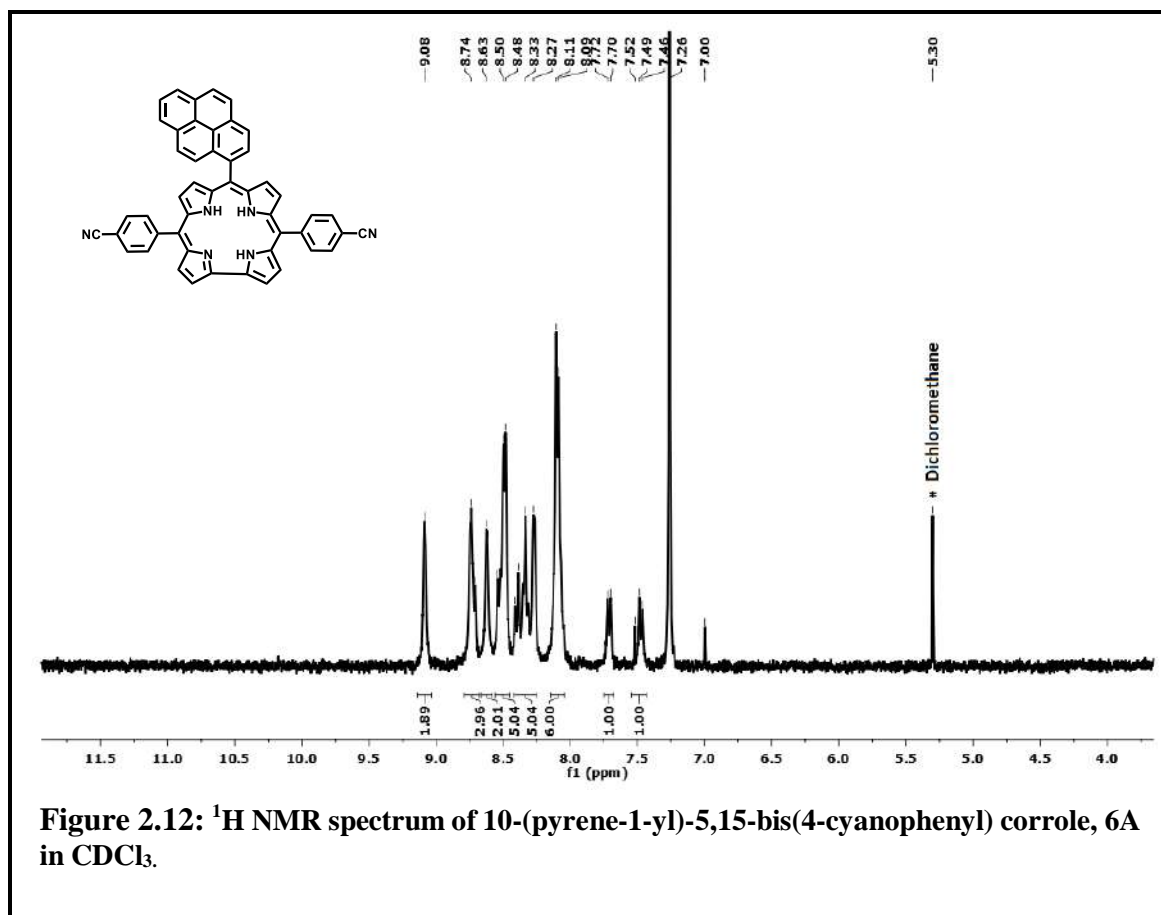
2.3.3 NMR Spectroscopy:

The novel free base corrole, **1A** displays characteristic ¹H NMR peaks in the region of 8.98-7.35 ppm for 17 aromatic protons (Figure 2.10). The ¹H NMR spectra of **1B** exhibit all the characteristic peaks within 9.21-7.38 ppm range (Figure 2.11). For another ligand **6A**, all the 25 aromatic protons appear within 9.08-7.47 ppm (Figure 2.12). Corresponding silver(III) complex **6B** shows characteristic peaks within 9.32-7.46 ppm (Figure 2.13). As the compounds **1A** and **1B** contain F atoms, we have also reported the ¹⁹F NMR spectra. In case of compound **1A**, we observe two separate peaks at -116.81 ppm (d, *J* = 17.3 Hz, 2F), -117.11 ppm (t, *J* = 21.0 Hz, 1F). Corresponding silver(III) complex, **1B** shows ¹⁹F NMR peaks within the range of -116.91 – -117.03 ppm.

2.3.4 Crystal Structure:

The crystal structures of the **3B** and **6B** are shown in Figure 2.14 and Figure 2.15 respectively. The crystal system is triclinic for **3B** and the unit cell has four **3B** molecules. The crystal system is monoclinic for **6B** and the unit cell has eight **6B** molecules. Important crystallographic parameters





for both the complexes, **3B** and **6B** are presented in Table 2.3. Bond distances and angles of **3B** and **6B** are in the line with the previously reported other corrolato-silver (III) molecules.¹³² Silver ions in both **3B** and **6B** are tetra-coordinated and the geometry around the silver ions are distorted square-planar and are due to the larger bite angle of $96.16(15)^\circ$ (for **3B**) and $96.46(11)^\circ$ (for **6B**) for the N(3)-Ag(1)-N(2) bonds. It is concluded that the corrole ring structures are indeed saddled-type as is observed by the distortion of the pyrrole ring nitrogen atoms from the mean corrolato plane by distances ranging from $(-0.14) \text{ \AA}$ to $(+0.09) \text{ \AA}$ for **3B** and $(-0.04) \text{ \AA}$ to $(+0.14) \text{ \AA}$ for **6B** respectively, while considering the 19-atom corrole ring as the mean corrole plane. Although a minimal deviation of 0.002 \AA (for **3B**) and 0.008 \AA (for **6B**) of silver ions are observed from the mean N_4 corrole planes. However, the deviation observed for the silver ion from the 19-atom mean corrole planes are 0.01 \AA (for **3B**) and 0.08 \AA (for **6B**). Angles between the planes of *meso*-substituted phenyl rings and the mean corrole (19-carbon atoms) plane (the dihedral angles) are in the ranges of 52.23 – 57.25° (for

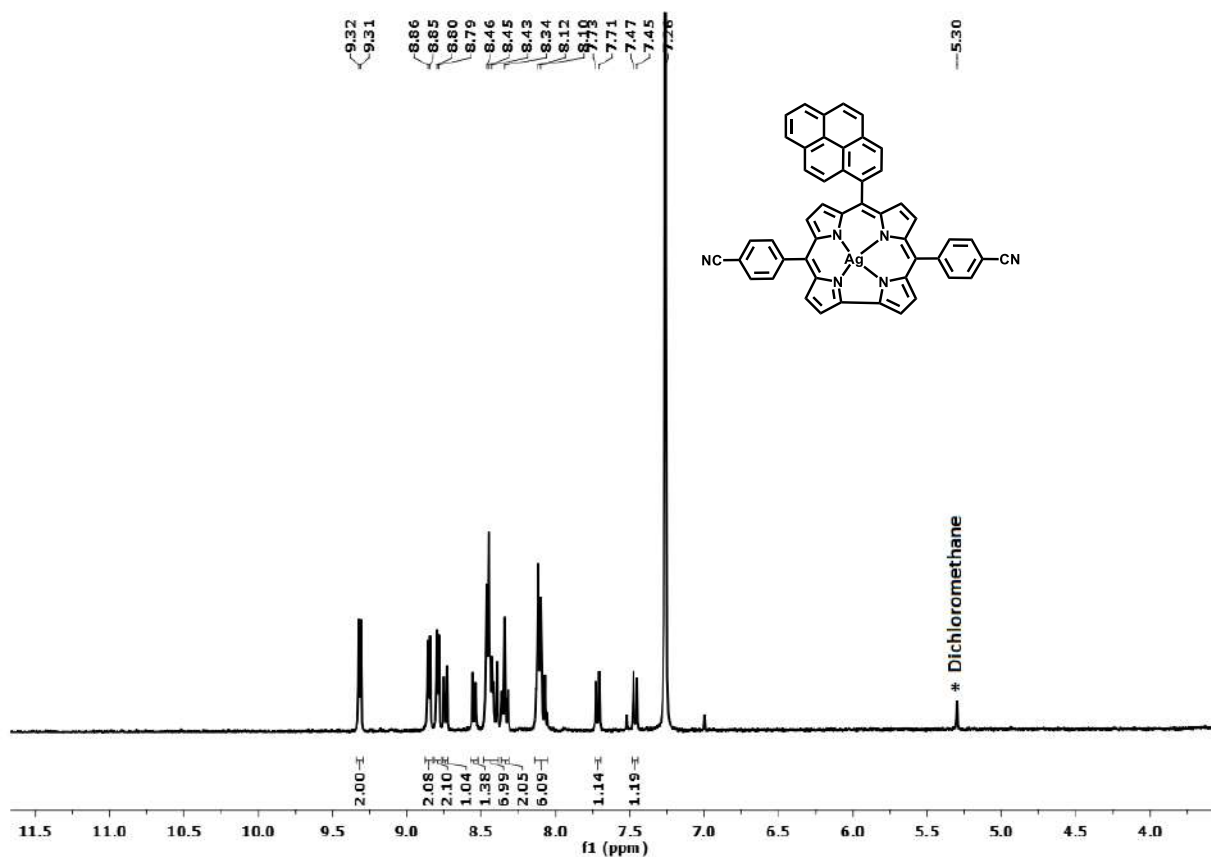


Figure 2.13: ^1H NMR spectrum of 10-(pyrene-1-yl)-5,15-bis(4-cyanophenyl)corrolato-silver(III), 6B in CDCl_3 .

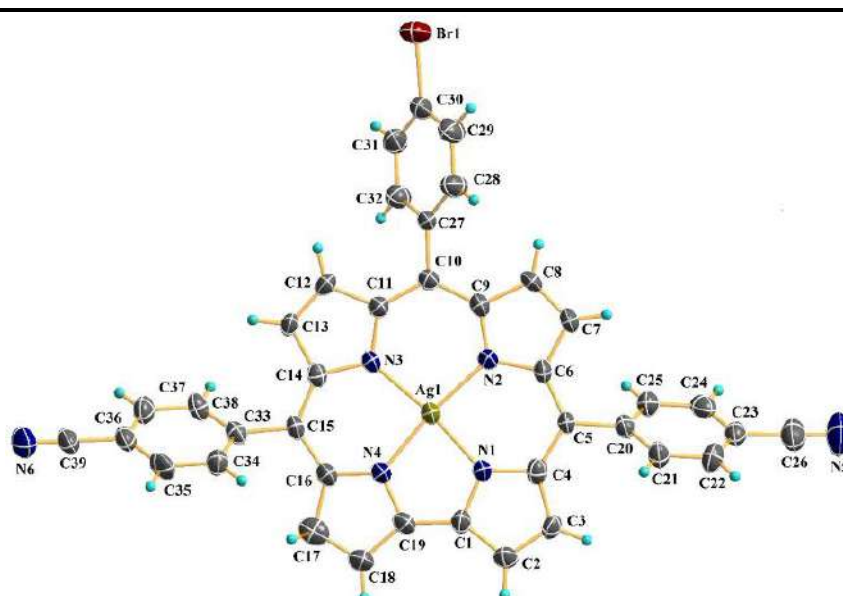


Figure 2.14: ORTEP diagram of 3B. Ellipsoids are drawn at 50% probability

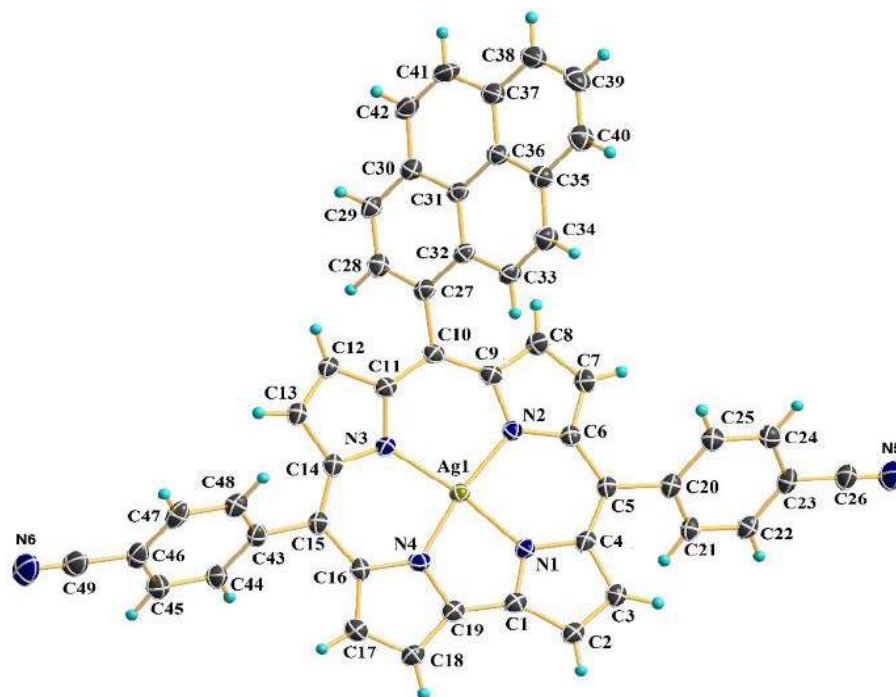


Figure 2.15: ORTEP diagram of **6B**. Ellipsoids are drawn at 50% probability

3B) and 41.26–64.70° (for **6B**). The Ag–N bond distances of **3B** are 1.929(2)Å (for N(1)-Ag(1)), 1.954(2)Å (for N(2)- Ag (1)), 1.944(2)Å (for N(3)- Ag(1)) and 1.934(2) Å (for N(4)- Ag(1)) respectively and of **6B** are 1.928(2)Å (for N(1)-Ag(1)), 1.957(2)Å (for N(2)-Ag (1)), 1.954(2)Å (for N(3)- Ag(1)) and 1.938(2) Å (for N(4)- Ag(1)) respectively.

Table 2.3: Crystallographic Data for Compounds **3B** and **6B**.

Compound codes	3B	6B
molecular formula	C ₃₉ H ₂₀ AgBrN ₆	C ₄₉ H ₂₅ AgN ₆
Fw	760.88	805.62
Radiation	MoK α	MoK α
Crystal size(mm)	0.18 \times 0.13 \times 0.12	0.2 \times 0.05 \times 0.01
crystal symmetry	triclinic	monoclinic
space group	P -1 (2)	C 2/c
<i>a</i> (Å)	10.2865(8)	36.514(5)

Compound codes	3B	6B
$b(\text{\AA})$	15.0964(12)	7.809(5)
$c(\text{\AA})$	22.6205(16)	32.017(5)
$\alpha(\text{deg})$	100.087(5)	90.000
$\beta(\text{deg})$	95.499(4)	116.233(5)
$\gamma(\text{deg})$	102.199(4)	90.000
$V(\text{\AA}^3)$	3348.0(4)	8189(6)
Z	4	8
$\mu (\text{mm}^{-1})$	1.833	0.533
$T(\text{K})$	296	100
$D_{\text{calcd}} (\text{g cm}^{-3})$	1.510	1.307
2θ range (deg)	4.09 to 55.17	6.20 to 59.28
e data (R_{int})	15276 (0.079)	11470 (0.084)
$R1$ ($I > 2\sigma(I)$)	0.0476	0.0453
wR2 (all data)	0.0745	0.1266
GOF	0.934	1.039
$\Delta\rho_{\text{max}}, \Delta\rho_{\text{min}} (\text{e \AA}^{-3})$	0.87, -0.77	1.13, -0.80

2.4. Conclusions:

In conclusion, we have developed an efficient one-step methodology for the conversion of corrolato-silver (III) complexes to the corresponding free base corroles. In comparison to previously reported methodologies, our methodology tolerated most of the functional groups and the isolated yields of the desired conversions are also much higher. Among the various other Grignard reagents, the methyl magnesium chloride is able to carry out the desired conversions almost quantitatively. However, the other two Grignard reagents, namely methyl/phenyl magnesium bromide are unable to perform the reactions quantitatively. A mechanism for these demetallation reactions has been proposed.

2.5 Experimental Section:

2.5.1 Materials:

The precursors pyrrole, *p*-chloranil, 2,4,5-trimethoxybenzaldehyde, silver acetate was purchased

from Aldrich, USA. 4-cyano benzaldehyde and 4-bromo benzaldehyde were purchased from Merck, India. Other chemicals were of reagent grade. Hexane and CH_2Cl_2 were distilled from KOH and CaH_2 respectively. For spectroscopy and electrochemical studies HPLC grade solvents were used. The synthetic methodologies and full spectroscopic characterization of **2A**,¹³³ **2B**,⁹⁶ **3A**,⁹⁶ **3B**,⁹⁶ **4A**,⁹⁶ **4B**,⁹⁶ **5A**,⁹⁶ and **5B**⁹⁶ has been reported earlier, however, the synthetic methodologies and spectroscopic characterization of **1A**, **1B**, **6A**, and **6B** has been reported for the first time here.

2.5.2 Physical measurements:

UV–Vis spectral studies were performed on a Perkin–Elmer LAMBDA-750 spectrophotometer. Emission spectral studies were performed on a Perkin Elmer, LS 55 spectrophotometer using optical cell of 1 cm path length. The elemental analyses were carried out with a Perkin–Elmer 240C elemental analyser. The NMR measurements were carried out using a Bruker AVANCE 400 NMR spectrometer. Chemical shifts are expressed in parts per million (ppm) relative to residual chloroform ($\delta = 7.26$). Electrospray mass spectra were recorded on a Bruker Micro TOF–QII mass spectrometer.

2.5.3 Crystal Structure Determination:

Single crystals of **3B** and **6B** were grown by vapour diffusion of a solution of either **3B** or **6B** in dichloromethane against hexane, followed by slow evaporation under atmospheric conditions. The crystal data of **3B** and **6B** were collected on a Bruker Kappa APEX II CCD diffractometer at 293 K and 100 K respectively. Selected data collection parameters and other crystallographic results are summarized in Table 2.1. All data were corrected for Lorentz polarization and absorption effects. The program package SHELXTL¹³⁴ was used for structure solution and full matrix least squares refinement on F^2 . Hydrogen atoms were included in the refinement using the riding model. Disordered solvent molecules were taken out using SQUEEZE command in PLATON.¹³⁵ CCDC 1505273-1505274 contains the supplementary crystallographic data's for **3B** and **6B** respectively. These data's can be obtained free of charge via www.ccdc.cam.ac.uk/data_request/cif.

2.5.4 Syntheses:

2.5.4.1 5,10,15-Tris(2-bromo-5-fluorophenyl)corrole, **1A**:

Compound **1A** was prepared by following a general procedure of corrole synthesis.¹³⁶ 2-Bromo-5-fluorobenzaldehyde (203 mg, 1 mmol) and pyrrole (134 mg, 2.0 mmol) were dissolved in 1:1 MeOH/H₂O (100 mL) mixture. The reaction mixture was stirred for 3 h in presence of HCl (36% HCl, 1.25 mL) and then extracted with CHCl₃. The organic layer was washed twice with water, dried with anhydrous Na₂SO₄, filtered, and diluted to 250 mL with chloroform. Then DDQ (227 mg, 1.0 mmol) was added and the mixture heated to reflux for three hours. The solvent was removed by rotary evaporation, and the green crude product was purified by column chromatography on silica gel (100–200 mesh) with 20% CH₂Cl₂ and 80% hexane as eluent. Yield: 24% (65 mg); Anal. Calcd (found) for C₃₇H₂₀Br₃F₃N₄ (**1A**): C, 54.37 (54.48); H, 2.47 (2.35); N, 6.86 (6.97). ¹H NMR (400 MHz, CDCl₃) δ 8.98 (d, *J* = 4.4 Hz, 2H), 8.61 (d, *J* = 4.7 Hz, 2H), 8.43–8.40 (t, *J* = 5.9 Hz, 4H), 7.99 – 7.92 (m, 3H), 7.87–7.81 (m, 3H), 7.43–7.35 (m, 3H), –2.10 (bs, 3H) (Figure 2.10). ¹⁹F NMR (376 MHz, CDCl₃) δ –116.81 (d, *J* = 17.3 Hz, 2F), –117.11 (t, *J* = 21.0 Hz, 1F). UV/Vis (CH₂Cl₂): λ_{max} (ε) = 410 (155197), 564 (25389), 604 (13949), 634 (5469) (Figure 2.8); MS (ESI⁺): *m/z* calcd for C₃₇H₂₀Br₃F₃N₄: 817.29; found: 818.53 [M+H]⁺ (Figure 2.4). **1A** displayed strong fluorescence at 646 nm (CH₂Cl₂, λ_{ex} = 550 nm).

2.5.4.2 5,10,15-tris(2-bromo-5-fluorophenyl)corrolato-silver(III), **1B**:

Compound **1B** was prepared by following a general procedure of corrolato silver(III) complex synthesis.¹³² 5,10,15-Tris(2-bromo-5-fluorophenyl)corrole, **1A** (82 mg, 0.1 mmol) was dissolved in dichloromethane (24 mL), and silver acetate (222 mg, 1.34 mmol) was added to the solution. Then trimethylamine (55 mL) was added to the reaction mixture and it was stirred for 1 hour at room temperature, during which the colour changed from purple to dark reddish. The solvent was then removed by rotary evaporation and the dark red crude product was purified by column chromatography on silica gel (100–200 mesh) with 15% CH₂Cl₂ and 85% hexane as eluent. Subsequent recrystallization (CH₂Cl₂/hexane) gave pure crystalline **1B**. Yield: 50% (46 mg); Anal.

Calcd (found) for $C_{37}H_{17}AgBr_3F_3N_4$ (**1B**): C, 48.19 (48.29); H, 1.86 (1.98); N, 6.08 (6.14). 1H NMR (400 MHz, $CDCl_3$) δ 9.21 (dd, $J = 4.5, 2.1$ Hz, 2H), 8.75 – 8.81 (m, 2H), 8.71 – 8.49 (m, 4H), 8.01–7.79 (m, 6H), 7.44–7.38 (m, 3H). (Figure 2.11) ^{19}F NMR (376 MHz, $CDCl_3$) δ –116.91 – –117.03 (m, 3F). UV/Vis (CH_2Cl_2): λ_{max} (ϵ) = 422 (121715), 531 (7532), 562 (23958), 570 nm (27677 $M^{-1}cm^{-1}$) (Figure 2.8); MS: m/z calcd for $C_{37}H_{17}AgBr_3F_3N_4$: 922.13; found: 921.37 $[M]^+$ (Figure 2.5).

2.5.4.3 10-(pyrene-1-yl)-5,15-bis(4-cyanophenyl) corrole, **6A**:

Compound **6A** was prepared by following a general procedure of corrole synthesis.¹³⁶ 5-(4-Cyanophenyl)dipyrrromethane (247 mg, 1 mmol) and 1-Pyrenecarboxaldehyde (115 mg, 0.5 mmol) were dissolved in 1:1 MeOH/ H_2O (100 mL). The reaction mixture was stirred for 1 h in presence of dilute HCl and then extracted with $CHCl_3$. The organic layer was washed twice with water, dried with anhydrous Na_2SO_4 , filtered, and diluted to 250 mL with chloroform. Then *p*-chloranil (370 mg, 1.5 mmol) was added and the mixture heated to reflux for an hour. The solvent was removed by rotary evaporation, and the green crude product was purified by column chromatography on silica gel (100–200 mesh) with 80% CH_2Cl_2 and 20% hexane as eluent. Yield: 34% (121 mg); Anal. Calcd (found) for $C_{49}H_{28}N_6$ (**6A**): C, 83.98(83.83); H, 4.03(4.05); N, 11.99 (12.12). 1H NMR (400 MHz, $CDCl_3$) δ 9.08 (s, 2H), 8.72 (d, $J = 12.3$ Hz, 3H), 8.63 (s, 2H), 8.56 – 8.44 (m, 5H), 8.35 (dd, $J = 37.6, 16.5$ Hz, 5H), 8.10 (d, $J = 7.9$ Hz, 6H), 7.71 (d, $J = 9.6$ Hz, 1H), 7.47 (d, $J = 9.4$ Hz, 1H) (Figure 2.12); UV/Vis (CH_2Cl_2): λ_{max} (ϵ) = 427 (140 200), 524 (10 200), 584 (26 400), 623 (18 000), 653 nm (13 900 $M^{-1}cm^{-1}$) ; MS: m/z calcd for $C_{49}H_{28}N_6$: 700.24; found: 701.24 $[M+H]^+$ (Figure 2.6). **6A** displayed strong fluorescence at 676 nm (CH_2Cl_2 , λ_{ex} = 560 nm).

2.5.4.4 10-(pyrene-1-yl)-5,15-bis(4-cyanophenyl)corrolato silver(III), **6B**:

Compound **6B** was prepared by following a general procedure of corrolato silver(III) complex synthesis.¹³² 10-(pyren-1-yl)-5,15-bis(4-cyanophenyl) corrole **6A** (26 mg, 0.038 mmol) was dissolved in dichloromethane (6 mL), and silver acetate (63 mg, 0.38 mmol) was added to the solution. Then trimethylamine (17.5 mL) was added to the reaction mixture and it was stirred for 1 hour at room temperature, during which the color changed from green to dark reddish brown. The

solvent was then removed by rotary evaporation and the dark red-brown crude product was purified by column chromatography on silica gel (100–200 mesh) with 60% CH₂Cl₂ and 40% hexane as eluent. Subsequent recrystallization (CH₂Cl₂/hexane) gave pure crystalline **6B**. Yield: 69% (20 mg); Anal. Calcd (found) for C₄₉H₂₅AgN₆ (**6B**): C, 73.05 (73.19); H, 3.13 (3.21); N, 10.43 (10.54). ¹H NMR (400 MHz, CDCl₃) δ 9.32 (d, *J* = 4.4 Hz, 2H), 8.85 (d, *J* = 4.7 Hz, 2H), 8.79 (d, *J* = 4.3 Hz, 2H), 8.74 (d, *J* = 7.7 Hz, 1H), 8.55 (d, *J* = 7.7 Hz, 1H), 8.48 – 8.39 (m, 7H), 8.34 (t, *J* = 7.9 Hz, 2H), 8.14 – 8.05 (m, 6H), 7.72 (d, *J* = 9.4 Hz, 1H), 7.46 (d, *J* = 9.3 Hz, 1H) (Figure 2.13); UV/Vis (CH₂Cl₂): λ_{max} (ε) = 429 (126 200), 499 (4800), 526 (7800), 542 (9700), 565 (22 100), 584 nm (33 600 M⁻¹cm⁻¹); MS (ESI⁺): *m/z* calcd for C₅₀H₂₉AgN₆O : 837.67; found: 838.58 [M+CH₃OH+H]⁺ (Figure 2.7).

2.5.4.5 Demetallation:

Demetallation of corrolato Ag (III) complexes were performed across a series of synthesized complexes (**1B–6B**), upon treatment with methylmagnesium chloride. However we will be discussing here a representative example, i.e. 10-(2,4,5-Trimethoxyphenyl)-5,15-bis(4-cyanophenyl)corrolato-silver(III), **4B** in details and the rest of the demetallation reactions could be performed by following the same procedure. 10-(2,4,5-Trimethoxyphenyl)-5,15-bis(4-cyanophenyl)corrolato-silver(III), **4B** (25 mg, 0.032 mmol) was weighed and kept in a two-necked round-bottomed flask under nitrogen atmosphere. Anhydrous dichloromethane (30 mL) was injected into the round-bottomed flask. Methyl magnesium chloride in THF (2.5 mmol) solution was added drop wise to the **4B** solution, which resulted an immediate colour change from deep reddish to a green coloured solution. The solution was stirred for another 15 min. Then aqueous solution of ammonium chloride was added, and it was extracted with water. Subsequently the organic layer was dried with anhydrous Na₂SO₄ and evaporated to dryness. The reaction mixture was then subjected to column chromatography through silica gel (100-200 mesh) column using 95% dichloromethane and 5% hexane as eluent. After recrystallization with dichloromethane and hexane, pure demetallated compound, **4A** (18.5 mg, 0.028 mmol) in 87% yield was obtained. The demetallated compound, i.e., the free base corrole, **4A**, was characterized by various analytical and spectroscopic techniques, including TLC examination,

¹H NMR studies and also by ESI mass spectroscopy and was found to be fully matching with the previously reported authentic data.

Chapter Three

Metal coordination induced ring contraction of porphyrin derivatives

3.1 Introduction

3.2 Synthetic Discussion

3.3 Spectral Characterization

3.3.1 Absorption spectroscopy

3.3.2 Electrochemistry

3.3.3 NMR spectroscopy

3.3.4 Mass Spectroscopy

3.3.5 EPR Spectroscopy

3.3.6 X-Ray Crystallography

3.3.7 ^1H NMR Experiment

3.3.8 GC-EIMS analysis

3.4 Conclusion

3.5 Experimental Part

3.5.1 All Materials details

3.5.2 Physical Studies

3.5.3 Determination of the Crystal Structure

3.5.4 Syntheses

3.5.4.1 Synthesis of 5,15-diferrocenyl-10,20-bis(4-cyanophenyl)porphyrin, 1

3.5.4.2 For 5,15-diferrocenyl-10,20-bis(4-cyanophenyl)porphyrin, 1

3.5.4.3 For 5,15-diferrocenyl-10,20-bis(4-nitrophenyl)porphyrin, 2

3.5.4.4 Synthesis of 5,15-diferrocenyl-10,20-bis(4-cyanophenyl)porphyrinato-Cu(II), 3

3.5.4.5 For 5,15-diferrocenyl-10,20-bis(4-cyanophenyl)porphyrinato-Cu(II), 3

3.5.4.6 For 5,15-diferrocenyl-10,20-bis(4-nitrophenyl)porphyrinato-Cu(II), 4

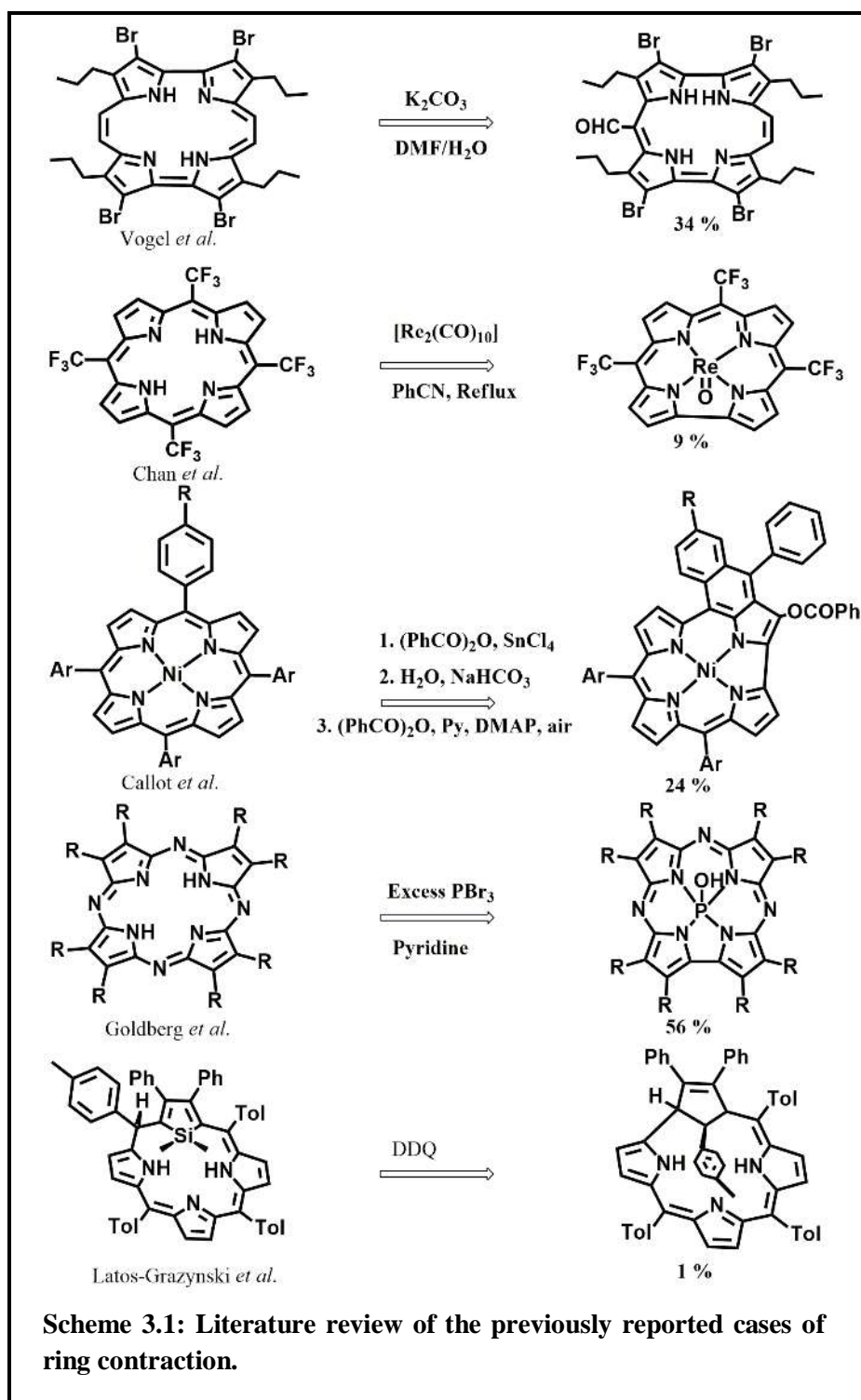
3.5.4.7 Synthesis of 10-ferrocenyl-5,15-bis(4-cyanophenyl)corrolato-Ag(III), 5

3.5.4.8 For 10-ferrocenyl-5,15-bis(4-cyanophenyl)corrolato-Ag(III), 5

3.5.4.9 For 10-ferrocenyl-5,15-bis(4-nitrophenyl)corrolato-Ag(III), 6

3.1 Introduction:

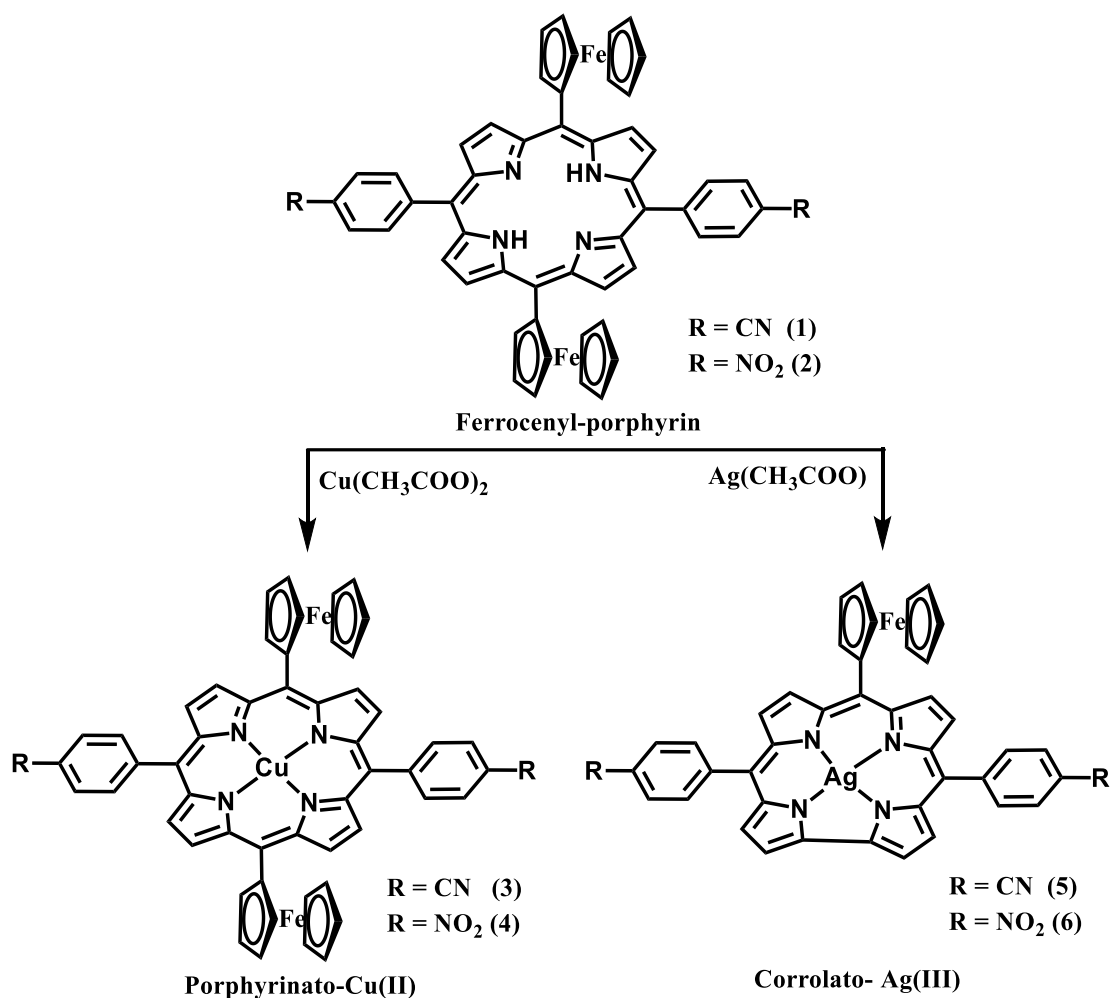
The synthesis of a corrole ring via ring contraction of a suitable porphyrin derivative has been rarely documented in the literature.¹³⁷⁻¹⁴⁴ Corroles are structurally related to corrins.¹⁴⁵⁻¹⁴⁸ However, in contrast to corrins, corroles possess aromaticity.^{94,95,149-166} Many challenging corrole based systems are under intensive research,^{94,95,149-166} and thus the ring contraction of porphyrins to corroles (rarely explored but a one-step protocol) has a lot of promise for the future development of porphyrinoid based compounds. Very few research reports indeed highlight the ring contraction methodology that leads to a porphyrin to corrole conversion (only one example of a real such conversion with 9% yield, see Scheme 3.1). Vogel *et al.* had first reported a porphycene–isocorrole rearrangement reaction and compared it with the ring contraction step for the facile synthesis of a corrin ring in association with the biosynthesis of vitamin B₁₂.¹³⁷ Porphycene and isocorrole can be considered as the related analogous macrocycles of porphyrin and corrole, respectively. In later years, during metalation of a highly electron deficient porphyrin ring by using Re₂(CO)₁₀ at higher temperature, Chan *et al.* have observed the formation of oxorhenium(V) corrolate in 9% yield. It was postulated that the reductive conditions favoured the porphyrin to corrole conversions.¹³⁸ Callot *et al.* have observed that a nickel complex of meso-tetraarylporphyrins upon treatment with benzoic anhydride and SnCl₄ and subsequent exposure to air under a basic medium resulted in the formation of nickel complexes of corroles (divalent form) in 24% yield.^{139,140} They have further demonstrated that the role of the metal ion is pivotal in this transformation and the same reaction was unsuccessful when copper was used instead of nickel. The size of the metal ion is considered to be a vital factor for this transformation. Goldberg *et al.* have described the synthesis of corrolazine by using a ring contraction methodology and have used porphyrazine as a starting material for this purpose.¹⁴¹ Latos-Grażyński *et al.* have also reported a 21-silaphlorin to iso-carbacorrole transformation in 1% yield¹⁴² (Scheme 3.1). Overall, the ring contraction methodology is poorly understood in porphyrin-based macrocycles, and no synthetic method with high yield is known.



3.2 Synthetic Discussion:

In the following, we present a modified synthetic protocol for the synthesis of two A_2B_2 -type ferrocenyl-porphyrin ligands (one new and one literature reported): 5,15-diferrocenyl-10,20-bis(4-cyanophenyl)porphyrin, **1**, and 5,15-diferrocenyl-10,20-bis(4-nitrophenyl)porphyrin, **2**,¹⁶⁶ and their relevant novel copper complexes with porphyrinato ligands 5,15-diferrocenyl-10,20-bis(4-

cyanophenyl)porphyrinato–Cu(II), **3**, and 5,15-diferrocenyl-10,20-bis(4-nitrophenyl)porphyrinato–Cu(II), **4**, and novel silver complexes with corrolato ligands (formed after ring contraction)10-ferrocenyl-5,15-bis(4-cyanophenyl)corrolato-Ag(III), **5**, and 10-ferrocenyl-5,15-bis(4-nitrophenyl)corrolato-Ag(III), **6** (Scheme 3.2).



Scheme 3.2: Comparative reactivities of ferrocenyl-porphyrin with copper acetate and silver acetate.

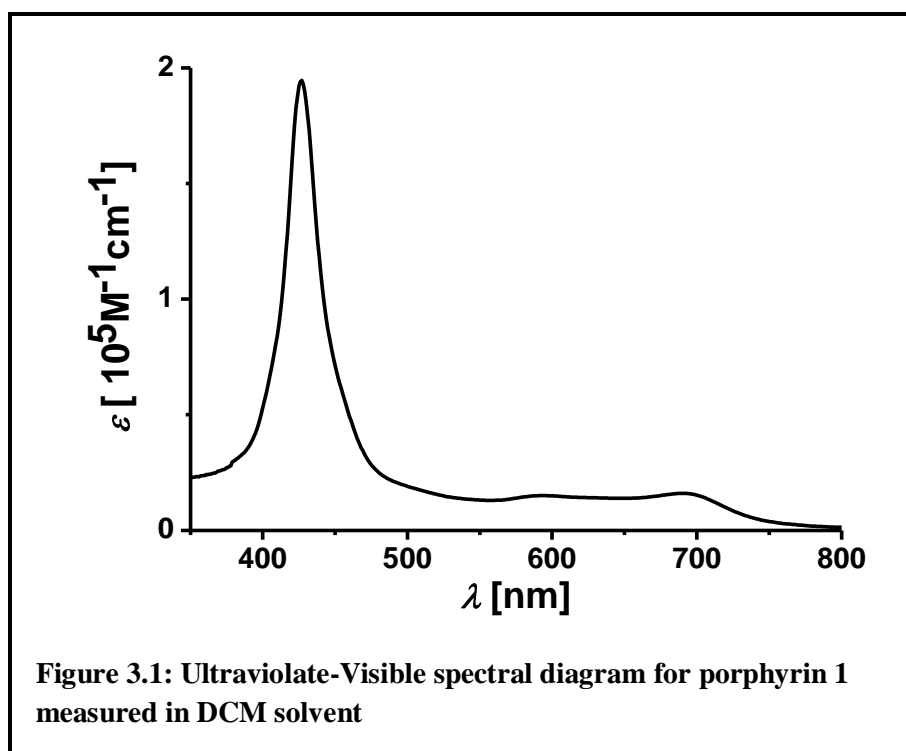
A combined synthetic, electrochemical, and crystallographic approach has been adopted to establish the reactivity pattern of the different metal precursors with the ferrocenyl-porphyrin derivatives. The two trans-A₂B₂-type ferrocenyl-porphyrin free base (FB) ligands, **1** and **2**, were prepared by following a modified synthetic strategy. The corresponding FB porphyrins, **1** and **2**, were dissolved in excess triethylamine and were stirred with excess copper acetate and silver acetate respectively. These

reactions led to the generation of complexes **3**, **4**, **5**, and **6** respectively in good yields. The composition and purity of complexes **1–6** were determined by elemental analyses, ^1H and ^{13}C NMR spectroscopy and ESI mass spectrometry.

3.3 Spectral Characterization:

3.3.1 Absorption spectroscopy:

The absorption spectra of **1** and **2** in dichloromethane are quite similar in shape; the same holds true for **3** and **4** as well as **5** and **6** (Figure 3.1-3.5). In contrast to the starting porphyrin derivatives (**1** and



2), one Q band was observed in DCM for **3** and **4**, probably as a result of a more symmetric structure, and the corresponding Soret and Q bands are blue shifted.¹⁶⁷⁻¹⁶⁹ In the cases of **5** and **6**, three Q bands were observed in DCM and the absorption spectra clearly indicate the formation of Ag-corrole derivatives^{50,96,120,121,132,170,171} (Table 3.1).

3.3.2 Electrochemistry:

The cyclic voltammogram and the differential pulse voltammogram of the complexes **3** and **5** were measured in $\text{CH}_2\text{Cl}_2/0.1\text{ M TBAP}$. The complexes **3** and **5** displayed two reversible oxidation and

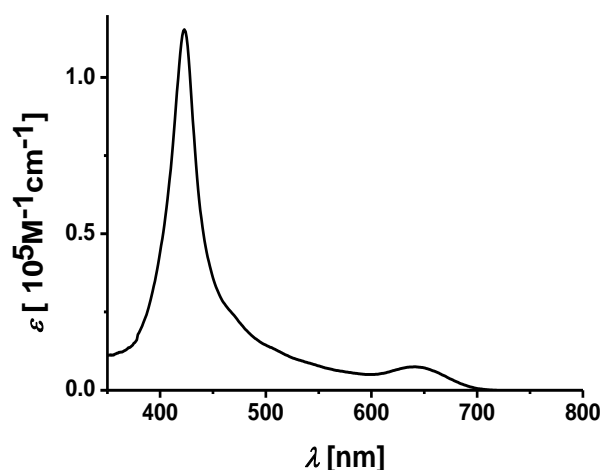


Figure 3.2: Ultraviolet-Visible spectroscopic diagram for complex **3** in DCM solvent.

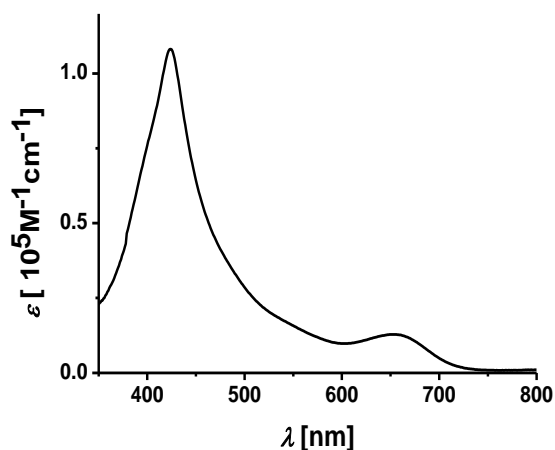


Figure 3.3: Ultraviolet-Visible spectroscopic diagram for complex **5** in DCM solvent.

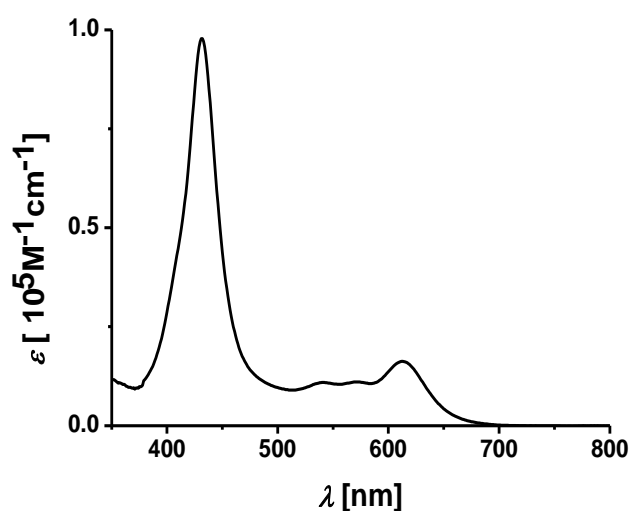


Figure 3.4: Electronic absorption spectrum of **5** in dichloromethane.

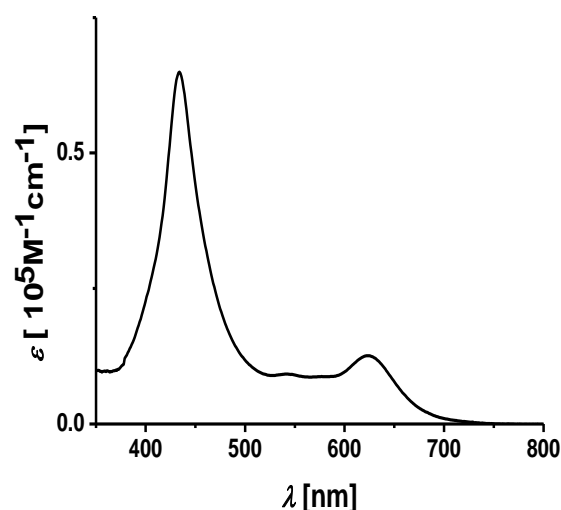
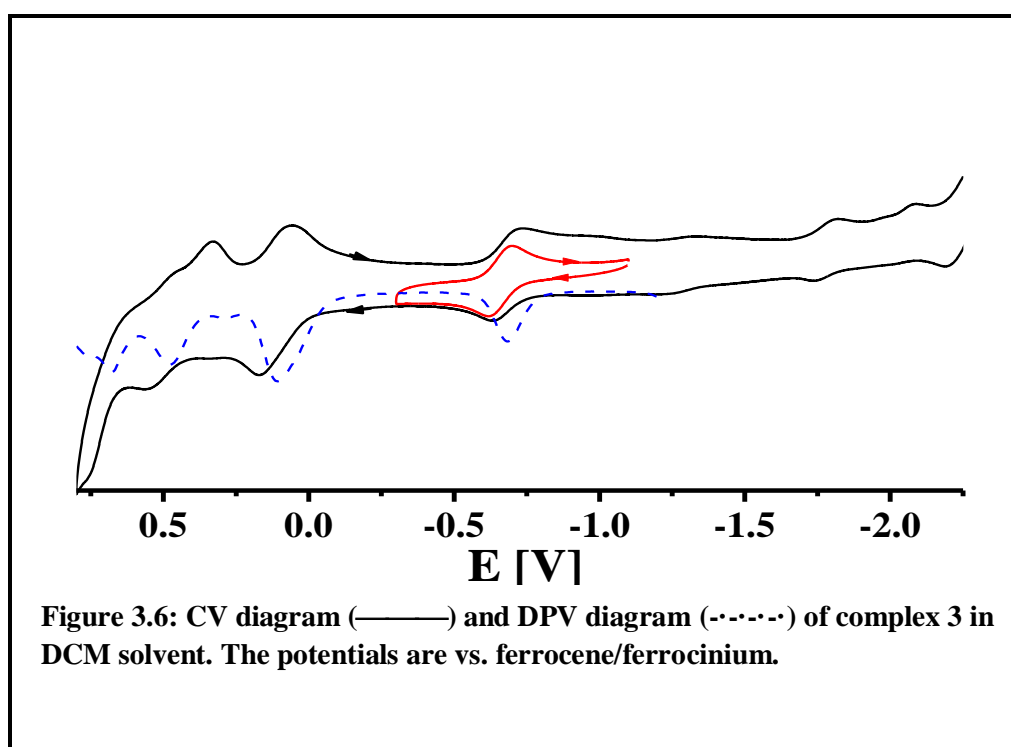


Figure 3.5: Electronic absorption spectrum of complex **6** measured in DCM solvent.

one reversible reduction steps vs. ferrocene/ferrocenium (Figure 3.6 and 3.7). The oxidation couples for **3** were observed at E_{298}^0 , V (ΔE_p , mV): 0.12 (100) and 0.49 (90) respectively. The reduction couple for **3** was observed at E_{298}^0 , V (ΔE_p , mV): -0.64 (80). The oxidation couples for **5** were observed at E_{298}^0 , V (ΔE_p , mV): 0.05 (80) and 0.51 (100) respectively. The reduction couple for **5** was observed at E_{298}^0 , V (ΔE_p , mV): -1.30 (100) (Table 3.1). The oxidation couples for the FB ligand, **1**, displayed two one-electron transfer processes at E_{298}^0 , V (ΔE_p , mV): 0.04 (80) and 0.16 (70)

respectively. These peaks probably arise due to the oxidation of the ferrocenyl moiety of the FB ligand, **1**.¹⁷²⁻¹⁷⁵ Based on these observations, we have tentatively assigned the 1st oxidation peaks at 0.12 V (for **3**) and 0.05 V (for **5**) as the ferrocene-based electron transfer process. It is clearly evident that a one-electron transfer process occurred at 0.05 V for **5** and two inseparable one-electron transfer processes occurred at 0.12 V for **3**. The one-electron transfer process (one Fc group is present) is a clear manifestation of the presence of a corrole based ring system contrary to the porphyrin-based ring system. In addition, all the oxidation and reduction couples in complex **5** correlate nicely with previously reported related Ag-corrole based systems.^{50,96,120,121,132,170,171}



3.3.3 NMR spectroscopy:

The ¹H NMR spectrum of **1** exhibited sharp lines in accordance with sixteen partially overlapping aromatic protons in the region δ, 10.0–8.0 ppm with ‘normal’ chemical shifts. The eighteen partially overlapping cyclopentadienyl ring protons are observed in the 5.5–4.0 ppm region. The two imine protons of porphyrin resonate at –1.75 ppm and all these observations are in line with the diamagnetic character of the porphyrin FB ligands (Figure 3.8). The ¹H NMR spectrum of the complexes **5** and **6** exhibited sharp lines with ‘normal’ chemical shifts and these observations are in line with the

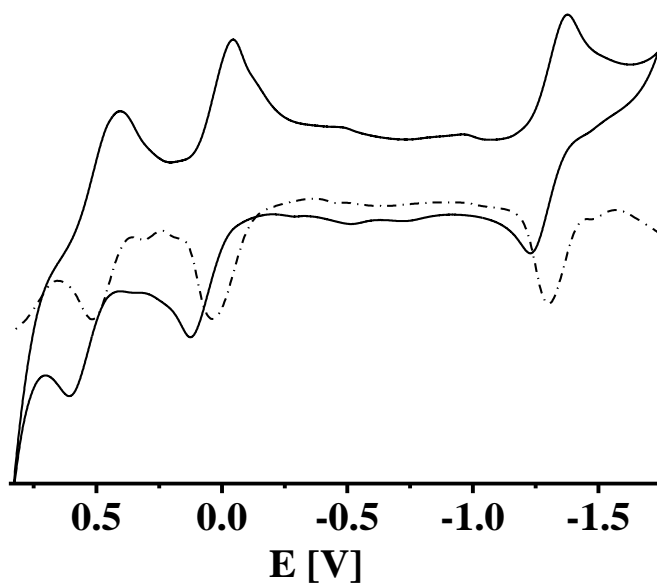


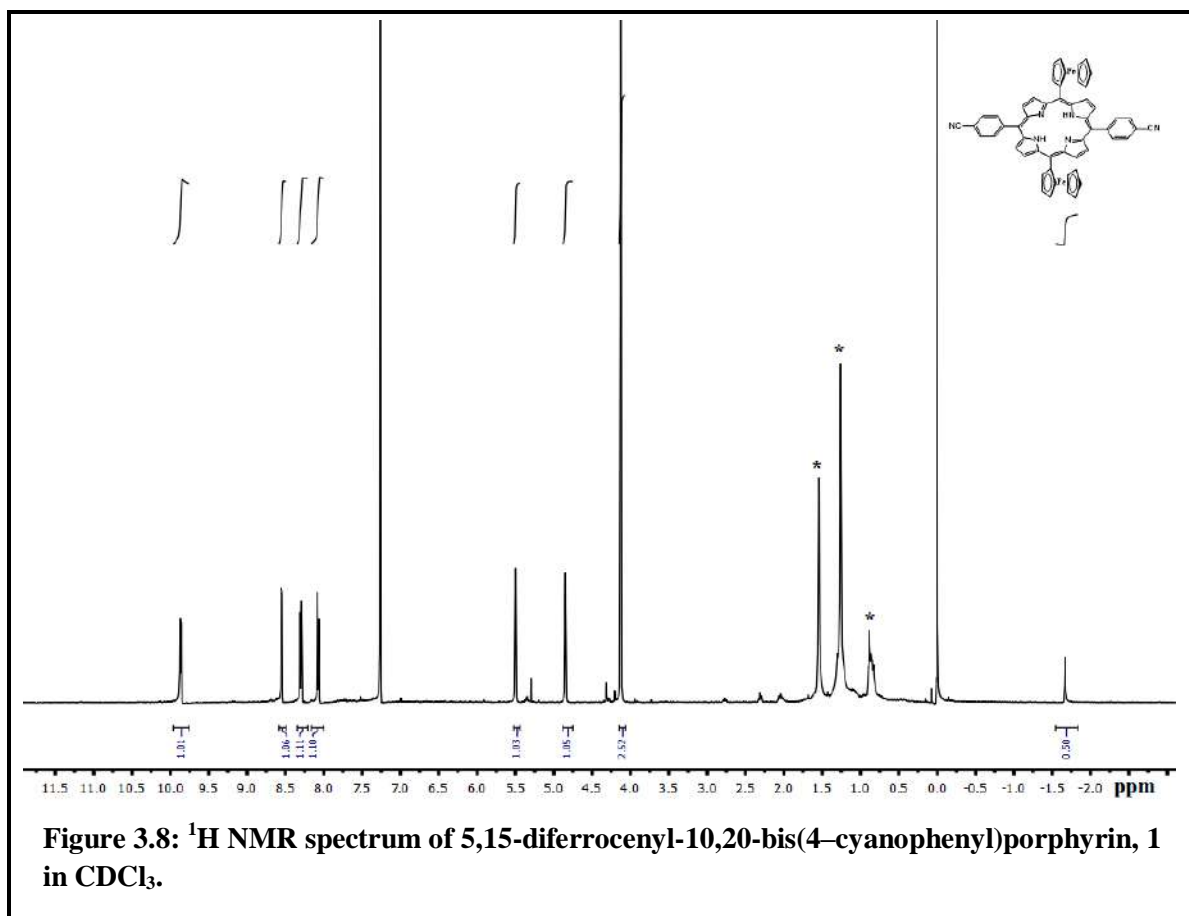
Figure 3.7: CV diagram (—) and DPV diagram (---) of complex 5 measured in DCM solvent. The potentials are vs. ferrocene/ferrocinium.

Table 3.1: UV–Vis. and CV data

Compound	UV–vis. Data ^a $\lambda_{\text{max}} / \text{nm} (\epsilon / \text{M}^{-1}\text{cm}^{-1})$	Electrochemical data ^a	
		Oxidation $E^0, \text{V} (\Delta E_p, \text{mV})$	Reduction $E^0, \text{V} (\Delta E_p, \text{mV})$
1	427 (195000), 593 (15000), 690 (16000).	0.04 (80), 0.16 (70).	–
2	428 (93000), 606 (18500), 695 (19000).	–	–
3	423 (115000), 642 (7500).	0.12 (100), 0.49 (90).	–0.64 (80).
4	423 (108000), 653 (13000).	–	–
5	431 (98000), 541 (11000), 571 (11000), 612 (16000).	0.05 (80), 0.51 (100).	–1.30 (100).
6	434 (65000), 542 (9200), 577 (8800), 624 (12700).		

^a in DCM solvent.

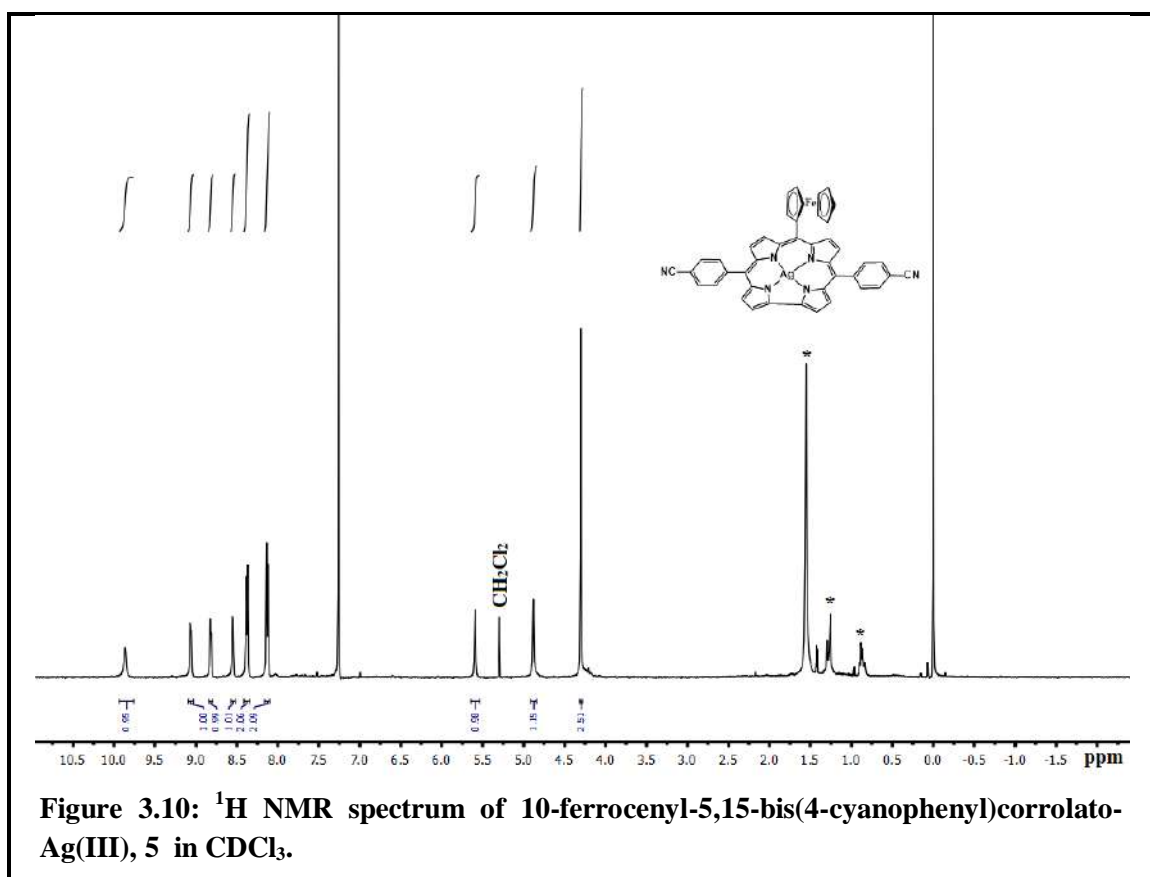
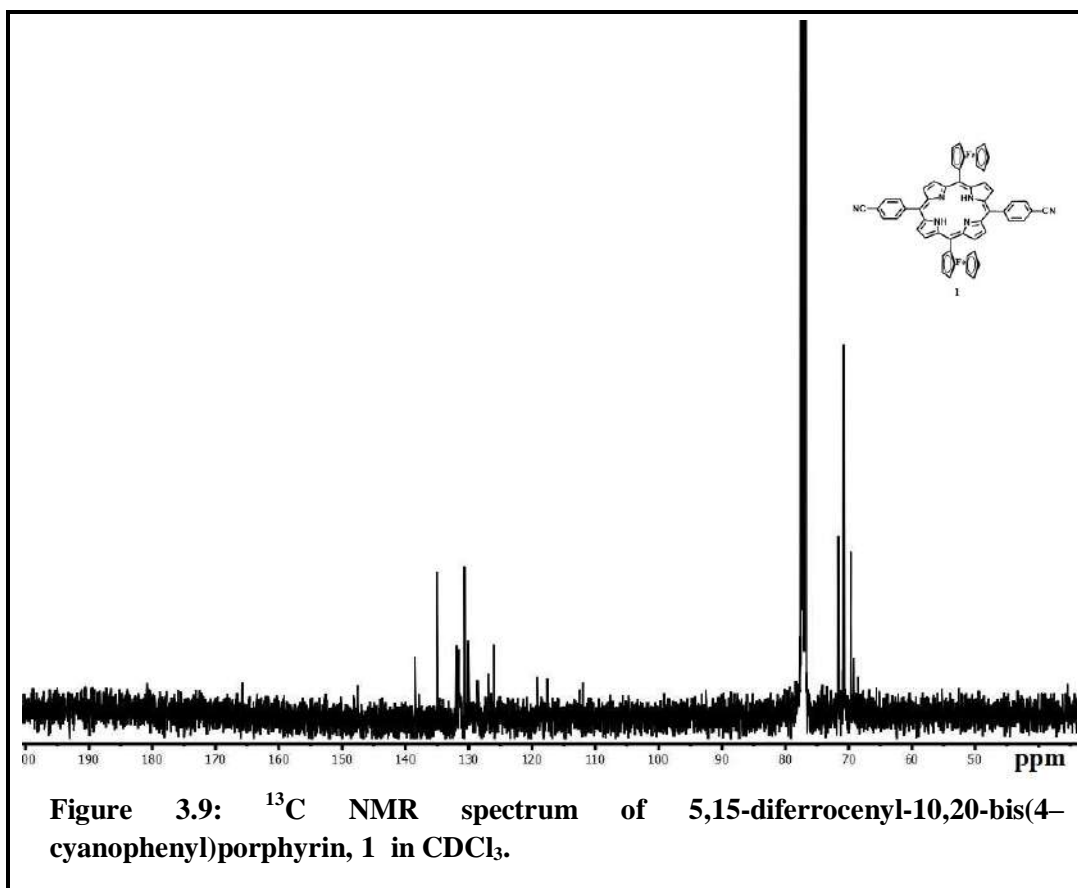
The potential values are vs. ferrocene/ferrocenium.



diamagnetic character of the complexes **5** and **6** (Figure 3.10 and 3.12) For example, the ¹H NMR spectrum of **5** exhibited sharp lines in accordance with sixteen partially overlapping aromatic protons in the region δ , 9.8–8.1 ppm. The nine partially overlapping cyclopentadienyl ring protons (for a similar porphyrin derivative this number will be eighteen) are observed in the 5.6–4.2 ppm region and all these observations tally well with the formulation of a diamagnetic corrolato-Ag^{III} complex formation.^{50,96,120,121,132,170,171} ¹³CNMR Spectra of compound **1**, **5** and **6** are also reported here (Figure 3.9, 3.11 and 3.13).

3.3.4 Mass Spectroscopy:

The electrospray mass spectrum of the free base corroles **1** and **2** are reported here. Compound **1** shows intense peak centred at $m/z = 880.17$ correspond to [**1**]⁺ (880.17 calcd for C₅₄H₃₆Fe₂N₆)



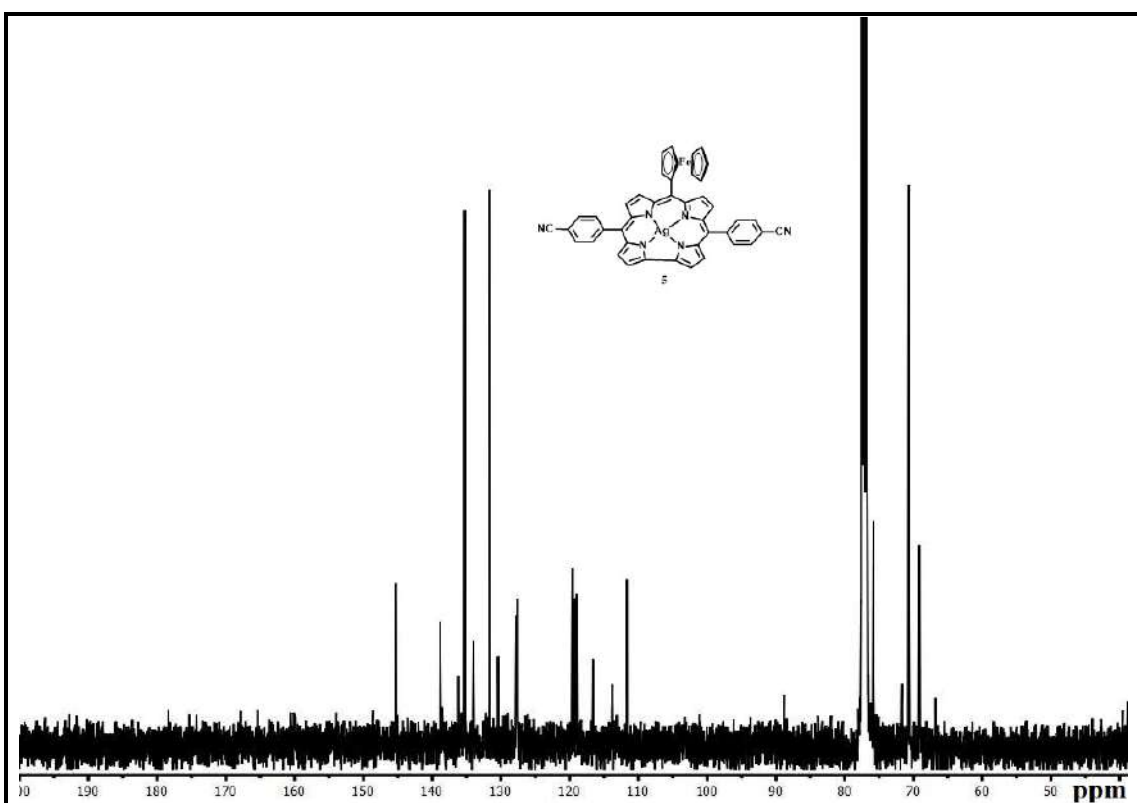


Figure 3.11: ^{13}C NMR spectrum of 10-ferrocenyl-5,15-bis(4-cyanophenyl)corrolato- $\text{Ag}(\text{III})$, 5 in CDCl_3 .

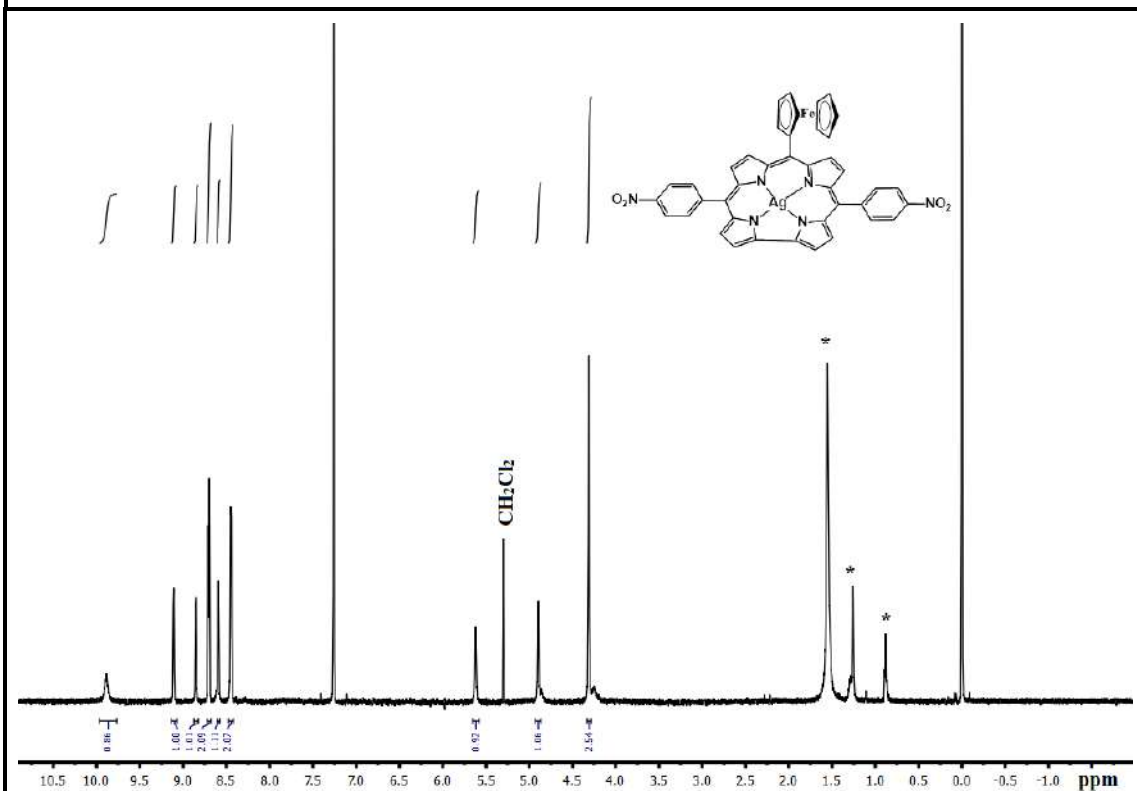
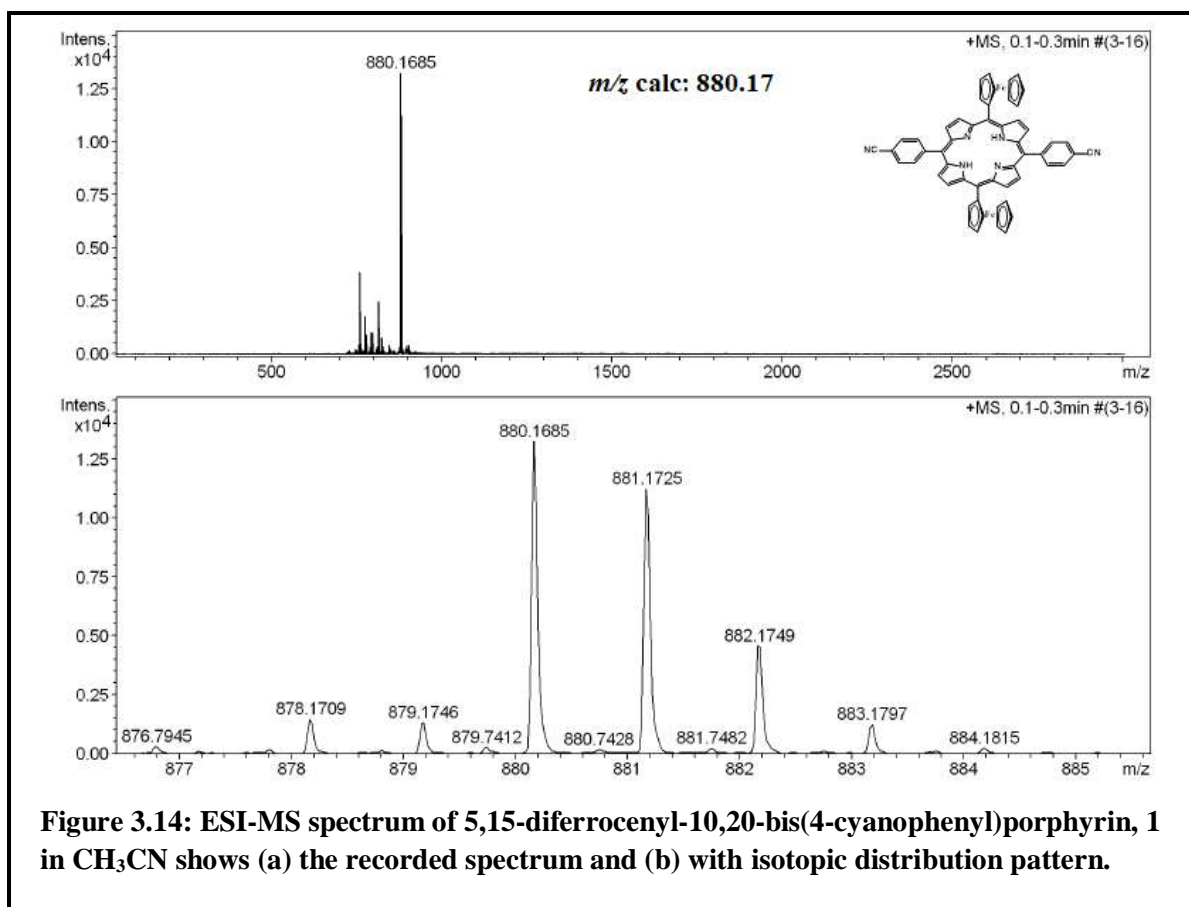
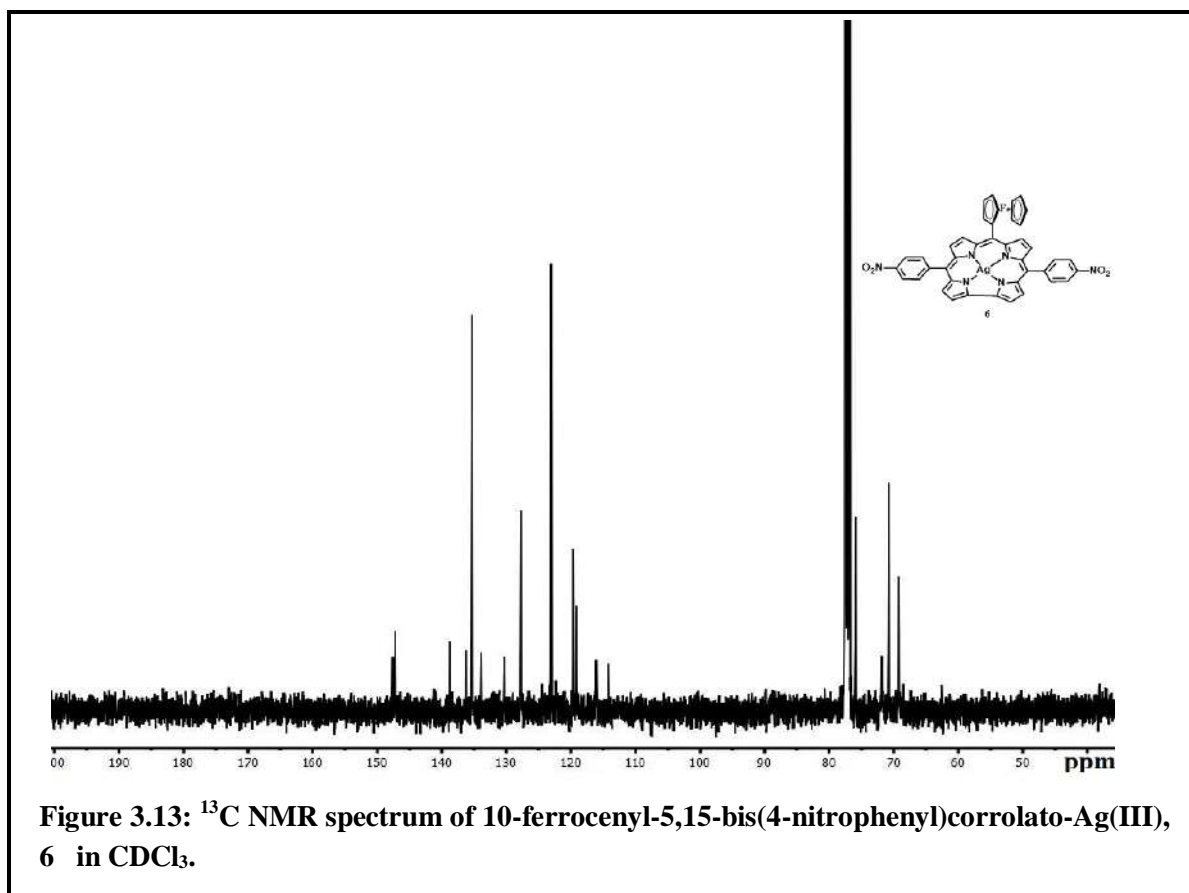
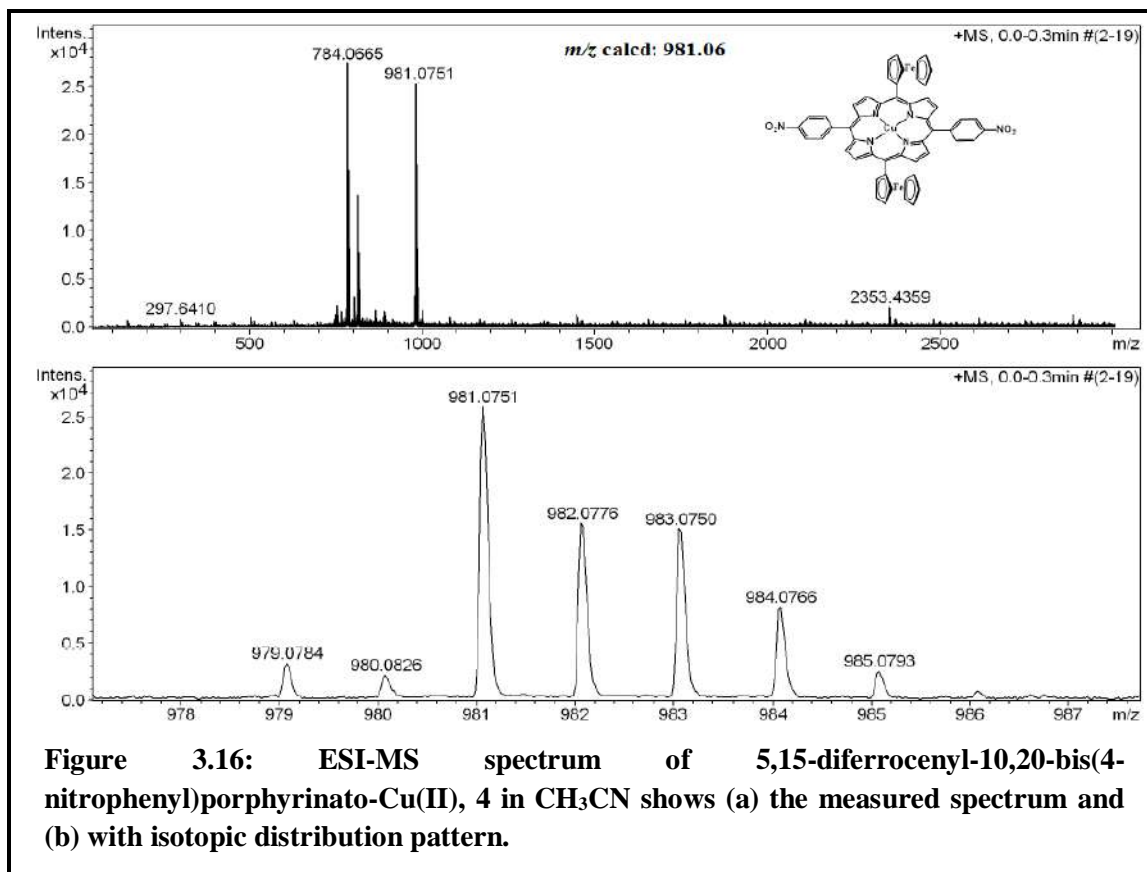
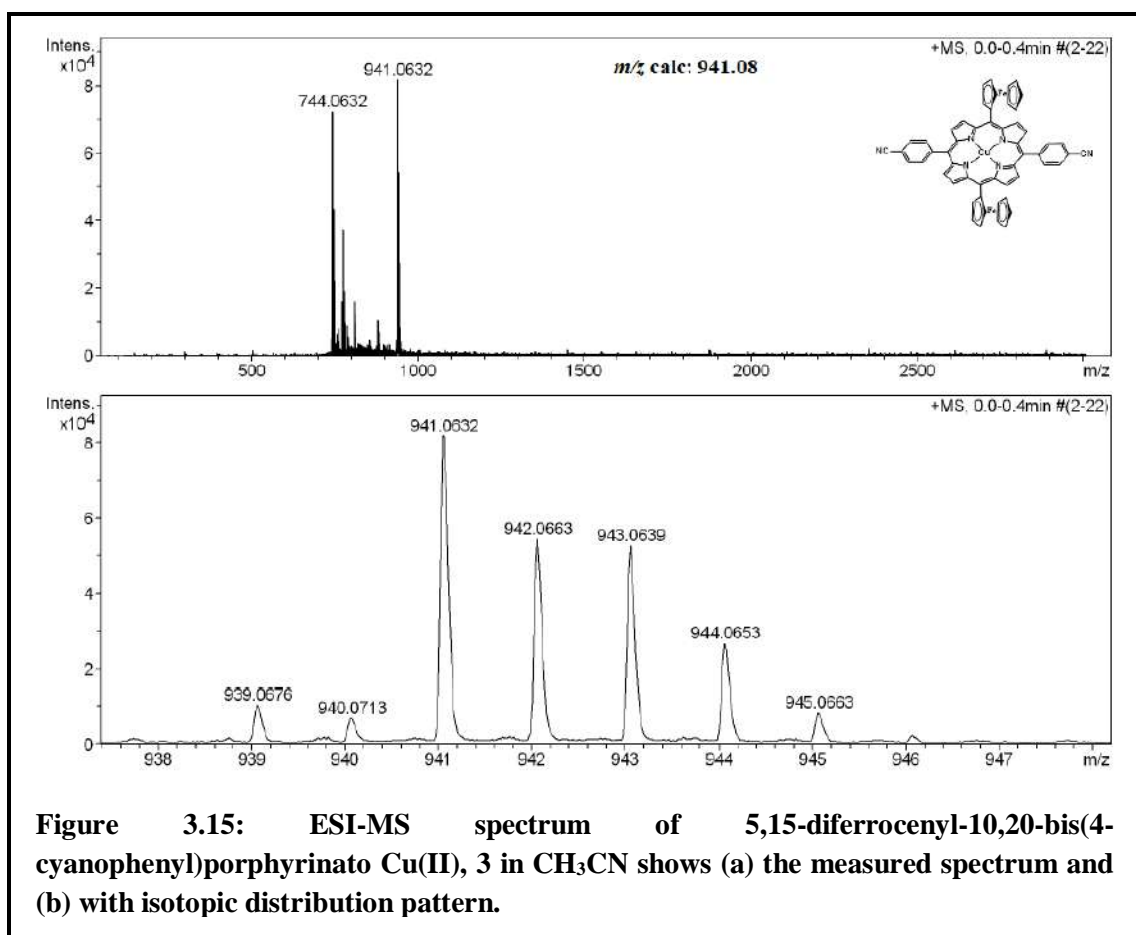
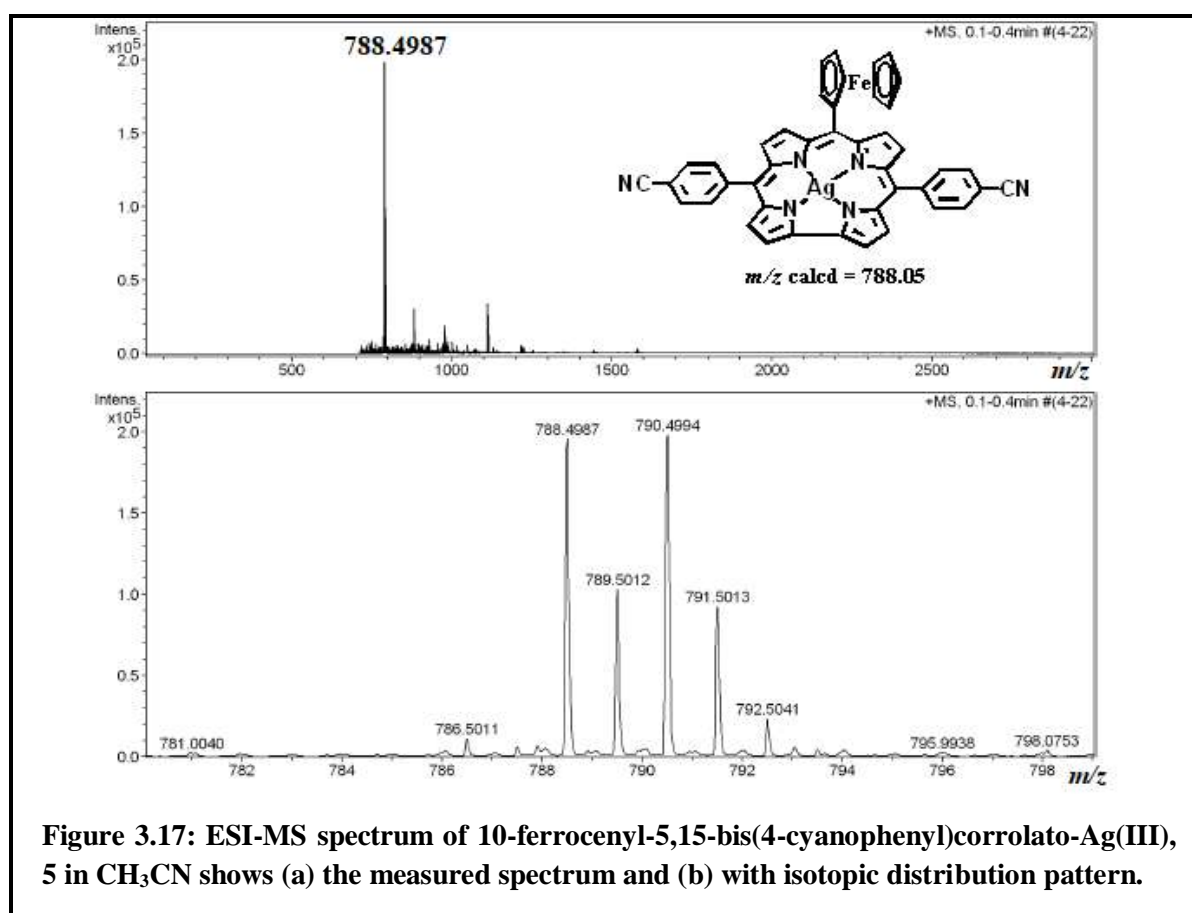


Figure 3.12: ^1H NMR spectrum of 10-ferrocenyl-5,15-bis(4-nitrophenyl)corrolato- $\text{Ag}(\text{III})$, 6 in CDCl_3 .



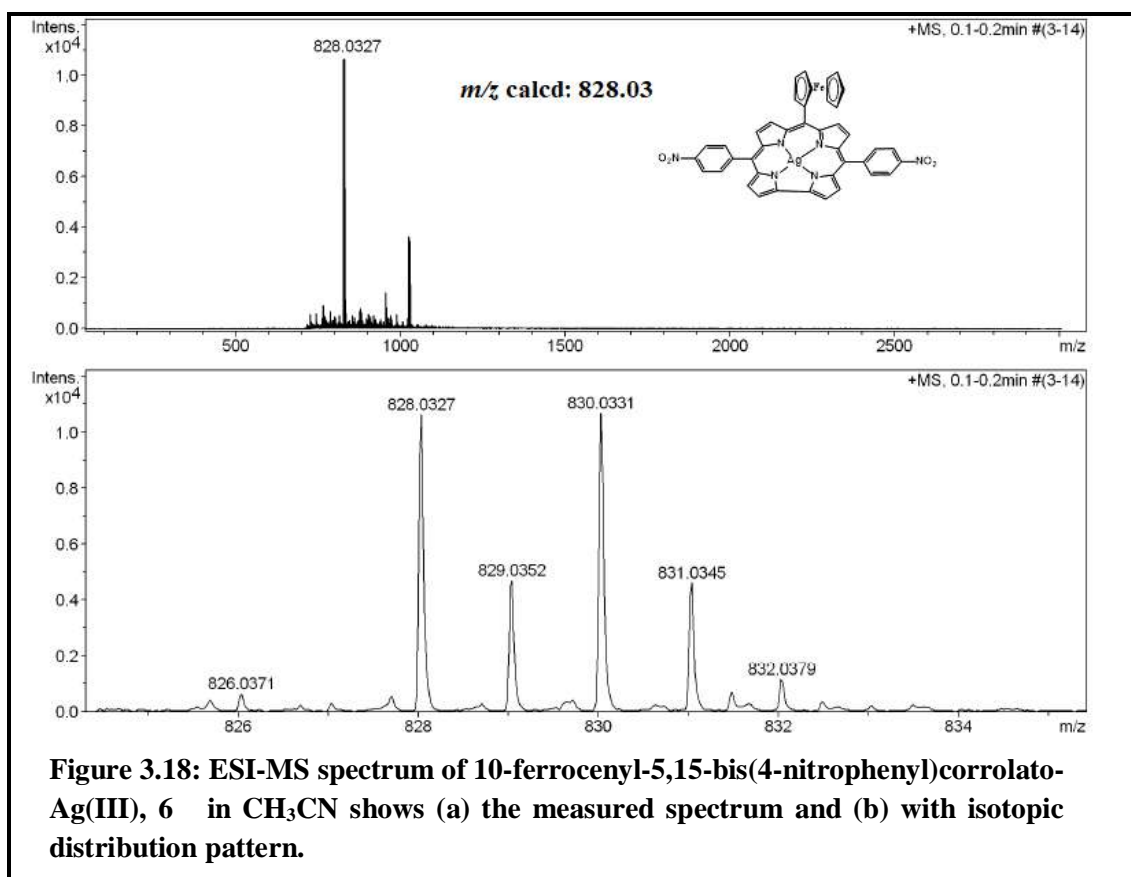


{Figure 3.14}. The electrospray mass spectrum of ligand **2** is measured in acetonitrile solvent which leads to the generation of intense peak centred at $m/z = 921.15$ correspond to $[\mathbf{2}+\mathbf{H}]^+$ (920.15 calcd for $\text{C}_{52}\text{H}_{36}\text{Fe}_2\text{N}_6\text{O}_4$). Corresponding Cu(II) porphyrin complexes **3** and **4** show intense peak centred at $m/z = 941.06$ correspond to $[\mathbf{3}]^+$ (941.08 calcd for $\text{C}_{54}\text{H}_{34}\text{CuFe}_2\text{N}_6$) {Figure 3.15} and at $m/z = 981.07$ correspond to $[\mathbf{4}]^+$ (981.06 calcd for $\text{C}_{52}\text{H}_{34}\text{CuFe}_2\text{N}_6\text{O}_4$) {Figure 3.16} respectively. Corresponding Ag(III) corrole complexes **5** and **6** show intense peak centred at $m/z = 788.04$ correspond to $[\mathbf{5}]^+$ (788.05 calcd for $\text{C}_{43}\text{H}_{25}\text{AgFeN}_6$) {Figure 3.17}. and $m/z = 828.03$ correspond to $[\mathbf{6}]^+$ (828.03 calcd for $\text{C}_{41}\text{H}_{25}\text{AgFeN}_6\text{O}_4$) {Figure 3.18} respectively.



3.3.5 EPR Spectroscopy:

The EPR data of the complexes (**3** and **4**) are presented in Figure 3.19, 3.20 and Table 3.2. In the native state (in DCM at RT) the compound **3** displays a typical Cu(II)-type EPR spectrum (Figure 3.19). The experimental data of **3** were simulated by considering an axial g -tensor with $g_{\parallel} = 2.110$ and $g_{\perp} = 2.040$ and the corresponding hyperfine coupling to the copper nuclei (Table 2). There are



some discrepancies between the experimental and the simulated spectra. Such discrepancies are an established phenomenon in the EPR spectra of copper(II)–porphyrin complexes, and have been documented elsewhere as well.^{176,177}

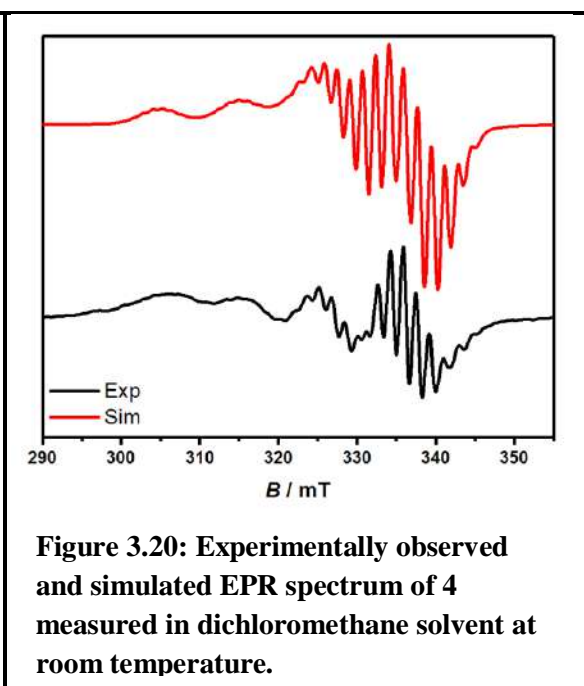
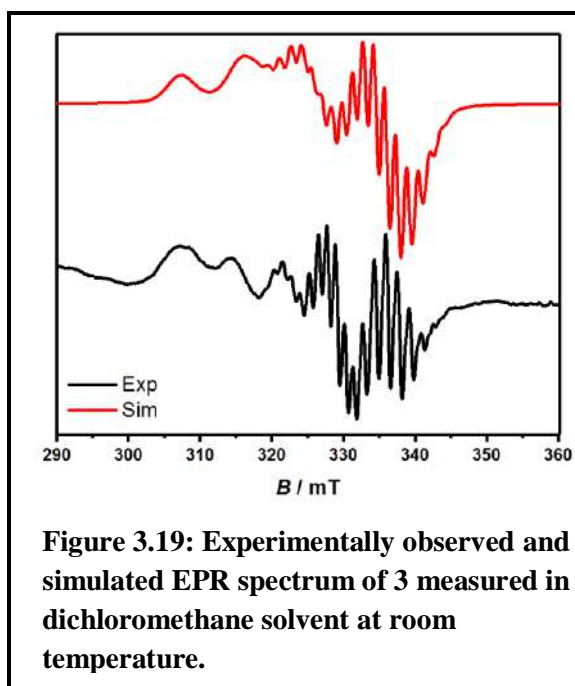
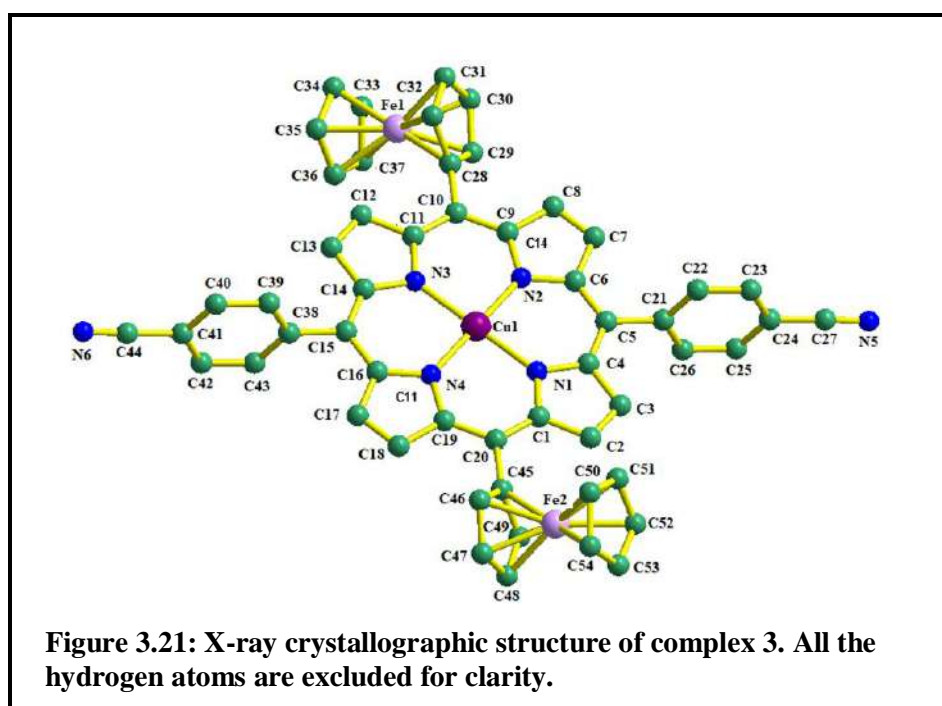


Table 3.2: Overview of g values and hyperfine coupling constants obtained from simulation.

	g_1	g_2	$A_1(^{63,65}\text{Cu})$	$A_2(^{63,65}\text{Cu})$	$A_1(^{14}\text{N})$	$A_2(^{14}\text{N})$
3	2.040	2.110	120	250	45	25
4	2.029	2.113	90	290	47	37

3.3.6 X-Ray Crystallography:

The molecular structure of **3** in the crystal is shown in Figure 3.21. Important crystallographic parameters are reported in Table 3.3. The bond distances and angles of **3** match nicely with those of the previously reported other authentic porphyrinato–copper(II) complexes.¹⁶⁷⁻¹⁶⁹ The Cu–N bonds in the corrolato-copper(III) complexes reported earlier are found out to be in the order of 1.873 Å and



1.907 Å.¹⁷⁸ The crystal structure of **5** is shown in Figure 3.22. Important crystallographic parameters are reported in Table 3.3. The asymmetric unit of **5** consists of three crystallographic independent molecules having different conformations. The Ag–N bond distances are 1.948 Å (for Ag1–N1), 1.949 Å (for Ag1–N2), 1.963 Å (for Ag1–N3) and 1.937 Å (for Ag1–N4). The bond distances and

angles of **5** match nicely with those of the previously reported related corrolato-silver(III) complexes.

50,96,120,121,132,170,171

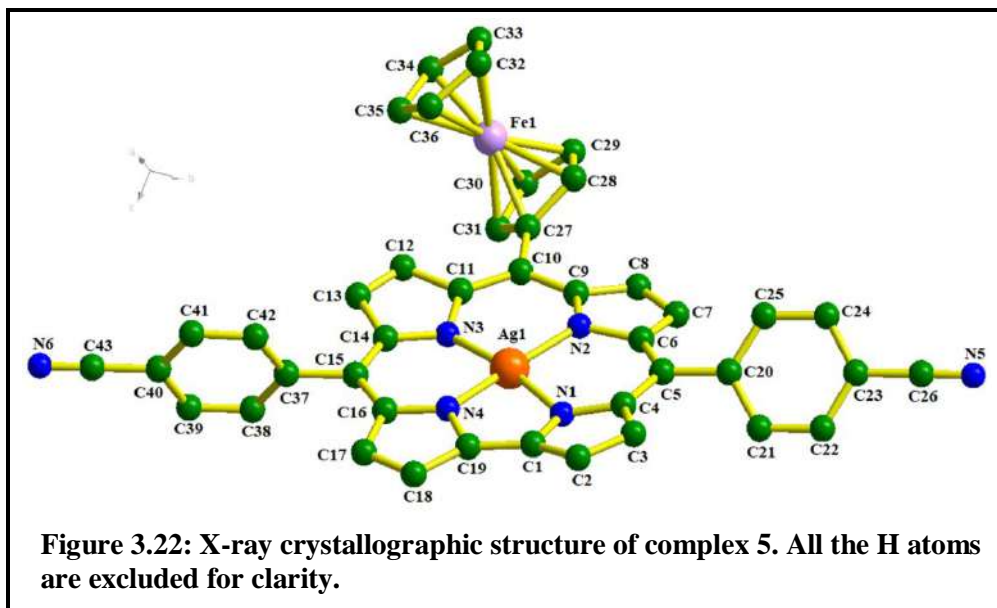


Table 3.3: Crystallographic Data for **3** and **5**.

Compound codes	3	5
molecular formula	C ₅₄ H ₃₄ CuFe ₂ N ₆	3(C ₄₃ H ₂₅ AgFeN ₆)
Fw	942.11	3 × 789.41
Radiation	MoKα	Cu Kα
crystal symmetry	Monoclinic	Triclinic
space group	<i>P</i> 2 ₁ / <i>c</i>	<i>P</i> -1
<i>a</i> (Å)	18.6124(8)	18.4767(6)
<i>b</i> (Å)	8.9540(4)	18.7775(7)
<i>c</i> (Å)	15.5768(7)	19.6170(5)
<i>α</i> (deg)	90	99.222(2)
<i>β</i> (deg)	113.979(2)	104.379(2)
<i>γ</i> (deg)	90	117.221(4)
<i>V</i> (Å ³)	2371.91(18)	5558.5(4)
<i>Z</i>	2	2
<i>μ</i> (mm ⁻¹)	1.089	7.677

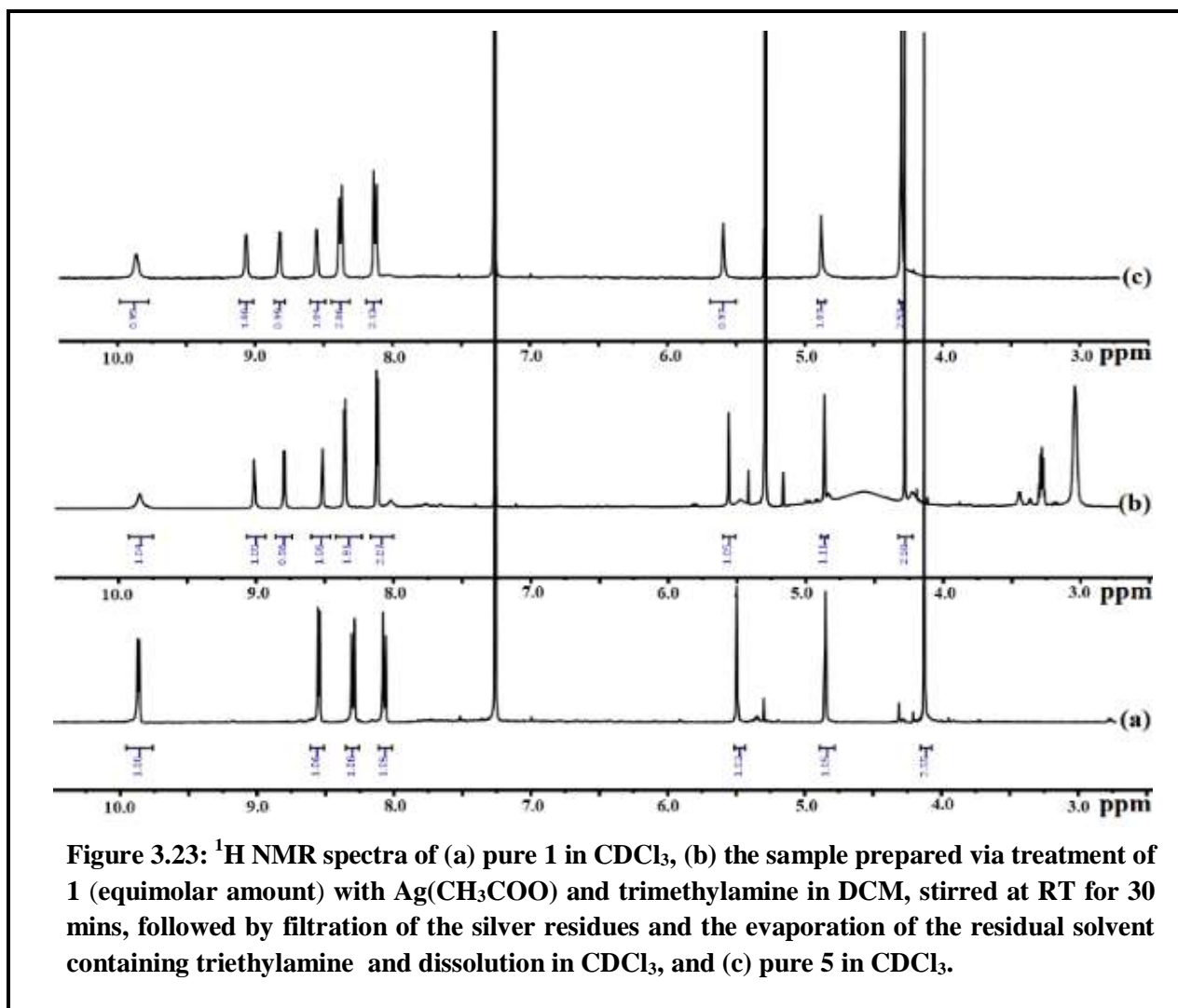
$T(K)$	296	298
$D_{\text{calcd}} (\text{g cm}^{-3})$	1.319	1.415
2θ range (deg)	2.395 to 26.057	2.452 to 66.999
e data (R_{int})	4676 (0.087)	19796 (0.058)
$R1$ ($I > 2\sigma(I)$)	0.0438(2799)	0.0533(16557)
WR2 (all data)	0.0996(4676)	0.1585(19796)
GOF	0.957	1.169
$\Delta\rho_{\text{max}}, \Delta\rho_{\text{min}} (\text{e } \text{\AA}^{-3})$	0.34, -0.32	2.510, -1.320

3.3.7 ^1H NMR Experiment:

An attempt has been made to understand the ring contraction methodology. We have performed in situ NMR experiments in order to get an idea about the ring contraction. For this purpose, 6 mg of compound **1** was taken and was dissolved in CDCl_3 and the obtained spectrum is shown in Figure 3.23 (a). The observed spectrum authenticates that the signals are due to the presence of FB porphyrin derivatives only and there are no traces of impurity signals that can suggest the presence of FB corrole derivatives. The ^1H NMR spectrum of the crude reaction mixture is shown in Figure 3.23. For the sake of comparison, we have also attached the spectrum of the pure compound **5** in CDCl_3 (Figure 3.23 (c)). One can easily identify that the peaks belonging to porphyrin **1** are totally consumed (Figure 3.23 (b) and new peaks due to corrolato-Ag(III) (**5**) appeared and all these changes are visible in Figure 3.23. In fact, both Figure 3.23 (b) and (c) demonstrate identical NMR spectra. Thus, the NMR spectra authenticate the conversion of FB porphyrin to the corrolato- Ag(III) derivative. An attempt has been made to decipher the mechanism of this ring contraction phenomenon (Scheme 3.2).

3.3.8 GC-EIMS analysis:

The silver corrole formation was almost quantitative and the formation of silver porphyrin was observed in negligible amount ($\sim 1\%$) over the entire reaction time frame. Over the entire course of the reaction, we have not observed any TLC spot that corresponds to the FB corrole derivatives, thus it appears that the silver chelation occurs very rapidly. There are many possibilities that can lead to



the corrole ring formation. GC-EIMS analysis of the crude reaction mixture (Figure 3.24-3.29) helped us to rule out several alternative possibilities of the corrole ring formation. We have monitored the course of the reaction via GC-EIMS (the corresponding FB porphyrin was dissolved in DCM and was treated with triethylamine and excess silver acetate) and identified the release of the ferrocenyl moiety from the starting FB porphyrin precursors (Figure 3.24-3.29). The retention time of this ferrocenyl moiety in the GC column is very close to that of the free ferrocene derivative (Figure 3.30 and 3.31) but significantly different from that of the authentic ferrocene aldehyde samples (Figure 3.32 and 3.33). This indicates that the ferrocenyl moiety is a cleavage product from the parent FB porphyrin. It has to be kept in mind that several control experiments have been performed under identical reaction conditions. When FB porphyrin was dissolved in DCM and was stirred with

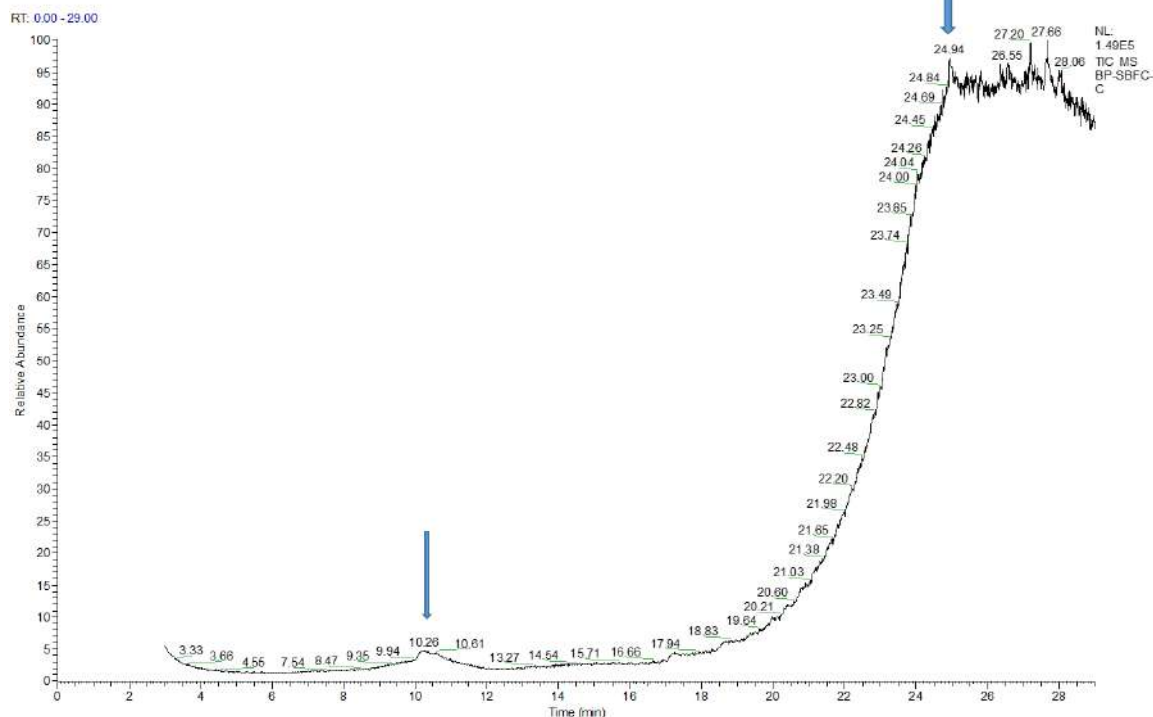


Figure 3.24: 5,15-diferrocenyl-10,20-bis(4-cyanophenyl)porphyrin, **1** was dissolved in DCM and subsequently silver acetate was added followed by the addition of triethylamine solvent into the reaction mixture and it was stirred continuously at room temperature. Aliquots of this reaction mixture were taken after 2 minutes and were monitored by GC-EIMS analysis.

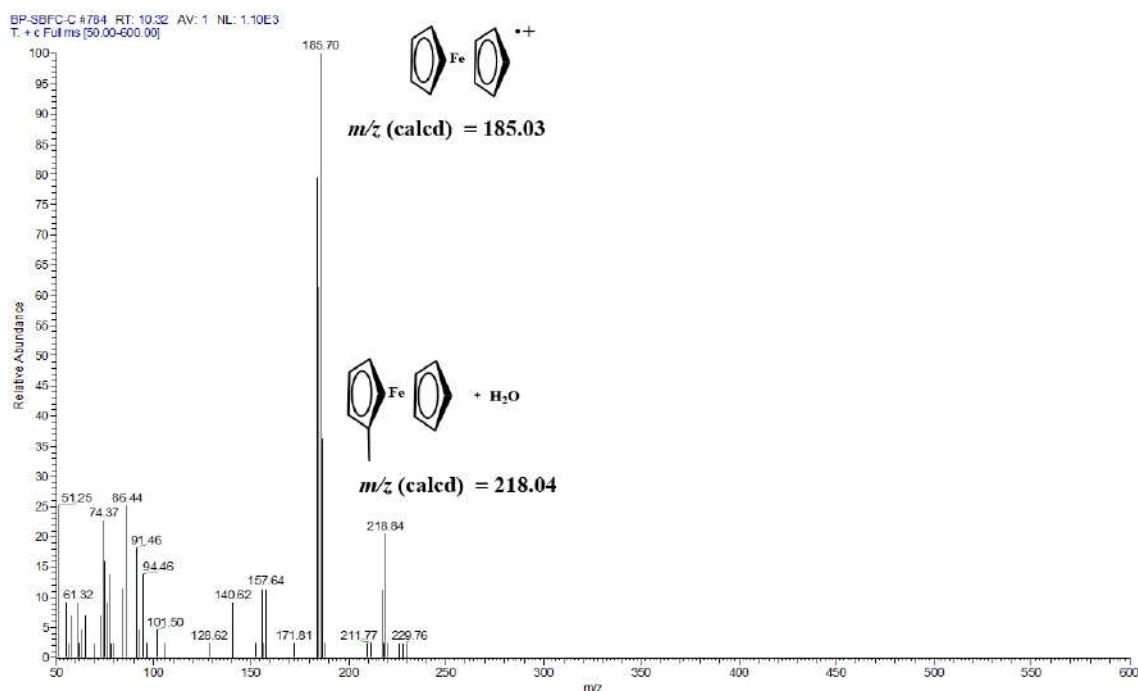


Figure 3.25: Mass spectrum (GC-EIMS) of ferrocenyl derivatives detected by GC of the reaction mixture.

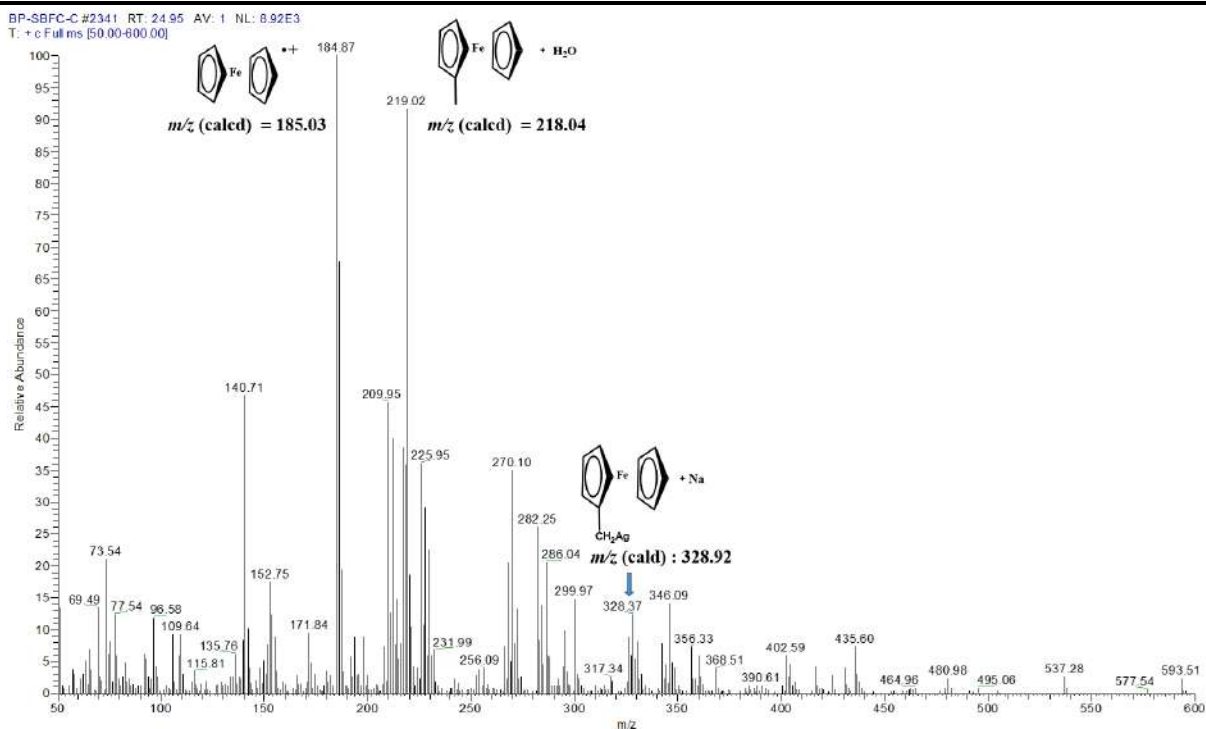


Figure 3.26: Mass spectrum (GC-EIMS) of ferrocenyl derivatives detected by GC of the reaction mixture.

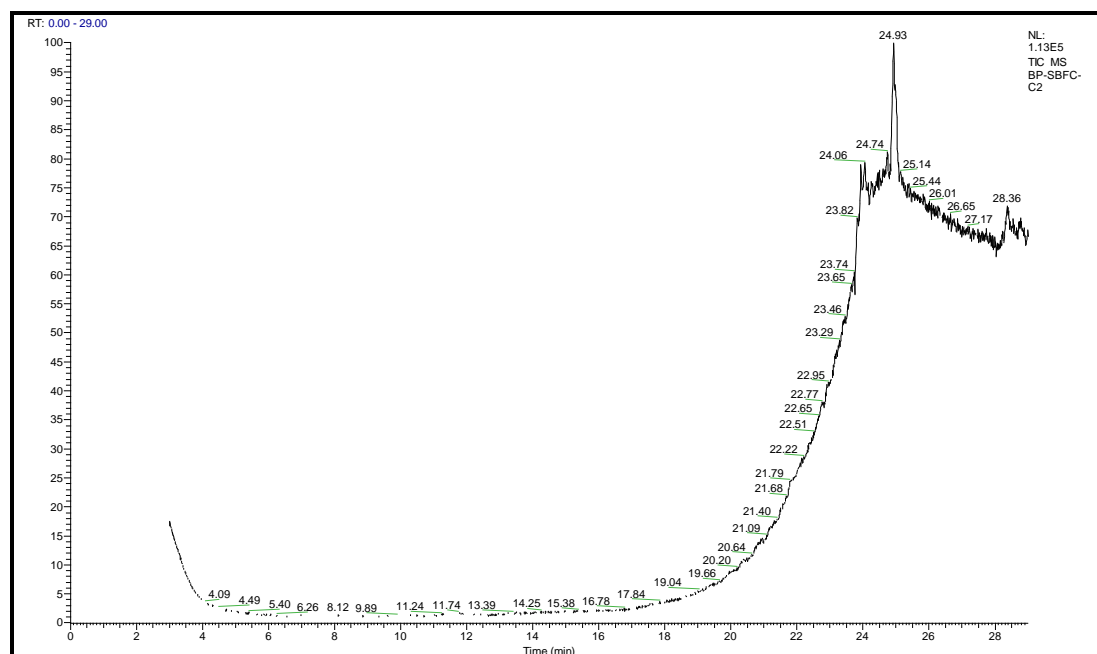


Figure 3.27: 5,15-diferrocenyl-10,20-bis(4-cyanophenyl)porphyrin, **1** was dissolved in DCM and subsequently silver acetate was added followed by the addition of triethylamine. The reaction solution was stirred continuously at room temperature. Aliquots of this reaction mixture were taken after 30 minutes and were monitored by GC-EIMS analysis.

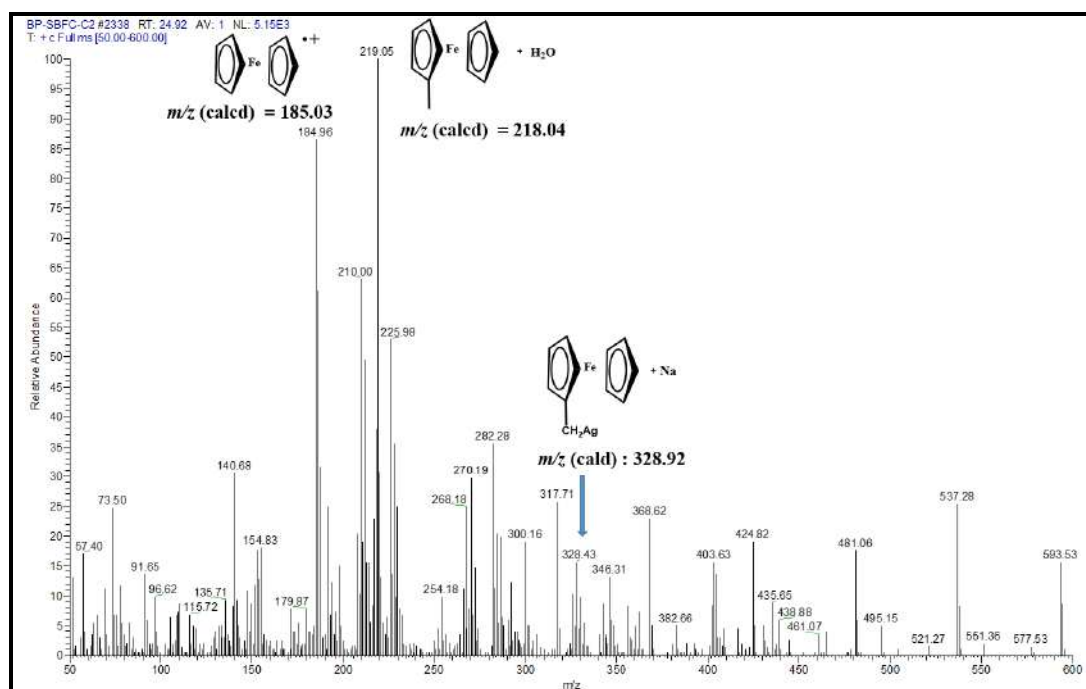


Figure 3.28: Mass spectrum (GC-EIMS) of ferrocenyl derivatives detected by GC of the reaction mixture.

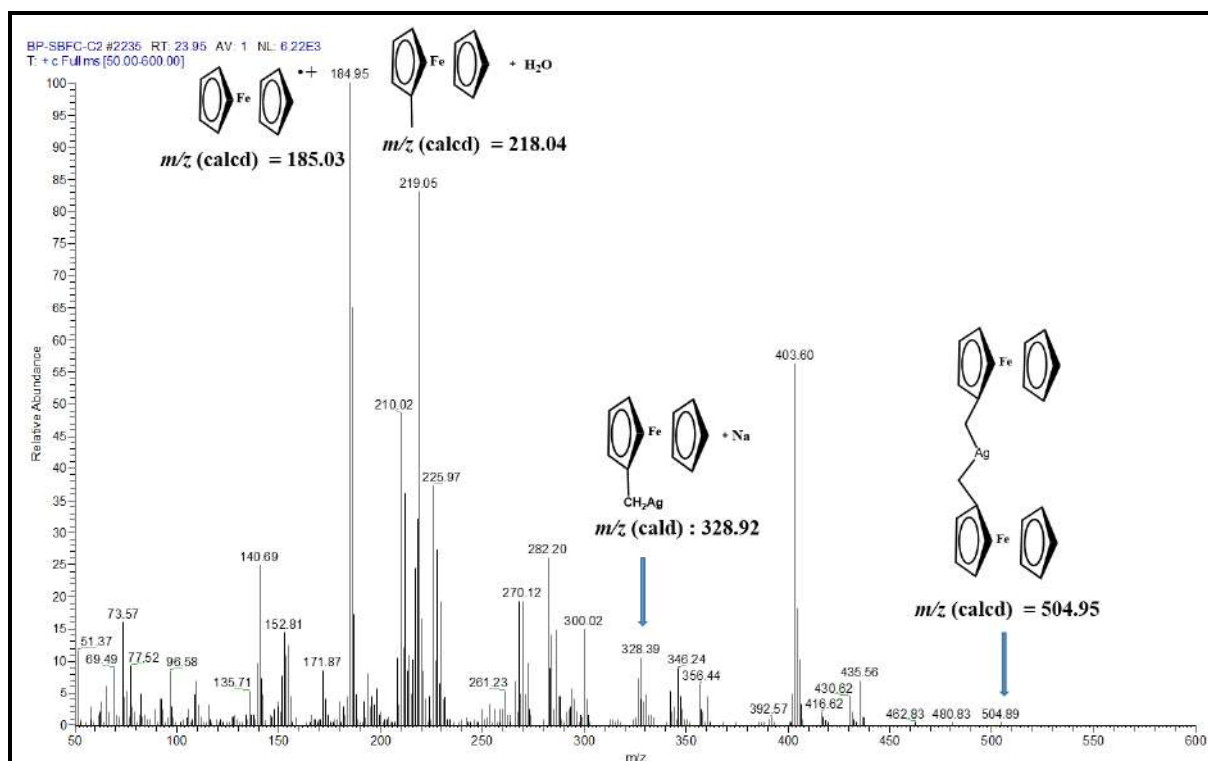
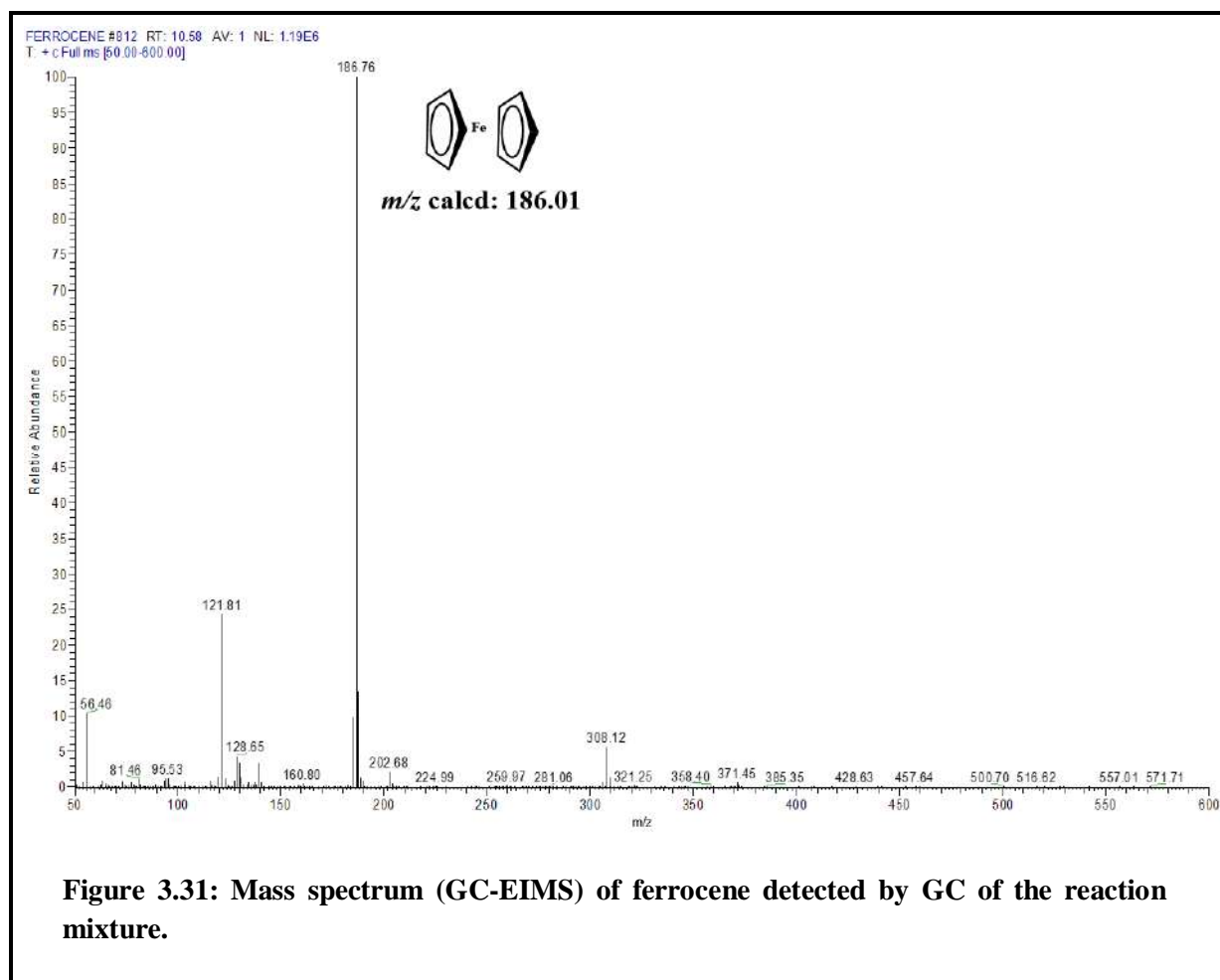
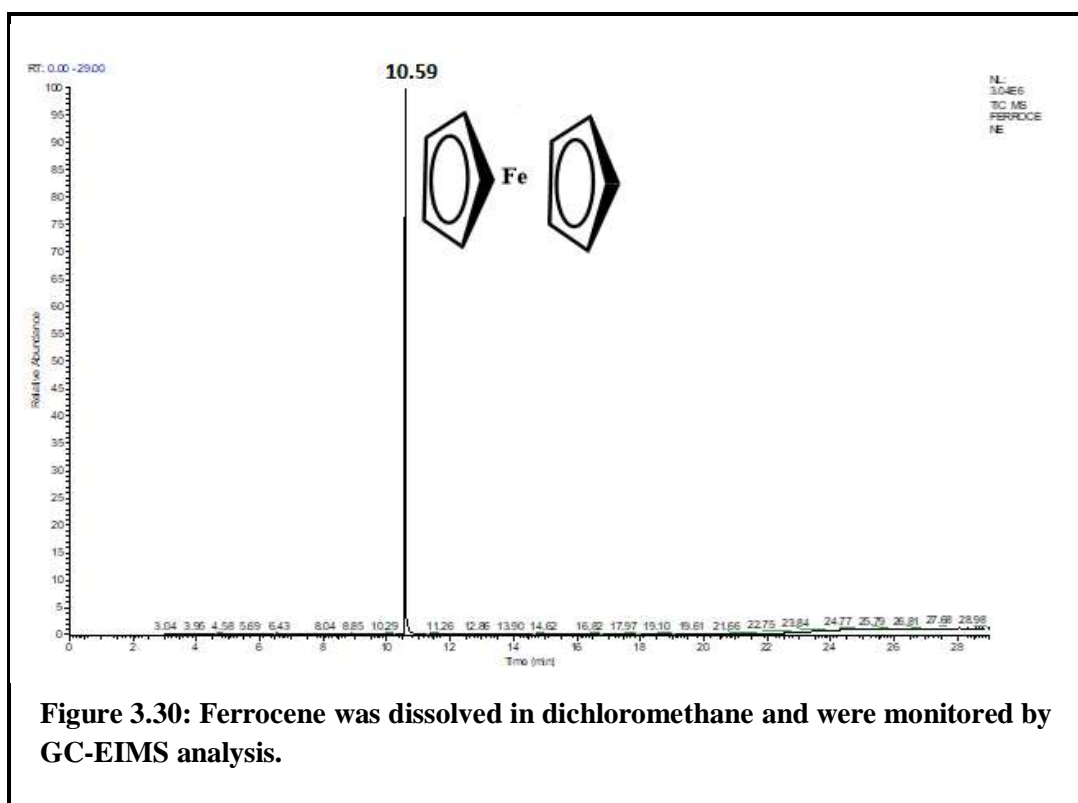
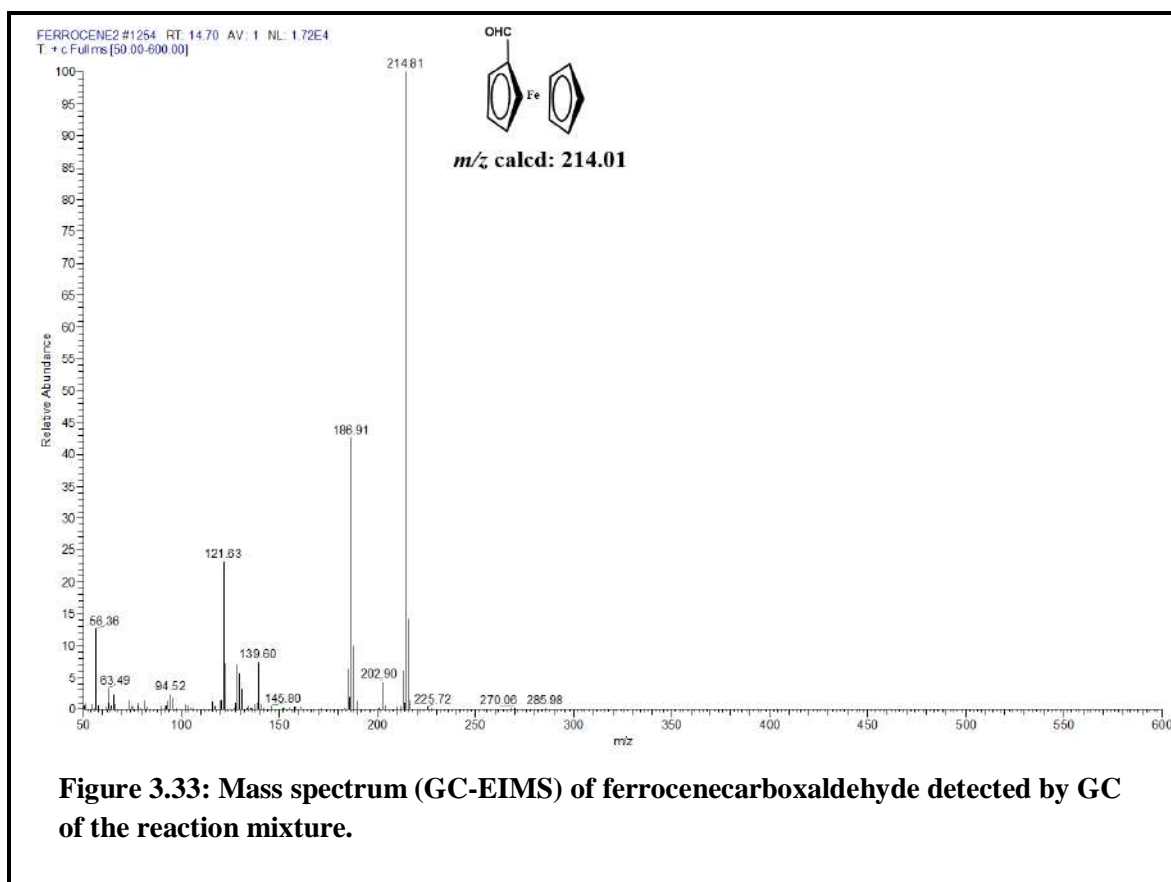
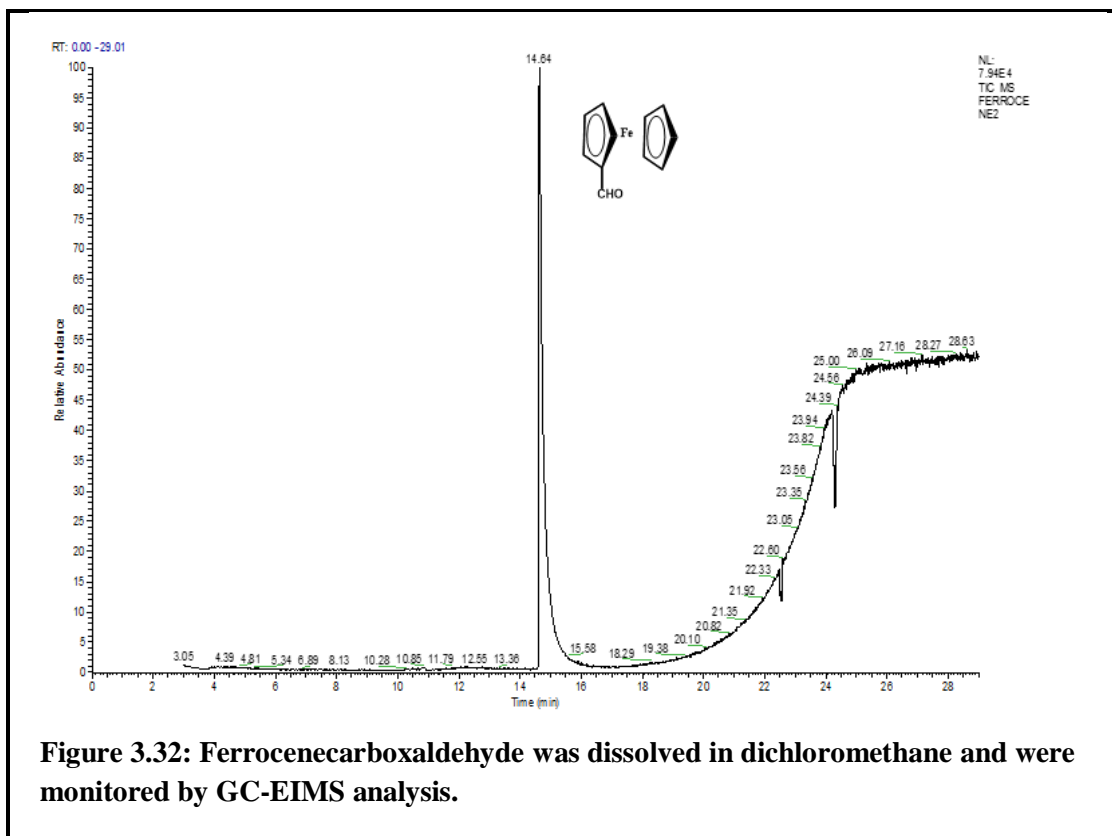
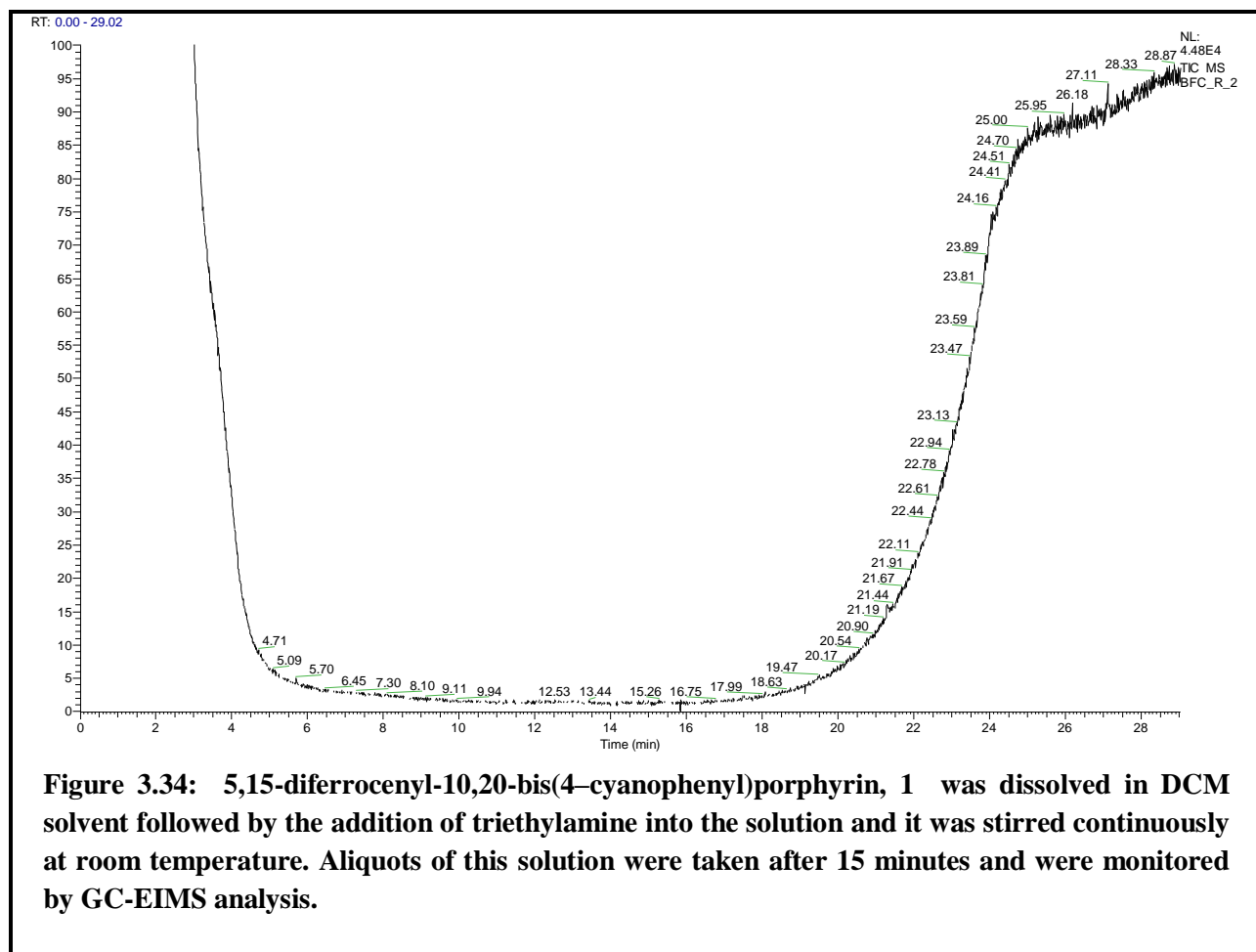


Figure 3.29: Mass spectrum (GC-EIMS) of ferrocenyl derivatives detected by GC of the reaction mixture.



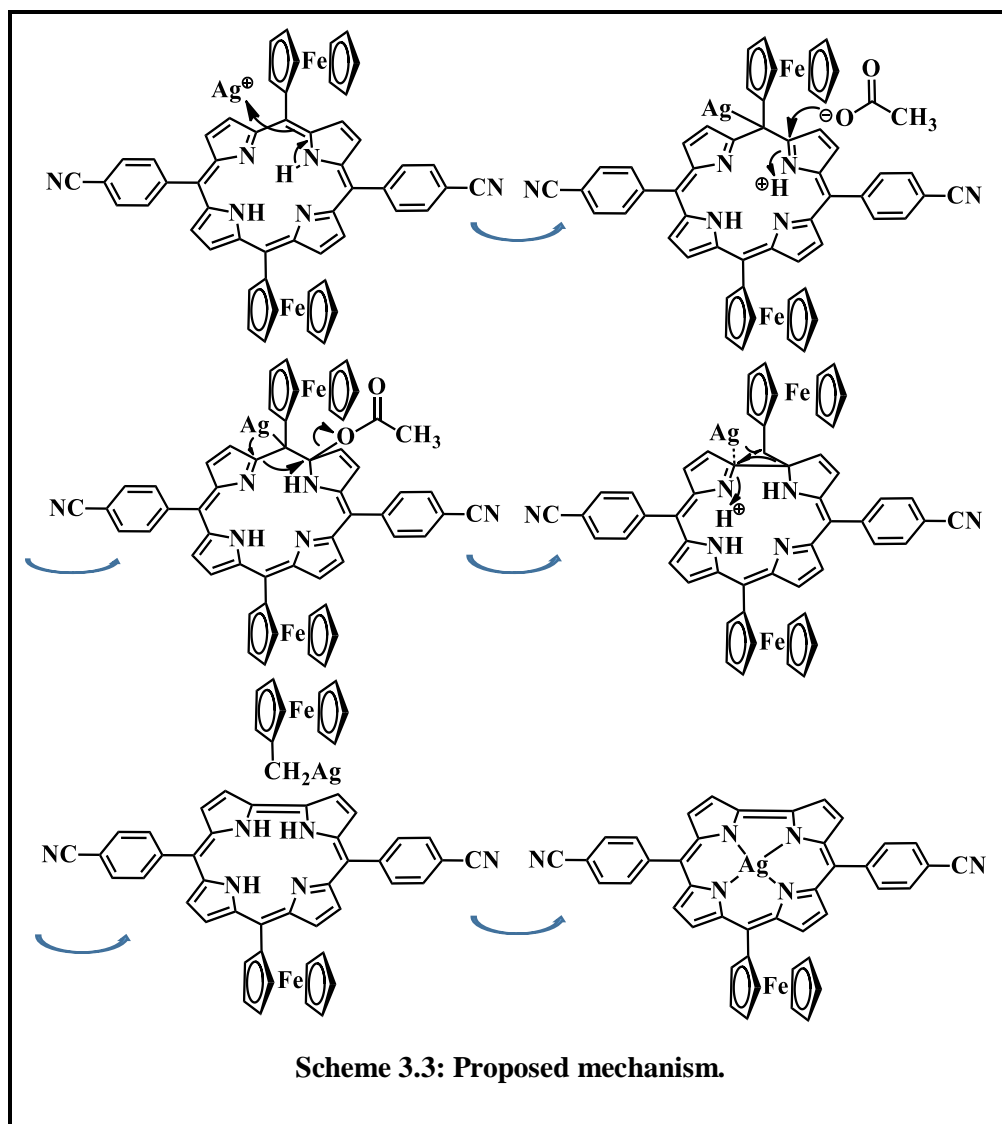


triethylamine (in the absence of silver acetate), it did not release any ferrocenyl moiety, as evident from the GC-EIMS analysis (Figure 3.34). In another control experiment, Ag-corrole was dissolved in DCM and was stirred with triethylamine and it also did not release any ferrocenyl moiety. These observations suggest the involvement of the silver acetate in the ring contraction step. This also indicates that the ring contraction occurs first followed by Ag-chelation.



If this occurs in the other way, then we would have detected the formation of silver porphyrin in significant concentration while performing the periodic control of the reaction mixture via TLC. The insertion of an Ag^+ ion at the meso-position and the concomitant insertion of the CH_3COO^- group at the neighboring α -position are pivotal and lead to the formation of a C–C bond (Scheme 3.3). Ag-salt catalyzed C–C bond formation is well documented in the literature.¹⁷⁹ Finally, an organometallic methylferrocenium species comes out from the reaction mixture (Scheme 3.3). GC EIMS strongly supports the formation of the methylferrocenium species (Figure 3.25). This methylferrocenium

species finally leads to the formation of several coupled ferrocenyl derivatives whose identities were established via GC-EIMS techniques (Figure 3.27-3.29). Thus, we can conclude that the ring contraction is purely metal assisted, and the silver is an ideal choice for the same and it is not feasible in the case of copper.



3.4 Conclusion:

In conclusion, we have synthesized two *trans*-A₂B₂-type ferrocenyl-porphyrin ligands (**1** and **2**) via a modified synthetic route. A combined synthetic, electrochemical, and crystallographic approach has been adopted to establish the reactivity pattern of Cu and Ag based metal precursors with these FB ligands. The paramagnetic nature of the compounds **3** and **4** is evident from the appearance of typical

Cu(II)-type EPR spectra for both compounds **3** and **4**. The ^1H NMR spectra of the complexes **5** and **6** exhibited sharp lines with ‘normal’ chemical shifts and thus indicate the presence of diamagnetic corrolato- Ag^{III} complexes. The single crystal X-ray structural analysis further supports the presence of a copper ion in **3** having a perfect square-planar geometry. Similarly, X-ray structural analysis reveals the presence of a silver ion in **5** having a corrolato anion in its coordination sphere. In situ NMR experiments clearly demonstrate the ring contraction and silver chelation. GC-EIMS experiments suggest the course of the reaction through identification of a key ferrocenyl moiety from the starting FB porphyrin ligand.

3.5 Experimental part:

3.5.1 All Materials details:

All the reagents like 4-CN benzaldehyde, *p*-chloranil, pyrrole, 4-Nitro benzaldehyde, Ferrocenecarboxaldehyde and Tetrabutyl Ammonium Perchlorate (TBAP) were ordered through SigmaAldrich, USA. Other reagents like Copper acetate and Silver acetate were ordered through Merck, India. Rest of the other reagents were from reagent grade quality. Solvents like hexane and DCM were purified with potassium hydroxide and Calcium hydride respectively. HPLC standard solvents were utilized for all the spectroscopic and electrochemical related studies.

3.5.2 Physical Studies:

Perkin–Elmer LAMBDA-750 spectrophotometer was used for all the Ultraviolet–Visible spectral studies. For the elemental analyses, Perkin-Elmer 240C elemental analyser were used. Nuclear Magnetic Resonance spectra of all the complexes have been measured by using Bruker Avance 400 NMR spectrometer using TMS (Tetramethylsilane) as the internal standard. For all the Electrospray Ionisation Mass Spectrometry data, the Bruker Micro TOF-QII mass spectrometer has been used. Gas Chromatography-Electron Impact Mass spectra were measured using the Thermo Scientific ITQ 900 spectrometer. Electrochemical studies were measured using the CH Instruments model CHI1120A electrochemical system. As the working electrode, the glassy carbon has been used and as the counter electrode and reference electrode, the platinum wire and a saturated calomel electrode (SCE) has been

utilized within the electrochemical cell. TBAP (Tetrabutyl ammonium perchlorate) has been utilized as supporting electrolyte (0.1M) with a 10^{-3} M conc. of the overall solution with respect to the complex. E_{298}^0 is called the half wave potential which can be determined using $0.5(E_{pc} + E_{pa})$, and the E_{pc} and E_{pa} stand for the cathodic and anodic peak positions, respectively. All the electrochemical experiments were carried out using 100 mV s^{-1} scan rate. All the X-band EPR spectra were performed using the Bruker EMX System and all the EPR simulations were performed through the Simfonia program.

3.5.3 Determination of the Crystal Structure:

Crystals of both the complexes **3** and **5** were obtained through the slow diffusion process in DCM solvent into hexane and this process was followed by the slow evaporation under atmospheric conditions. Bruker Kappa APEX II CCD and Rigaku Oxford diffractometer have been used for recording the crystal data for complex **3** and **5** respectively at room temperature. All the crystallographic parameters were arranged within the Table 3 and have been optimized for absorption effects and Lorentz polarization effect. In order to solve and refine both the crystals, the SHELXTL¹³⁷⁻¹⁴⁴ program package has been utilized. During the refinement process, all the Hydrogen atoms has been attached through riding model. Hydrogen atoms of the water molecules were included without fixing. Spots for all the disordered solvent molecules has been eliminated through the SQUEEZE command in PLATON.¹⁴⁵⁻¹⁴⁸ CCDC number 1842435-1842436 accommodate all the X-Ray crystal data for complexes **3** and **5**. www.ccdc.cam.ac.uk/data_request/cif can be used to access the crystal data without any charge.

3.5.4 Syntheses:

3.5.4.1 Synthesis of 5,15-diferrocenyl-10,20-bis(4-cyanophenyl)porphyrin, **1**:

The *trans*-ferrocenyl-porphyrins (**1–2**) were synthesized by following the slight modification of a general synthetic protocol developed earlier by Gryko *et al.* for the synthesis of F B corrole derivatives.^{94,95,149-166} Hence, only one representative case is discussed below. 5-(4-Cyanophenyl)dipyrromethane (247 mg, 1 mmol) and ferrocene carboxaldehyde (107mg, 0.5mmole)

were dissolved in 1:1 MeOH/H₂O (100 mL) mixture. The reaction was kept for stirring for 1 h in presence of dil. HCl and then was extracted with CHCl₃. The organic layer was washed twice with H₂O, dried by anhydrous Na₂SO₄, filtered, and diluted to 250 mL with CHCl₃. Then *p*-chloranil (360 mg, 1.5 mmol) was added, and the mixture was stirred for 10 min. The solvent was removed by rotary evaporation and the yellowish green colored crude product was purified by column chromatography through silica gel (100–200 mesh) with 65% CH₂Cl₂ and 35% hexane as eluent.

3.5.4.2 For 5,15-diferrocenyl-10,20-bis(4-cyanophenyl)porphyrin, **1**:

Yield: 8% (0.035 g). Anal. Calcd (found) for C₅₄H₃₆Fe₂N₆ (**1**): C, 73.65 (73.78); H, 4.12 (4.22); N, 9.54 (9.46). λ_{\max} / nm (ϵ /M⁻¹cm⁻¹) in dichloromethane: 427 (195000), 593 (15000), 690 (16000). (Figure 3.1, Table 3.1). Proton NMR (400 MHz, CHCl₃-*d*): δ 9.87 (d, *J* = 4.8 Hz, 4H, β -pyrrole), 8.55 (d, *J* = 4.9 Hz, 4H, β -pyrrole), 8.30 (d, *J* = 8.1 Hz, 4H, aryl-H), 8.07 (d, *J* = 8.2 Hz, 4H, aryl-H), 5.50 (t, *J* = 1.9 Hz, 4H, Fc-H), 4.85 (t, *J* = 1.8 Hz, 4H, Fc-H), 4.13 (s, 10H, Fc-H), -1.67 (s, 2H, Por-NH) (Figure 3.8). ¹³C NMR (101 MHz, CDCl₃): δ 147.49, 138.39, 137.86, 135.04, 132.00, 131.58, 131.50, 130.65, 130.10, 128.62, 126.85, 126.07, 119.21, 117.62, 112.02, 71.62, 70.81, 69.65, 69.21, 68.50 (Figure 3.9). The ESI-MS spectrum of this porphyrin ligand in CH₃CN showed peaks centred at *m/z* = 880.17 correspond to [**1**]⁺ (880.17 calcd for C₅₄H₃₆Fe₂N₆) {Figure 3.14}.

3.5.4.3 For 5,15-diferrocenyl-10,20-bis(4-nitrophenyl)porphyrin, ¹⁶⁶ **2**:

All the analytical data are consistent with literature values. ¹⁶⁶ Yield: 8% (0.036 g). Anal. Calcd (found) for C₅₂H₃₆Fe₂N₆O₄ (**2**): C, 67.84 (67.75); H, 3.94 (3.86); N, 9.13 (9.03). λ_{\max} /nm (ϵ /M⁻¹cm⁻¹) in dichloromethane: 428 (93000), 606 (18500), 695 (19000). {Table 3.1}. Proton NMR (700 MHz, CHCl₃-*d*): δ 9.88 (s, 4H, β -pyrrole), 8.65 (d, *J* = 7.8 Hz, 4H, aryl-H), 8.57 (d, *J* = 4.6 Hz, 4H, β -pyrrole), 8.36 (d, *J* = 7.8 Hz, 4H, aryl-H), 5.50 (s, 4H, Fc-H), 4.86 (s, 4H, Fc-H), 4.13 (s, 10H, Fc-H), -1.64 (s, 2H, Por-NH). The ESI-MS spectrum in CH₃CN displayed peaks centred at *m/z* = 921.15 correspond to [**2**+H]⁺ (920.15 calcd for C₅₂H₃₆Fe₂N₆O₄).

3.5.4.4 Synthesis of 5,15-diferrocenyl-10,20-bis(4-cyanophenyl)porphyrinato-Cu(II), 3:

0.050 g of 5,15-diferrocenyl-10,20-bis(4-cyanophenyl)porphyrin, **1** (0.056 mmol) was dissolved in 10 mL of dichloromethane and subsequently 0.046 g of copper acetate hydrate (0.24 mmol) was added to it. Then triethylamine (34 mL) was added to the reaction mixture and it was stirred for 1 hour at room temperature during which the colour changed from yellowish green to dark brown. The solvent was then removed by rotary evaporation and the brown crude product was purified by column chromatography through silica gel (100-200 mesh) column with 55% CH₂Cl₂ and 45% hexane as eluent. Subsequent recrystallization (CH₂Cl₂/hexane) gave the pure crystalline **3**.

3.5.4.5 For 5,15-diferrocenyl-10,20-bis(4-cyanophenyl)porphyrinato-Cu(II), 3:

Yield: 80% (0.043 g). Anal. Calcd (found) for C₅₄H₃₄CuFe₂N₆ (**3**): C, 68.84 (68.95); H, 3.64 (3.51); N, 8.92 (8.99). $\lambda_{\text{max}}/\text{nm}$ ($\epsilon/\text{M}^{-1}\text{cm}^{-1}$) in dichloromethane: 423 (115000), 642 (7500) {Figure 3.2, Table 3.1}. The ESI-MS spectrum in CH₃CN solvent showed peaks centred at $m/z = 941.06$ correspond to [**3**]⁺ (941.08 calcd for C₅₄H₃₄CuFe₂N₆) {Figure 3.15}.

3.5.4.6 For 5,15-diferrocenyl-10,20-bis(4-nitrophenyl)porphyrinato-Cu(II), 4:

Yield: 79% (0.042g). Anal. Calcd (found) for C₅₂H₃₄CuFe₂N₆O₄ (**4**): C, 63.59 (63.71); H, 3.49 (3.60); N, 8.56 (8.44). $\lambda_{\text{max}}/\text{nm}$ ($\epsilon/\text{M}^{-1}\text{cm}^{-1}$) in dichloromethane: 423 (108000), 653 (13000) {Figure 3.3, Table 3.1}. The ESI-MS spectrum of complex **4** in CH₃CN displayed peaks centred at $m/z = 981.07$ correspond to [**4**]⁺ (981.06 calcd for C₅₂H₃₄CuFe₂N₆O₄) {Figure 3.16}.

3.5.4.7 Synthesis of 10-ferrocenyl-5,15-bis(4-cyanophenyl)corrolato-Ag(III), 5:

0.050 g of 5,15-diferrocenyl-10,20-bis(4-cyanophenyl)porphyrin, **1** (0.057 mmol) was dissolved in 10 ml of DCM solvent and subsequently 0.096 g of silver acetate (0.57 mmol) was added to it. Then triethylamine (34 mL) was added to the reaction mixture and it was stirred for 30 minutes at room temperature during which the colour changed from yellowish green to deep green. The solvent was then removed by rotary evaporation and the deep green crude product was purified by column chromatography immediately through alumina oxide active neutral column with 50% CH₂Cl₂ and 50% hexane as eluent. Subsequent recrystallization (CH₂Cl₂/hexane) gave the pure crystalline **5**.

3.5.4.8 For 10-ferrocenyl-5,15-bis(4-cyanophenyl)corrolato-Ag(III), 5:

Yield: 85% (0.038 g). Anal. Calcd (found) for $C_{43}H_{25}AgFeN_6$ (**5**): C, 65.42 (65.33); H, 3.19 (3.34); N, 10.65 (10.51). λ_{\max}/nm ($\epsilon/M^{-1}cm^{-1}$) in dichloromethane: 431 (98000), 541 (11000), 571 (11000), 612 (16000) {Figure 3.4, Table 3.1}. Proton NMR (400 MHz, $CHCl_3-d$): δ 9.87 (s, 2H, β -pyrrole), 9.07 (d, $J = 4.2$ Hz, 2H, β -pyrrole), 8.82 (d, $J = 4.5$ Hz, 2H, β -pyrrole), 8.55 (d, $J = 4.0$ Hz, 2H, β -pyrrole), 8.38 (d, $J = 7.8$ Hz, 4H, aryl-H), 8.13 (d, $J = 7.7$ Hz, 4H, aryl-H), 5.59 (s, 2H, Fc-H), 4.88 (s, 2H, Fc-H), 4.30 (s, 5H, Fc-H) {Figure 3.10}. ^{13}C NMR (101 MHz, $CDCl_3$): δ 145.30, 138.82, 136.19, 135.25, 133.97, 131.64, 130.41, 127.76, 127.63, 119.60, 119.33, 119.00, 116.57, 111.66, 75.83, 71.63, 70.68, 69.13 {Figure 3.11}. The ESI-MS spectrum in CH_3CN solvent showed peaks centred at $m/z = 788.04$ correspond to $[5]^+$ (788.05 calcd for $C_{43}H_{25}AgFeN_6$) {Figure 3.17}.

3.5.4.9 For 10-ferrocenyl-5,15-bis(4-nitrophenyl)corrolato-Ag(III), 6 :

Yield: 84% (0.038 g). Anal. Calcd (found) for $C_{41}H_{25}AgFeN_6O_4$ (**6**): C, 59.37 (59.26); H, 3.04 (3.15); N, 10.13 (10.01). λ_{\max}/nm ($\epsilon/M^{-1}cm^{-1}$) in dichloromethane: 434 (65000), 542 (9200), 577 (8800), 624 (12700) {Figure 3.5, Table 3.1}. Proton NMR (700 MHz, $CHCl_3-d$): δ 9.89 (s, 2H, β -pyrrole), 9.11 (s, 2H, β -pyrrole), 8.85 (d, $J = 4.4$ Hz, 2H, β -pyrrole), 8.70 (d, $J = 7.8$ Hz, 4H, aryl-H), 8.59 (d, $J = 4.0$ Hz, 2H, β -pyrrole), 8.45 (d, $J = 7.9$ Hz, 4H, aryl-H), 5.62 (s, 2H, Fc-H), 4.90 (s, 2H, Fc-H), 4.31 (s, 5H, Fc-H) {Figure 3.12}. ^{13}C NMR (101 MHz, $CHCl_3-d$): δ 147.59, 147.23, 138.75, 136.22, 135.34, 133.90, 130.33, 127.73, 123.06, 119.68, 119.15, 116.10, 114.20, 114.10, 75.89, 71.90, 70.76, 69.24 {Figure 3.13}. The ESI-MS spectrum in CH_3CN solvent showed peaks centred at $m/z = 828.03$ correspond to $[6]^+$ (828.03 calcd for $C_{41}H_{25}AgFeN_6O_4$) {Figure 3.18}.



Chapter Four

*Ruthenium-Ruthenium Bonded [Bis{corrolato-ruthenium(III)}]ⁿ (*n* = 0, +1, -1) Complexes: Model Compounds for the Photosynthetic Special Pair*

4.1 Introduction

4.2 Synthetic Discussion

4.3 Spectroscopic Characterization

4.3.1 ESI-Mass Spectra

4.3.2 Nuclear Magnetic Resonance spectra

4.3.3 Crystal structure

4.3.4 Electrochemistry

4.3.5 EPR spectroelectrochemistry and Spin density calculations

4.3.6 Ultraviolet-Visible/NIR spectroelectrochemistry and TD-DFT calculations

4.4 Conclusions

4.5 Experimental Part

4.5.1 Materials

4.5.2 Detailed discussion of all the physical studies

4.5.3 Crystal structure determination

4.5.4 Synthesis and characterization:

4.5.4.1 Synthesis of bis(5,10,15-tris(4-cyanophenyl)corrolato-ruthenium(III)) (1)

4.5.4.2 Synthesis of bis(10-(2,4,5-trimethoxyphenyl)-5,15-bis(4-cyanophenyl) corrolato-ruthenium(III)) (2)

4.5.4.3 Synthesis of bis(10-(4,7-dimethoxynaphthalen-1-yl)-5,15-bis(4-cyanophenyl)corrolato-ruthenium(III)) (3)

4.6 TD-DFT Calculations

4.7 Details for the calculation of redox potentials

4.1 Introduction:

Porphyrinoids are the most prominent ligands used in metal-complex-mediated organic transformations.¹⁸⁰⁻¹⁸⁶ The most common example is cytochrome P450 with iron porphyrin as its cofactor. In many cases, the use of other ligands is not feasible, and porphyrinoids remain as the only viable choice.¹⁸⁰⁻¹⁸⁶ In this context, ruthenium porphyrin complexes are extensively used in a variety of organic transformations, including cyclopropanation,^{187,188} C-H insertion,¹⁸⁹⁻¹⁹¹ cycloaddition,¹⁹² and carbenoid transformation reactions.^{187,191} Metalloporphyrin dimers with multiple metal-metal bonds have attracted significant interest in recent years.¹⁹³⁻¹⁹⁷ The native state electronic structures of these dimers may be qualitatively described by a model proposed by Cotton et al.^{198,199} It was indeed observed that the bond order of the metal-metal bond in these metalloporphyrin dimers is solely dependent on the number of valence d electrons on each metal center.^{198,199} However, systematic tuning of the metal-metal bond order of these metalloporphyrin/corrole dimers still remains a challenging task. One simple way of changing the bond order of the metalloporphyrin dimers is selective oxidation and reduction of the dimeric species. Among the various metalloporphyrin-based dimers, ruthenium (II) porphyrin dimers are of particular interest. $[(\text{Ru}(\text{octaethylporphyrin}))_2]$ was the first such structurally characterized homodimer of ruthenium.^{195,200} These homodimers of ruthenium have been found to be broadly applicable in various catalytic reactions.¹⁹⁶ Thus, study of the redox state distribution of these dimers in various oxidation states is of great importance.

Corrole,^{99,103,104,105,107,114,154,155,157,201-217} a contracted porphyrin analogue, is known to stabilize metals in higher oxidation states.^{218,219} Recently, metallocorroles have been extensively applied for various catalytic reactions. For example, iron and manganese corroles proved to be useful in hydroxylation reactions.^{104,203} Antimony corroles have been successfully used in oxidation reactions of hydrocarbons.²⁰³ Rhodium corroles have been shown to be useful in cyclopropanation reactions.²⁰³ Iron and rhodium corroles have been used in N-H and C-H insertion reactions, respectively.²⁰³ A detailed understanding of the electronic structures of metalloporphyrin/corrole dimers in various oxidation states has relevance to the photosynthetic “special pair”.^{220,221} Moreover, it should also

provide insight into the electronic conductivities in stacked π -systems and in various π -aggregates.²²² Metal-metal bonded dimeric porphyrin complexes in various accessible oxidation states have been studied by means of resonance Raman scattering (RR),¹⁹⁶ infrared absorption,¹⁹⁶ and X-ray absorption spectroscopy.¹⁹⁷ Kadish et al.²²³ have characterized the one-electron-oxidized forms of ruthenium-ruthenium-bonded dimeric corrole complexes through a combination of UV/Vis spectrophotometry and EPR spectroelectrochemistry. However, their studies were limited to rotationally disordered metal-metal bonded dimeric corrole complexes (only β -substituted). To the best of our knowledge, a combined UV/Vis/NIR/EPR spectroelectrochemical and DFT approach to probe the electronic structures of metal-metal-bonded rotationally ordered porphyrin/corrole dimers (meso-substituted) in various accessible redox states has not previously been attempted.

Herein, we present the synthesis and characterization of three new ruthenium complexes, bis(5,10,15-tris(4-cyanophenyl)corrolato-ruthenium(III)) (**1**), bis(10-(2,4,5-trimethoxyphenyl)-5,15-bis(4-cyanophenyl)corrolato-ruthenium(III)) (**2**), and bis(10-(4,7-dimethoxynaphthalen-1-yl)-5,15-bis(4-cyanophenyl)-corrolato-ruthenium(III)) (**3**), with various meso-substituted corrolato ligand functionalities (Figure 4.1). Furthermore, detailed UV/Vis/NIR/EPR spectroelectrochemical and DFT studies have been conducted to establish the electronic nature of the electro-generated species.

4.2 Synthetic Discussion:

The new bis(corrolato-ruthenium(III)) derivatives were synthesized according to a procedure reported for related dimers,²²³⁻²²⁵ with slight modifications. The respective free-base corrole and the organometallic ruthenium precursor, dichloro(1,5-cyclooctadiene)ruthenium(II) dimer, were dissolved in 2-methoxyethanol containing triethylamine, and the mixture was heated under reflux to afford the corresponding bis(corrolato-ruthenium(III)) derivatives **1**, **2**, and **3**. The purities and identities of the products were confirmed by satisfactory elemental analyses and their electrospray mass spectra.

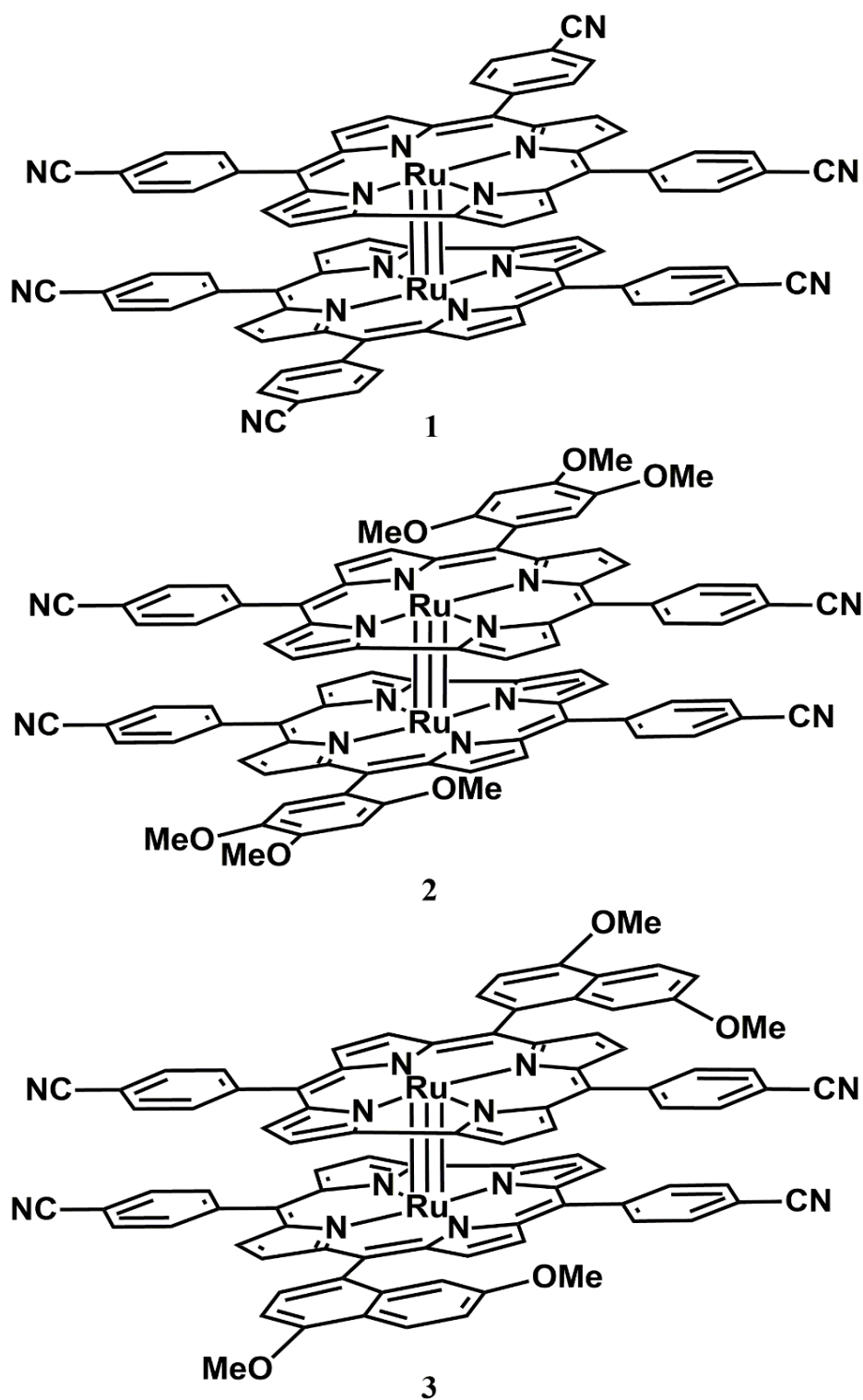
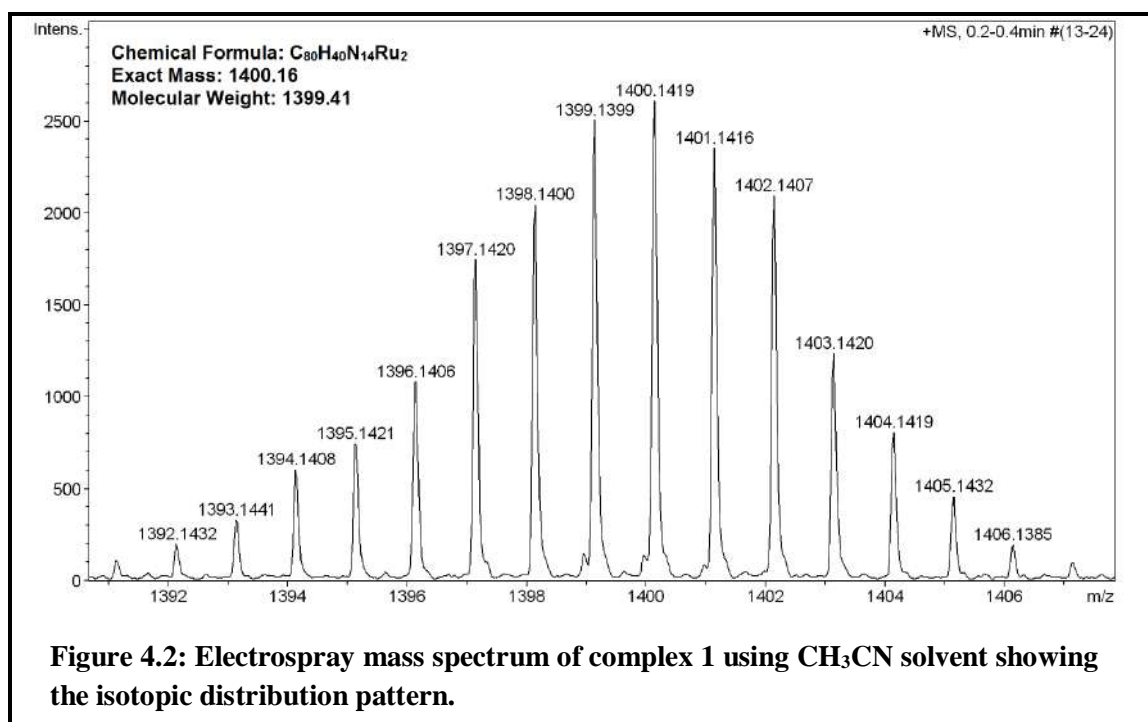


Figure 4.1: Structures of the ruthenium corrole complexes: 1) bis(5,10,15-tris(4-cyanophenyl)corolato-ruthenium(III)), 2) bis(10-(2,4,5-trimethoxyphenyl)-5,15-bis(4-cyanophenyl)corolato-ruthenium(III)), and 3) bis(10-(4,7-dimethoxynaphthalen-1-yl)-5,15-bis(4-cyanophenyl)corolato-ruthenium(III)).

4.3 Spectroscopic Characterization:

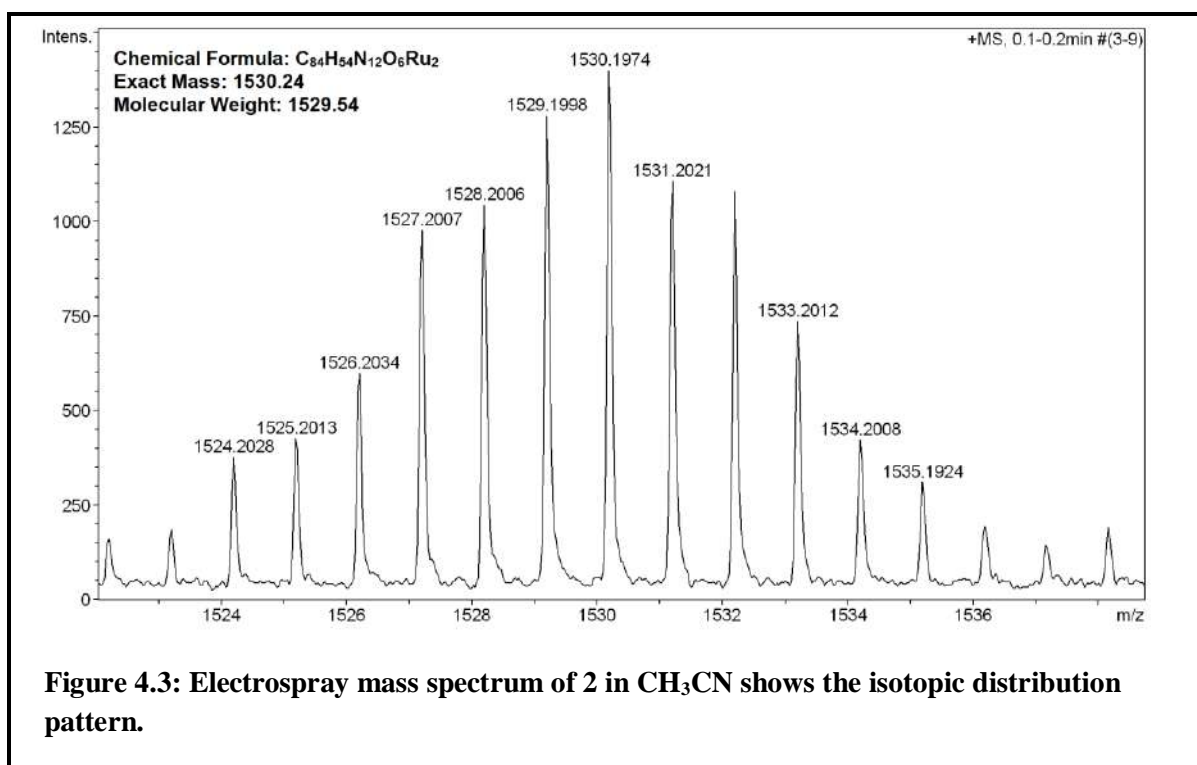
4.3.1 ESI-MS Spectra:

The ESI-MS spectrum of the complex **1** shows intense peak centred at m/z : calcd for $C_{80}H_{40}N_{14}Ru_2$: 1400.1600; found: 1400.1419 $[M]^+$; (Figure 4.2). The electrospray mass spectrum of **2** is measured in acetonitrile solvent which leads to the generation of intense peak centred at m/z : calcd for $C_{84}H_{54}N_{12}O_6Ru_2$: 1530.2400; found: 1530.1974 $[M]^+$ (Figure 4.3).

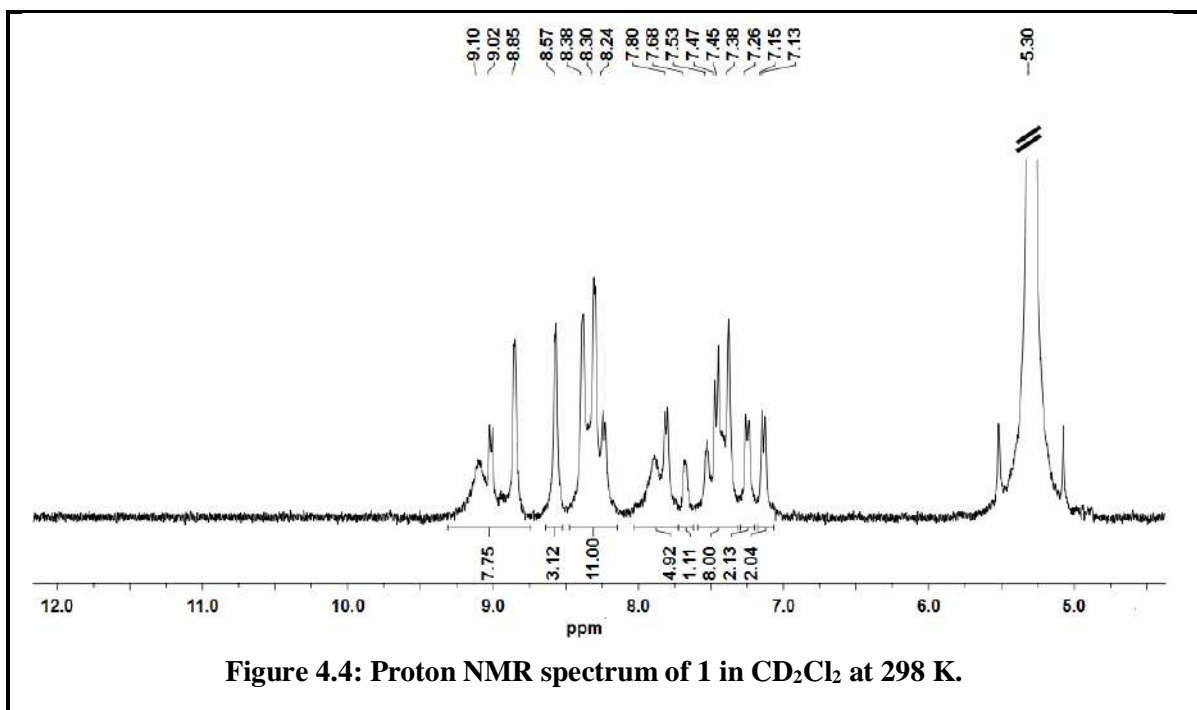


4.3.2 Nuclear Magnetic Resonance spectra:

The observed chemical shifts in the 1H NMR spectra of the ruthenium corrole complexes are in close agreement with those of other related diamagnetic corrolato-metal complexes (Figures 4.4-4.7).^{99,103,104,105,107,114,154,155,157,201-217} This is a clear indication of the diamagnetic nature of the ruthenium(III) corrole complexes.^{223,224,225} One can construct a qualitative MO diagram ($\sigma^2\pi^4\delta^2\delta^{*2}$) for bonding in the bis(corrolato-ruthenium(III)) complexes.^{224,225} This MO diagram also predicts a diamagnetic ground state. However, this is in contrast to what has been observed in known porphyrinato-ruthenium dimers.¹⁹³⁻¹⁹⁷ The proton NMR of complex **1** in CD_2Cl_2 at room temperature



features several peaks in the aromatic region, $\delta=9.31\text{--}7.14$ ppm, with a total integral corresponding to 40 protons (Figure 4.4). In order to ascertain whether any dynamic process occurs in the samples



on the NMR timescale, variable-temperature NMR measurements were performed. Due to the broadening of some of the proton resonances, both high-temperature and low-temperature

experiments were performed to obtain properly resolved spectra of complexes **2** and **3**. The best ^1H NMR spectrum for **2**, with satisfactorily resolved peaks, was obtained at 273 K (Figure 4.5 and 4.6).

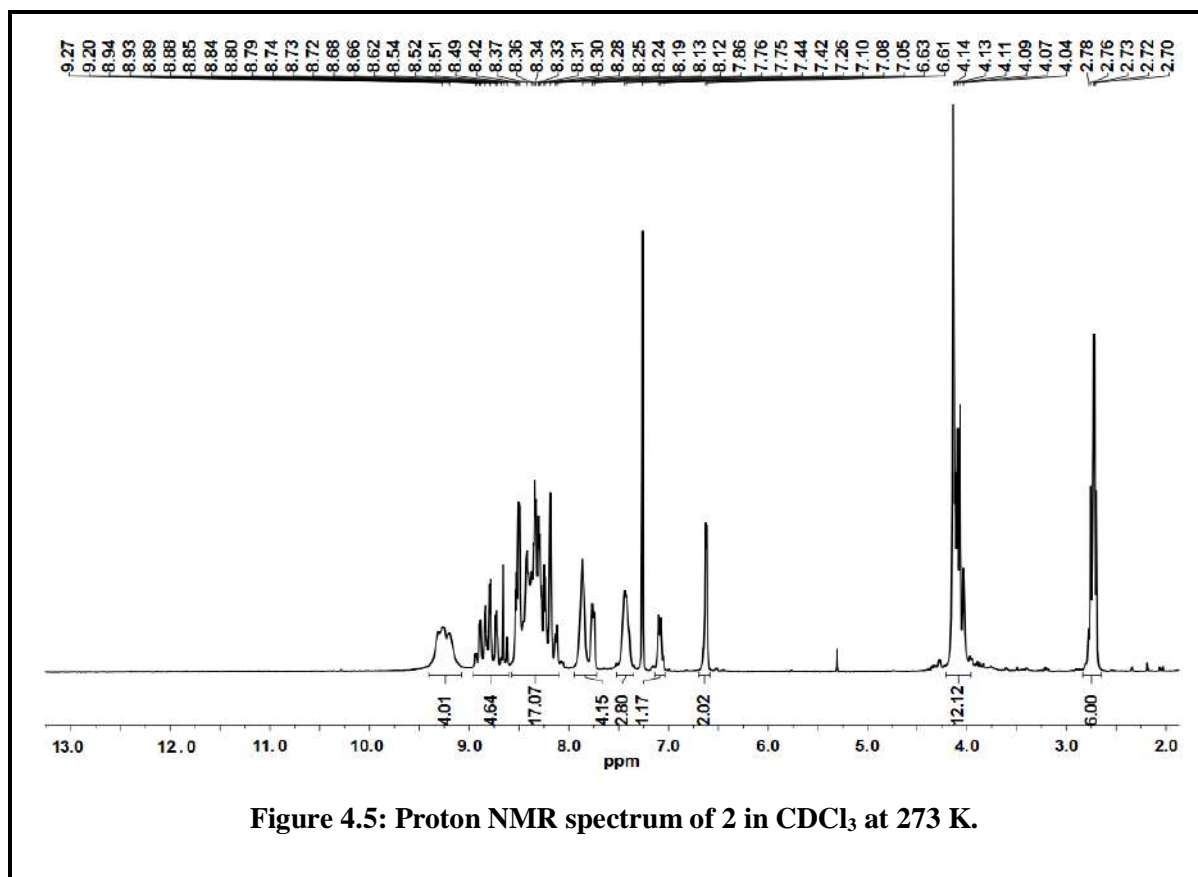


Figure 4.5: Proton NMR spectrum of 2 in CDCl_3 at 273 K.

On gradually lowering the temperature to 223 K, broadening was again observed, which can be attributed to the involvement of dynamic processes on the NMR time scale (Figure 4.6). As the temperature is progressively lowered, the signal gets broader due to the sluggishness of the dynamic process involved on the NMR time scale.²²⁵ We assume that the spectral broadening at lower temperatures is due to hindered rotation of the appended aryl substituents. The aromatic region of the ^1H NMR spectrum of **2** at 273 K features signals due to 36 protons between $\delta = 9.23$ and 6.62 ppm, with contributions from the β -pyrrolic protons as well as meso-substituted aryl groups of the two metal-metal-bonded rings (Figure 4.5). The 18 methoxy protons give rise to two separate multiplets at $\delta = 4.21$ – 3.96 ppm (12H) and 2.84 – 2.65 ppm (6H). On lowering the temperature, although signal broadening was observed, a characteristic splitting of one of the methoxy multiplets was also seen, with the development of a broad doublet at $\delta = 4.00$ ppm at 248 K (Figure 4.6)

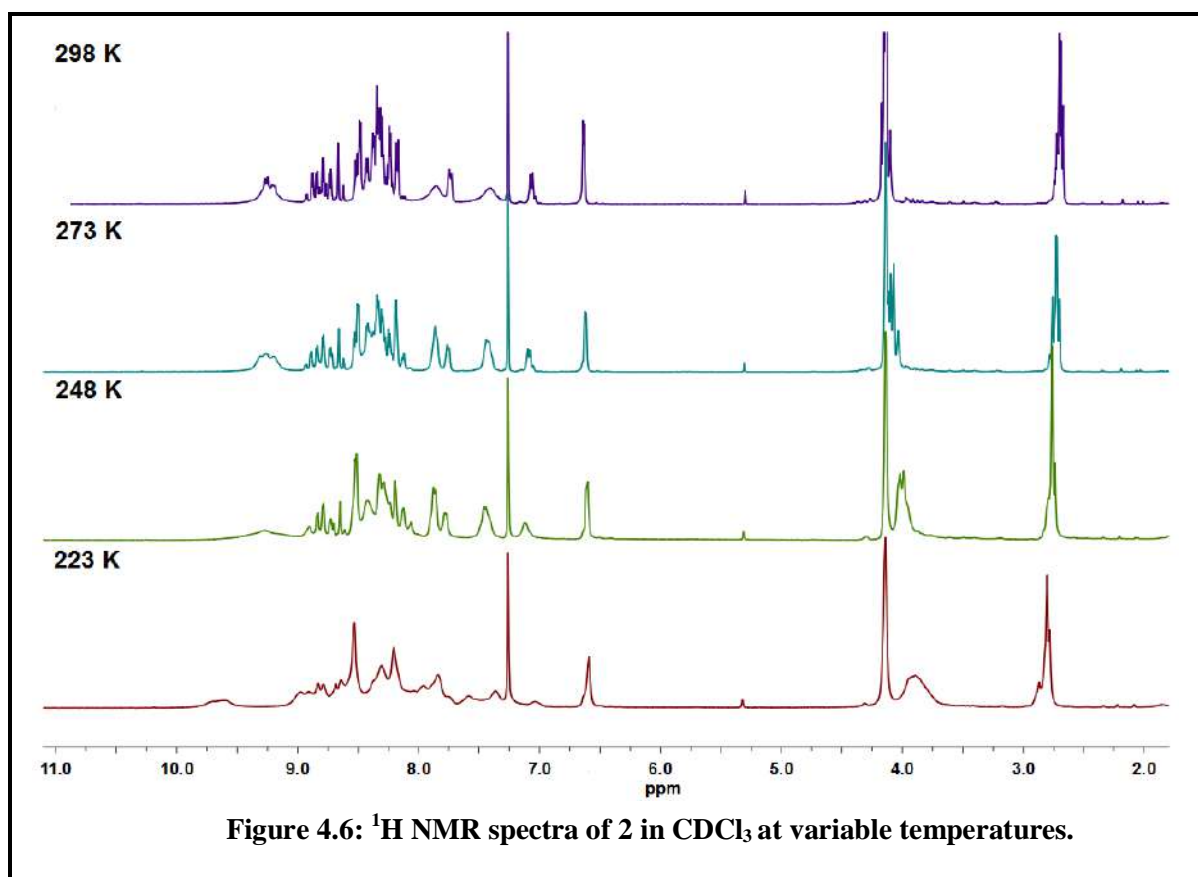


Figure 4.6: ^1H NMR spectra of **2** in CDCl_3 at variable temperatures.

Variable-temperature ^1H NMR experiments were also performed on complex **3** (Figure 4.8), and a

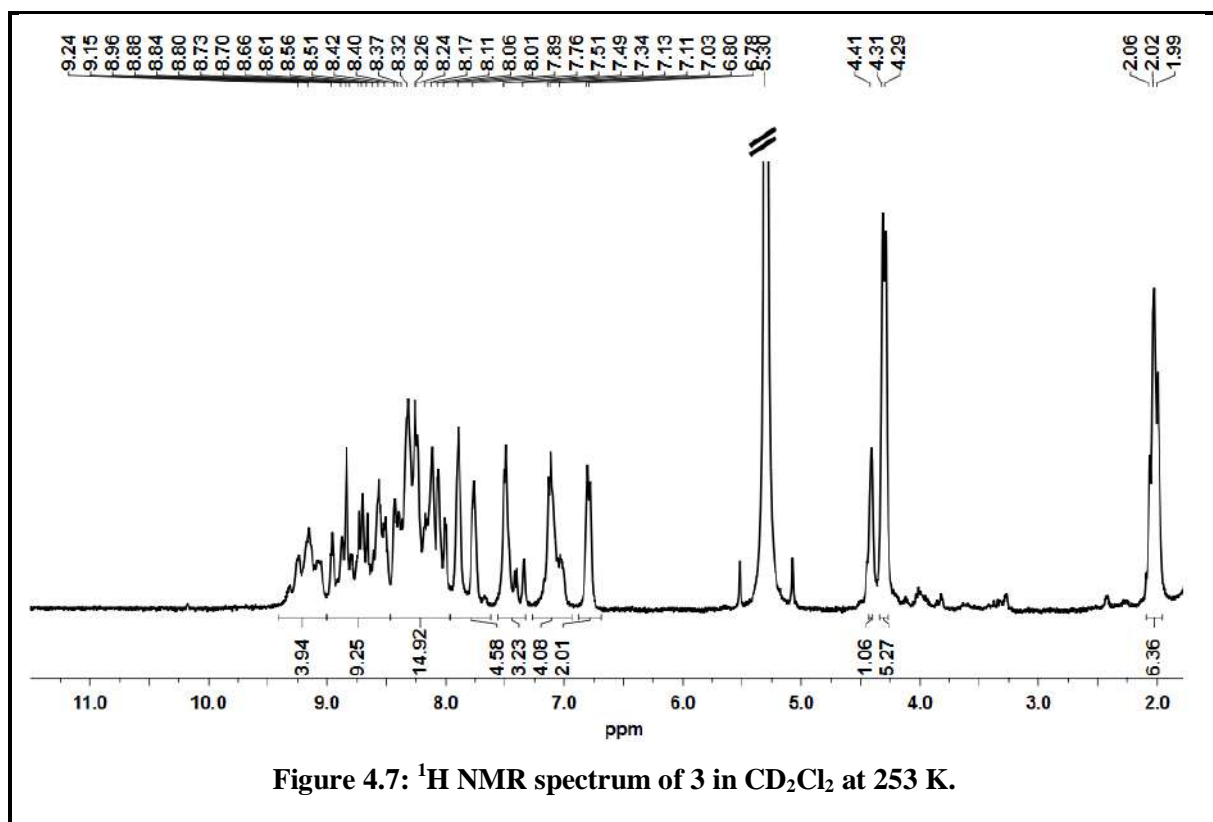
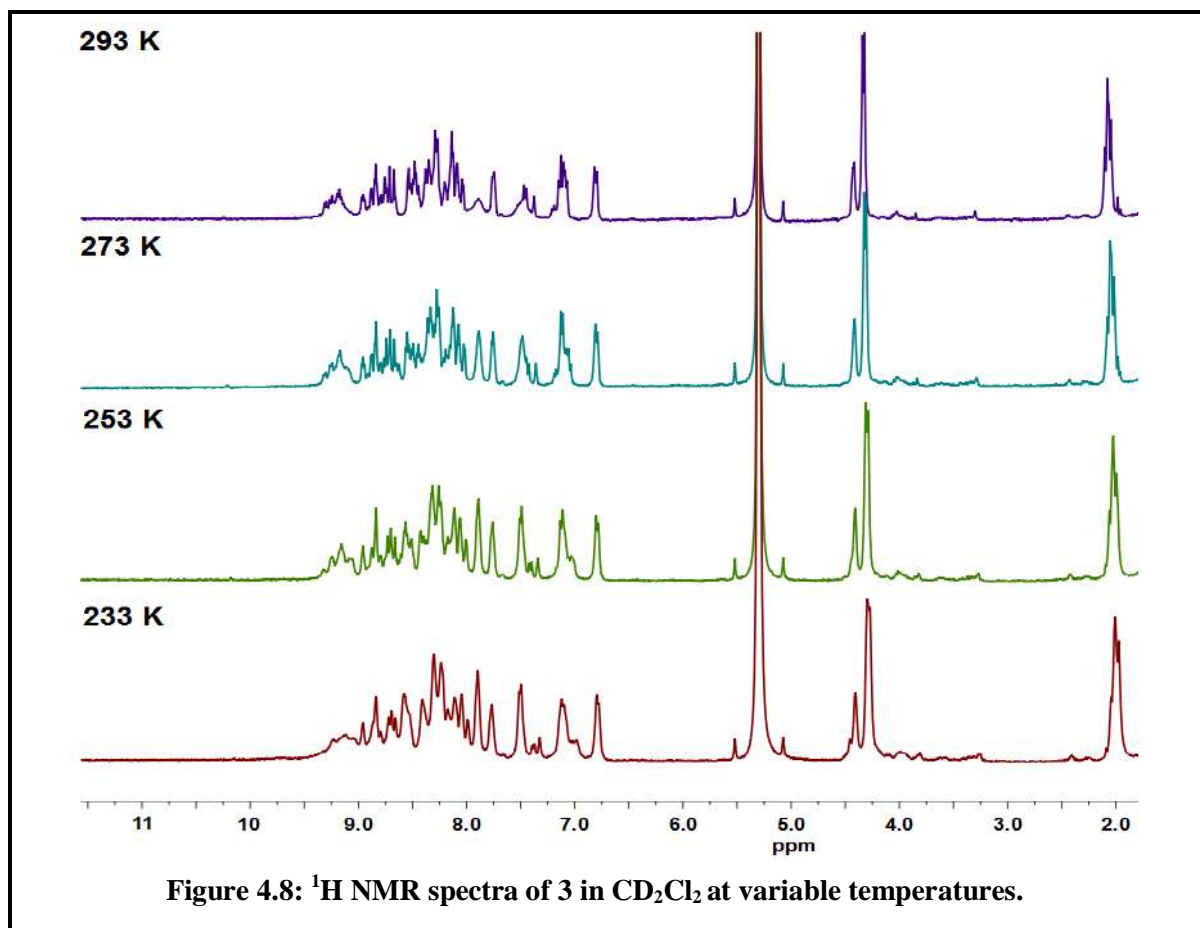


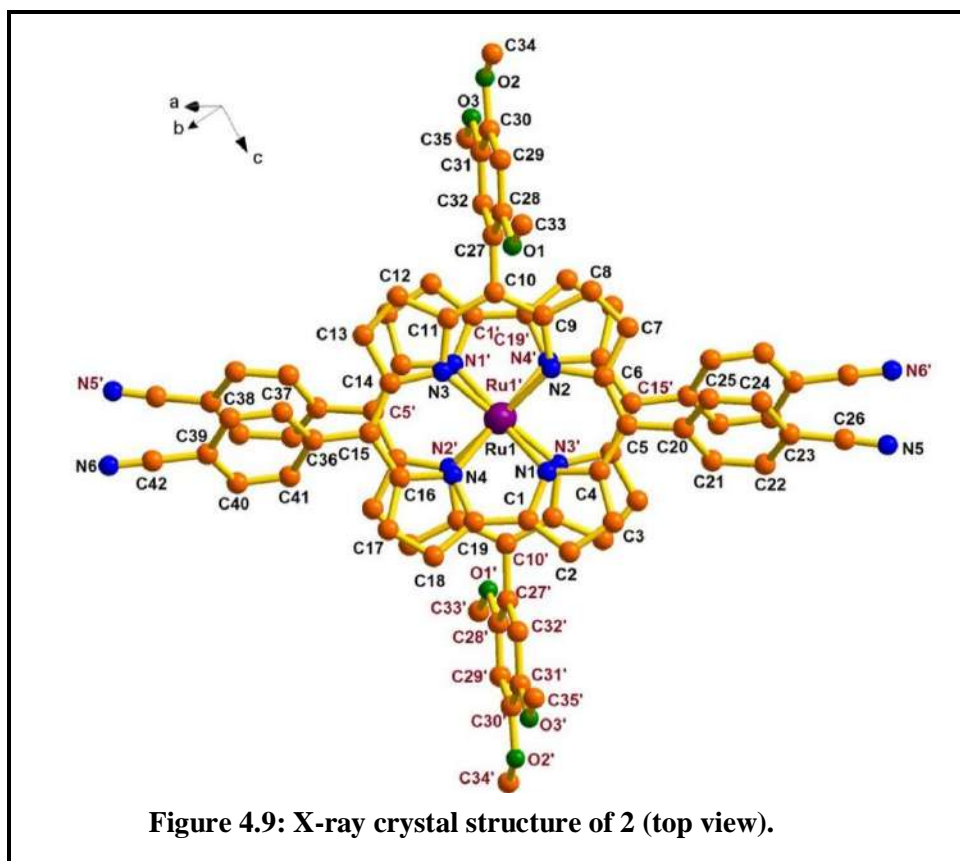
Figure 4.7: ^1H NMR spectrum of **3** in CD_2Cl_2 at 253 K.

well-resolved spectrum was observed at 253 K (Figure 4.7). Partially overlapping aromatic peaks corresponding to 42 protons from the two macrocycles were observed in the region $\delta=9.16\text{--}6.79$ ppm. The 12 methoxy protons resonate in the region $\delta=4.41\text{--}2.02$ ppm.



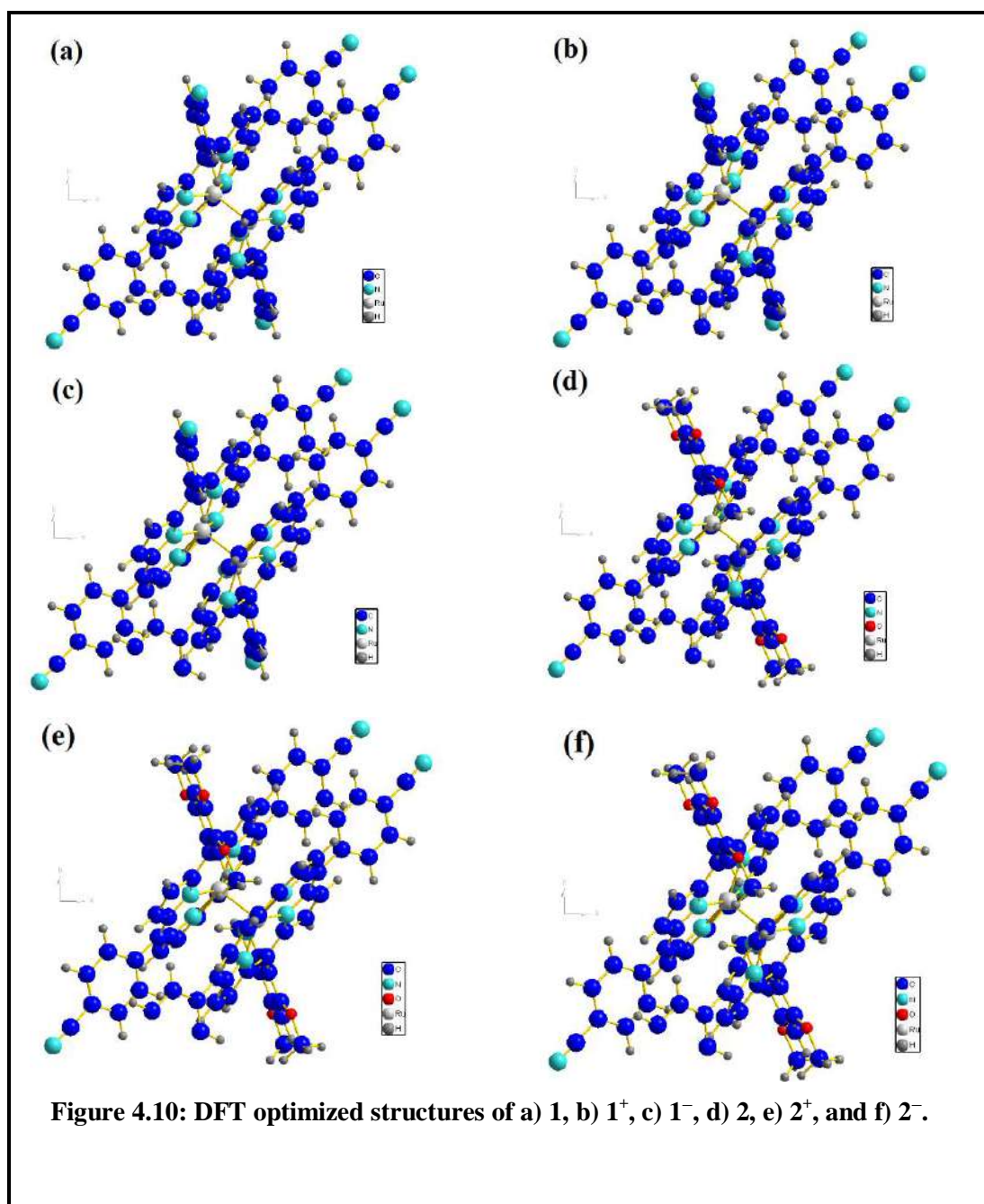
4.3.3 Crystal structure:

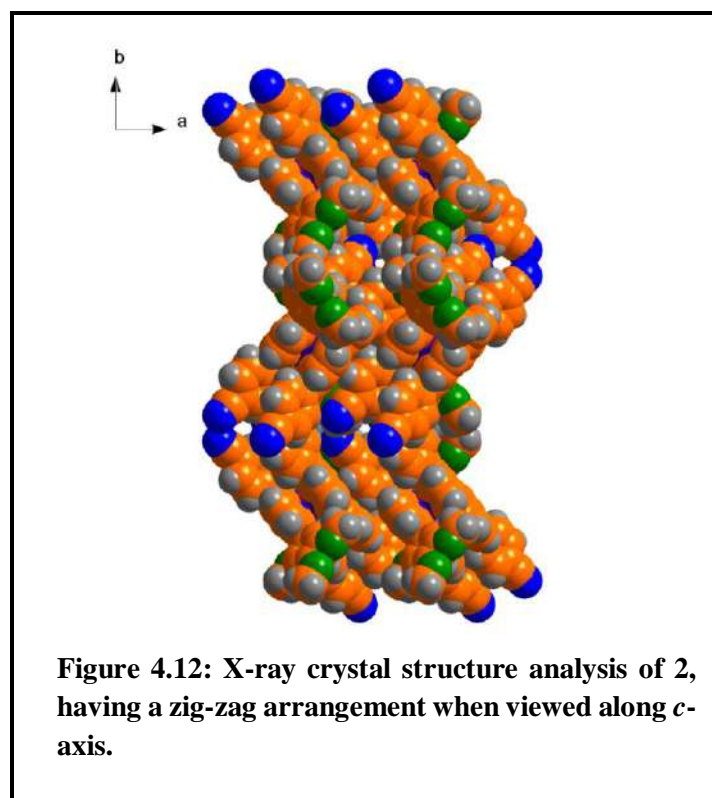
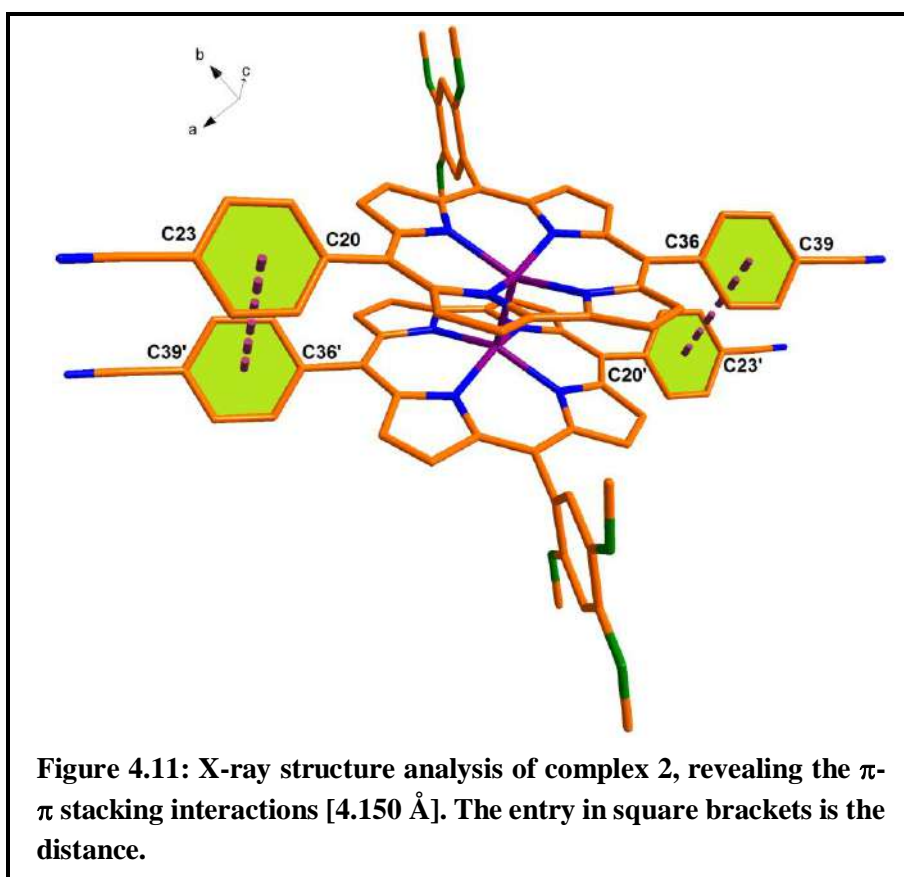
A top view of the molecular structure of **2** in the crystal is depicted in Figure 4.9. Salient crystallographic parameters are given in Table 4.1. DFT- calculated bond distances and angles (Figure 4.10) were in good agreement with the experimental values for **2**. The structure reveals a dimeric metal complex, in which two identical ruthenium corrole units are directly connected through their central Ru atoms by a metal-metal bond. The Ru–Ru bond distance is 2.175 Å (DFT: 2.190 Å), which falls in the range of triple bonds.²²⁵ In accordance with previously reported ruthenium homodimers, the Ru–Ru bond distances are in the order: corrole dimer (2.175 Å) < porphyrin dimer cation²²⁶ (2.293 Å) < porphyrin dimer (2.408 Å). The two corrole skeletons are positioned about the metal-metal bond so as to minimize the steric encumbrance and to obtain the maximum stability through intramolecular



interactions between the meso-substituted aryl groups of oppositely stacked dimers. The two meso-substituted corrole rings in **2** are mutually arranged in a centrosymmetric geometry. Each Ru atom is axially displaced from the N_4 plane by 0.512 Å towards the other, resulting in a domed conformation of each corrole ring. The deviation of the Ru atom from the 19-atom corrole plane is somewhat more prominent at 0.745 Å. Due to this domed distortion of the pyrrole rings, the intramolecular N_4 planes approach each other quite closely at a distance of 3.198 Å. Steric hindrance dictates a gap between the 19-atom corrole planes of the stacked dimers of 3.659 Å. The average Ru-N distance is 1.969 Å (DFT: 1.979 Å) and is comparable to those of other such bonds in ruthenium-coordinated corrole rings.^{223,225} The N-Ru-N bite angles in each of the rings vary from 78.578° (DFT: 78.598°) to 91.848° (DFT: 91.968°). A dihedral angle of 0° between the two interconnected corrole rings implies that the meso substituents of one ring are arranged diametrically opposite to those of the other. This leads to the comparatively bulky 2,4,5-trimethoxyphenyl moieties at C-10/C'-10 occupying the more spacious region above or below the C1-C19 bond of the other ring and maintains co-planarity between the

stacked macrocycles. The bulkier substituent at C-10 deviates only by an angle of 14° from the normal to the mean corrole plane due to the availability of space. The substituents at C-5 and C-15, however, form dihedral angles of 51.10° and 48.84° , respectively, with respect to the mean corrole plane. This arrangement is facilitated by the obvious π - π stacking between the two macrocyclic skeletons as well as that between the aryl rings at the C-5 and C-15 positions with the opposite pairs at C'-15 and C'-5, respectively (the centroid-centroid distance is 4.150 \AA ; the closest interatomic distance between the rings is that between C-36 and C-21' of 3.519 \AA ; Figures 4.11-4.14).





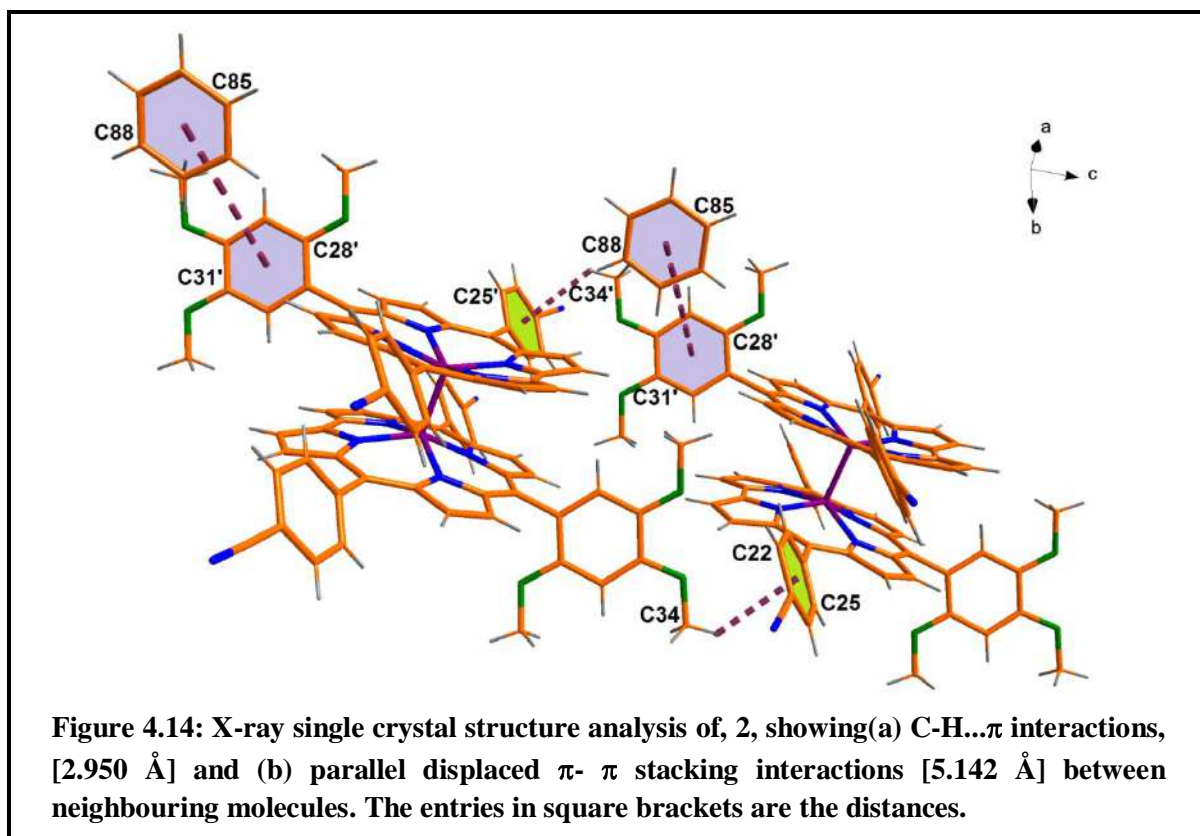
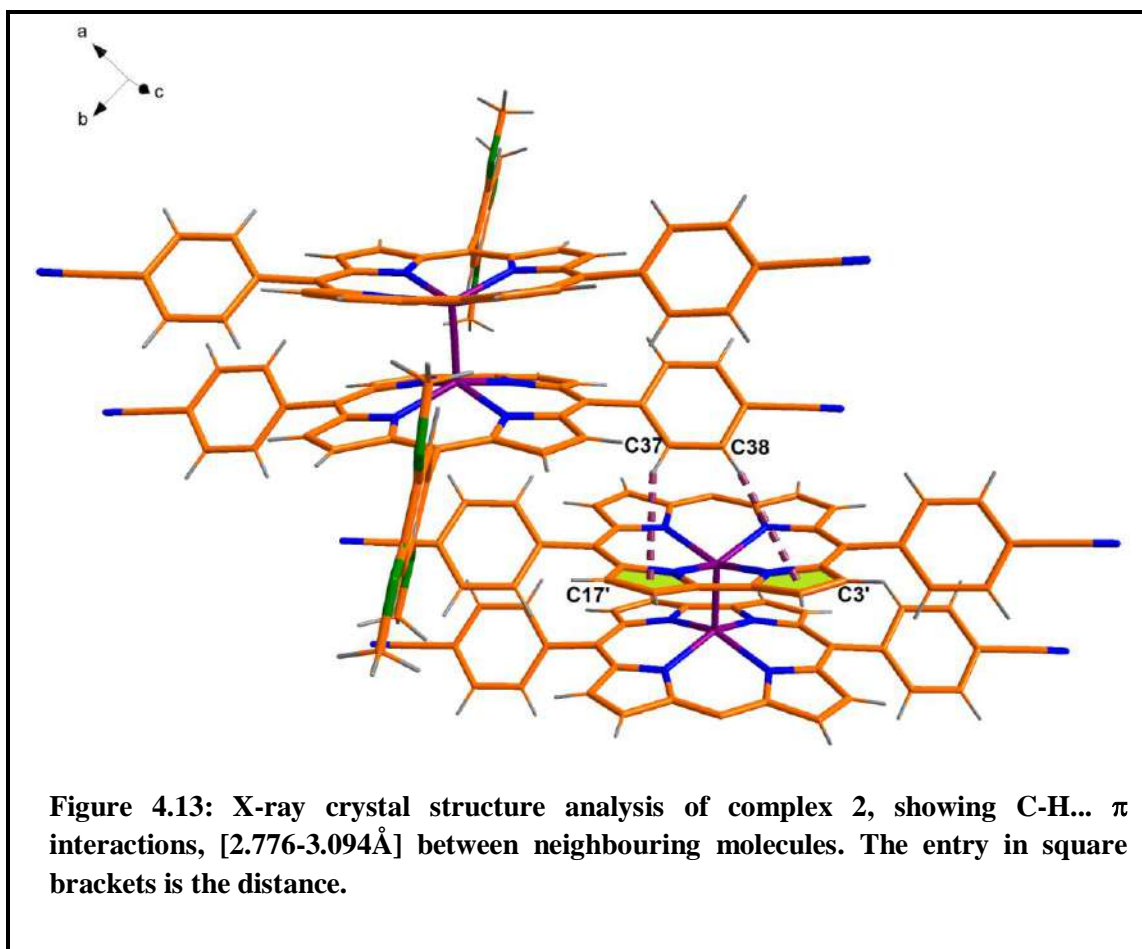


Table 4.1: X-Ray Crystallographic data

Compound code	2
molecular formula	C ₉₆ H ₆₆ N ₁₂ O ₆ Ru ₂
Fw	1685.80
Radiation	MoK α
crystal symmetry	Monoclinic
space group	<i>P</i> 2 ₁ /c
<i>a</i> (Å)	10.2536(3)
<i>b</i> (Å)	27.9267(8)
<i>c</i> (Å)	14.1265(4)
α (deg)	90.00
β (deg)	103.960(2)
γ (deg)	90.00
<i>V</i> (Å ³)	3925.6(2)
<i>Z</i>	2
μ (mm ⁻¹)	0.451
<i>T</i> (K)	100
<i>D</i> _{calcd} (g cm ⁻³)	1.426
2 θ range (deg)	4.10 to 50.92
<i>e</i> data (<i>R</i> _{int})	7239 (0.0794)
<i>R</i> 1 (<i>I</i> > 2 σ (<i>I</i>))	0.0444
WR2 (all data)	0.1138
GOF	1.046
Largest diff. peak and hole(e \cdot Å ⁻³)	0.464 and -0.566

4.3.4 Electrochemistry:

Electrochemical measurements (cyclic voltammetry and differential pulse voltammetry) on the three dinuclear ruthenium corroles **1**, **2**, and **3** were performed at room temperature in dichloromethane containing 0.1M tetrabutylammonium perchlorate (Figure 4.15). The redox potentials have been tabulated in Table 4.2. Each of the synthesized complexes, **1**, **2**, and **3**, undergoes two successive

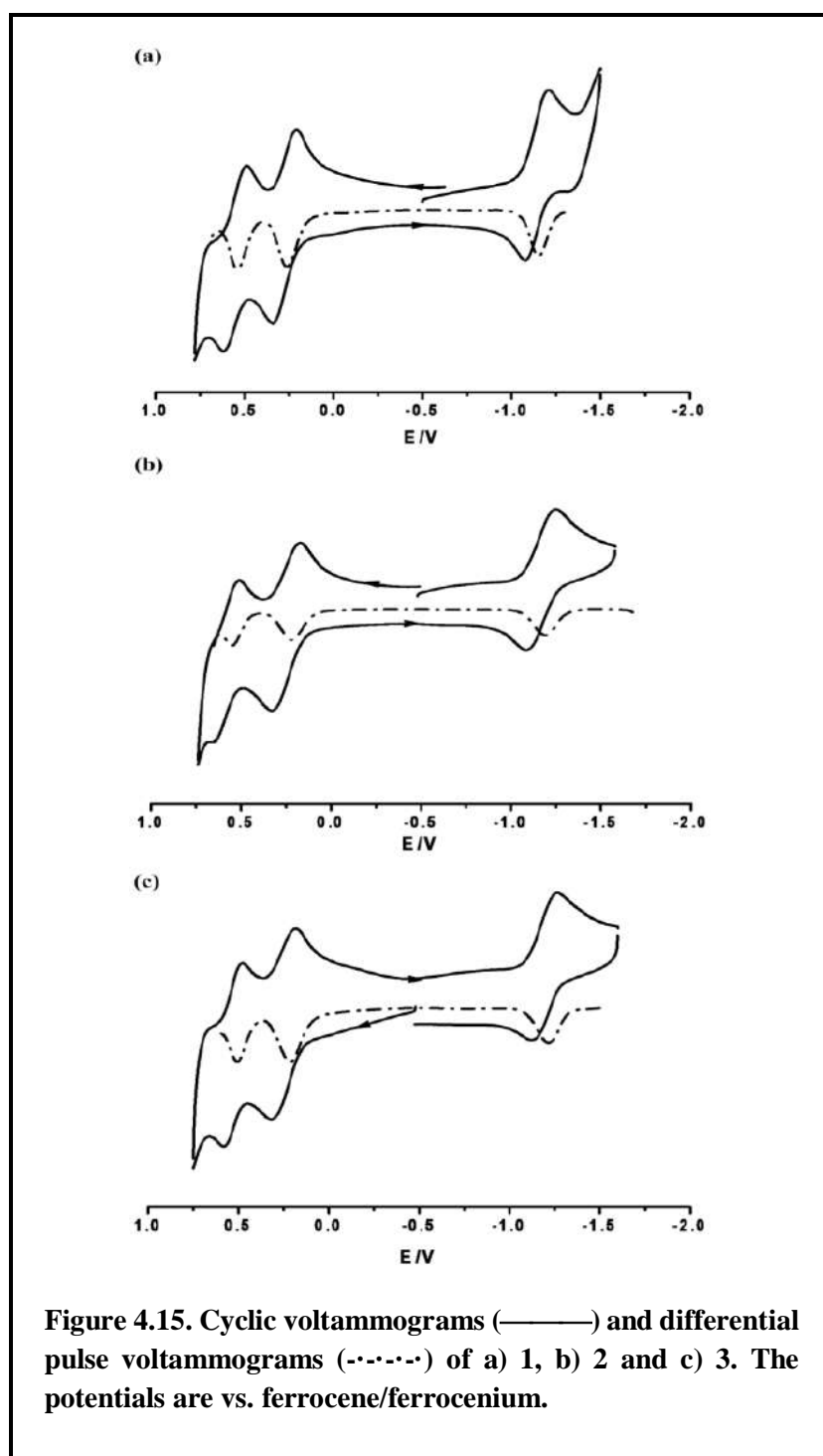


Figure 4.15. Cyclic voltammograms (—) and differential pulse voltammograms (---) of a) **1**, b) **2** and c) **3**. The potentials are vs. ferrocene/ferrocenium.

reversible oxidations, the first at 0.27 V (DFT: 0.71 V), 0.25 V (DFT: 0.35 V), and 0.25 V and the second at 0.55 V, 0.55 V, and 0.53 V, respectively, versus ferrocene/ferrocenium. Each of them displays a single reversible reduction couple at -1.14 V (DFT: -0.98 V) (**1**), -1.16 V (DFT: -1.19 V) (**2**), and -1.19 V (**3**) versus ferrocene/ferrocenium. The DFT-calculated redox potentials for **2** matches quite well with the experimentally determined values, but those for **1** show some deviations. To gain a deeper understanding of the electronic structures of these ruthenium complexes in various redox states, UV/Vis/NIR and EPR spectroelectrochemical measurements and DFT and TD-DFT calculations were performed.

Table 4.2: Electrochemical data

Compound	Electrochemical data ^{a,b}	
	Oxidation $E^0, \text{V} (\Delta E_p, \text{mV})$	Reduction $E^0, \text{V} (\Delta E_p, \text{mV})$
1	0.27(80), 0.55(80)	-1.14(90)
2	0.25(80), 0.55(80)	-1.16(80)
3	0.25(80), 0.53(80)	-1.19(90)

^aIn dichloromethane.

^bThe potentials are vs. ferrocene/ ferrocenium.

4.3.5 EPR spectroelectrochemistry and spin density calculations:

As expected, no characteristic EPR signals were obtained from the diamagnetic native states of the three complexes, implying antiferromagnetic coupling between the unpaired electrons of the two formal ruthenium(III) centers (**1–3**). This clearly indicated a ground spin state of the $\text{Ru}_2^{\text{III}, \text{III}}$ corrole dimers of $S=0$. The in-situ generated one-electron-reduced species **1**^{•-} in DCM solvent/0.1M tetrabutylammonium hexafluorophosphate is EPR-silent down to liquid-nitrogen temperature. This

fact points to fast relaxation processes that are normally typical of metal-centered spin and the usually resulting energetically close-lying states. The spin densities calculated from the Löwdin population analysis of $\mathbf{1}^{\bullet-}$ indicated that about 41% spin density resides on each ruthenium center for the one-electron-reduced forms of the complexes (Table 4.4 and Figure 4.16). This was also reflected in the increase in the Ru–Ru bond distance on going from $\mathbf{1}$ (2.191 Å) to $\mathbf{1}^{\bullet-}$ (2.269 Å) seen in their DFT-optimized structures (Figure 4.10).

Table 4.3: Electron paramagnetic resonance data of paramagnetic states. ^{[a], [b]}

Complex	EPR data ($g_x; g_y; g_z$) ^[a]	EPR data ($g_x; g_y; g_z$) ^[b]
$\mathbf{1}^{*+}$	1.858; 2.051; 2.250	1.915; 2.002; 2.107
$\mathbf{1}^{\bullet-}$	1.390; 2.042; 2.209	—
$\mathbf{2}^{*+}$	1.879; 2.049; 2.217	1.917; 2.003; 2.113
$\mathbf{2}^{\bullet-}$	1.378; 2.042; 2.207	—
$\mathbf{3}^{*+}$	—	1.924; 2.005; 2.085

[a] g values (from DFT calculations).

[b] g values (from experiment).

Additionally, the calculated g values for the reduced forms show huge g anisotropies, as would be expected for predominantly ruthenium-centered spins (Table 4.3). The non-observance of an EPR signal down to liquid-nitrogen temperature, together with the data from spin-population calculations, thus point to a major contribution of the $\text{Ru}_2^{\text{II, III}}$ (more likely $\text{Ru}_2^{(2.5, 2.5)}$) corrole form to the one-electron-reduced forms of these complexes. The one-electron-oxidized species $\mathbf{1}^{*+}$ produced through in-situ process in DCM solvent/0.1M tetrabutylammonium hexafluorophosphate is EPR-silent at room temperature. At 151 K, $\mathbf{1}^{*+}$ displays an EPR spectrum in which the rhombicity of the g tensor is clearly visible and the g values are 2.107, 2.002, and 1.915 (Figure 4.17). The g -anisotropy, Δg , is

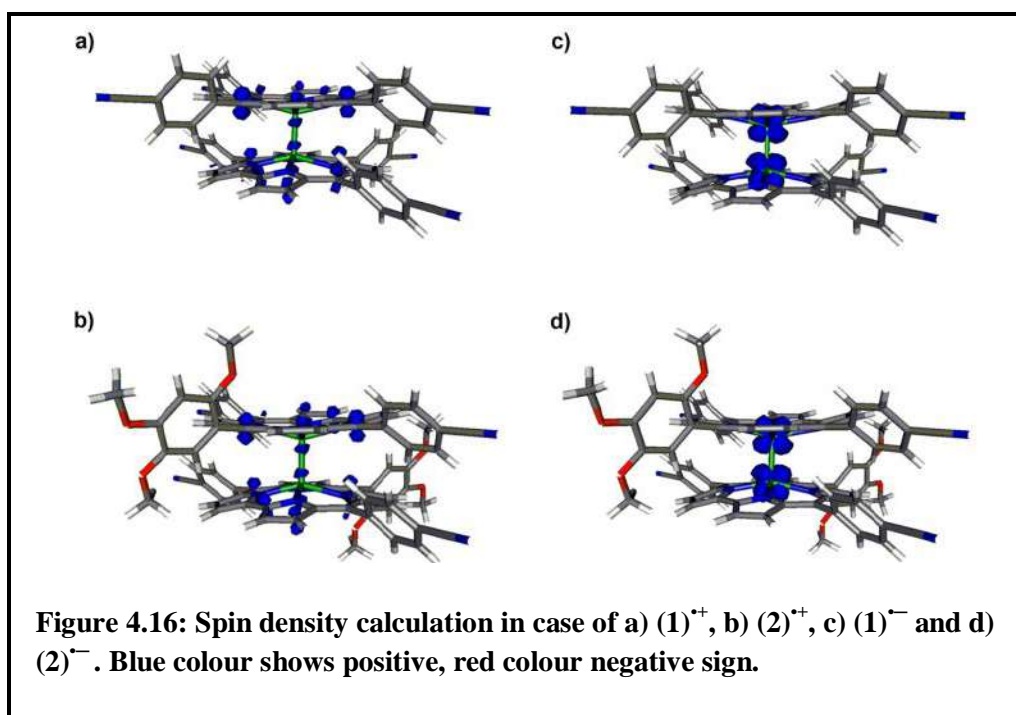
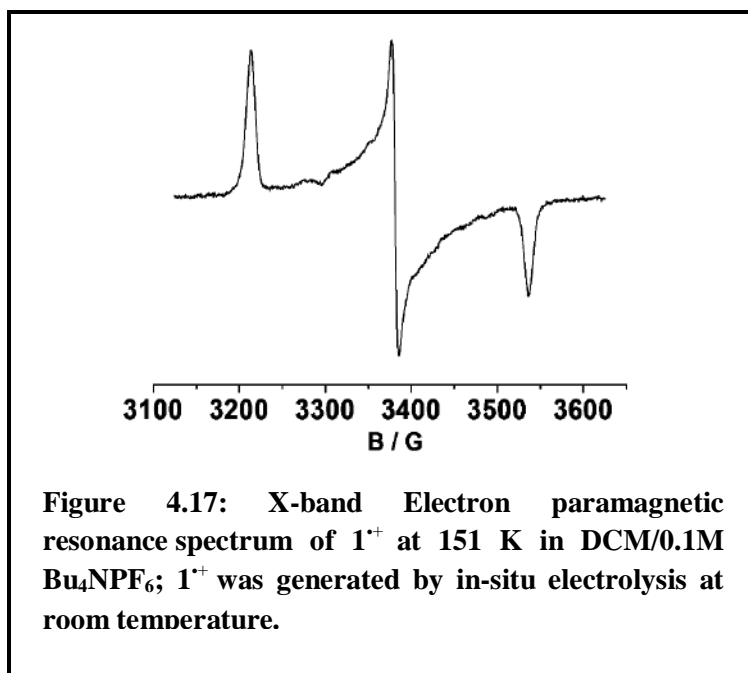


Table 4.4: (B3LYP/TZVPP-ZORA) calculated Löwdin spin densities on each Ru and on each Corrole.

Complex	Ru	Corrole
1 ^{•+}	0.08	0.42
1 ^{•-}	0.41	0.09
2 ^{•+}	0.08	0.42
2 ^{•-}	0.41	0.09

thus 0.192, and more notably the average g value is 2.008. Although EPR silence at room temperature in fluid solutions is often taken as an indication of ruthenium-centered spin,²²⁷ this need not always be the case. Organic radicals having close-lying states can also display fast relaxation and hence be EPR-silent at room temperature in fluid solution. For **1^{•+}**, the average g value of 2.008 and the relatively small g -anisotropy are perhaps indicative of predominantly ligand-centered spin. Structure-based DFT calculations on the EPR parameters of **1^{•+}** yielded g values of 2.250, 2.051, and 1.858, in reasonable agreement with the experimentally observed values. Additionally, spin densities

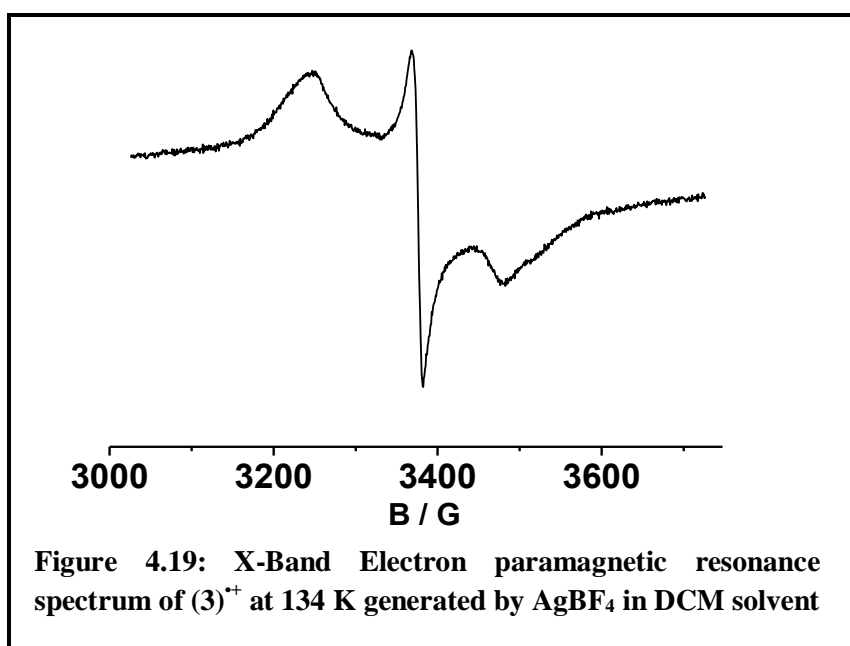
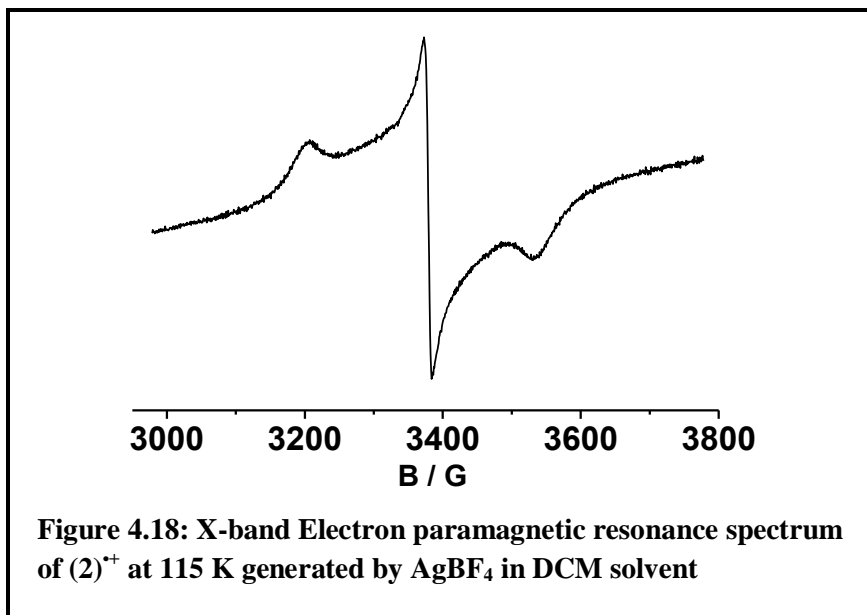


calculated from the Löwdin population analysis indicated that only 8% of the total spin density resides on each ruthenium center for the one-electron-oxidized form of the complex. This was also reflected in the negligible change in the Ru–Ru bond distance on going from **1** (2.191 Å) to 1^{+} (2.186 Å) seen in their DFT-optimized structures (Figure 4.10). Thus, the experimentally observed *g* value and the spin density calculations point to a predominantly corrole-centered spin for 1^{+} . These results are in contrast to what has previously been reported²²² for the one-electron-oxidized forms of unsupported corrole-ruthenium dimers. In those cases, the oxidized forms were formulated as $\text{Ru}_2^{\text{III, IV}}$ corrole species. The EPR properties and the related spin density calculations for the one-electron-oxidized and -reduced forms of complexes **2** and **3** are very similar to those described above for the various redox forms of **1** (Table 4.3, Figure 4.17-4.19).

4.3.6 Ultraviolet/Visible/NIR spectroelectrochemistry and TD-DFT calculations:

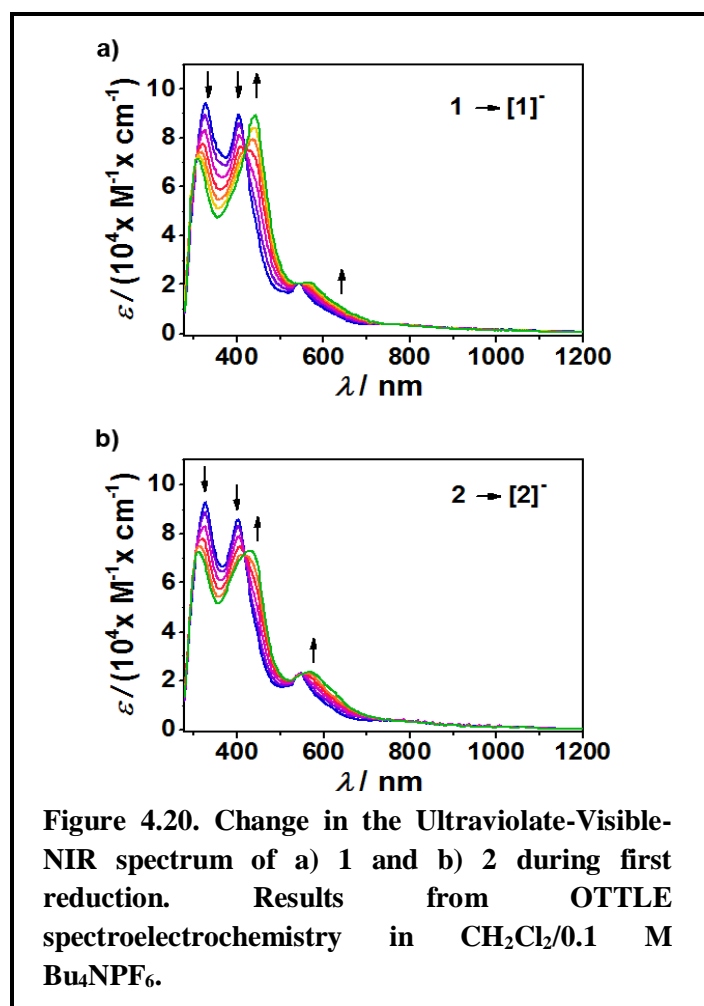
The native state complexes display typical spectra expected for a $\text{Ru}_2^{\text{III, III}}$ corrole dimer species (Table 4.5).²²⁵ Metalation of the respective free-base corroles led to significant blue shifts of their Soret bands (around 100 nm). These shifts were even larger than those in previously reported rotationally disordered metal-metal-bonded dimeric corrole complexes, indicating significant electronic

interaction between the p-clouds of the macrocycles.²²⁴ As the spectra of **1–3** in all redox states are very similar, only the various redox forms of **2** are discussed in detail below (Figures 4.20–



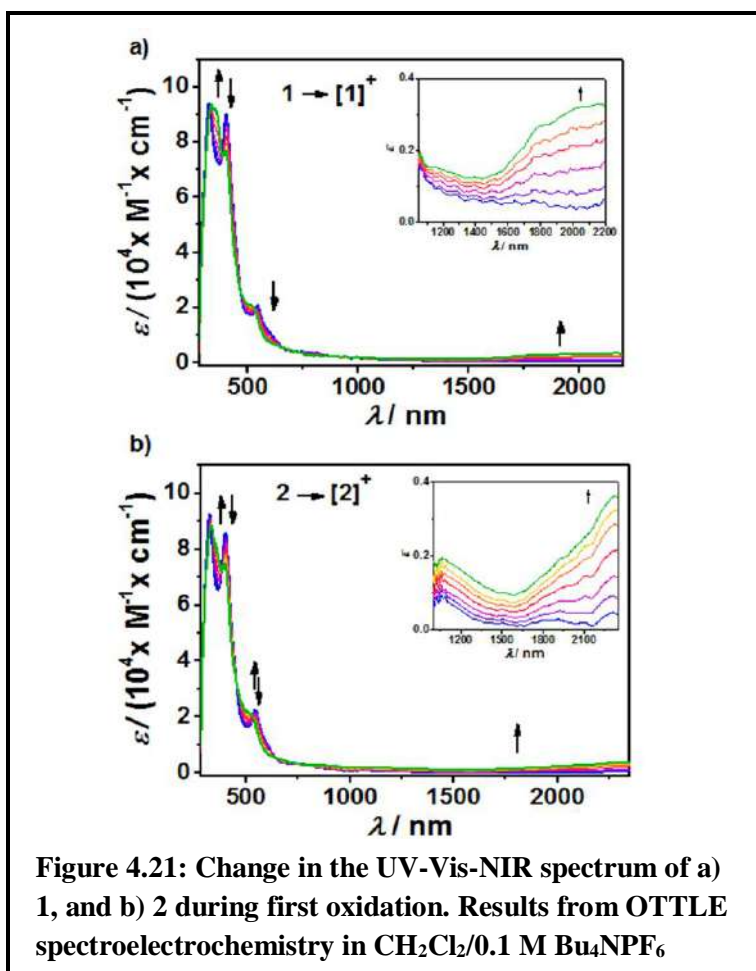
4.23). Details of the interpretation obtained through TD-DFT calculations on **1** and **2** are given in the Tables 4.6–4.11 and Figures 4.24–4.29. The intense band in the visible region, that is, at 546 nm, can be ascribed to a HOMO–2→LUMO+3 transition (Table 4.6). These transitions in the visible region are due in part to ligand-to metal charge transfer (LMCT). On addition of an electron to **2**, all of the original bands in the visible region are found to decrease in intensity (Table 4.3). Concomitantly, the

most intense peak at 326 nm is shifted to higher energy at 311 nm, and the band at 403 nm is shifted to lower energy at 430 nm (Figure 4.20). The Q-band at 546 nm is also shifted to 567 nm in the lower-energy region and shows increased intensity. This low-energy band has contributions from the transitions $\text{HOMO}\alpha \rightarrow \text{LUMO}+6\alpha$ and $\text{HOMO}-2\alpha \rightarrow \text{LUMO}+5\alpha$, as indicated by TD-DFT calculations (Table 4.8). The origin of the band at 567 nm was thus calculated by TD-DFT to be a mixture of MLCT and ILCT (intra- and inter-ligand charge transfer) transitions. Despite the presence of a formally mixed-valent situation in the reduced complexes, no long wavelength bands in the NIR



region was observed for these forms. Although NIR bands are typically expected for mixed valent compounds, there have been numerous examples in the literature where no such bands have been observed, despite the clear presence of a mixed-valent form.^{228,229} The reduced forms of the compounds presented here fall into this category. On oxidation, similar spectral signatures were

observed for all of the studied complexes (Figure 4.21 and 4.23a). On one-electron-oxidation of **2**, the most prominent peaks at 326 and 403 nm were found to shift to 333 and 351 nm, respectively (Table 4.3 and Figure 4.21b), and the initial Q-band was found to retain similar intensity with a small shift to the lower-wavelength region. Theoretical calculations indicated that this band at 531 nm has contributions from HOMO-2 $\alpha \rightarrow$ LUMO+5 α , HOMO-4 $\beta \rightarrow$ LUMO+3 β , and HOMO $\beta \rightarrow$ LUMO+6 β transitions (Table 4.7). The band at 531 nm was thus calculated by TD-DFT to originate from ILCT transitions. Unique features were seen in the high-wavelength region for the oxidized species. Broad bands were observed at 1064 and 2315 nm in the near-IR (NIR) region (Figure 4.21). Such NIR transitions have not been observed for previously studied ruthenium-corrole dimers. Interestingly, the characteristic absorption band observed at about 1064 and 1054 nm for **2**⁺ and **3**⁺, respectively, was clearly absent in the case of **1**⁺. TD-DFT calculations revealed major contributions from HOMO-1 $\alpha \rightarrow$ LUMO+1 α and HOMO-1 $\beta \rightarrow$ LUMO+2 β transitions for the band at 1064 nm (Table 4.7). The



broad band at 2315 nm originates from the HOMO-3 β →LUMO β and HOMO-4 β → LUMO β transitions. The origins of the bands at 1064 and 2315 nm were thus calculated by TD-DFT to be predominantly LMCT and ILCT in nature, respectively. Thus, the one-electron oxidized forms of these dimers show charge-transfer transitions between the Ru₂ core and the corrole ligands, which appear in the NIR region. Although there is a caveat when considering these strongly bound (Ru≡Ru) sandwich-type complexes as model systems for the weakly bound photosynthetic “special pair”, the appearance of two NIR bands at 1064 nm (LMCT-type) and 2315 nm (ILCT-type) upon oxidation is particularly interesting. These bands closely resemble the bands of the radical cations of the photosynthetic “special pair”. It has been reported that the NIR absorptions of the radical cations of the photosynthetic special pair appear at 1250 nm and 3846 nm due to monomeric transitions and inter-valence transitions, respectively.²³⁰ On further oxidation to **2**²⁺, the broad band at 2315 nm decreases in intensity with the appearance of a new band at higher energy at 1557 nm (Figure 4.22). The obtained NIR transitions in **1**²⁺ showed clear isosbestic behaviour. Similar behaviour was also seen for the **2**⁺ to **2**²⁺ transformation.

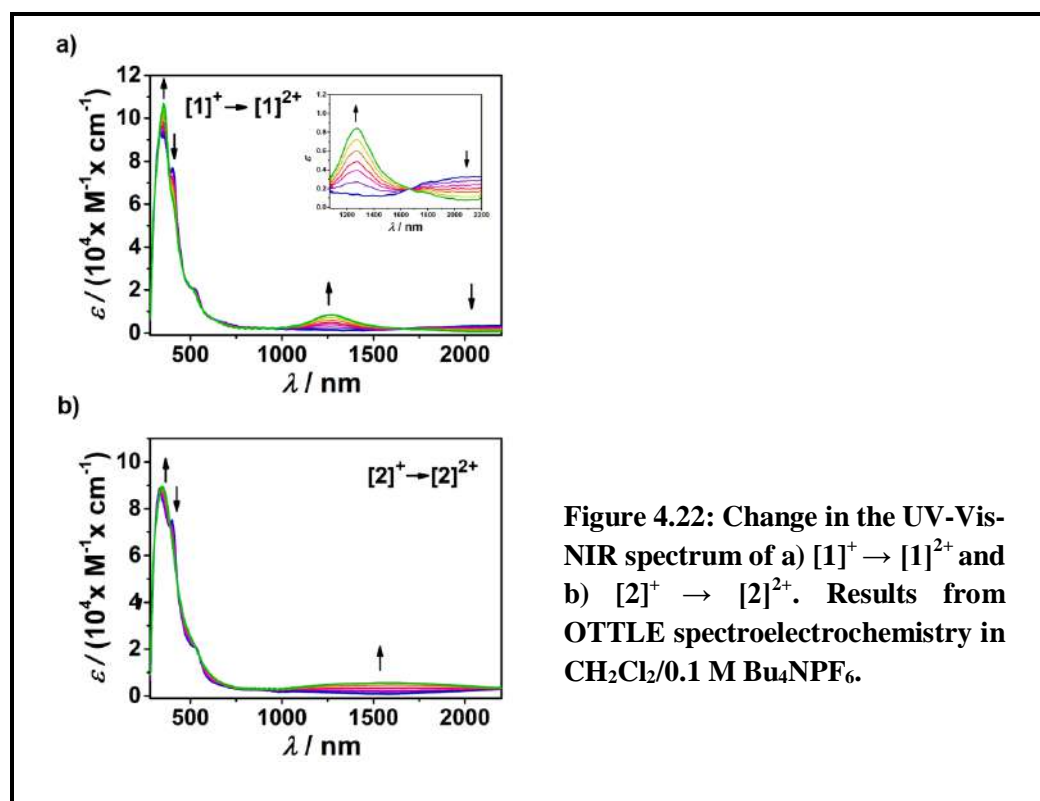


Figure 4.22: Change in the UV-Vis-NIR spectrum of a) **[1]**⁺ → **[1]**²⁺ and b) **[2]**⁺ → **[2]**²⁺. Results from OTTLE spectroelectrochemistry in CH₂Cl₂/0.1 M Bu₄NPF₆.

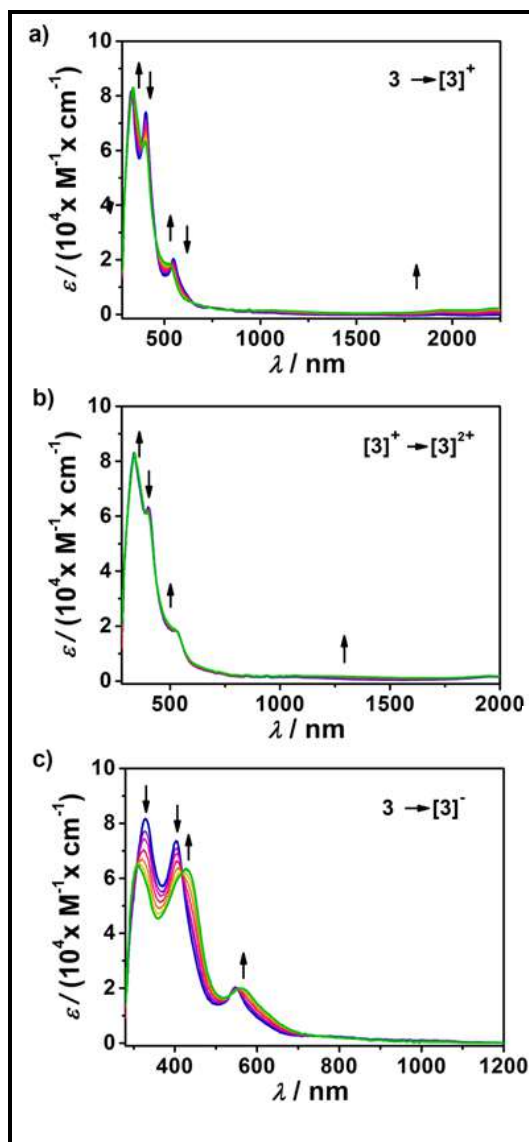


Figure 4.23: Variation in the Ultraviolet-visible-NIR spectra of complex 3 during a) $[3] \rightarrow [3]^+$ b) $[3]^+ \rightarrow [3]^{2+}$ and c) $[3] \rightarrow [3]^-$. Results from OTTLE spectroelectrochemistry in DCM solvent/0.1 M Bu_4NPF_6 .

4.4 Conclusions:

In conclusion, the MO diagrams of these complexes in the native state can be qualitatively expressed as $\sigma^2\pi^4\delta^2\delta^{*2}$, thus yielding a triple bond (one σ and two π bonds) between the two antiferromagnetically coupled ruthenium centers (d^5 configuration).²²³⁻²²⁵ These predictions were further supported by NMR and EPR data of the dimers in their native states. X-ray data showed the distance between the two ruthenium centers to be 2.175 Å, as befits triple-bond formation. Despite the presence of a formally mixed-valent situation $\{\text{Ru}_2^{\text{II, III}}\}$ in the reduced complexes, no long-wavelength bands in the NIR region were observed for these forms. The in-situ-generated one-

electron-reduced species in $\text{CH}_2\text{Cl}_2/0.1\text{M Bu}_4\text{NPF}_6$ are also EPR silent down to liquid-nitrogen temperature. The one-electron oxidized species, on the other hand, display EPR properties that are best fitted by a corrole radical bound to a homovalent $\text{Ru}_2^{\text{III, III}}$ unit. Both of the aforementioned formulations were also corroborated through structure-based spin density calculations on the complexes. We have further demonstrated that the two corrole units of a given dimer participate in strong π – π interactions. This is evident from the appearance of NIR transitions in the oxidized radical forms of these dimers. As the mean plane separation between two corrole units in a given dimer is

Table 4.5: Ultraviolet-Visible-NIR Data of 1^n , 2^n and 3^n [$n = -1, +1, +2, 0$] from Spectroelectrochemistry^[a]

Complex	λ / nm (ϵ / $\text{M}^{-1}\text{cm}^{-1}$)
1	325(94200), 405(89700), 544(20700)
$1^{+\cdot}$	338(93700), 352(92200), 403(76700), 530(20100), 2173(3300)
$1^{+2\cdot}$	352(10600), 402(63000) sh, 513(20200) sh, 1273(8400)
$1^{-\cdot}$	309(71600), 442(89300), 569(20700)
2	326(92700), 403(85700), 546(22300)
$2^{+\cdot}$	333(88300), 351(82900), 399(75000), 531(20800), 1064(1900) sh, 2315(3600)
$2^{+2\cdot}$	345(89600), 1557(5600)
$2^{-\cdot}$	310(72400), 430(73000), 567(23600)
3	328(81700), 404(74000), 547(20200)
$3^{+\cdot}$	337(83000), 401(63200), 527(18200), 1054(1530) sh, 2242(2170)
$3^{+2\cdot}$	338(82900), 399(61400), 529(17900), 1172(1800)
$3^{-\cdot}$	310(64600), 428(63300), 562(20000)

[a] Measurements in DCM solvent/0.1M tetrabutylammonium hexafluorophosphate (OTTLE spectroelectrochemistry).

around 3.543 Å (from X-ray data) and this distance is in close agreement with that of the “special pair” in chlorophyll (the mean plane separation in the “special pair” of bacteriochlorophylls is about 3.5 Å), the oxidized forms of these dimers appear to be good spectroscopic models for this “special pair”. We have observed here for the first time that the ruthenium complexes of ordered corrolato derivatives exhibit NIR transitions on oxidation that are due to the presence of radical corrole units bound to homovalent ruthenium centers. Thus, we can conclude that the observed NIR transitions solely originate from these dimeric radical forms. The origin of the two NIR bands at 1064 nm (LMCT-type) and 2315 nm (ILCT-type) following one-electron-oxidations of **1–3** closely resembles the radical cations of the photosynthetic “special pair”. Previously reported model compounds of the “special pair” in bacteriochlorophylls have typically been metalloporphyrin derivatives having minimal steric strain at the periphery. In contrast, this work concerns rare examples having significant steric encumbrance at the periphery of the metallocorrole derivatives. The results presented here thus point to intriguing properties that can be generated in metal-metal-bonded corrole dimers.

4.5 Experimental Section:

4.5.1 Materials:

The precursors pyrrole, p-chloranil, 4-cyanobenzaldehyde, 2,4,5-trimethoxybenzaldehyde, and tetrabutylammonium perchlorate (TBAP) were purchased from Aldrich, USA. Ruthenium trichloride was purchased from Merck, India. Other chemicals were of reagent grade. Hexane and DCM solvents were purified with potassium hydroxide and Calcium hydride respectively. HPLC standard solvents were utilized for all the spectroscopic and electrochemical related studies.

4.5.2 Detailed discussion of all the physical studies:

Ultraviolet/Visible spectroscopic measurements were carried out using the Perkin-Elmer-Lambda 750 spectrophotometer. For kind of elemental analyses, Perkin-Elmer 240C elemental analyser were used. NMR spectra of all the compounds were measured by using Bruker Avance 400 Nuclear Magnetic Resonance spectrometer. All the chemical shifts values are demonstrated in parts per million (ppm) unit with respect to the residual chloroform ($\delta = 7.26$). Bruker Micro TOF-QII mass

spectrometer was used to measure the ESI-MS spectra of all compounds. Electrochemical studies were measured using the CH Instruments model CHI1120A electrochemistry system. A glassy-carbon working electrode, a platinum wire as an auxiliary electrode, and a saturated calomel reference electrode (SCE) were used in a three-electrode configuration. TBAP (0.1M) served as the supporting electrolyte and the concentration of the solution was 10^{-3} M in terms of the complex. E_{298}^0 is called the half wave potential which can be determined using $0.5(E_{pc} + E_{pa})$, and the E_{pc} and E_{pa} stand for the cathodic and anodic peak positions, respectively. All the electrochemical experiments were carried out using 100 mV s^{-1} scan rate. All the X-band EPR spectra were performed using the Bruker EMX System and all the EPR simulations were performed through the Simfonia program. In order to record the Ultraviolet/Visible spectra of all these complexes have been performed using Avantes spectrometer consist of AvaLight-DH-S-Bal as the light source, AvaSpec-ULS2048 as the UV/Vis detector, and AvaSpec-NIR256-2.5TEC as an NIR detector. For the Spectroelectrochemical data collection, an optically transparent thin-layer electrochemical (OTTLE) cell.²³¹

4.5.3 Crystal structure determination:

Crystals of complex **2** was obtained through the slow diffusion process in DCM solvent into hexane and this process was followed by the slow evaporation under atmospheric conditions. Bruker Kappa APEX II CCD has been used for recording the crystal data for complex **2** at 100 K. All the crystallographic parameters were arranged within the Table 4.1 and have been optimized for absorption effects and Lorentz polarization effect. In order to solve and refine both the crystals, the SHELXTL²³² program package has been utilized. During the refinement process, all the Hydrogen atoms has been attached through riding model. Hydrogen atoms of the water molecules were included without fixing. Spots for all the disordered solvent molecules has been eliminated through the SQUEEZE command in PLATON.¹³⁵ CCDC 1507111 (**2**) contains the supplementary crystallographic data for this paper. These data are provided free of charge by the Cambridge Crystallographic Data Centre. Computational details DFT calculations were carried out with the ORCA 3.0.0 program package²³³ using the BP86 and B3LYP functionals for the geometry

optimization and single-point calculations, respectively.²³⁴⁻²³⁶ The restricted and unrestricted DFT methods were employed for closed shell and open-shell molecules, respectively. All calculations were run with empirical Van der Waals corrections (D3).²³⁷ Convergence criteria were set to default for the geometry optimizations (OPT), and to tight for SCF calculations (TIGHTSCF). Relativistic effects were included with the zeroth-order relativistic approximation (ZORA).²³⁸ Triple-z valence basis sets (TZVPP-ZORA)²³⁹ were employed for all atoms. Calculations were performed using the resolution of the identity approximation²⁴⁰⁻²⁴³ with matching auxiliary basis sets. Low-lying excitation energies were calculated with time-dependent DFT (TD-DFT). Solvent effects were taken into account with the conductor-like screening model (COSMO(CH₂Cl₂))^{244,245} for all calculations. Programs like modified Avogadro 1.1.1 with extended ORCA support and the Molekel 5.4.0.8^{246, 247} have been applied to anticipate the Molecular orbitals and spin densities.

4.5.4 Synthesis and characterization:

4.5.4.1 Synthesis of bis(5,10,15-tris(4-cyanophenyl)corrolato-ruthenium(III)) (1):

Complex **1** was synthesized by a procedure similar to that reported by Guillard and co-workers,²²³ with slight modifications. 5,10,15-Tris(4-cyanophenyl)corrole (100 mg, 0.17 mmol)^{95,96,97,126,136,248-250} and the organometallic precursor dichloro(1,5-cyclooctadiene)ruthenium(II) dimer (95 mg, 0.34 mmol) were weighed and placed in a two-necked round-bottomed flask under nitrogen atmosphere. 2-Methoxyethanol (10 mL) and triethylamine (100 mL) were then added, and the reaction mixture was stirred under reflux conditions in an inert atmosphere for 30 min. The progress of the reaction was monitored by TLC analysis, with completion being indicated by the disappearance of the fluorescent green spot of the starting material. The brown reaction mixture was then concentrated to dryness in a rotary evaporator. The crude product was subjected to column chromatography on silica gel (100–200 mesh), eluting with 100% CH₂Cl₂. The desired compound was collected as a reddish-brown solid, and subsequent recrystallization from CH₂Cl₂/hexane afforded pure **1**. Yield: 43% (0.050 g, 0.036 mmol). ¹H NMR (400 MHz, CD₂Cl₂, 298 K, TMS): δ=9.31–8.74 (m, 8H), 8.57 (s, 3H), 8.31 (br m, 11 H), 7.84 (br m, 5H), 7.68 (s, 1H), 7.46 (br m, 8H), 7.26 (d, 7.6 Hz, 2H), 7.14 ppm

(d, $J=8.0$ Hz, 2H); UV/Vis (CH_2Cl_2): λ_{max} (ϵ)=325 (94000), 404 (89800), 544 nm (24000 $\text{M}^{-1}\text{cm}^{-1}$); MS (ESI⁺): m/z : calcd for $\text{C}_{80}\text{H}_{40}\text{N}_{14}\text{Ru}_2$: 1400.1600; found: 1400.1419 $[\text{M}]^+$; elemental analysis calcd (%) for $\text{C}_{80}\text{H}_{40}\text{N}_{14}\text{Ru}_2$ (**1**): C 68.66, H 2.88, N 14.01; found: C 68.46, H 2.65, N 13.78.

4.5.4.2 Synthesis of bis(10-(2,4,5-trimethoxyphenyl)-5,15-bis(4-cyanophenyl) corrolato-ruthenium(III)) (**2**):

10-(2,4,5-Trimethoxyphenyl)-5,15-bis(4-cyanophenyl)corrole^{95,96,97,126,136,248-250} (100 mg, 0.15 mmol) and the organometallic precursor dichloro(1,5-cyclooctadiene)ruthenium(II) dimer (84 mg, 0.30 mmol) were weighed and placed in a two necked round-bottomed flask under nitrogen atmosphere. 2-Methoxyethanol (10 mL) and triethylamine (100 μL) were then added and the reaction mixture was stirred under reflux conditions in an inert atmosphere for 30 min. The progress of the reaction was monitored by TLC analysis, with completion being indicated by the disappearance of the fluorescent green spot of the starting material. The brown reaction mixture was then concentrated to dryness in a rotary evaporator. The crude product was subjected to column chromatography on silica gel (100–200 mesh), eluting with $\text{CH}_2\text{Cl}_2/\text{MeCN}$ (95:5, v/v). The desired compound was collected as a reddish-brown solid, and subsequent recrystallization from CH_2Cl_2 /hexane afforded crystalline **2**. Yield: 52% (0.060 g, 0.039 mmol). ¹H NMR (400 MHz, CDCl_3 , 273 K, TMS): δ =9.23 (br m, 4H), 8.96–8.60 (m, 5H), 8.57–8.10 (m, 17H), 7.95–7.72 (m, 4H), 7.46 (br t, $J=19.1$ Hz, 3H), 7.14–7.03 (m, 1H), 6.62 (d, $J=5.1$ Hz, 2H), 4.21–3.96 (m, 12H), 2.84–2.65 ppm (m, 6H); UV/Vis (CH_2Cl_2): λ_{max} (ϵ)=325 (92000), 402 (85800), 545 nm (26100 $\text{M}^{-1}\text{cm}^{-1}$); MS (ESI⁺): m/z : calcd for $\text{C}_{84}\text{H}_{54}\text{N}_{12}\text{O}_6\text{Ru}_2$: 1530.2400; found: 1530.1974 $[\text{M}]^+$; elemental analysis calcd (%) for $\text{C}_{84}\text{H}_{54}\text{N}_{12}\text{O}_6\text{Ru}_2$ (**2**): C 65.96, H 3.56, N 10.99; found: C 65.78, H 3.48, N 10.69.

4.5.4.3 Synthesis of bis(10-(4,7-dimethoxynaphthalen-1-yl)-5,15-bis(4-cyanophenyl)corrolato-ruthenium(III)) (**3**):

10-(4,7-Dimethoxynaphthalen-1-yl)-5,15-bis(4-cyanophenyl)corrole^{95,248,249} (100 mg, 0.15 mmol) and the organometallic precursor dichloro(1,5-cyclooctadiene) ruthenium(II) dimer (84 mg, 0.30 mmol) were weighed and placed in a two-necked round-bottomed flask under nitrogen atmosphere.

2-Methoxyethanol (10 mL) and triethylamine (100 μ L) were then added and the reaction mixture was stirred under reflux conditions in an inert atmosphere for 30 min. The progress of the reaction was monitored by TLC analysis, with completion being indicated by the disappearance of the fluorescent green spot of the starting material. The brown reaction mixture was then concentrated to dryness in a rotary evaporator. The crude product was subjected to column chromatography on silica gel (100–200 mesh), eluting with 100% CH_2Cl_2 . The desired compound was collected as a reddish-brown solid, and subsequent recrystallization from CH_2Cl_2 /hexane afforded pure **3**. Yield: 64% (0.073 g, 0.047 mmol). ^1H NMR (400 MHz, CD_2Cl_2 , 298 K, TMS): δ =9.16 (br m, 4H), 9.00–8.47 (m, 9H), 8.47–7.96 (m, 15H), 7.83 (br m, 5H), 7.56–7.33 (m, 3H), 7.09 (br m, 4H), 6.79 (d, J =8.3 Hz, 2H), 4.41 (s, 1H), 4.30 (d, J =9.5 Hz, 5H), 2.02 ppm (br t, J =12.6 Hz, 6H); UV/Vis (CH_2Cl_2): $\lambda_{\text{max}}(\epsilon)$ =328 (79600), 403 (73600), 554 nm (32800 $\text{M}^{-1}\text{cm}^{-1}$); elemental analysis calcd (%) for $\text{C}_{90}\text{H}_{54}\text{N}_{12}\text{O}_4\text{Ru}_2$ (**3**): C 68.87, H 3.47, N 10.71; found: C 68.65, H 3.38, N 10.52.

4.6: TD-DFT Calculations:

Table 4.6: Time-dependent density functional theory Calculated Electronic Transitions for 1

Compound	Contribution of excitation (%)	Transition wavelength (nm)	Oscillator strength	Exp. transition wavelength (nm)	Molar absorption coefficient, $\text{M}^{-1}\text{cm}^{-1}$
1	HOMO -1 \rightarrow LUMO+1 (92)	910	0.007		
	HOMO \rightarrow LUMO+1 (89)	855	0.012		
	HOMO-2 \rightarrow LUMO+3 (90)	610	0.039	544	20 700
	HOMO-2 \rightarrow LUMO+2 (65)	582	0.023		
	HOMO-1 \rightarrow LUMO+4 (28)				
	HOMO-5 \rightarrow LUMO+1 (10)	522	0.146	405	890800
	HOMO-2 \rightarrow LUMO+2 (10)				
	HOMO-1 \rightarrow LUMO+4 (28)				
	HOMO \rightarrow LUMO+6 (24)				
	HOMO-5 \rightarrow LUMO+1 (67)	490	0.035		
	HOMO-4 \rightarrow LUMO (13)				

	HOMO-3 \rightarrow LUMO+5 (27)	476	0.180		
	HOMO \rightarrow LUMO+6 (55)				

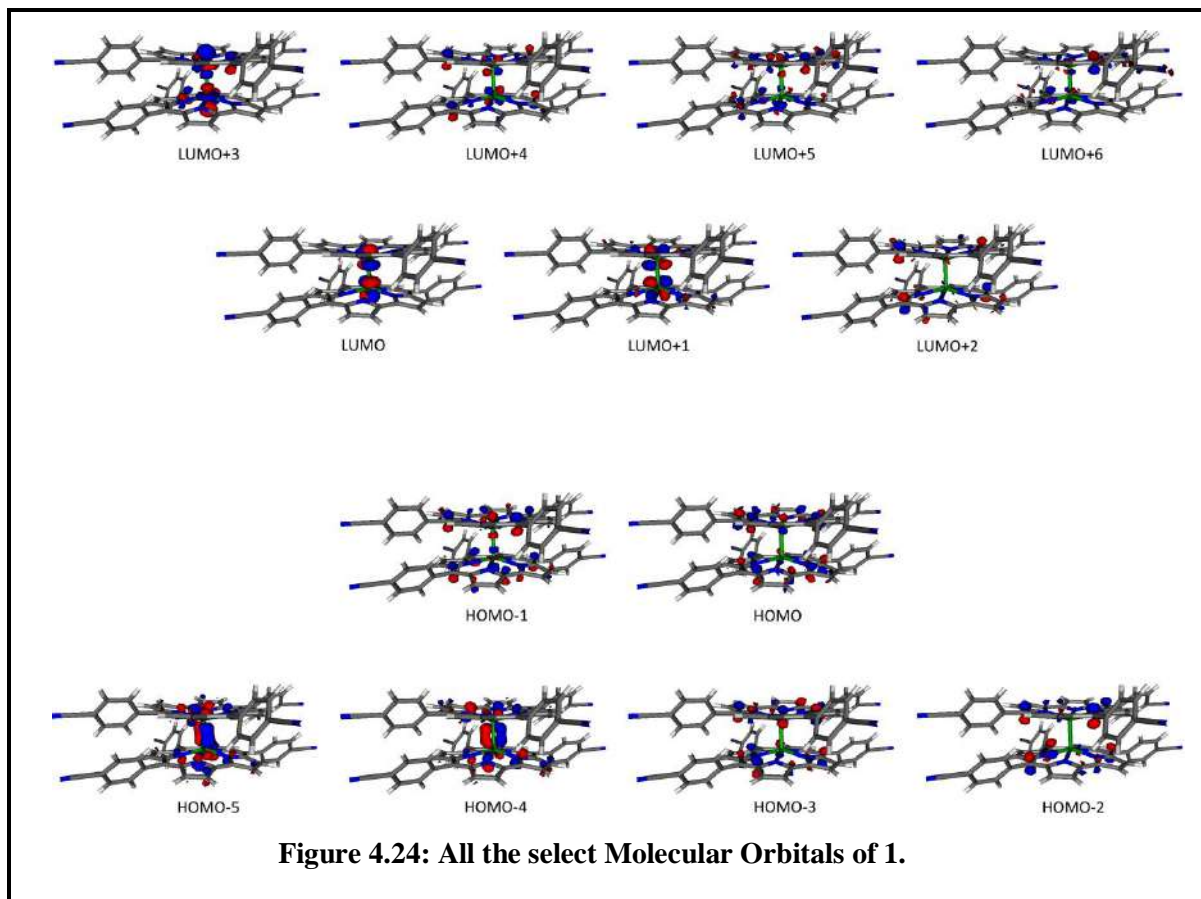


Table 4.7: Time-dependent density functional theory Calculated Electronic Transitions for 1^+

Compound	Contribution of excitation (%)	Transition wavelength (nm)	Oscillator strength	Exp. transition wavelength (nm)	Molar absorption coefficient, $M^{-1}cm^{-1}$
1^+	HOMO-1 $\beta \rightarrow$ LUMO β (95)	2404	0.033	2173	8400
	HOMO $\alpha \rightarrow$ LUMO+1 α (35)	972	0.010		
	HOMO $\beta \rightarrow$ LUMO+2 β (56)				
	HOMO-5 $\beta \rightarrow$ LUMO β (85)	758	0.055		
	HOMO-2 $\alpha \rightarrow$ LUMO+2 α (45)	618	0.046	530	20 300 sh
	HOMO-1 $\beta \rightarrow$ LUMO+4 β (33)				

	HOMO-5 $\alpha \rightarrow$ LUMO α (11)	535	0.028	403	63100 sh
	HOMO-4 $\alpha \rightarrow$ LUMO+1 α (11)				
	HOMO-4 $\beta \rightarrow$ LUMO+1 β (11)				
	HOMO-3 $\beta \rightarrow$ LUMO+2 β (15)				
	HOMO-2 $\beta \rightarrow$ LUMO+4 β (22)				
	HOMO-1 $\alpha \rightarrow$ LUMO+4 α (15)	537	0.125		
	HOMO-14 $\beta \rightarrow$ LUMO β (28)				
	HOMO-16 $\beta \rightarrow$ LUMO β (57)	534	0.049		
	HOMO-2 $\beta \rightarrow$ LUMO+4 β (27)	511	0.057		
	HOMO-5 $\alpha \rightarrow$ LUMO+1 α (19)	506	0.088		
	HOMO-4 $\beta \rightarrow$ LUMO+2 β (21)				

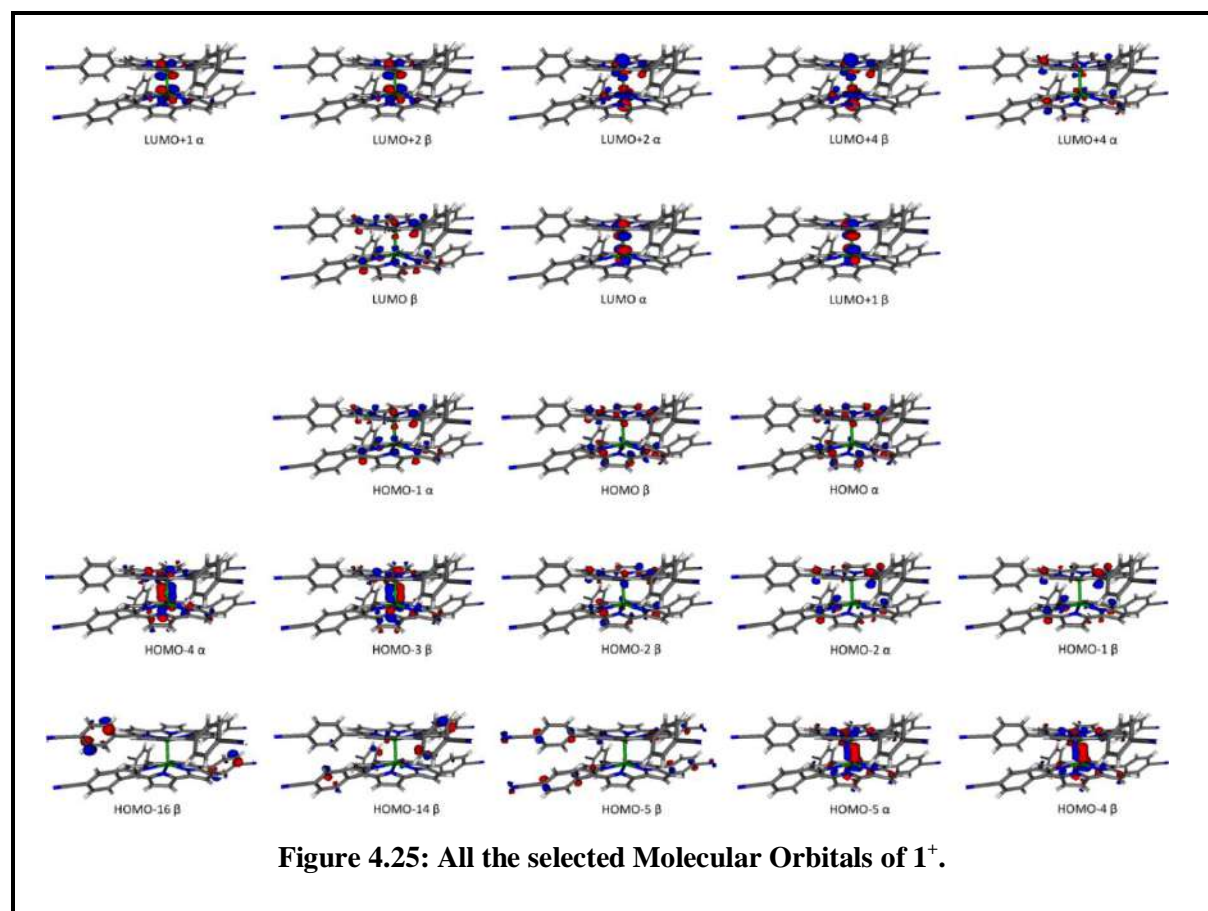


Table 4.8: Time-dependent density functional theory Calculated Electronic Transitions for 1⁺

Compound	Contribution of excitation (%)	Transition wavelength (nm)	Oscillator strength	Exp. transition wavelength (nm)	Molar absorption coefficient, M ⁻¹ cm ⁻¹
1 ⁺	HOMO β → LUMO+1 β (12)	761	0.007		
	HOMO β → LUMO+2 β (22)				
	HOMO-2 α → LUMO+3 α (16)	722	0.010		
	HOMO-1 β → LUMO+1 β (23)				
	HOMO-1 β → LUMO+2 β (13)				
	HOMO-2 β → LUMO β (15)	698	0.006		
	HOMO-1 β → LUMO+5 β (17)				
	HOMO-3 α → LUMO α (11)	695	0.007		
	HOMO-2 α → LUMO+1 α (11)				
	HOMO-2 β → (LUMO β) (18)				
	HOMO β → LUMO+5 β (18)				
	HOMO-2 α → LUMO+5 α (26)	563	0.044	569	20 800
	HOMO-1 α → LUMO+5 α (11)				
	HOMO β → LUMO+5 β (10)				
	HOMO-4 α → LUMO+2 α (28)	522	0.282		
	HOMO-2 α → LUMO+5 α (14)				
	HOMO-1 β → LUMO+6 β (11)				
	HOMO-4 α → LUMO+2 α (20)	512	0.050		
	HOMO α → LUMO+9 α (14)				
	HOMO-3 β → LUMO+3 β (35)				
	HOMO-2 β → LUMO+4 β (65)	498	0.044		

	HOMO-4 $\alpha \rightarrow$ LUMO+4 α (47)	479	0.131	442	89 400
	HOMO-3 $\beta \rightarrow$ LUMO+3 β (13)				
	Mixed	459	0.283		
	HOMO-4 $\beta \rightarrow$ LUMO+1 β (14)	456	0.137		
	HOMO-4 $\beta \rightarrow$ LUMO+5 β (21)				

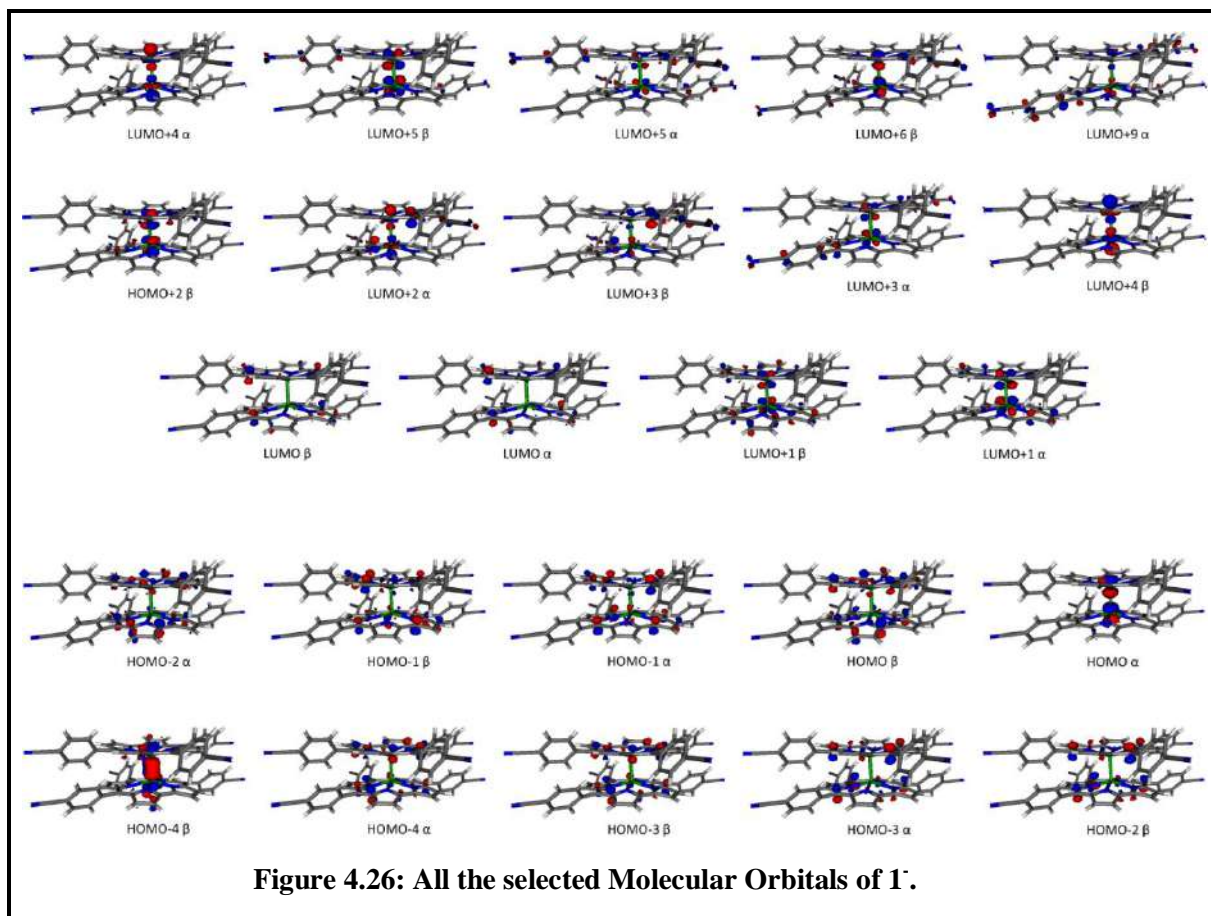


Table 4.9: Time-dependent density functional theory Calculated Electronic Transitions for 2

Compound	Contribution of excitation (%)	Transition wavelength (nm)	Oscillator strength	Exp. transition wavelength (nm)	Molar absorption coefficient, $M^{-1}cm^{-1}$
2	HOMO-1 \rightarrow LUMO+1 (83)	913	0.007	777	Weak sh
	HOMO \rightarrow LUMO+1 (82)	851	0.012		
	HOMO-2 \rightarrow LUMO+3 (75)	611	0.036	546	22 400

	HOMO-2 \rightarrow LUMO+2 (66)	608	0.035		
	HOMO-2 \rightarrow LUMO+3 (11)				
	HOMO-1 \rightarrow LUMO+4 (18)				
	HOMO-6 \rightarrow LUMO (45)	551	0.047	403	85 800
	HOMO-1 \rightarrow LUMO+4 (28)				
	HOMO-4 \rightarrow LUMO+2 (21)	526	0.123		
	HOMO-4 \rightarrow LUMO+3 (27)				
	HOMO-7 \rightarrow LUMO (12)	526	0.073		
	HOMO-5 \rightarrow LUMO+3 (15)				
	HOMO-4 \rightarrow LUMO+3 (22)				
	HOMO-7 \rightarrow LUMO+1 (69)	487	0.053		
	HOMO-6 \rightarrow LUMO (11)				
	HOMO-5 \rightarrow LUMO+5 (14)	471	0.137		
	HOMO \rightarrow LUMO+6 (61)				
	HOMO-4 \rightarrow LUMO+5 (26)	462	0.122		
	HOMO-2 \rightarrow LUMO+5 (21)				
	HOMO-1 \rightarrow LUMO+6 (16)				

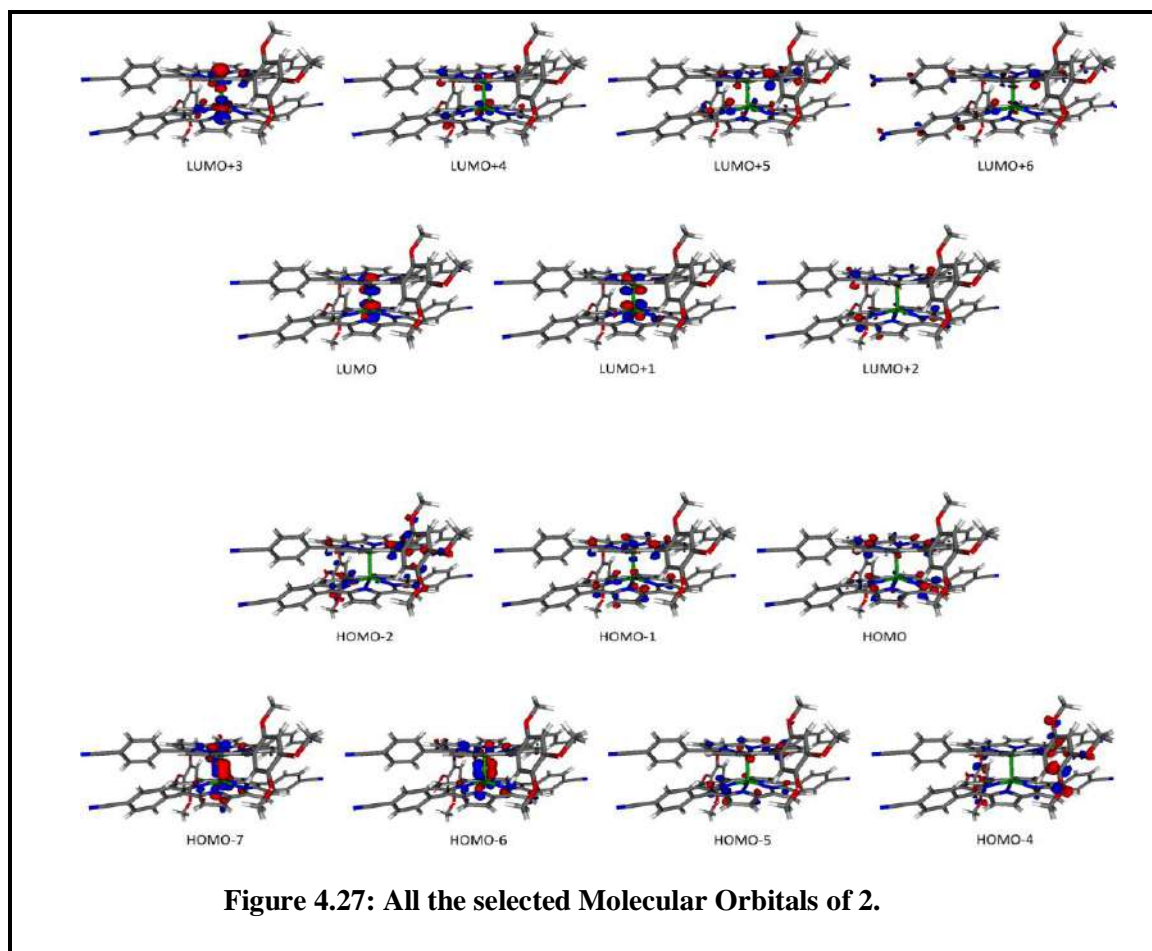
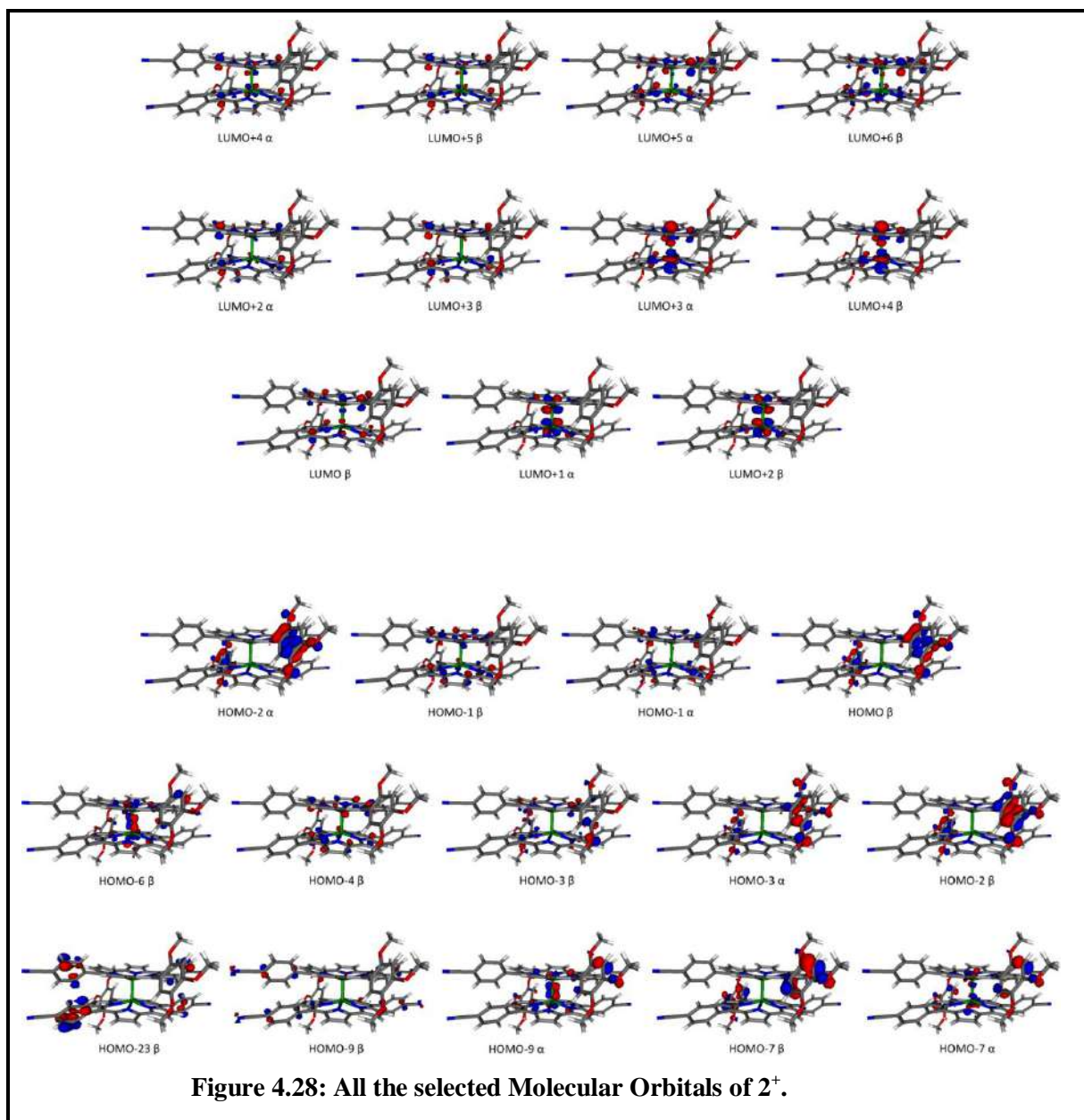


Table 4.10: Time-dependent density functional theory Calculated Electronic Transitions for 2⁺

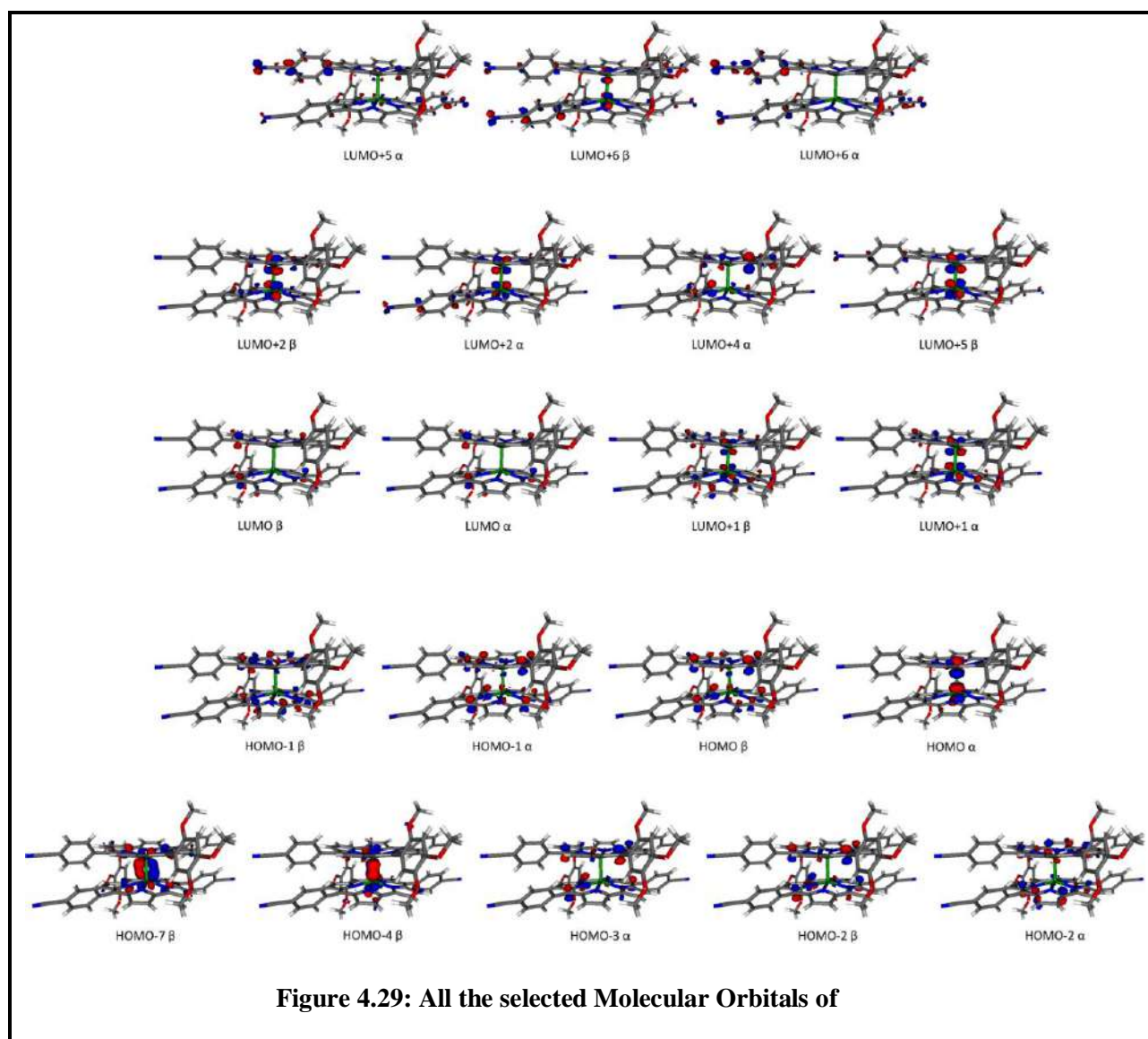
Compound	Contribution of excitation (%)	Transition wavelength (nm)	Oscillator strength	Exp. transition wavelength (nm)	Molar absorption coefficient, M ⁻¹ cm ⁻¹
2 ⁺	HOMO-3 β → LUMO β (94)	1965	0.045	2315	3 600
	HOMO-4 β → LUMO β (98)	1675	0.006		
	HOMO-1 α → LUMO+1 α (27)	952	0.011	1064	2 000
	HOMO-1 β → LUMO+2 β (53)				
	HOMO-9 β → LUMO β (13)	751	0.012		
	HOMO -7 β → LUMO β (60)				
	HOMO-9 β → LUMO β (51)	738	0.018		
	HOMO -7 β → LUMO β (30)				

	HOMO-2 $\alpha \rightarrow$ LUMO+2 α (68)	705	0.053		
	HOMO $\beta \rightarrow$ LUMO+3 β (18)				
	HOMO-2 $\alpha \rightarrow$ LUMO+3 α (34)	696	0.083		
	HOMO $\beta \rightarrow$ LUMO+4 β (49)				
	HOMO-2 $\alpha \rightarrow$ LUMO+5 α (28)	524	0.033	531	20 800
	HOMO-4 $\beta \rightarrow$ LUMO+3 β (15)				
	HOMO $\beta \rightarrow$ LUMO+6 β (12)				
	HOMO-4 $\beta \rightarrow$ LUMO+4 β (50)	532	0.061		
	HOMO-3 $\alpha \rightarrow$ LUMO+4 α (28)	500	0.067		
	HOMO-2 $\beta \rightarrow$ LUMO+4 β (53)				
	HOMO-23 $\beta \rightarrow$ LUMO β (16)	486	0.066		
	HOMO-3 $\beta \rightarrow$ LUMO+6 β (28)				
	HOMO-9 $\alpha \rightarrow$ LUMO+1 α (14)	505	0.035		
	HOMO-7 $\alpha \rightarrow$ LUMO+1 α (12)				
	HOMO-6 $\beta \rightarrow$ LUMO+2 β (22)				

**Table 4.11: Time-dependent density functional theory Calculated Electronic Transitions for 2⁻**

Compound	Contribution of excitation (%)	Transition wavelength (nm)	Oscillator strength	Exp. transition wavelength (nm)	Molar absorption coefficient, M ⁻¹ cm ⁻¹
2 ⁻	HOMO-1 α → LUMO+1 α (20)	789	0.007	750	Weak sh
	HOMO-1 α → LUMO+2 α (15)				
	HOMO β → LUMO+1 β (27)				
	HOMO-2 α → LUMO+2 α (19)	724	0.008		

	HOMO -1 $\beta \rightarrow$ LUMO+1 β (21)				
	HOMO-3 $\alpha \rightarrow$ LUMO α (11)	710	0.006		
	HOMO-2 $\beta \rightarrow$ LUMO β (32)				
	HOMO $\beta \rightarrow$ LUMO+1 β (18)				
	HOMO $\beta \rightarrow$ LUMO+5 β (16)				
	HOMO-2 $\alpha \rightarrow$ LUMO+1 α (22)	698	0.012		
	HOMO-1 $\beta \rightarrow$ LUMO+5 β (18)				
	HOMO-2 $\alpha \rightarrow$ LUMO+5 α (18)	581	0.025	567	23 600
	HOMO $\alpha \rightarrow$ LUMO+6 α (47)				
	mixed	575	0.035		
	HOMO-2 $\alpha \rightarrow$ LUMO+5 α (22)	574	0.046		
	HOMO $\alpha \rightarrow$ LUMO+6 α (45)				
	HOMO-7 $\beta \rightarrow$ LUMO+2 β (17)	571	0.032		
	HOMO-4 $\beta \rightarrow$ LUMO+2 β (12)				
	HOMO-1 $\beta \rightarrow$ LUMO+5 β (17)				
	HOMO-1 $\beta \rightarrow$ LUMO+6 β (14)				
	mixed	556	0.074		
	HOMO-7 $\beta \rightarrow$ LUMO+2 β (25)	526	0.112	430	73 100
	HOMO-1 $\beta \rightarrow$ LUMO+6 β (25)				
	HOMO-2 $\alpha \rightarrow$ LUMO+5 α (26)	522	0.235		
	HOMO-1 $\beta \rightarrow$ LUMO+6 β (25)				
	HOMO-3 $\alpha \rightarrow$ LUMO+4 α (29)	518	0.057		
	HOMO-1 $\alpha \rightarrow$ LUMO+5 α (19)				
	HOMO-1 $\beta \rightarrow$ LUMO+6 β (11)				
	mixed	507	0.067		



4.7 Details for the calculation of redox potentials:

The redox potentials E versus the Fc/Fc^+ couple were calculated on the BP86 level of theory from the differences of gibbs free enthalpies (ΔG) of the respective oxidation sates (including solvation effects by means of COSMO) according to $\Delta G = -FE$ with the Faraday constant F and subtraction of the absolute potential of 4.6488 V of the Fc/Fc^+ couple (4.1888 V for saturated calomel electrode (SCE)²⁵¹ and 0.46 V for Fc/Fc^+ vs SCE²⁵²) (Table 4.12).

Table 4.12: Gibbs free enthalpies used for calculation of redox potentials.

Compound	gibbs free enthalpy / Eh
1⁺	-13001.71520
1	-13001.90999
1⁻	-13002.04481
2⁺	-13504.97589
2	-13505.15962
2⁻	-13505.28693

Chapter Five

Isovalent Ag^{III}/Ag^{III}, Ag^{II}/Ag^{II}, Mixed-valent Ag^{II}/Ag^{III} and Corrolato-Based Mixed-Valency in β,β' Linked [Bis{corrolato-silver}]ⁿ Complexes

5.1 Introduction

5.2 Synthetic Discussion

5.3 Spectral Characterizations

5.3.1 Crystal Structure

5.3.2 NMR Spectroscopy

5.3.3 Mass Spectroscopy

5.3.4 Electrochemistry

5.3.5 EPR Spectroscopy

5.3.6 Löwdin Spin population analysis

5.3.7 UV/Vis-NIR spectroscopy

5.4 Conclusion

5.5 Experimental Section

5.5.1 Syntheses

5.5.1.1 3,3'-Bis(5,10,15-tris(pentafluorophenyl)corrole, 1A

5.5.1.2 3,3'-Bis{(5,10,15-tris(pentafluorophenyl)corrolato-silver(III))}, 1

5.5.2 Determination of the X-Ray Crystal Structure

5.6 General Remarks and Instrumentation

5.6.1 Details of all materials used

5.6.2 Physical Studies

5.6.3 Cyclic Voltammetry

5.6.4 Spectroelectrochemistry

5.6.5 Electron Paramagnetic Resonance

5.6.6 Computational Details

5.7 TD-DFT Calculations

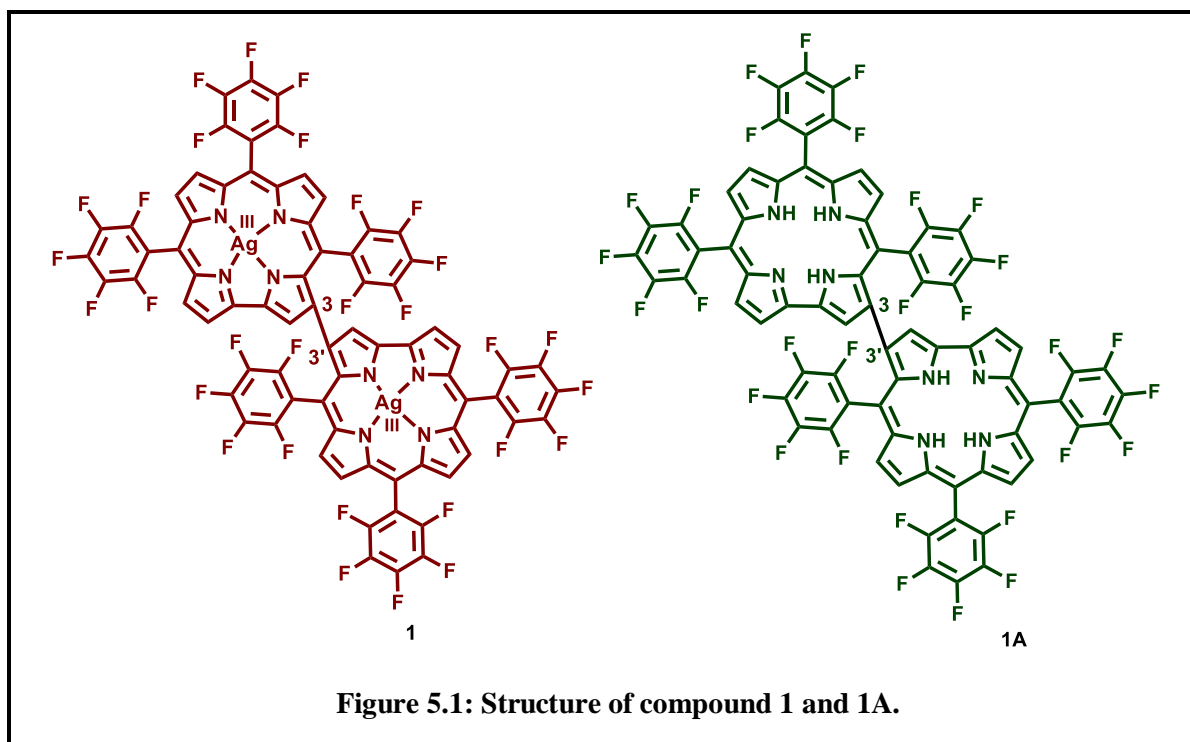
5.8 Gouterman Orbitals for the Monomer and Dimer

5.1 Introduction:

Mixed-valent compounds impart intense colours to certain minerals,²⁵³ are useful for understanding electron-transfer properties in many metallo-proteins,^{228,254-259} and are invoked for explaining the high electrical conductivities in certain solids.²⁶⁰ As the variable valency is a prerequisite for mixed-valency, most d-block transition elements show mixed-valency in various coordination complexes and in certain metal salts. In biology, the Cu_A center (mixed-valent dicopper unit) facilitates efficient electron transfer.^{261,262} In analogy to the mixed-valent dicopper complexes, there are few examples of discrete Ag^I/Ag^{II} species for the higher congener.^{263,264} There are only few reports on mixed-valent Ag^{II}/Ag^{III} species and iso-valent Ag^{II}/Ag^{II} species in discrete coordination complexes.^{265,266} However, to the best of our knowledge, the spectroscopic nature of such Ag^{II}/Ag^{III} compounds were never investigated before. In this context, it is worthwhile to mention that the various mixed-valent species in silver complexes are still in their infancy. It has been described earlier that the mixed-valent Ag^I/Ag^{II} and Ag^{II}/Ag^{III} are indeed very difficult to generate.²⁶⁷⁻²⁶⁹ Based on theoretical considerations, Hoffmann et al. have reported that Ag^{II}/Ag^{III} fluoride systems may have applications in superconductors.²⁶⁷⁻²⁶⁹ Both Ag^{II} and Ag^{III} are known to be potent oxidizing agents in solvated conditions.²⁶⁷⁻²⁶⁹ In the solid state, such species are usually stabilized by using fluorido ligands.²⁶⁷⁻²⁶⁹ It was recently shown that a corrolato core provides a good environment for stabilizing both mononuclear Ag^{III} and mononuclear Ag^{II} in discrete molecular complexes.^{96,270}

In porphyrinoid chemistry, there has long been widespread research interest in multiple porphyrin-based systems^{169, 272-289} due to their superior performances in many areas, such as catalysis, photonic devices, and molecular-recognition, and very often they are considered to be superior to their monomeric analogues. Even though the ring-contracted corrole system displays many different properties compared to their porphyrin analogues,^{100,150-152,154-163,290-292} multiple corrole-based systems have been less well explored.²⁹³⁻²⁹⁶ To the best of our knowledge, spectroscopic properties of corrolato-based mixed-valency in bis-corrolato systems have never been investigated before.²⁶⁵ Such investigations are vital for the understanding of electron/hole (de)localization that will play an

important role in the future development of molecular electronics. Based on our recent observation that discrete mononuclear Ag^{II} and Ag^{III} complexes can be stabilized within a mono-corrolato framework,⁹⁶ we have now turned our attention to a bis-corrolato unit. In the following, we present the synthesis of a new β,β' (3,3')-linked bis{corrolato-silver(III)} complex, **1**, and show that this



core is ideal for the stabilization and investigation of the isovalent $\text{Ag}^{\text{III}}/\text{Ag}^{\text{III}}$ and $\text{Ag}^{\text{II}}/\text{Ag}^{\text{II}}$ forms. Additionally, the same core allows us to access the mixed-valent $\text{Ag}^{\text{II}}/\text{Ag}^{\text{III}}$ combination, as well as ligand-centered corrolato-based mixed-valency. Results from a combined synthetic, crystallographic, electrochemical, spectro-electrochemical (UV/Vis-NIR and EPR) and DFT investigation are presented below.

5.2 Synthetic Discussion:

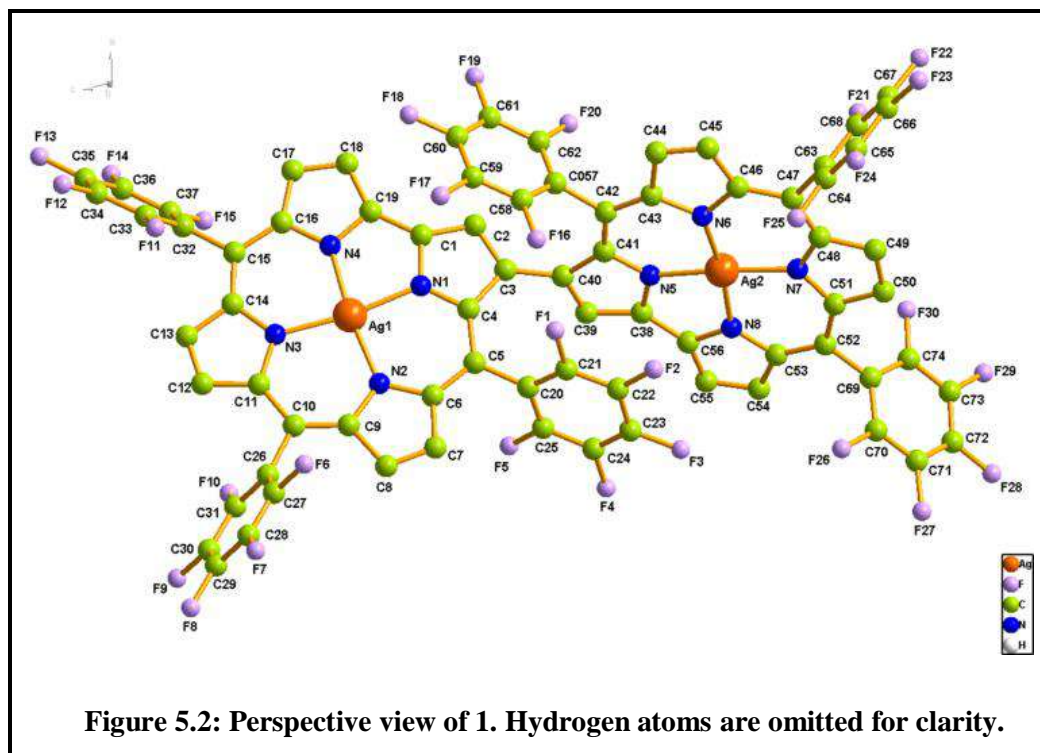
The free base (FB) ligand 3,3'-bis(5,10,15-tris(pentafluorophenyl) corrole, **1A** was prepared by following a synthetic strategy developed earlier by Osuka et al.²⁹⁵ (Figure 5.1). The β,β' (3,3')-linked bis{corrolato-silver(III)} complex, **1** (Figure 5.1), was synthesized by following a general synthetic procedure for the silver metallation.^{96,270,271} The corresponding FB corrole (**1A**) was dissolved in excess triethylamine and was stirred with excess silver acetate. This reaction led to the generation of

complex **1** in good yield. Composition and purity of complex **1** were determined by elemental analyses, $^1\text{H}/^{19}\text{F}$ -NMR spectroscopy and ESI mass spectrometry.

5.3 Spectral Characterizations:

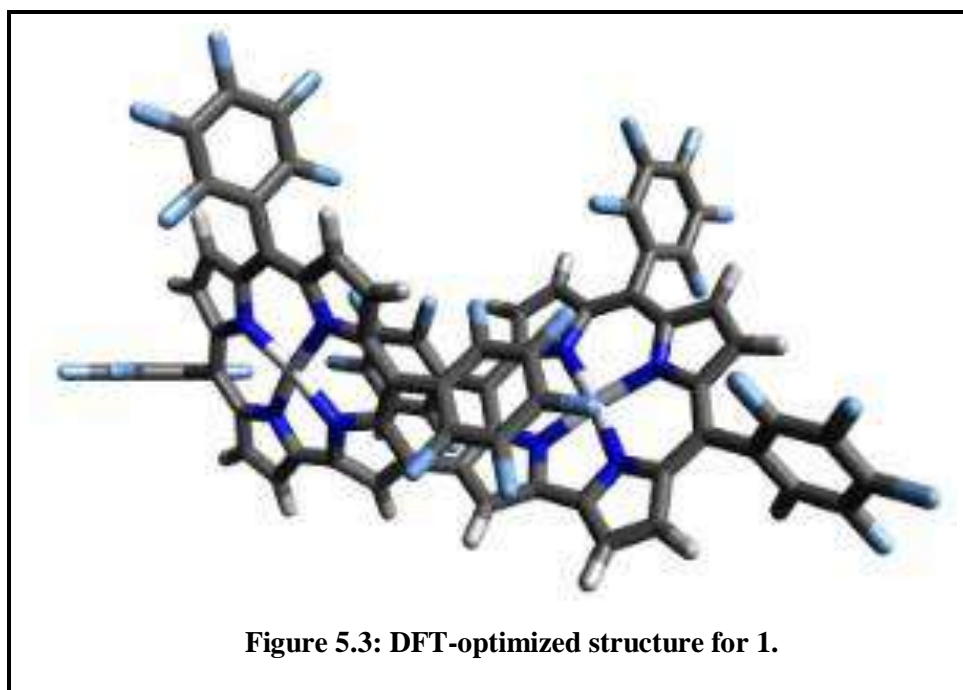
5.3.1 Crystal Structure:

The molecular structure in the crystal of **1** is shown in Figure 5.2. The bond lengths and angles in **1** are comparable with the previously reported monomeric corrolato-silver(III) complexes.^{96,270,271} The central silver atoms in **1** fit well into the cavity of the corrolato rings in a slightly distorted square planar geometry with minimal deviations of 0.007 Å (DFT: 0.03 Å) and 0.005 Å (DFT: 0.03 Å) from the respective N_4 planes. The distortions in both the rings from the ideal ones are due to slight deviations in the bite angles of N-Ag-N in the ranges of 81.3–96.68° (DFT: 80.6–95.88°) and 80.3–95.18° (DFT: 80.8–95.48°), respectively. As a consequence, the pyrrole ring nitrogen atoms of both the rings are tilted with respect to the mean corrolato planes (19-atom corrole ring) by distances varying from (–0.12) Å to (+0.01) Å and (–0.06) Å to (+0.09) Å alternately. The average of Ag–N



distances in **1** is 1.935 Å (DFT: 1.96 Å) and is on a par with the earlier reported characteristic Ag^{III} –N bonds.^{96,270,271} The meso-substituted phenyl groups at –5, –10, and –15 positions of both the rings

display dihedral angles of 62.68°, 65.18°, and 66.28° and 76.58°, 78.58°, and 86.98°, respectively, with the mean corrolato plane. The dihedral angle between the two corrolato rings is 64.48° (DFT: 50.38°). The C–C bond connecting the two corrolato units is 1.46 Å (DFT: 1.45 Å), which is shorter than the typical sp^3 – sp^3 distance (1.54 Å). The closest Ag...F distance is 3.55 Å (DFT: 3.40 Å), and thus it is non-bonding in nature. Both the experimental and the DFT optimized structure clearly display the twisting of the corrolato rings with respect to each other. Furthermore, in the DFT



optimized structure, the two rings slightly fold and approach each other (Figure 5.3), a fact that is not observed in the experimental structure. By taking the NMR and the crystallographic data into consideration, **1** can be best described as a $[Ag^{III}(cor^{3-})-(cor^{3-})Ag^{III}]$ dimer.

5.3.2 NMR Spectroscopy:

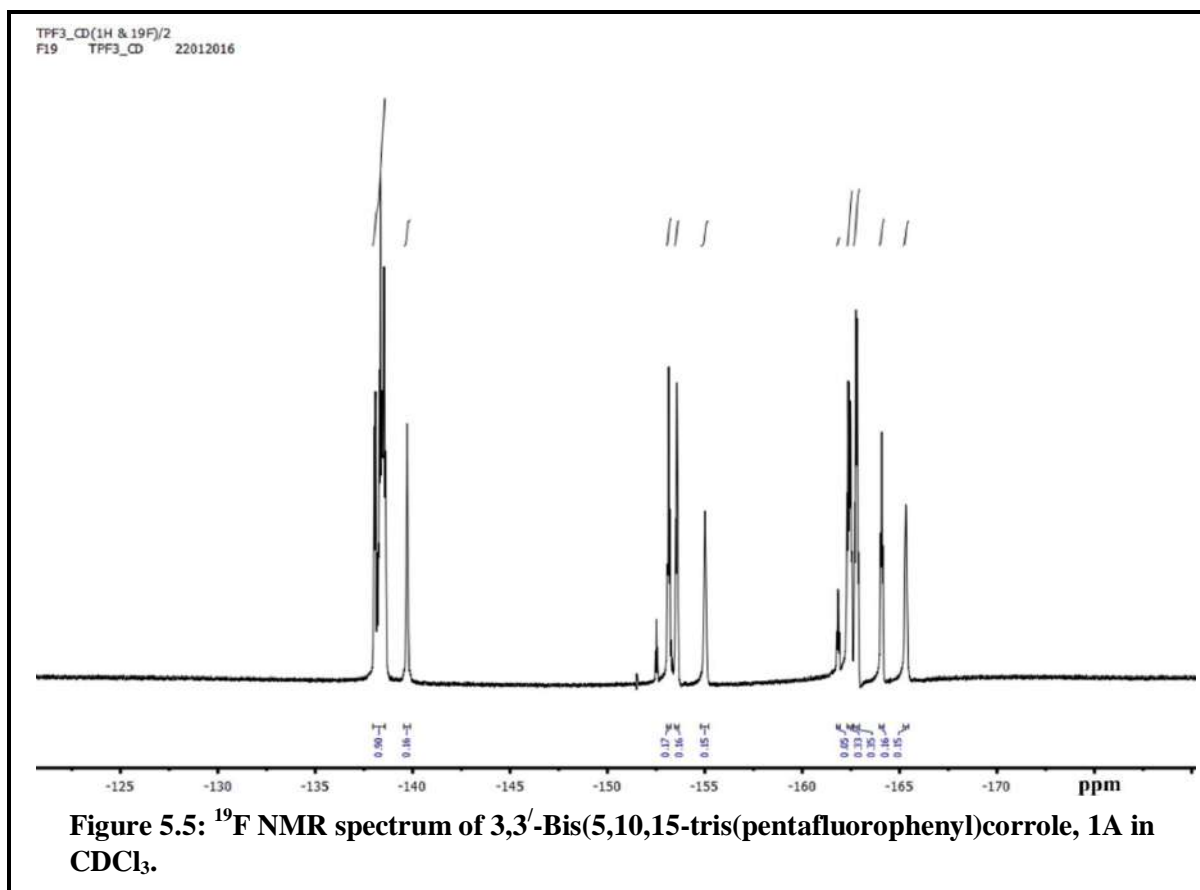
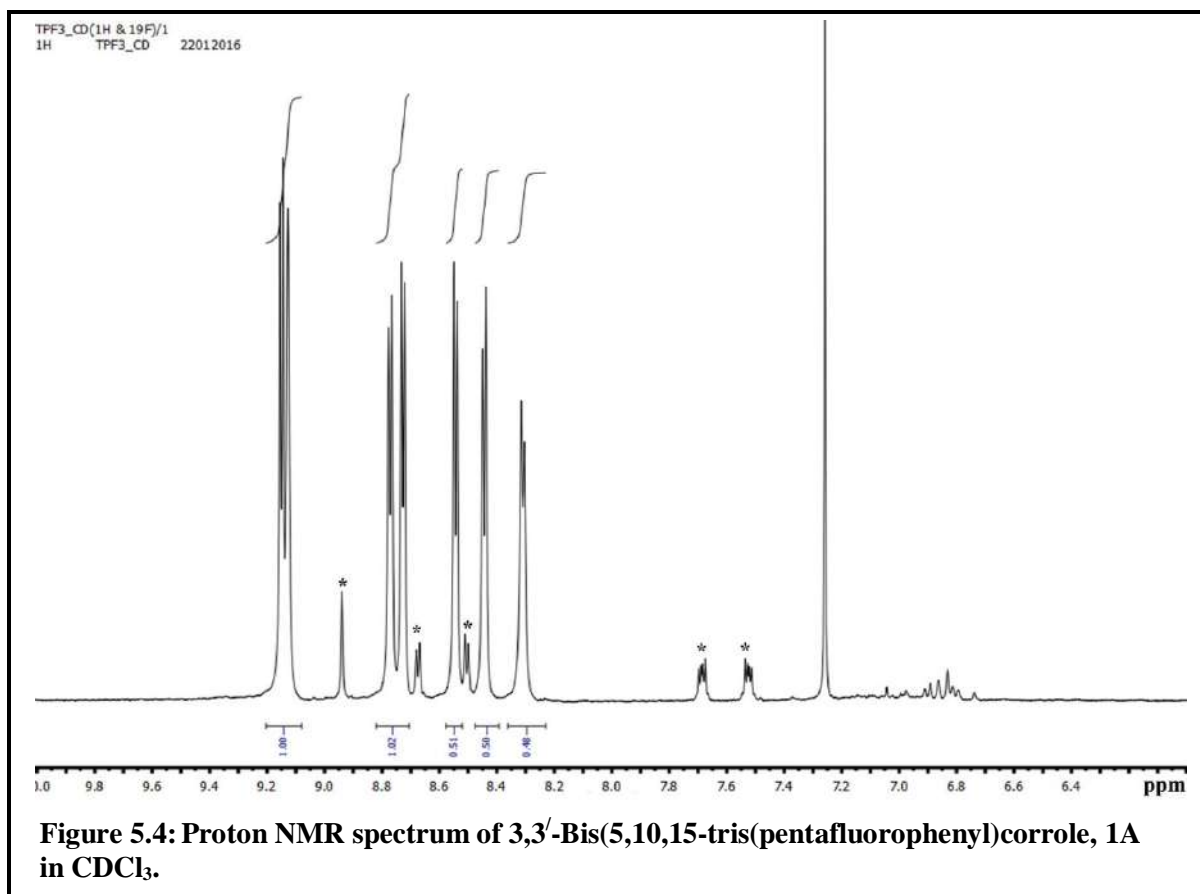
The 1H NMR spectrum of complex **1** exhibited sharp lines and also a significant deshielding of the β -pyrrolic protons (in comparison to the FB corrole, **1A**) and these observations are in line with the diamagnetic character of the complex **1** (Figure 5.4-5.7).

Table 5.1: X-Ray Crystallographic data for complex 1.

Molecular formula	C₇₄H₁₄Ag₂F₃₀N₈
Fw	1800.67
Radiation	MoK α
crystal symmetry	Triclinic
space group	<i>P</i> -1
α (Å)	11.938(5)
β (Å)	14.496(5)
γ (Å)	23.161(5)
α (deg)	107.127(5)
β (deg)	100.571(5)
γ (deg)	96.209
V (Å ³)	3708.8(20)
Z	2
μ (mm ⁻¹)	0.652
<i>T</i> (K)	100K
D_{calcd} (g cm ⁻³)	1.61233
2θ range (deg)	5.52 to 51.50
<i>e</i> data (R_{int})	13666 (0.095)
R1 ($I > 2\sigma(I)$)	0.0735
WR2	0.2013
GOF	1.000

5.3.3 Mass Spectroscopy:

The electrospray mass spectrum of the complex **1A** shows intense peak centred at m/z : calcd for C₇₄H₂₀F₃₀N₈ (**1A**): 1590.13; found: 1591.72 [M+H]⁺; (Figure 5.8). In case of complex **1**, the electrospray mass spectrum is measured in acetonitrile solvent which leads to the generation of intense peak centred at m/z : calcd for C₇₄H₁₄F₃₀N₈Ag₂ (**1**): 1797.90; found: 1796.87 [M-H]⁺ (Figure 5.9).



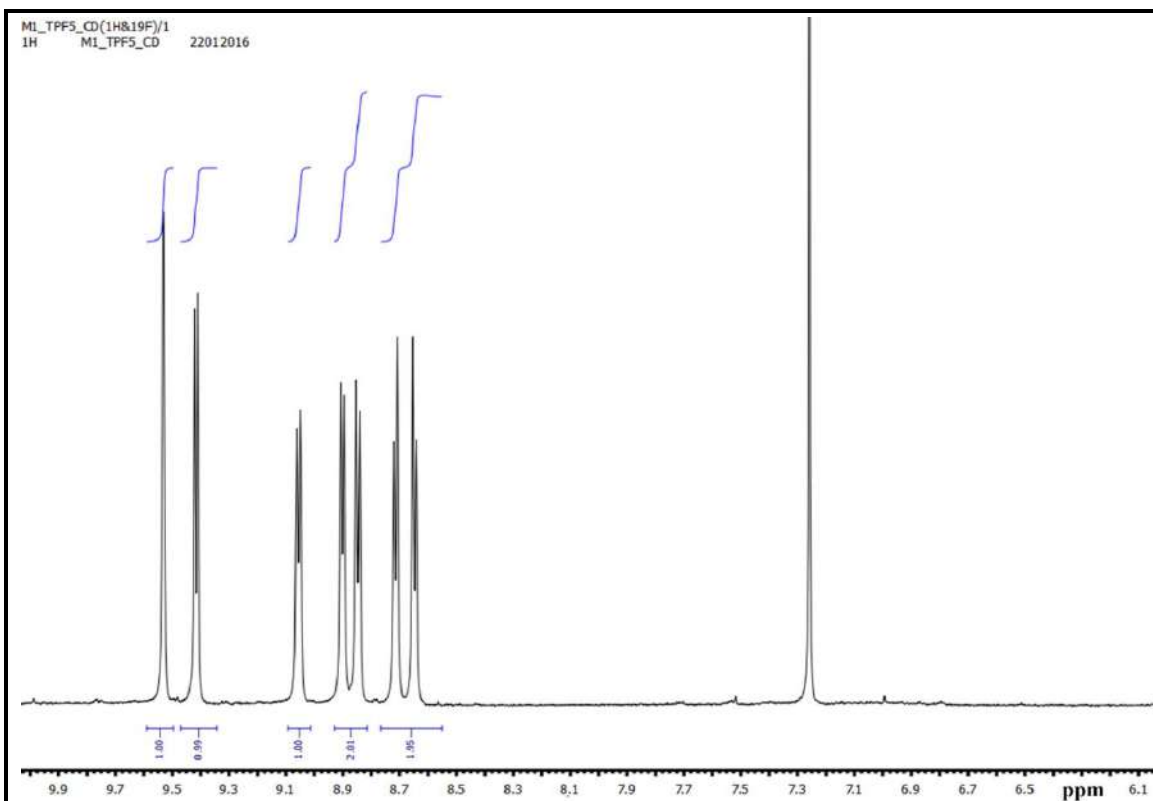


Figure 5.6: ^1H NMR spectrum of 3,3'-Bis{(5,10,15-tris(pentafluorophenyl)corrolato)silver(III)}, 1 in CDCl_3 .

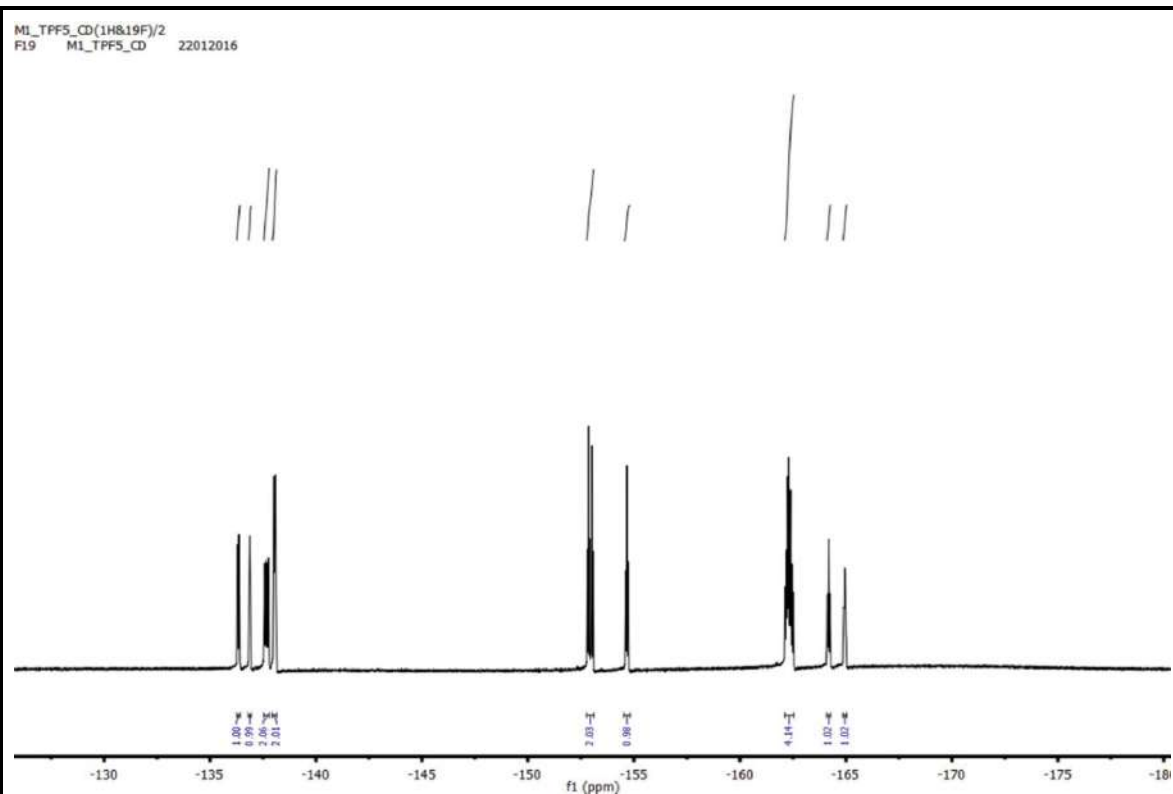


Figure 5.7: ^{19}F NMR spectrum of 3,3'-Bis{(5,10,15-tris(pentafluorophenyl)corrolato)silver(III)}, 1 in CDCl_3 .

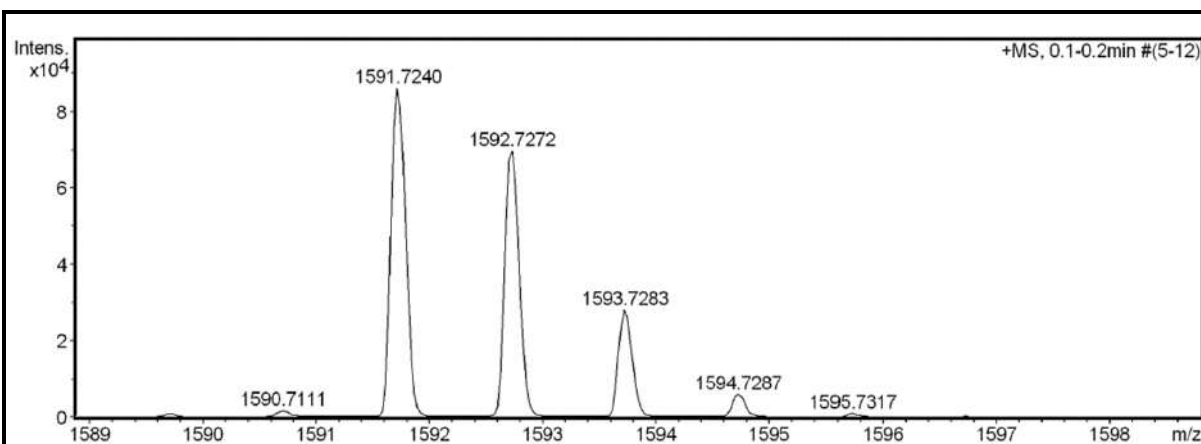


Figure 5.8: ESI-MS spectrum of 3,3'-Bis(5,10,15-tris(pentafluorophenyl)corrole, **1A** in CH₃CN display the studied spectrum with isotopic distribution pattern.

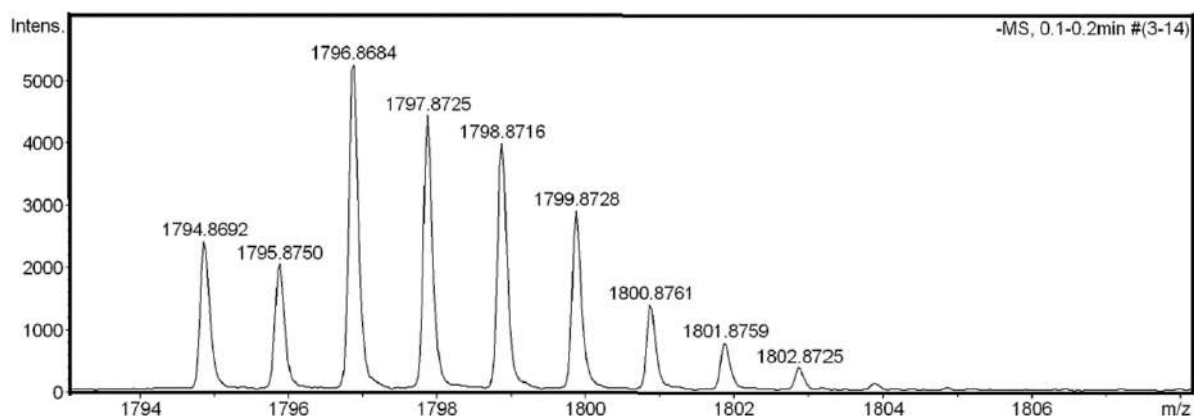
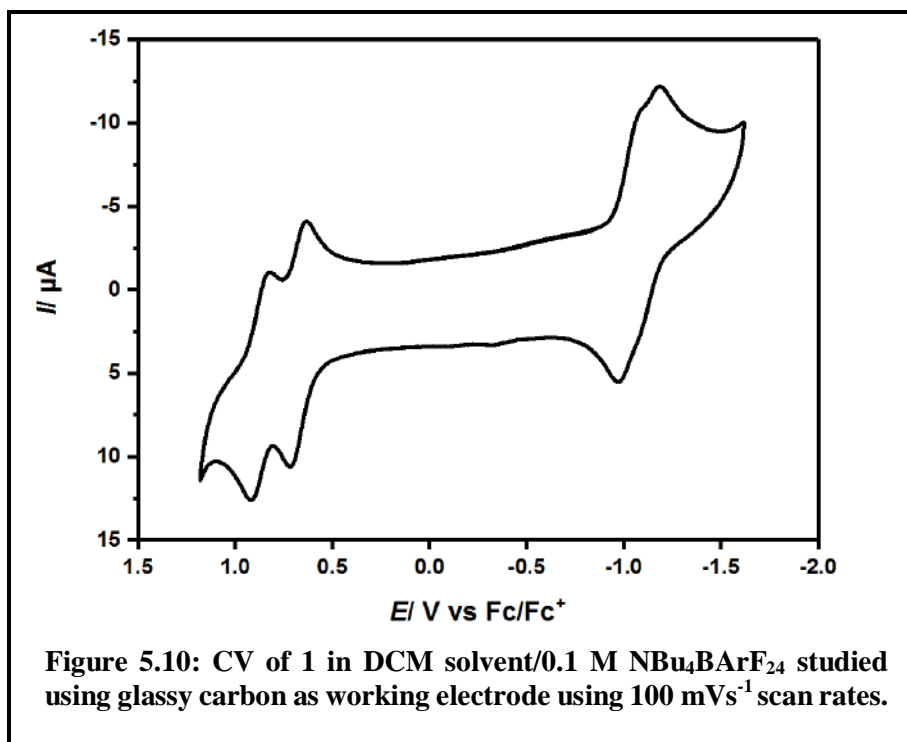


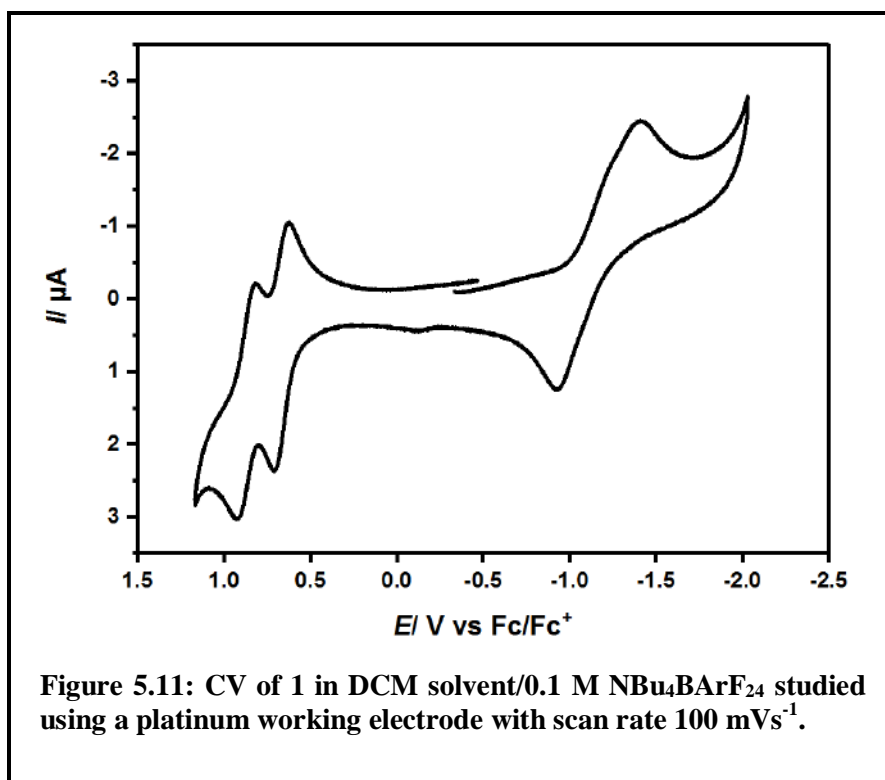
Figure 5.9: ESI-MS spectrum of 3,3'-Bis{(5,10,15-tris(pentafluorophenyl)corrolato-silver(III))}, **1** in CH₃CN display the studied spectrum with isotopic distribution pattern.

5.3.4 Electrochemistry:

The cyclic voltammogram and the differential pulse voltammogram of complex **1** were measured in CH₂Cl₂ using a range of electrolytes and working electrodes (Figure 5.10-5.11). Under every condition, **1** displayed two one-electron oxidations, and two one-electron reductions. The separation between the two one electron oxidation steps is 210, 150, and 120 mV in Bu₄NBArF₂₄, Bu₄NPF₆, and Bu₄NClO₄ as supporting electrolytes, thus displaying the utility of weakly coordinating anions in stabilizing the one-electron oxidized species. The comproportionation constant (K_c) for the one-electron oxidized form in CH₂Cl₂/Bu₄NBArF₂₄ is 3.5×10^3 , which points to a moderate thermodynamic stability of the one-electron oxidized form. The separation between the two reduction



steps was strongly dependent on the nature of the working electrode, with very little separation between the waves observed when using a Pt working electrode (Figure 5.11). With a glassy carbon



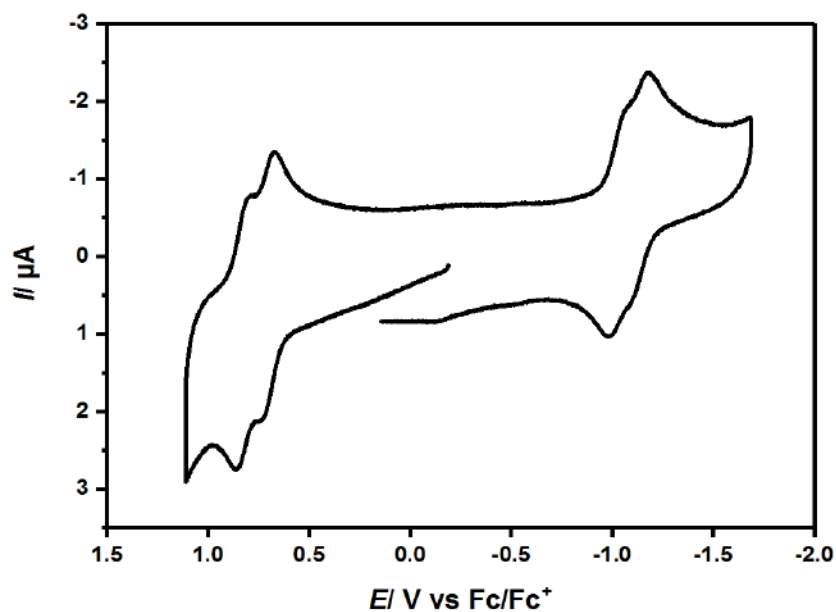


Figure 5.12: CV of 1 in DCM solvent/0.1 M NBu_4BPF_6 measured using glassy carbon working electrode using 100 mVs^{-1} scan rate.

working electrode, two one-electron reduction steps were observed, and as expected for reductive processes, the separation between these waves was found to be virtually independent of the nature of the three aforementioned electrolytes. The separation of 140 mV between the reduction steps

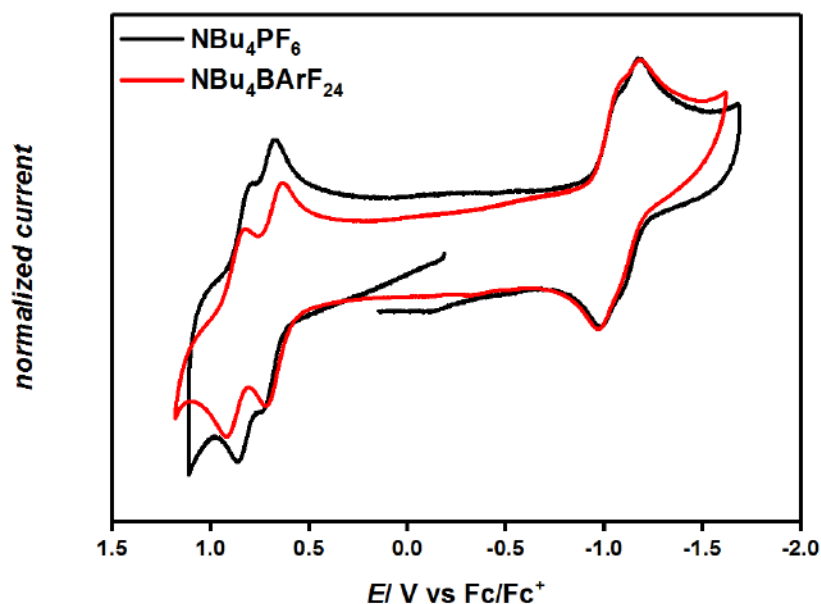


Figure 5.13: Comparison of CV of 1 measured with different electrolytes. For comparative reasons the current has been normalized to unity.

translates into a K_c of 2.3×10^2 for the one-electron reduced species. As has been shown before,^{228,254-259} K_c is a complex parameter that depends on many different factors. For the one electron reduced form, the main contribution to K_c is likely mostly electrostatic in nature, as there is no observable electronic coupling for this case. The thermodynamic stability of the one-electron oxidized form is an order of magnitude higher than that of the one-electron reduced form.

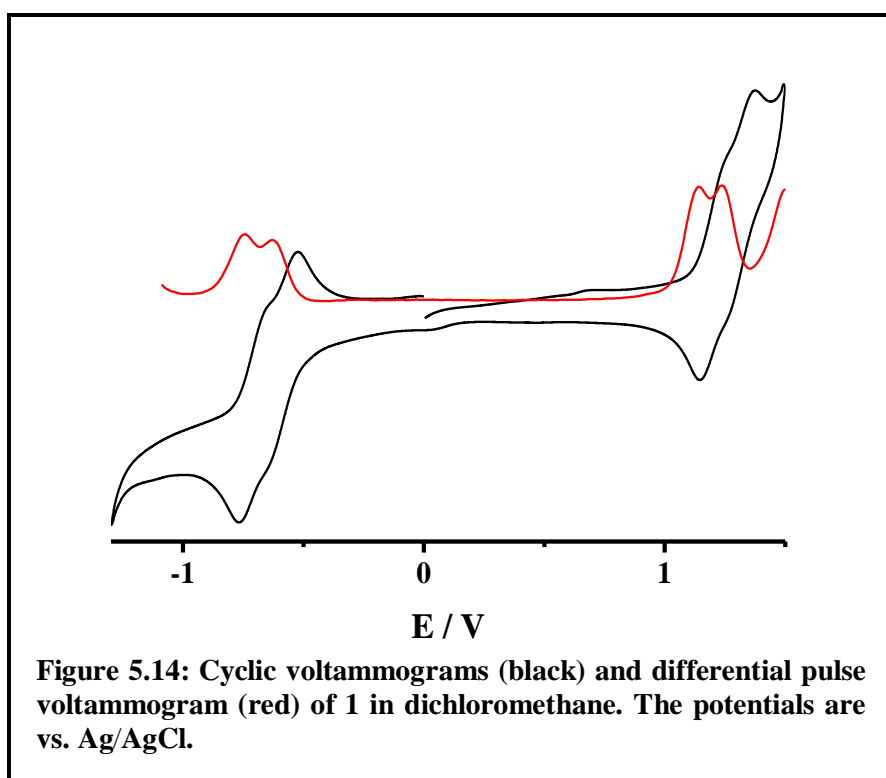
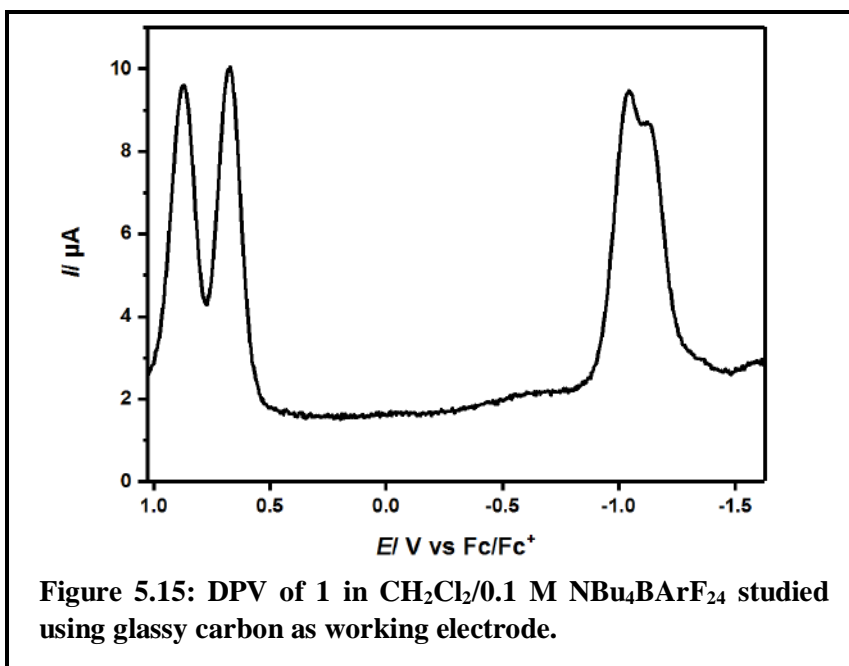


Table 5.2: Electrochemical data for **1**

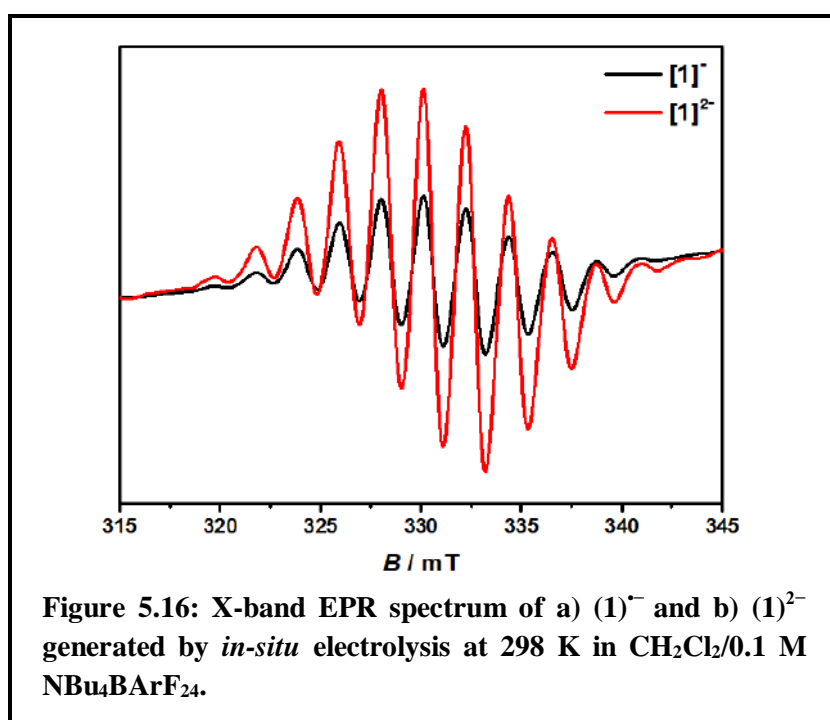
	E_{PtWE} (Peak to Peak separation) with NBu₄BArF₂₄	E_{GcWE} (Peak to Peak separation) with NBu₄BArF₂₄	E_{GcWE} (Peak to Peak separation) with NBu₄PF₆	E_{PtWE} with Bu₄NClO₄
E _{ox1}	0.67 (89)	0.66 (78)	0.71 (80)	0.67
E _{ox2}	0.87 (108)	0.87 (92)	0.86 (70)	0.79
E _{red1}	1.17	-1.12 (216 for both)	-1.12 (216 for both)	-1.10
E _{red2}	--	-1.25 determined from dpv	-1.24 determined from dpv	-1.24

*The values for the oxidation potentials and especially the corresponding Peak to Peak separation are quite error-prone due to close lying redox events.



5.3.5 EPR Spectroscopy:

The diamagnetic nature of the 3,3'-bis{corrolato-silver(III)} complex, **1** is concluded based on its ¹H NMR spectrum. Accordingly, **1** is EPR silent. The in situ generated one-electron reduced species (**1**)^{•−} in CH₂Cl₂/0.1M NBu₄BArF₂₄ displays a line rich EPR spectrum centered at g=2.044 at 298 K (Figure 5.16). The deviation of the g-value from the free-electron g of 2.0023 already points to substantial



metal participation at the singly occupied molecular orbital. This spectrum can be simulated by considering hyperfine coupling to four ^{14}N ($I=1$) nuclei and also to ^{107}Ag ($I=1/2$, natural abundance: 52%) and ^{109}Ag ($I=1/2$, natural abundance: 48%, Table 5.3). The simulated spectrum reproduced the experimental spectrum with excellent accuracy (Figure 5.17). The hyperfine coupling constant to the silver center obtained from the simulation is 42.9 G and further confirms the substantial spin

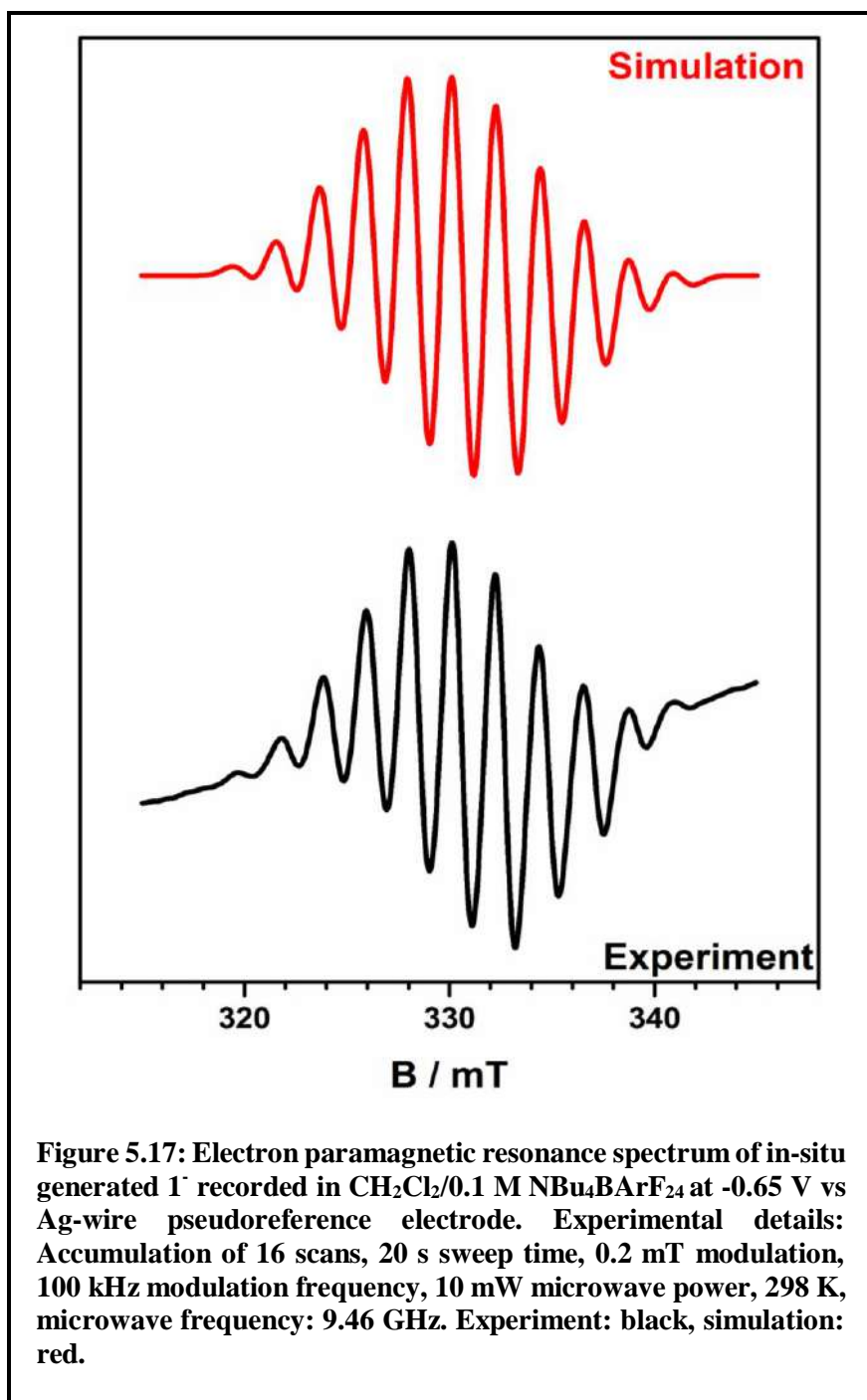
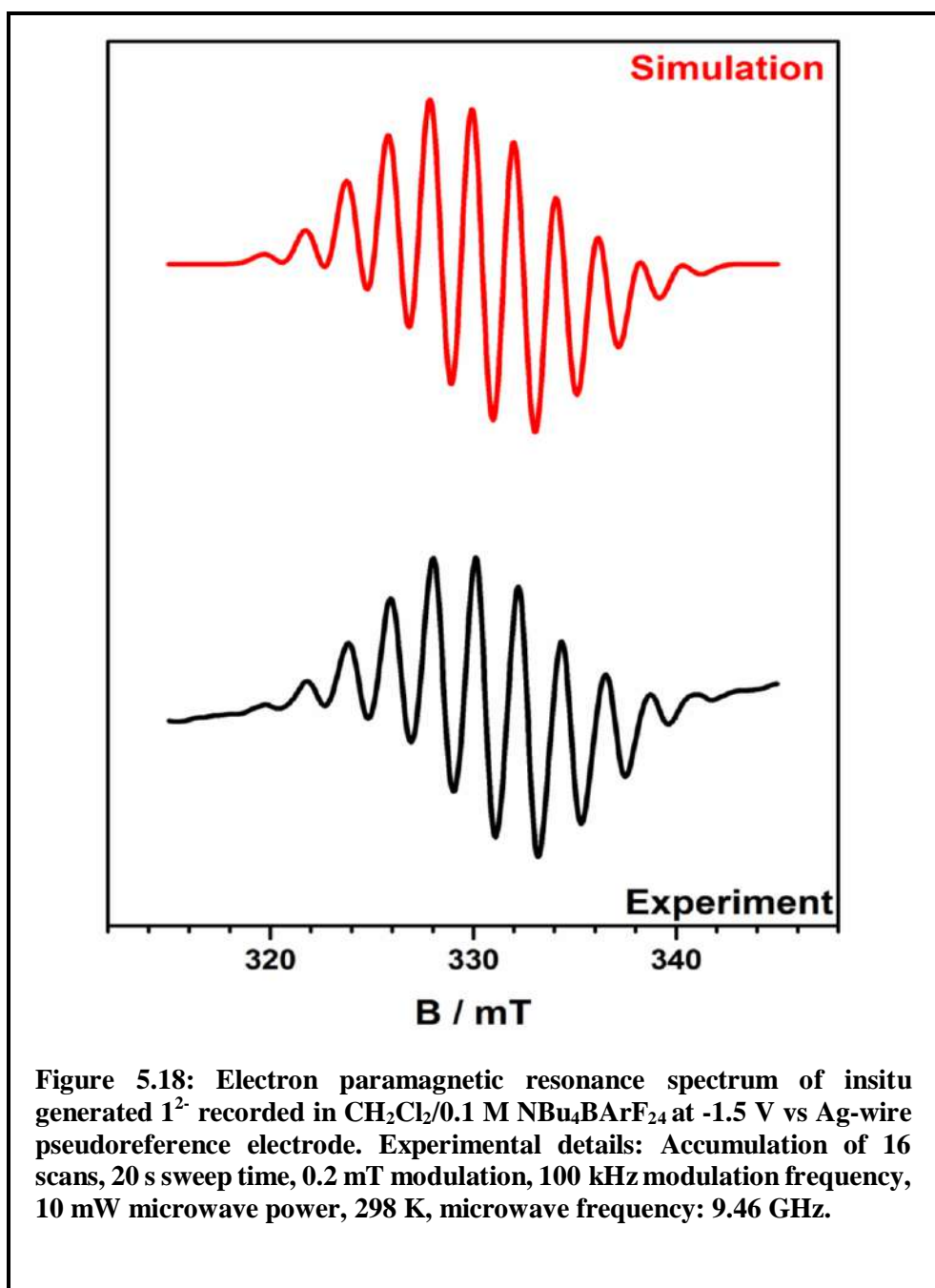


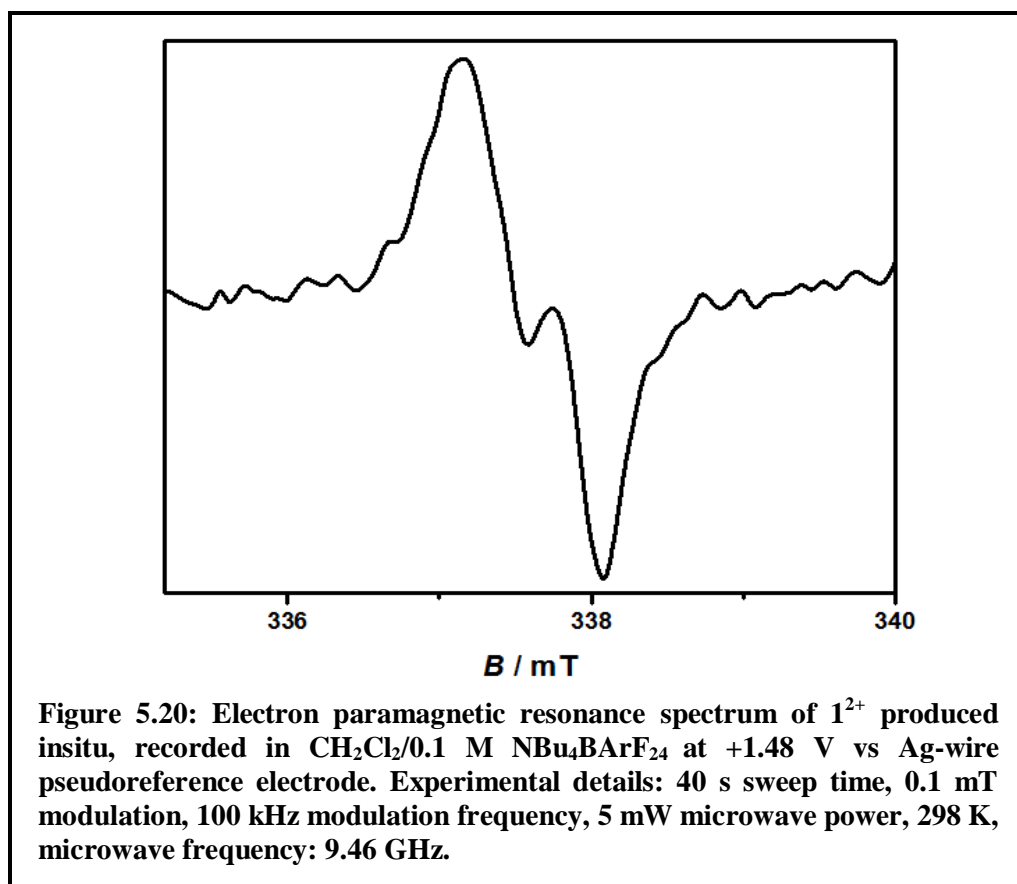
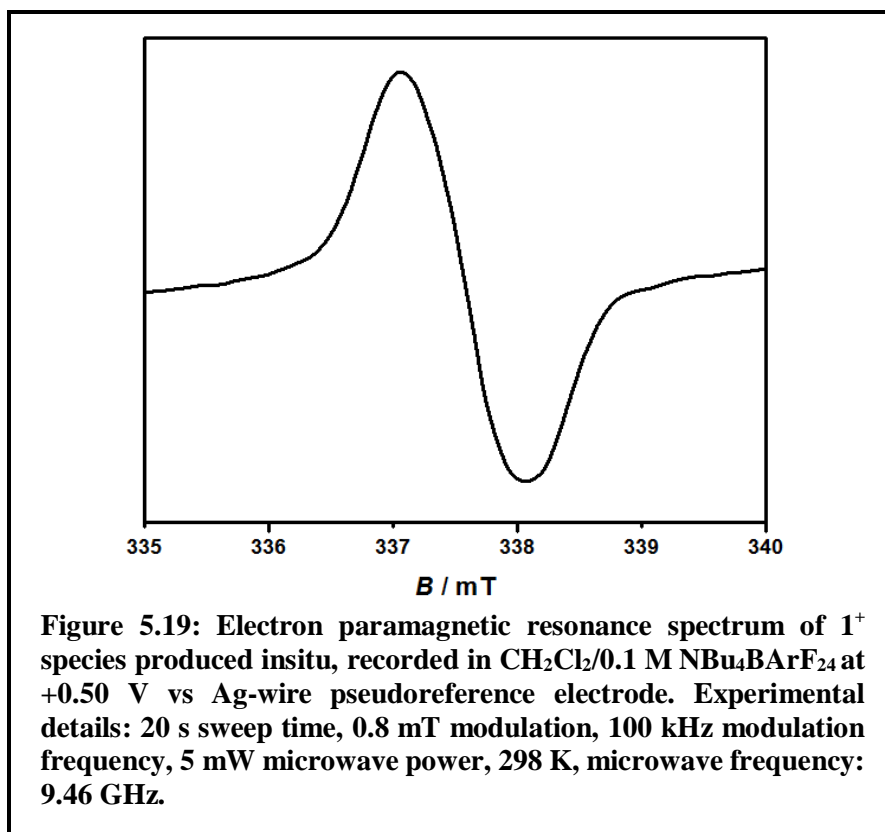
Table 5.3: Electron paramagnetic resonance data of paramagnetic states.

Electron paramagnetic resonance data^[a] of paramagnetic species	
Complex	Electron Paramagnetic Resonance data (g and A) ^[b]
1^{•+}	$g = 2.002$
1²⁺	$g = 2.002$
1^{•[b]}	$g = 2.044$; $a(^{14}\text{N}) = 21.2 \text{ G}$; $a(^{14}\text{N}) = 21.3 \text{ G}$; $a(^{14}\text{N}) = 21.3 \text{ G}$; $a(^{14}\text{N}) = 21.1 \text{ G}$; $a(^{107,109}\text{Ag}) = 42.9 \text{ G}$;
1^{2-[b]}	$g = 2.045$; $a(^{14}\text{N}) = 19.3 \text{ G}$; $a(^{14}\text{N}) = 19.4 \text{ G}$; $a(^{14}\text{N}) = 19.7 \text{ G}$; $a(^{14}\text{N}) = 21.7 \text{ G}$; $a(^{107,109}\text{Ag}) = 40.8 \text{ G}$;
[a] From Electron paramagnetic resonance spectroelectrochemistry in $\text{CH}_2\text{Cl}_2/0.1 \text{ M NBu}_4\text{BArF}_{24}$ in room temperature.	
[b] g values and A values (from simulated data).	

localization at the silver center. The calculated Löwdin spin population analysis of (**1**)[•] delivers close to 45% spin on the silver centers. The EPR spectrum and the spin population analysis thus points to a predominantly silver-centered spin in (**1**)[•] and hence the best description of this species is the rare mixed valent $[\text{Ag}^{\text{II}}(\text{cor}^{3-})-(\text{cor}^{3-})\text{Ag}^{\text{III}}]^{\bullet}$ form. By using a three-electrode electrochemical cell, we were able to generate the two electron reduced species (**1**)²⁻ in situ. Surprisingly, the spectrum for (**1**)²⁻ is identical to that of (**1**)[•] with doubling of the signal intensity (Figure 5.16). As the number of lines observed in the EPR spectra of (**1**)²⁻ and (**1**)[•] are the same, we conclude that the two spins in (**1**)²⁻ do not interact with each other. The EPR spectrum of (**1**)²⁻ was simulated by using parameters that are very similar to those of (**1**)[•] (Table 5.3 and Figure 5.18). The calculated Löwdin spin population analysis of (**1**)²⁻ delivers close to 90% spin on the silver centers. The above data point to a best formulation of (**1**)²⁻ as the isovalent $[\text{Ag}^{\text{II}}(\text{cor}^{3-})-(\text{cor}^{3-})\text{Ag}^{\text{II}}]^{2-}$, making this a rare case of a discrete metal complex containing two Ag^{II} centers. In contrast to the reduced species, the one-electron oxidized form (**1**)^{•+} displays an isotropic EPR signal centered at $g=2.002$ at 298 K (Figure 5.19). The g value for this case is virtually identical to the free electron g value. No hyperfine coupling is resolved for this species. The calculated Löwdin spin population analysis shows no spin on the



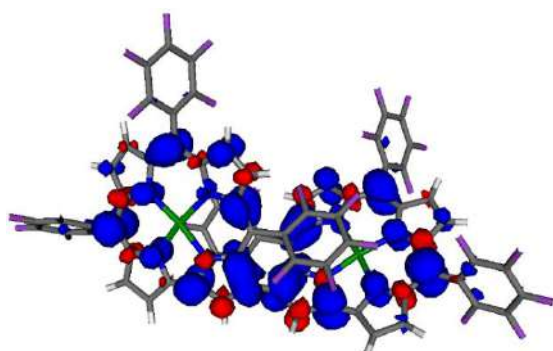
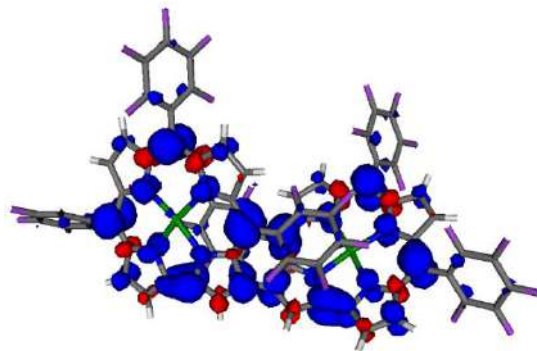
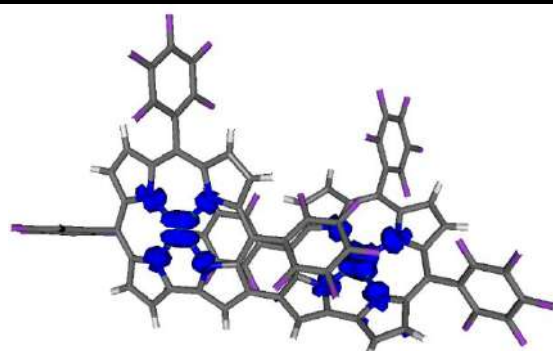
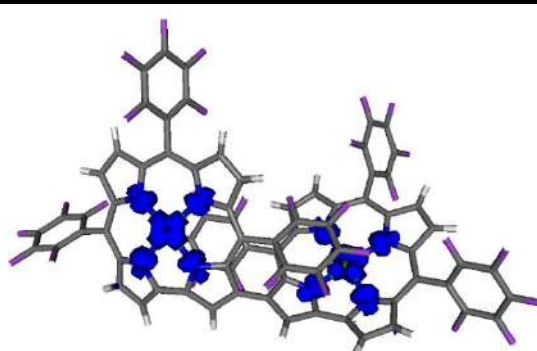
silver centers (Figure 5.21 and Table 5.4). Radical cation $(1)^{+\bullet}$ can thus be best described as a ligand-centered, corrolato-based mixed-valent species $[\text{Ag}^{\text{III}}(\text{cor}^{3-})-(\text{cor}^{2-\bullet})\text{Ag}^{\text{III}}]^{\bullet+}$. The two-electron oxidized compound $(1)^{2+}$ was also characterized by EPR spectroscopy (Figure 5.20) and shows a signal whose features are very similar to those of $(1)^{+\bullet}$. The calculated Löwdin spin population analysis of $(1)^{2+}$ delivers less than 3% spin on the silver centers. These results point to the best description of $(1)^{2+}$ as $[\text{Ag}^{\text{III}}(\text{cor}^{2-\bullet})-(\text{cor}^{2-\bullet})\text{Ag}^{\text{III}}]^{2+}$ containing two oxidized corrolato units.



5.3.6 Löwdin Spin population analysis:

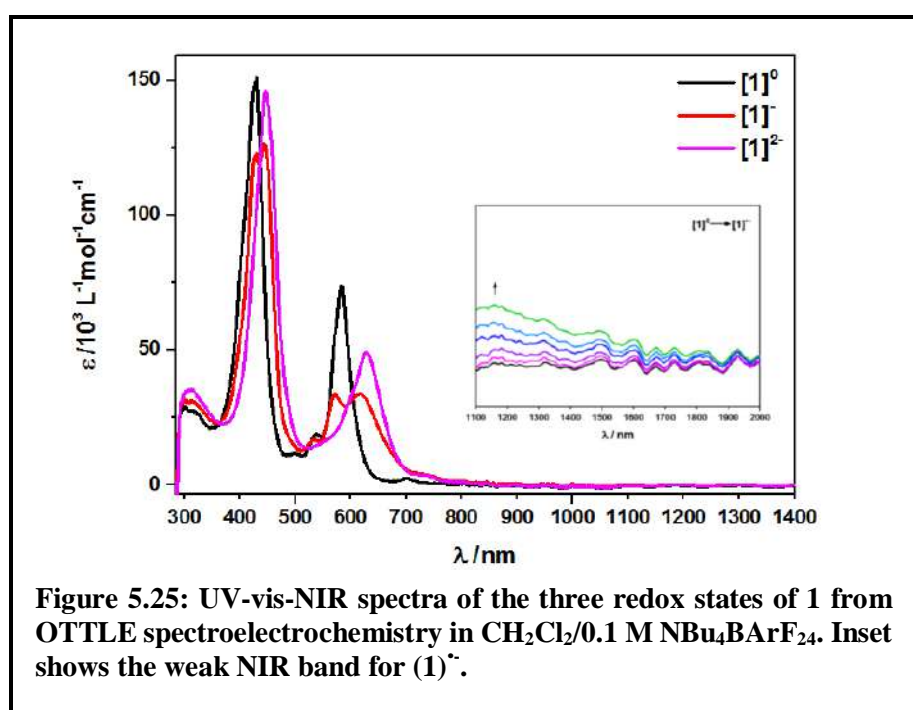
Table 5.4: Löwdin spin density calculations using DFT (B3LYP/TZVPP-ZORA) for the various paramagnetic species.

Atoms / spin density in %	$\rho(1ox)$	$\rho(2ox)$	$\rho(1red)$	$\rho(2red)$
0 Ag	-0.0	1.7	17.8	44.5
1 N	2.9	4.0	4.3	11.0
2 N	0.7	4.2	3.5	9.5
3 N	2.2	4.6	5.1	10.1
4 N	-0.4	1.8	3.1	11.3
5 Ag	-0.0	0.8	25.2	44.5
6 N	3.3	3.5	6.0	11.0
7 N	1.3	4.7	5.2	9.5
8 N	-0.6	2.2	5.0	11.3
9 N	3.1	5.0	6.5	10.1

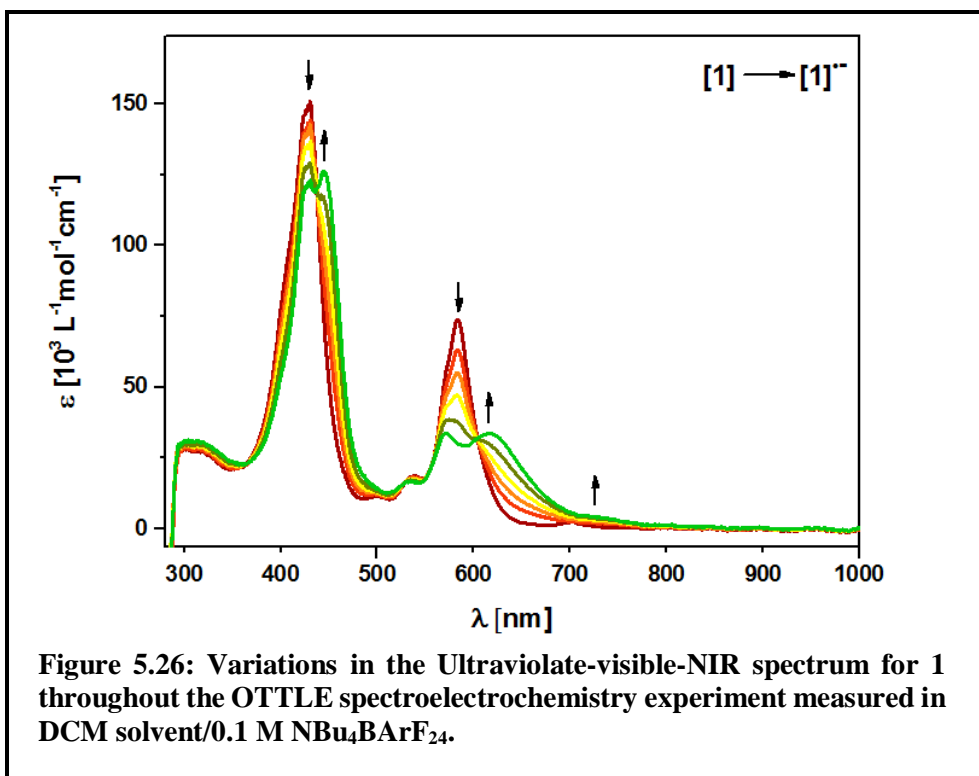
**Figure 5.21: Spin density from DFT calculation of 1^+ .****Figure 5.22: Spin density from DFT calculation of 1^{2+} .****Figure 5.23: Spin density from DFT calculation of 1^- .****Figure 5.24: Spin density from DFT calculation of 1^{2-} .**

5.3.7 UV/Vis-NIR spectroscopy:

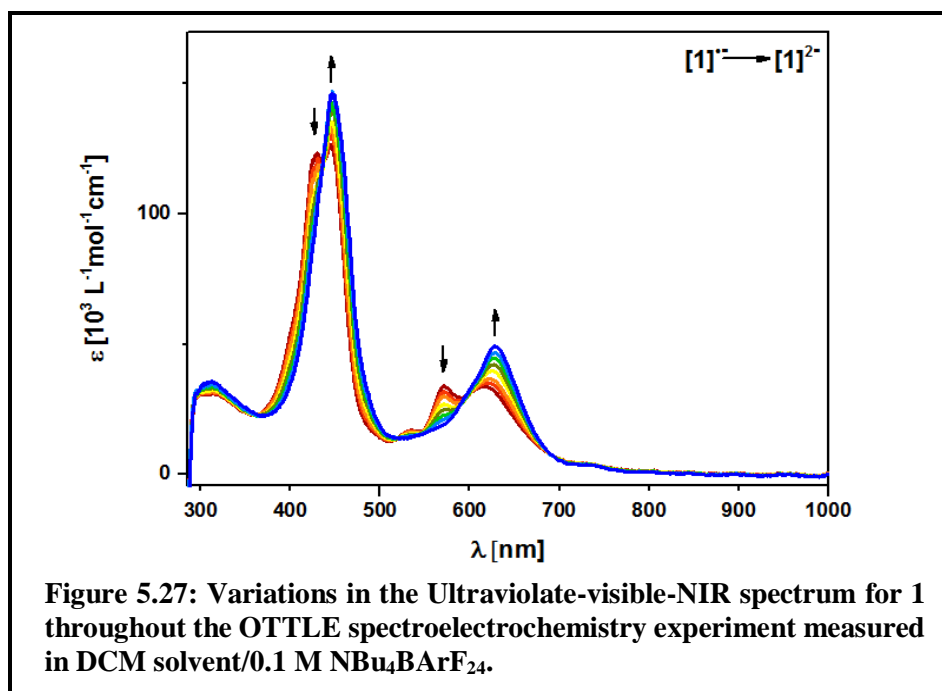
The native state of the complex **1** displays typical spectra for a neutral Ag-corrolato species. The Soret and the Q bands appear at 430 and 583 nm (Figure 5.25). Remarkably, the intensity of the Soret band is very high, with an extinction coefficient of more than $151600 \text{ M}^{-1} \text{ cm}^{-1}$. The value is roughly double of what is observed for mononuclear Ag-corrolato complexes.^{96,270,271} The position of the Soret band is, however, very similar to that in the mononuclear Ag-corrolato complexes.^{96,270,271} This observance likely points to a lack of thorough conjugation in this system, as also seen through a

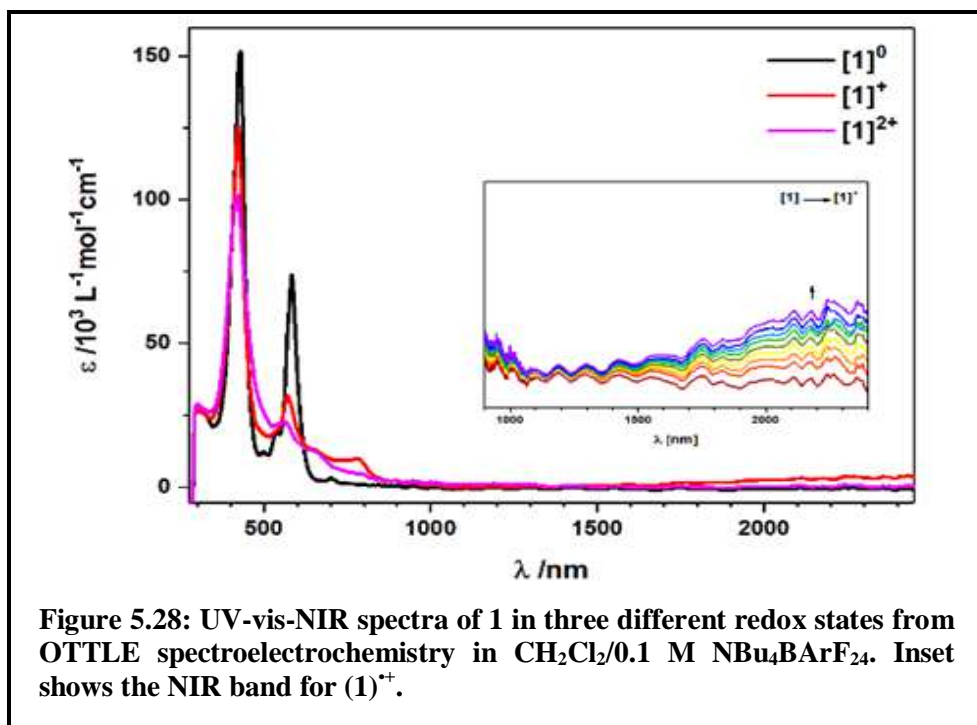


twisting of the corrolato rings with respect to each other. On one-electron reduction to $(1)^{\cdot-}$ both the Soret and the Q bands are split, with maxima at 430, 444 and 571, 617 nm (Figure 5.25, Table 5.5). Such a situation would fit with one reduced and one unreduced unit, as has been discussed in the EPR section above. Additionally, the one-electron reduced form also displays a very weak band at 1100 nm in the NIR region (Figure 5.25), which disappears on further reduction (Figure 5.27). It is tempting to assign this band to an inter-valence charge transfer (IVCT) transition for an $\text{Ag}^{\text{III}}\text{--Ag}^{\text{II}}$ mixed-valent form, with the lack of conjugation between the corrolato rings likely explaining the very low intensity of this band. TD- DFT calculations reproduce the position of the Soret and Q bands for the

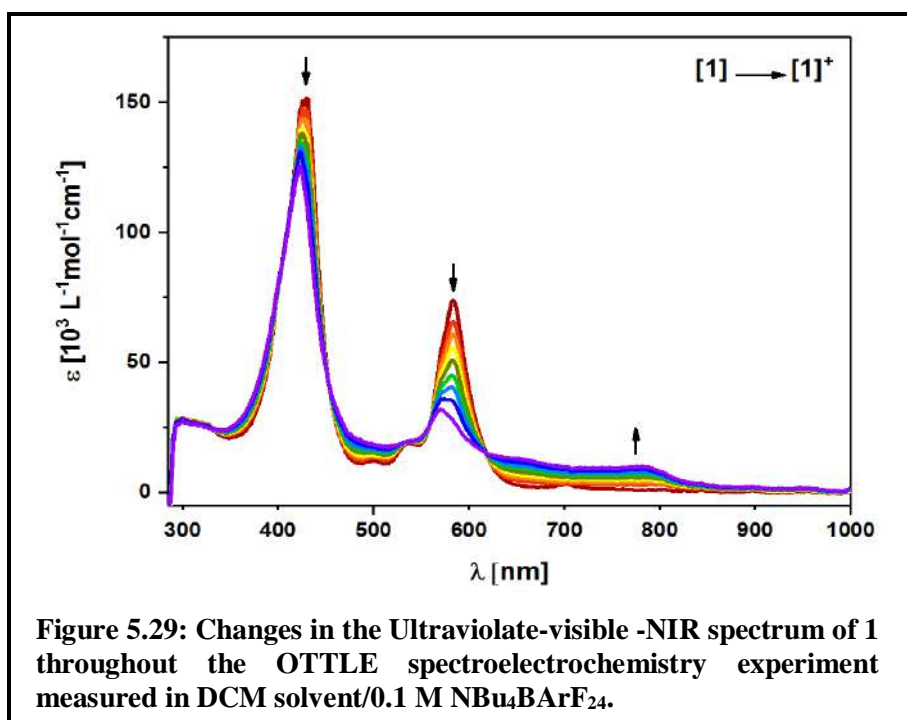


native as well as the reduced states with excellent accuracy (Figure 5.35-5.43). The same calculations also predict an NIR band for the one-electron reduced species. However, the intensity of this transition is exaggerated by the calculations (Figure 5.44). However, TD-DFT predicts this NIR band to be a transition from HOMO α →LUMO α and HOMO α →LUMO α +2 (Table 5.18), thus pointing to a

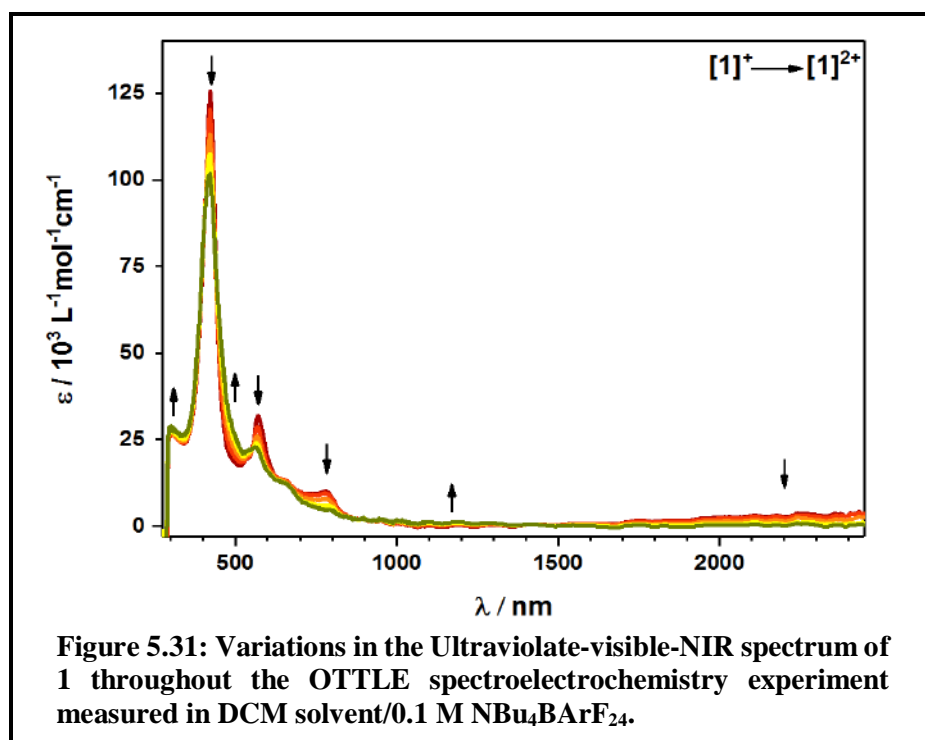
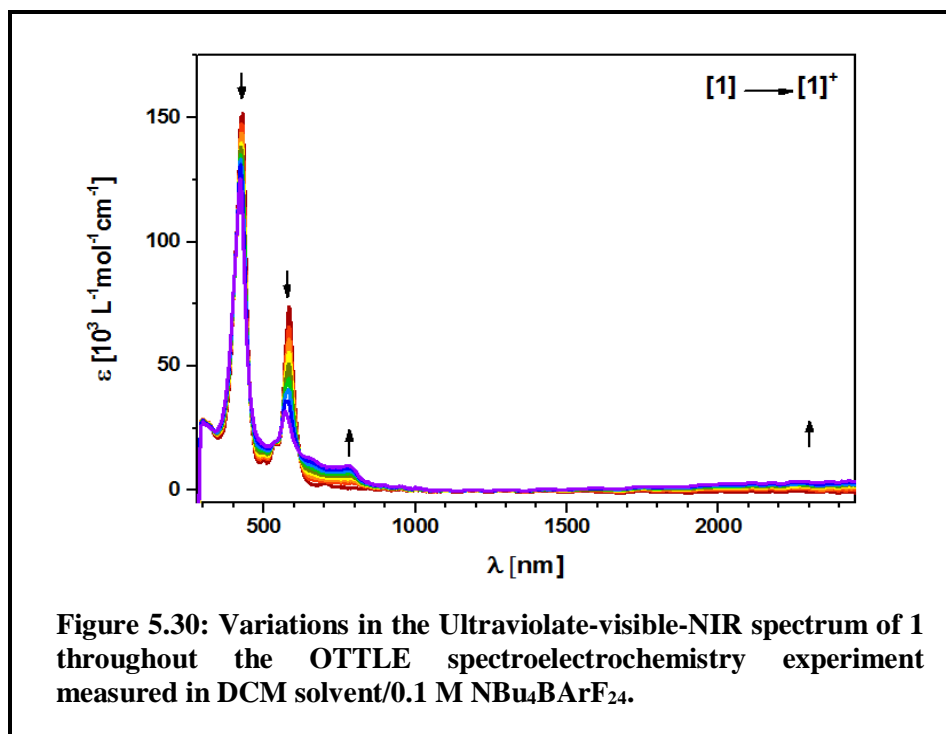


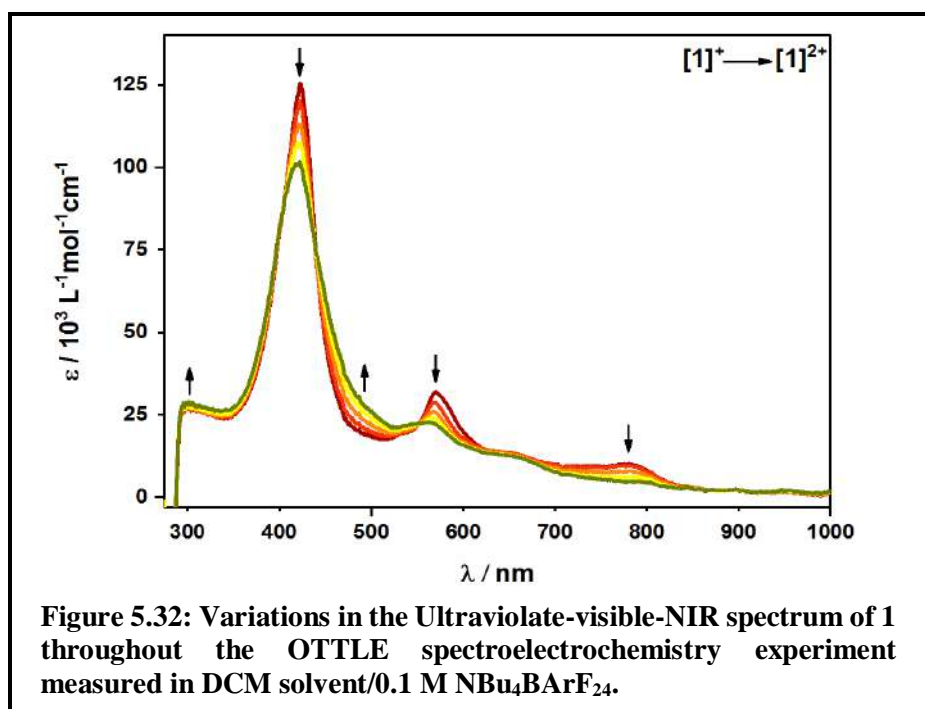


MLCT-type transition for a low-valent silver center. Such a description of the NIR band (as opposed to IVCT) would also fit better with two non-interacting silver centers, as observed through EPR spectroscopy. In contrast to the reduced species, the stepwise oxidation of **1** does not lead to a change in the position of either the Soret or the Q band. Their intensities, however, progressively decrease



on stepwise oxidation (Figure 5.31). The most significant change on the conversion of **1** to **(1)⁺⁺** is the appearance of a broad band in the NIR region centered at around 1850 nm (Figure 5.28 and 5.30). This band disappears on further oxidation to **(1)²⁺**. We assign this band to an intervalence-ligand-to-



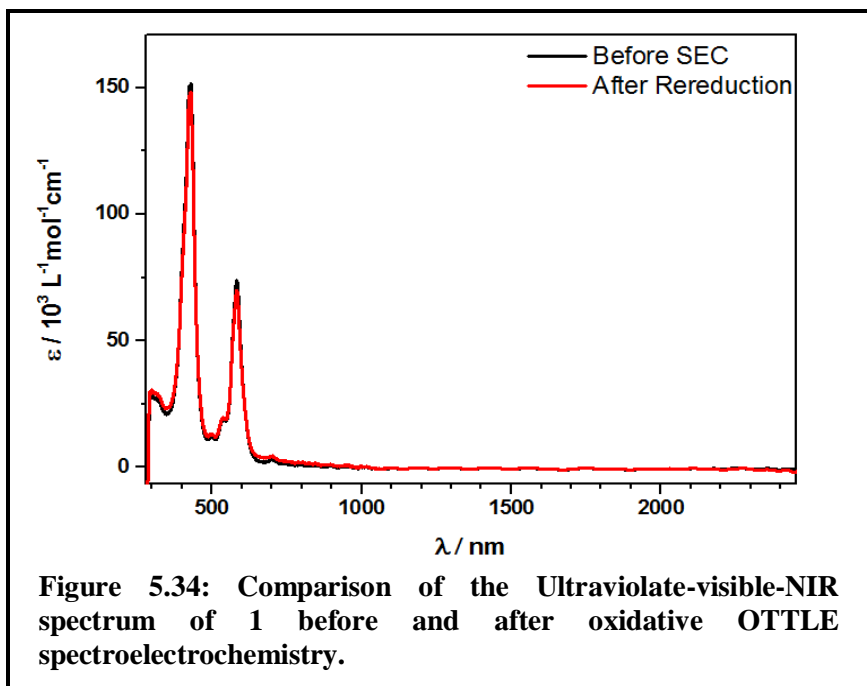
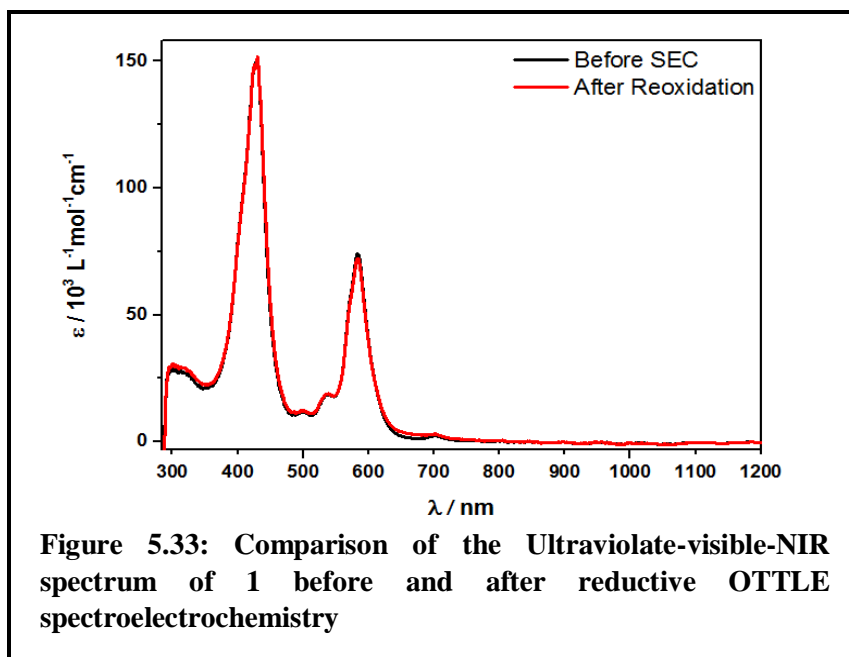


-ligand-charge-transfer (IVLLCT) between two corrolato units based on the formulation $[\text{Ag}^{\text{III}}(\text{cor}^{3-})-(\text{cor}^{2-})\text{Ag}^{\text{III}}]^{++}$. TD-DFT reproduces the position of this band with reasonable accuracy (albeit with exaggerated intensity) and predicts this to be a transition from $\text{HOMO}\beta \rightarrow \text{LUMO}\beta$, which would fit

Table 5.5: Data from UV-Vis-NIR spectroelectrochemical measurements

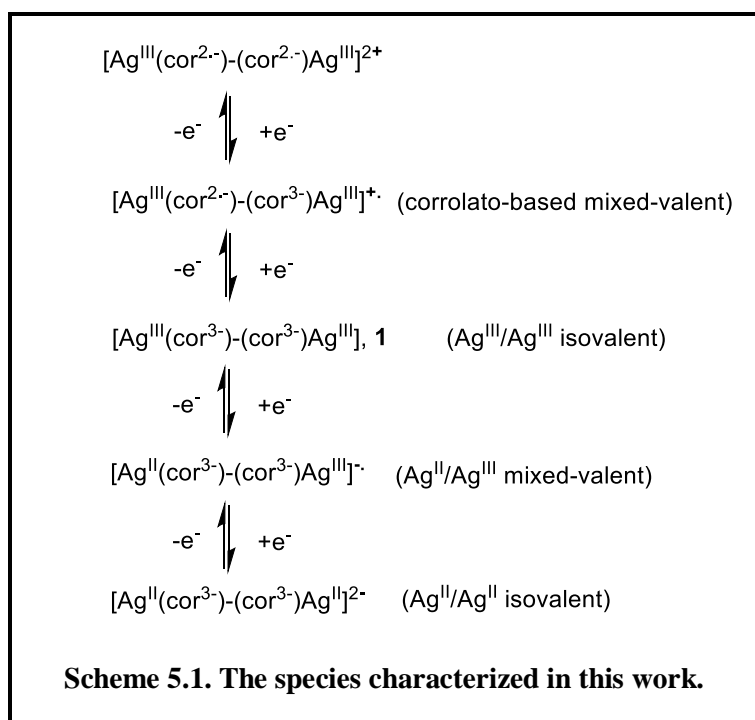
λ [nm] (ϵ [$10^3 \text{ M}^{-1} \cdot \text{cm}^{-1}$])	
[1]	302 (28.3) br, 430 (151.6), 499sh, 538sh, 583 (73.9), 703sh
[1] ⁺	300 sh (27.8) br, 423 (125.4), 570 (31.9), 657 (12.6) sh, 779 (9.9) br, 1350-2400 (3.4) br
[1] ²⁺	300 sh (28.6) br, 422 (101.6), 563 (22.5), 653 (12.5) sh, 900-1400 (1.3) br
[1] ⁻	308 (30.5) br, 430 (123.1), 444 (126.4), 531sh, 571 (33.8), 617 (33.8), 730sh, 1100 (0.4)
[1] ²⁻	311 (35.4) br, 446 (146.0), 628 (49.1)
Observed from the spectroelectrochemical experiment utilized an OTTLE-cell using the gold working electrode in CH ₂ Cl ₂ /0.1 M NBu ₄ BArF ₂₄ at 295K. The wavelength below ~295 nm was blocked beforehand due to absorption of the electrolyte NBu ₄ BArF ₂₄ in this region.	

with a corrolato based $\pi \rightarrow \pi^*$ transition (Table 5.9, 5.11 and Figure 5.37). Additionally, the use of Gouterman orbitals^{167,168} for these systems deliver results that are in excellent agreement with the TD-DFT calculations. Calculations on the hypothetical mono-silver-corrole and its comparison with the dinuclear complex **1** show that the number of Gouterman orbitals for **1** are double those for the hypothetical monomer, with very little changes in the relative orbital energies (Figure 5.53).



5.4 Conclusion:

Summarizing, we have presented here the utility of a rare bis-corrolato core for designing a discrete $\text{Ag}^{\text{III}}/\text{Ag}^{\text{III}}$ complex. The protection provided by the stable macrocycle has allowed us to demonstrate the first example of a thoroughly characterized molecular mixed-valent, non-interacting Class I $\text{Ag}^{\text{II}}/\text{Ag}^{\text{III}}$ ($K_c \approx 10^2$) and an isovalent $\text{Ag}^{\text{II}}/\text{Ag}^{\text{II}}$ complex in the bis-corrolato core. Furthermore, a ligand-centered, moderately interacting mixed-valent Class II corrolato-based species ($K_c \approx 10^3$, broad IVCT band) was characterized as well (Scheme 5.1). Though the connection of two corrolato rings through a C–C single bond is enough to generate electronic coupling between the two corrolato units in the ligand-centered mixed valency in the one-electron oxidized form, there is no observable electronic coupling between the silver centers in the metal-centered mixed-valent one-electron reduced form. Results obtained from X-ray crystallography, electrochemistry, spectroelectrochemistry, and DFT calculations have helped us in making those assignments. Even though covalency is always a factor in corrolato complexes, our approach here shows that a bis-corrolato unit is an ideal platform for stabilizing unusual and hitherto unknown mixed-valent systems. The results presented here are likely to be relevant for generating other intriguing species and for the



use of such cores in cooperative catalysis. The electronic coupling observed for the corrolato-based mixed-valent system will be an important attribute while investigating multi-corrolato units as components of molecular electronics. It will be intriguing to see if enhancing the conjugation between the corrolato units will increase the electronic coupling between the metal centers. Future efforts will be directed towards increasing the conjugation between the rings and using these and related systems in catalysis.

5.5 Experimental Section:

5.5.1 Syntheses:

5.5.1.1 3,3'-Bis(5,10,15-tris(pentafluorophenyl)corrole, **1A**:

1A was prepared by following a literature reported procedure developed by Osuka *et al.*²⁹⁵ Proton NMR (400 MHz, CHCl₃-*d*) δ = 9.22 – 9.09 (m, 4H), 8.77 (d, J = 4.8 Hz, 2H), 8.73 (d, J = 4.3 Hz, 2H), 8.55 (d, J = 4.7 Hz, 2H), 8.45 (d, J = 4.8 Hz, 2H), 8.31 (d, J = 4.9 Hz, 2H) (Figure 5.4); ¹⁹F NMR (376 MHz, Chloroform-*d*) δ = -138.32 (ddtd, J =96.2, 72.4, 24.4, 8.0, 10F), -139.72 (d, J =12.2, 2F), -153.15 (t, J =21.0, 2F), -153.56 (t, J =20.9, 2F), -155.02 (m, 2F), -162.42 (dtd, J =47.7, 22.5, 8.4, 4F), -162.78 (ddt, J =33.4, 23.7, 11.4, 4F), -164.09 (t, J =22.3, 2F), -165.35 (d, J =19.8, 2F) (Figure 5.5). MS (ESI): m/z : calcd for C₇₄H₂₀F₃₀N₈ (**1A**): 1590.13; found: 1591.72 [M+H]⁺ (Figure 5.8); elemental analysis calcd (%) for C₇₄H₂₀F₃₀N₈ (**1A**): C 55.87, H 1.27, N 7.04; found: C 55.99, H 1.35, N 7.17.

5.5.1.2 3,3'-Bis{(5,10,15-tris(pentafluorophenyl)corrolato-silver(III))},**1**:

3,3'-Bis(5,10,15-tris(pentafluorophenyl)corrole, **1A** (20 mg, 0.013 mmol) was dissolved in triethylamine (6 mL) and silver acetate salt (42mg, 0.25 mmol) was added into the solution. Whole solution was kept at stirring for next 45 min at 298 K and the solution colour changed from green colour to dark reddish-green. Using the rotary evaporator, the solvent of the reaction mixture was evaporated, and finally the dark purple colored crude product was collected after the purification using column chromatography through silica gel (100-200 mesh) column using 10% DCM + 90% hexane as eluent. Subsequent recrystallization (CH₂Cl₂/hexane) gave the pure crystalline 3,3'-

Bis{(5,10,15-tris(pentafluorophenyl)corrolato-silver(III))}, **1**. Yield: 54% (12 mg); Proton NMR (400 MHz, CHCl₃-*d*) δ 9.53 (d, *J* = 1.5 Hz, 2H), 9.42 (d, *J* = 4.5 Hz, 2H), 9.06 (d, *J* = 4.9 Hz, 2H), 8.90 (d, *J* = 4.5 Hz, 2H), 8.85 (d, *J* = 5.0 Hz, 2H), 8.72 (d, *J* = 4.9 Hz, 2H), 8.65 (d, *J* = 4.9 Hz, 2H) (Figure 5.6); ¹⁹F NMR (376 MHz, Chloroform-*d*) δ = -136.35 (dd, *J*=24.8, 8.0, 2F), -136.89 (d, *J*=10.5, 2F), -137.68 (dddd, *J*=47.6, 24.2, 8.6, 3.3, 4F), -137.87 – -138.31 (m, 4F), -152.94 (dt, *J*=61.9, 20.9, 4F), -154.67 (t, *J*=21.1, 2F), -161.45 – -163.91 (m, 8F), -163.35 – -164.68 (m, 2F), -164.95 (dq, *J*=20.4, 9.4, 2F). (Figure 5.7); UV/Vis (dichloromethane): λ_{max} (ϵ) = 430 (151600), 499 (12400), 538 (19100), 583(73900), 703 (3300 M⁻¹cm⁻¹); MS (ESI): *m/z*: calcd for C₇₄H₁₄F₃₀N₈Ag₂ (**1**): 1797.90; found: 1796.87 [M-H]⁺ (Figure 5.9); elemental analysis calcd (%) for C₇₄H₁₄F₃₀N₈Ag₂ (**1**): C, 49.36; H, 0.78; N, 6.22; found: C 49.44, H 0.91, N 6.43.

5.5.2 Determination of the X-Ray Crystal Structure:

Crystals of both the complex **1** was obtained through the slow diffusion process in DCM solvent into hexane and this process was followed by the slow evaporation under atmospheric conditions. Bruker Kappa APEX II CCD diffractometer has been used for recording the crystal data for complex **1** at 100 K temperature. All the crystallographic parameters were arranged within the Table 5.1 and have been optimized for absorption effects and Lorentz polarization effect. In order to solve and refine both the crystals, the SHELXTL²³² program package has been utilized. During the refinement process, all the Hydrogen atoms has been attached through riding model. Hydrogen atoms of the water molecules were included without fixing. Spots for all the disordered solvent molecules has been eliminated through the SQUEEZE¹³⁵ command in PLATON.¹⁴⁵⁻¹⁴⁸ CCDC number 1557571 accommodate all the X-Ray crystal data for complexe **1**. www.ccdc.cam.ac.uk/data_request/cif can be used to access the crystal data without any charge.

5.6 General Remarks and Instrumentation:

5.6.1 Details of all materials used:

All the starting materials like 2,3,4,5,6-pentafluorobenzaldehyde, pyrrole, *p*-chloranil, and Tetrabutyl Ammonium Perchlorate (TBAP) were ordered through SigmaAldrich, USA. Other reagents like

Silver acetate were ordered through Merck, India. Rest of the other reagents were from reagent grade quality. Solvents like hexane and DCM were purified with potassium hydroxide and Calcium hydride respectively. HPLC standard solvents were utilized for all the spectroscopic and electrochemical related studies.

5.6.2 Physical Studies:

For the elemental analyses, Perkin-Elmer 240C elemental analyser were used. Nuclear Magnetic Resonance spectra of all the complexes have been measured by using Bruker Avance 400 NMR spectrometer using TMS (Tetramethylsilane) as the internal standard. For all the Electrospray Ionisation Mass Spectrometry data, the Bruker Micro TOF-QII mass spectrometer has been used.

5.6.3 Cyclic Voltammetry:

In order to record the electrochemical data, a PAR VersaStat 4 potentiostat (Ametek) has been utilized by using the degassed and anhydrous Dimethylformamide solvent purchased from Acros Organics (99.8 % extra dry). As the electrolyte, 0.1 M tetrabutylammonium hexafluorophosphate which is almost 99.0 % dried (electrochemical grade, Fluka). The electrochemical solution contains complex **1** with 1×10^{-4} M. As the working electrode, the glassy carbon and platinum have been used and as the counter electrode and pseudoreference electrode, the coiled platinum wire and coiled silver wire have been utilized respectively within the electrochemical cell. The electrochemical experiment has been performed by using the ferrocene/ferrocenium couple as the internal reference.

5.6.4 Spectroelectrochemistry:

In order to record the Ultraviolet/Visible spectra of complex **1** has been performed using Avantes spectrometer consist of AvaLight-DH-S-Bal as the light source, AvaSpec-ULS2048 as the UV/Vis detector, and AvaSpec-NIR256-TEC as an NIR detector. For the Spectroelectrochemical data collection, an OTTLE (optically transparent thin-layer electrochemical) cell (CaF_2 windows) were performed using the Pt working electrode, a platinum wire as the counter electrode, and a silver wire as the pseudoreference electrode. Degassed and anhydrous Dimethylformamide solvent has been

utilized which was purchased from Acros Organics (99.8 % extra dry) and as the electrolyte, 0.1 M tetrabutylammonium hexafluorophosphate (99.0 % dried) has been used.

5.6.5 Electron Paramagnetic Resonance:

The X-band Electron paramagnetic resonance spectra (ca. 9.5 GHz) were measured using the Magnettech MS-5000 benchtop EPR spectrometer containing a rectangular shaped TE 102 cavity and TC HO4 temperature controller. For all the data collections, a synthetic quartz glass tubes have been used. A three-electrode system consist of working, counter electrode and pseudoreference electrode has been used. EasySpin 5.1.4. and MatLab R2012a have been utilized for the simulation process.

5.6.6 Computational Details:

For the DFT calculations²³³, ORCA 3.0.0 has been used as the program package. BP86^{235,297,298} functional^{234,299} has been utilized for the geometry optimizations of complex **1** considering the X-Ray crystal structure. For all the single-point calculations, the B3LYP functional^{234,299} have been used and all of these calculations were performed following empirical Van der Waals correction (D3).³⁰⁰⁻³⁰³ Both the restricted and unrestricted DFT calculations were utilized in case of all the closed and open shell molecules respectively. For all the geometric optimization (OPT) and tight for SCF calculations (TIGHTSCF) processes, the convergence criteria were set as the default and the zeroth-order regular approximation (ZORA)³⁰⁴ were comprised for the relativistic effects. For all atoms in the complex, the triple- ζ -valence basis sets (TZVP-ZORA)²³⁹ were utilized. For the optimized geometry and numerical frequency calculations and the RIJCOSX (combined identity resolution and chain of spheres algorithms) approximation for single point calculations, all the simulation processes were performed using resolution of the identity approximation^{240-243,307-309} with matching auxiliary basis sets.^{310,311} Corresponding crystal structures helped to optimize the geometry of complex and any kind of symmetry limitation were not forced throughout the optimization process. The time-dependent DFT (TD-DFT) process was used to determine the low-lying excitation energies. For all kind of calculations, the solvent effects were considered along with the conductor-like screening model (COSMO).^{244,245} Löwdin spin population calculations²⁴⁶ were used to calculate the spin densities. All

the optimized geometries showed local minima which establish the absence of any imaginary frequency. MO Analyzer tool³¹² has been applied to evaluate the overall contribution of molecular fragments in case of molecular orbitals. Programs like modified Avogadro 1.1.1 with extended ORCA support and the Molekel 5.4.0.8^{313,314,247} have been applied to anticipate the Molecular orbitals and spin densities.

5.7 TD-DFT calculations:

5.7.1 TD-DFT calculations of 1:

5.7.1.1 Calculated spectra, Comparison with Experimental spectrum and TD-DFT Transitions of 1:

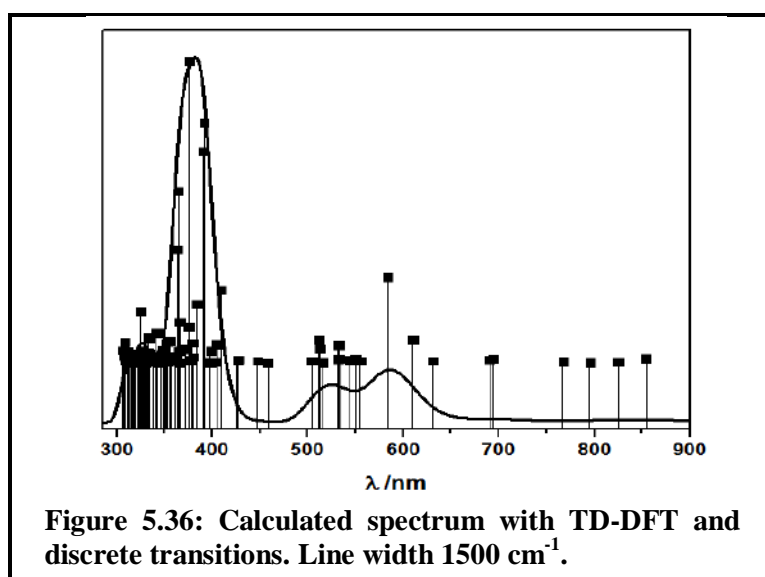
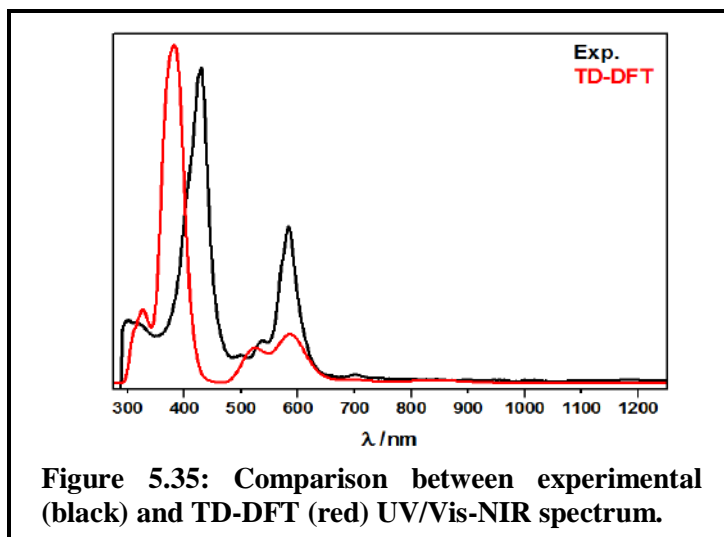
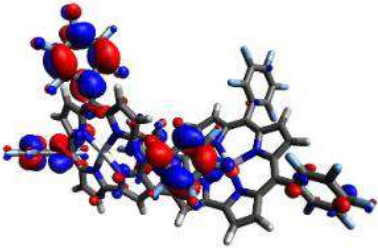
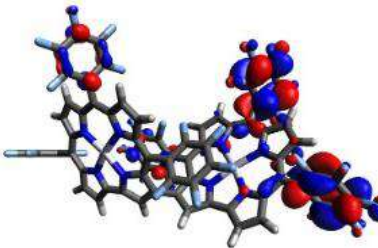
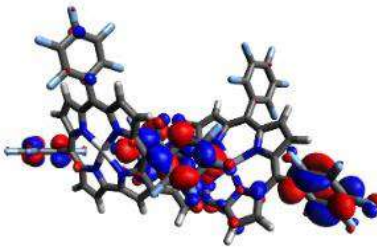
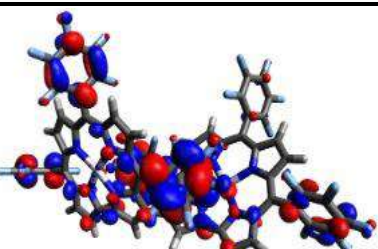
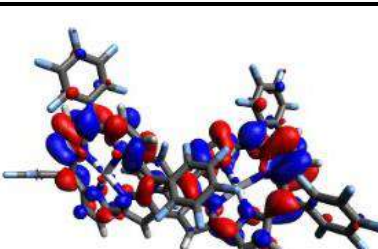
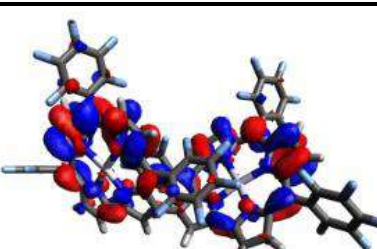
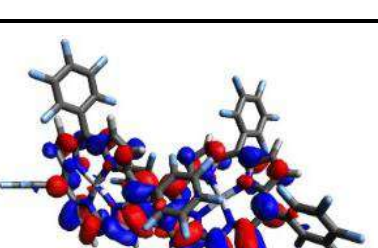
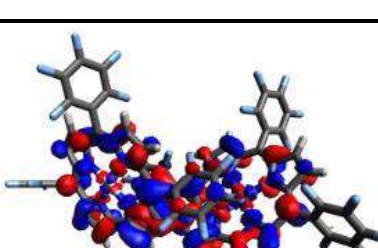
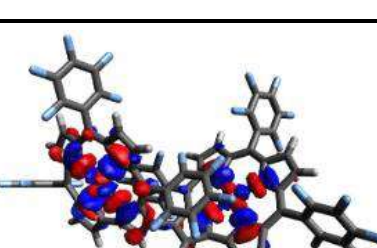
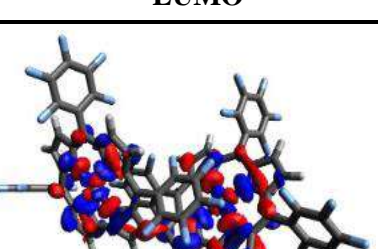
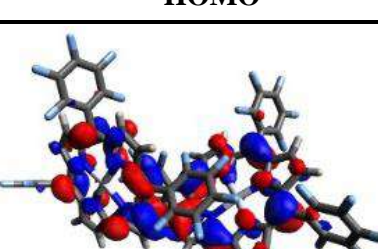
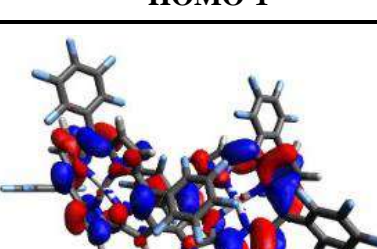





Table 5.6: TD-DFT calculated electronic transitions of 1. (Including raw data)

State	Transition	Transition HOMO LUMO	Calculated Transition energy	Oscillator strength	Experimental transition energy	Molar absorption coefficient 10 ³
68	431a → LUMO+4 (0.15) 434a → LUMO+6 (0.39)	HOMO-7 → LUMO+4 (0.15) HOMO-4 → LUMO+6 (0.39)	324.6	0.133	302	28.3
31	430a → 439a 0.177685 434a → 441a 0.317805 435a → 444a 0.122136	HOMO-8 → LUMO (0.17) HOMO-4 → LUMO+2 (0.31) HOMO-3 → LUMO+5 (0.12)	375.8	0.784	430 nm	151.6
28	Mixed (all below 10%)	Mixed (all below 10%)	391.6	0.624		
29	436a → 444a 0.11	HOMO-2 → LUMO+5 (0.11)	390.1	0.549		
35	421a → 439a : 0.18 436a → 443a : 0.09	HOMO-17 → LUMO (0.18) HOMO-2 → LUMO+4 (0.10)	364.4	0.446		
36	422a → 439a : 0.19 434a → 442a : 0.33	HOMO-16 → LUMO (0.19) HOMO-4 → LUMO+3 (0.33)	363.4	0.294		
25	434a → 441a : 0.35 435a → 444a : 0.13	HOMO-4 → LUMO+2 (0.35) HOMO-3 → LUMO+5 (0.13)	583.7	0.188		
30	429a → 439a : 0.11 431a → 439a : 0.12 434a → 442a : 0.33	HOMO-9 → LUMO (0.11) HOMO-7 → LUMO (0.12) HOMO-4 → LUMO+3 (0.33)	409.1	0.151	538	19.1
14	436a → 443a (0.10) 437a → 442a (0.60) 438a → 444a (0.18)	HOMO-2 → LUMO+4 (0.10) HOMO-1 → LUMO+3 (0.60) HOMO → LUMO+5 (0.18)	512.7	0.037		
15	436a → 442a (0.73) 437a → 443a (0.12)	HOMO-2 → LUMO+3 (0.73) HOMO-1 → LUMO+4 (0.12)	511.1	0.060		
21	435a → 443a (0.26) 435a → 444a (0.16) 437a → 443a (0.30) 437a → 444a (0.16)	HOMO-3 → LUMO+4 (0.26) HOMO-3 → LUMO+5 (0.16) HOMO-1 → LUMO+4 (0.30) HOMO-1 → LUMO+5 (0.16)	531.6	0.044		
22	435a → 443a (0.23) 435a → 444a (0.25) 437a → 443a (0.16) 437a → 444a (0.22)	HOMO-3 → LUMO+4 (0.23) HOMO-3 → LUMO+5 (0.25) HOMO-1 → LUMO+4 (0.16) HOMO-1 → LUMO+5 (0.22)	532.7	0.045		
9	438a → 441a (0.76)	HOMO → LUMO+2 (0.76)	583.7	0.222	583	73.9
6	436a → 440a (0.57) 437a → 440a (0.12) 438a → 439a (0.21)	HOMO-2 → LUMO+1 (0.57) HOMO-1 → LUMO+1 (0.12) HOMO → LUMO (0.21)	609.8	0.060		
1	436a → 439a (0.10) 436a → 440a (0.14) 438a → 439a (0.52) 438a → 440a (0.11)	HOMO-2 → LUMO (0.10) HOMO-2 → LUMO+1 (0.14) HOMO → LUMO (0.52) HOMO → LUMO+1 (0.11)	854.2	0.011	703	3.3
3	435a → 439a (0.19) 435a → 440a (0.10) 437a → 439a (0.43) 437a → 440a (0.14)	HOMO-3 → LUMO (0.19) HOMO-3 → LUMO+1 (0.10) HOMO-1 → LUMO (0.43) HOMO-1 → LUMO+1 (0.14)	795.3	0.0008		
4	435a → 439a (0.21) 435a → 440a (0.15) 437a → 439a (0.16) 437a → 440a (0.30)	HOMO-3 → LUMO (0.21) HOMO-3 → LUMO+1 (0.15) HOMO-1 → LUMO (0.16) HOMO-1 → LUMO+1 (0.30)	767.2	0.004		

5.7.1.2 Molecular orbitals and orbital energies of 1

Table 5.7: Composition of selected molecular orbitals of 1.

LUMO+9	LUMO+8	LUMO+7
		
LUMO+6	LUMO+5	LUMO+4
		
LUMO+3	LUMO+2	LUMO+1
		
LUMO	HOMO	HOMO-1
		
HOMO-2	HOMO-3	HOMO-4
		

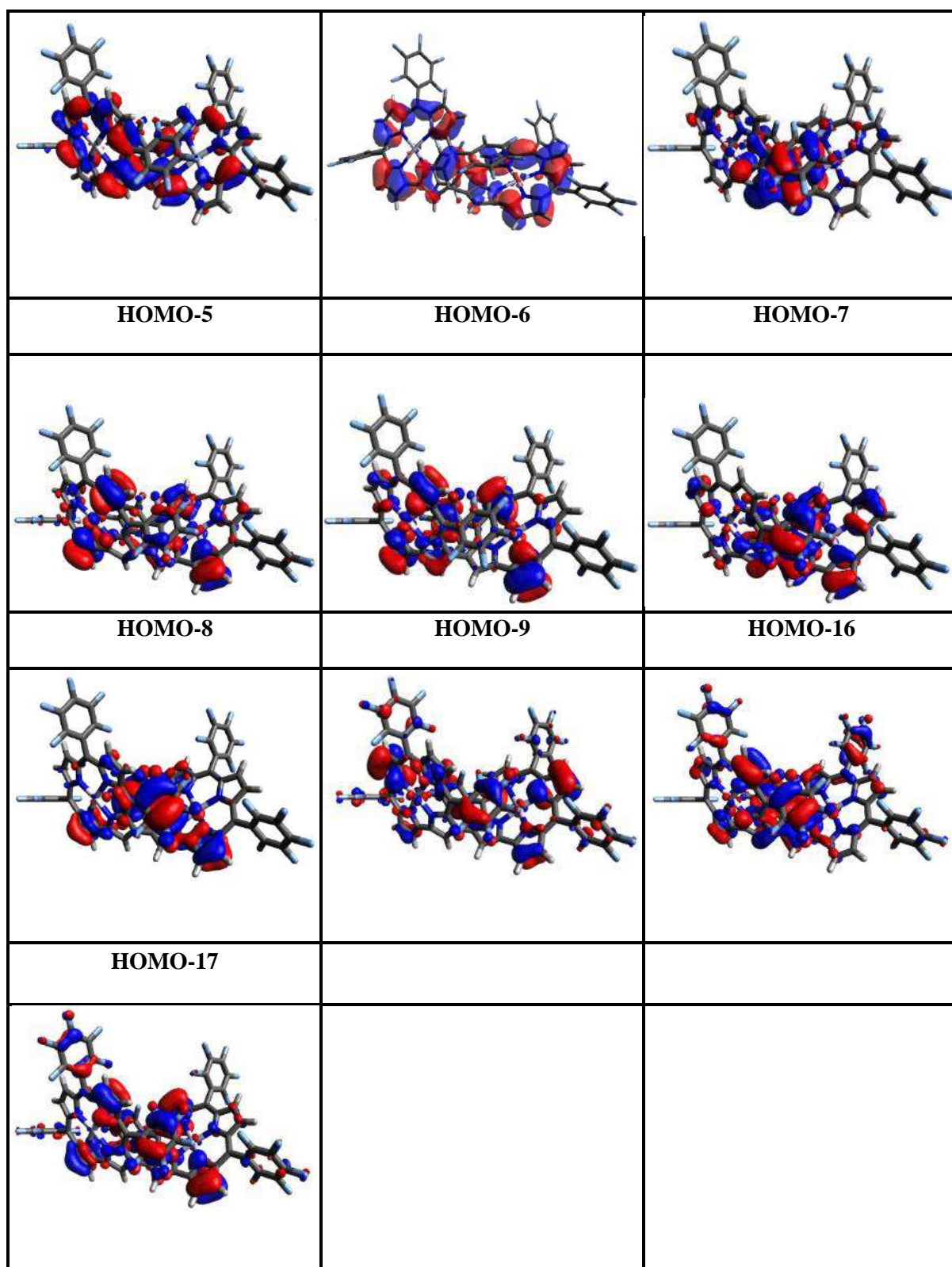
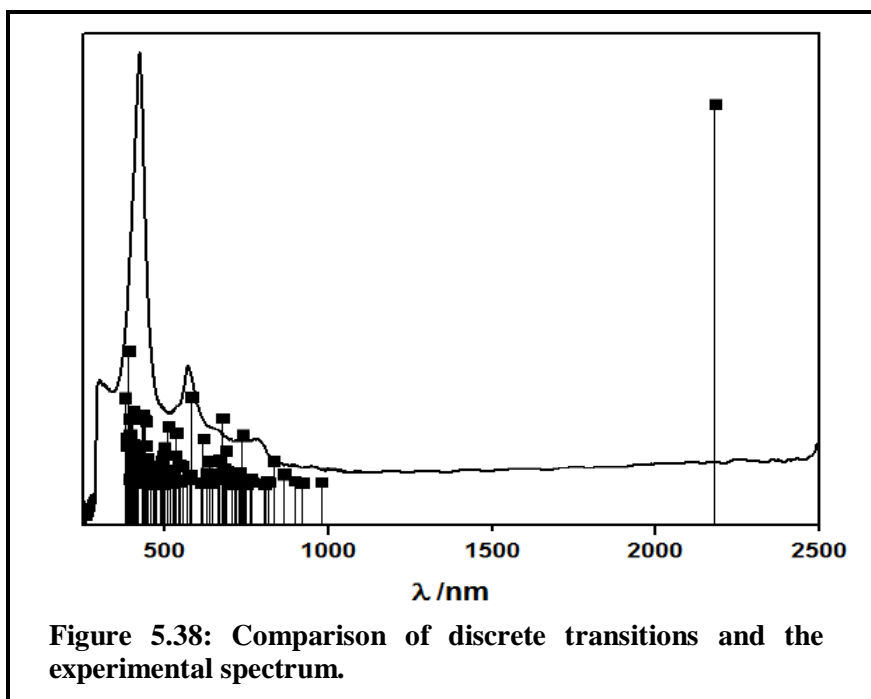
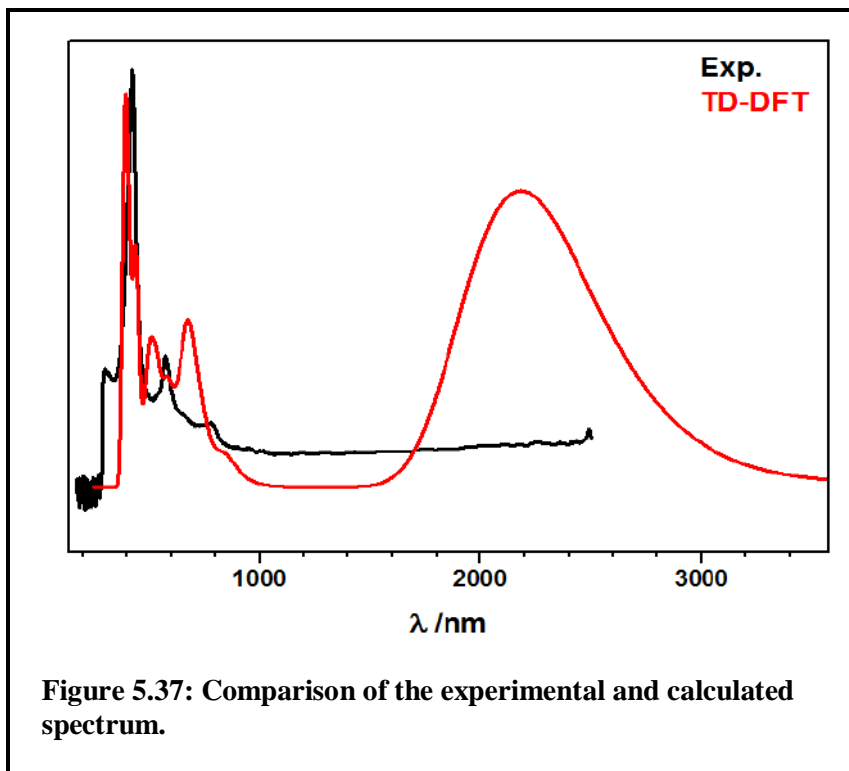


Table 5.8: Orbital energies of 1 from DFT-calculation

Orbital No.	HOMO/LUMO	Energy (Eh)	Energy (eV)
450	LUMO+11	-0.039826	-1.0837
449	LUMO+10	-0.040324	-1.0973
448	LUMO+9	-0.041134	-1.1193
447	LUMO+8	-0.041571	-1.1312
446	LUMO+7	-0.043292	-1.1780
445	LUMO+6	-0.044292	-1.2052
444	LUMO+5	-0.090660	-2.4670
443	LUMO+4	-0.092690	-2.5222
442	LUMO+3	-0.104671	-2.8482
441	LUMO+2	-0.110108	-2.9962
440	LUMO+1	-0.116541	-3.1712
439	LUMO	-0.121152	-3.2967
438	HOMO	-0.203223	-5.5300
437	HOMO-1	-0.206732	-5.6255
436	HOMO-2	-0.208919	-5.6850
435	HOMO-3	-0.210025	-5.7151
434	HOMO-4	-0.248169	-6.7530
433	HOMO-5	-0.261178	-7.1070
432	HOMO-6	-0.262468	-7.1421
431	HOMO-7	-0.263294	-7.1646
430	HOMO-8	-0.265881	-7.2350
429	HOMO-9	-0.267531	-7.2799
428	HOMO-10	-0.267780	-7.2867
427	HOMO-11	-0.269155	-7.3241
426	HOMO-12	-0.269370	-7.3299
425	HOMO-13	-0.269460	-7.3324
424	HOMO-14	-0.269651	-7.3376
423	HOMO-15	-0.272142	-7.4054
422	HOMO-16	-0.273124	-7.4321
421	HOMO-17	-0.273543	-7.4435
420	HOMO-18	-0.276480	-7.5234

5.7.2 TD-DFT Calculations of (1)⁺ (doublet)

5.7.2.1 Calculated spectra, Comparison with Experimental spectrum and TD-DFT Transitions of (1)⁺



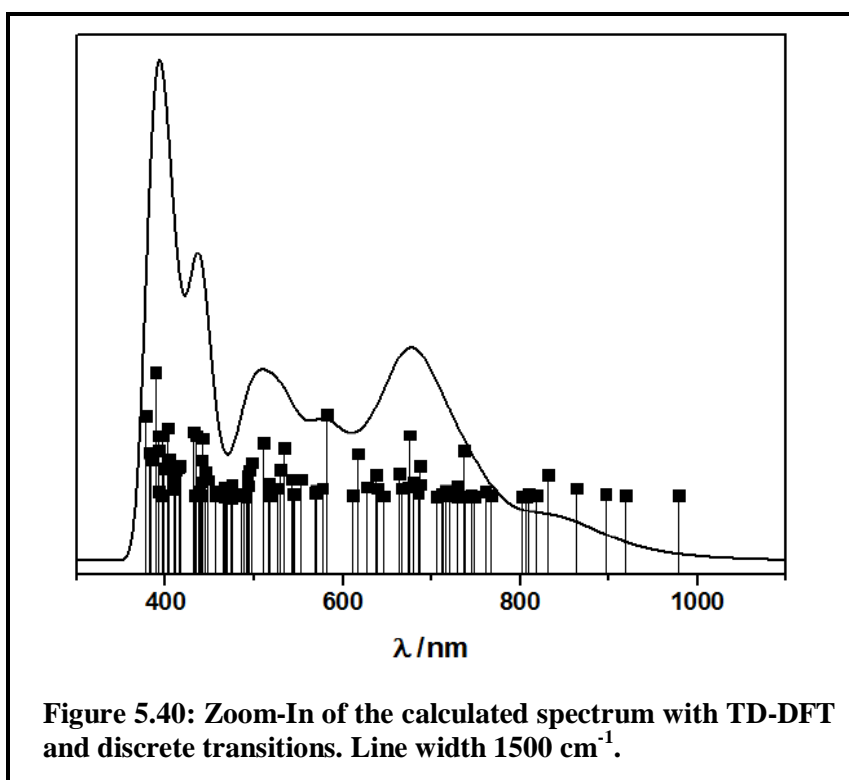
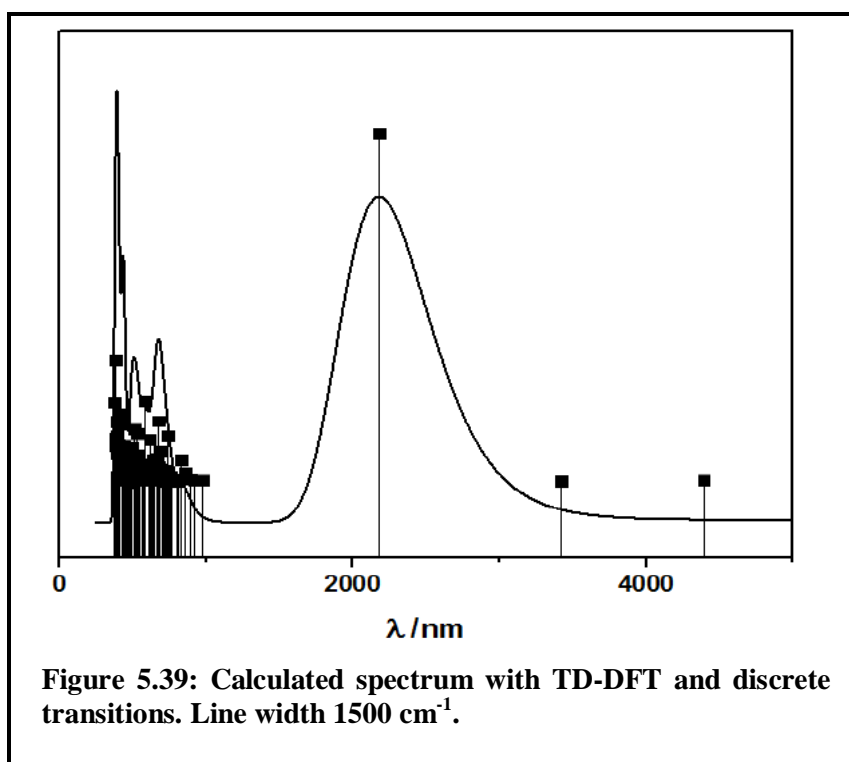


Table 5.9: TD-DFT calculated electronic transitions of 1⁺. (Including raw data)

State	Transition	Transition HOMO LUMO	Calculated Transition energy	Oscillator strength	Experimental transition energy	Molar absorption coefficient 10 ³
89	418a → 439a (0.16)	HOMO α -20 → LUMO α (0.16)	392.7	0.055	423	125.4
92	Mixed	Mixed	388.6	0.112		
97	432a → 439a (0.28) 432a → 440a (0.20)	HOMO α -6 → LUMO α (0.28) HOMO α -6 → LUMO α +1 (0.20)	396.9	0.055		
100	mixed	mixed	378.3	0.073		
41	437a → 441a (0.10) 438a → 441a (0.18) 437b → 442b (0.19)	HOMO α -1 → LUMO α +2 (0.10) HOMO α → LUMO α +2 (0.18) HOMO β → LUMO β +4 (0.19)	581.6	0.074	570	31.9
47	417b → 438b (0.44)	HOMO β -20 → LUMO β (0.44)	534.1	0.044		
52	435a → 442a (0.45) 415b → 438b (0.13) 437b → 442b (0.14)	HOMO α -3 → LUMO α +3 (0.45) HOMO β -22 → LUMO β (0.13) HOMO β → LUMO β +4 (0.14)	510.2	0.049		
25	424b → 438b (0.49)	HOMO β -13 → LUMO β (0.49)	687.1	0.028	657	12.6
27	422b → 438b (0.23) 423b → 438b (0.16)	HOMO β -15 → LUMO β (0.23) HOMO β -14 → LUMO β (0.16)	664.1	0.021		
28	438a → 439a (0.20) 421b → 438b (0.13)	HOMO α → LUMO α (0.20) HOMO β -16 → LUMO β (0.13)	675.2	0.055		
35	418b → 438b (0.10) 420b → 438b (0.47)	HOMO β -19 → LUMO β (0.10) HOMO β -17 → LUMO β (0.47)	617.4	0.038		
26	425b → 438b (0.21) 433b → 438b (0.35)	HOMO β -12 → LUMO β (0.21) HOMO β -4 → LUMO β (0.35)	737.0	0.041		
3	437b → 438b (0.91)	HOMO β → LUMO β (0.91)	2181.2	0.321	1350	3.4

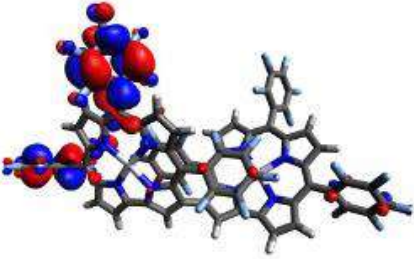
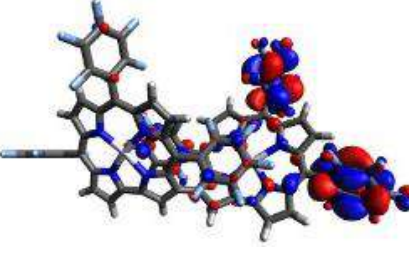
Table 5.10: Orbital energies of (1)⁺ from DFT-calculation.

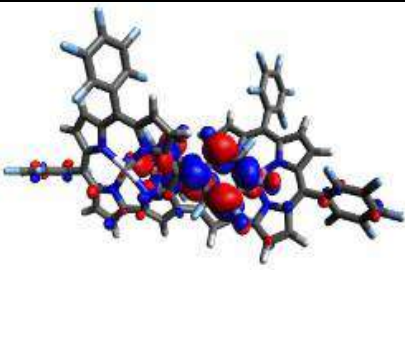
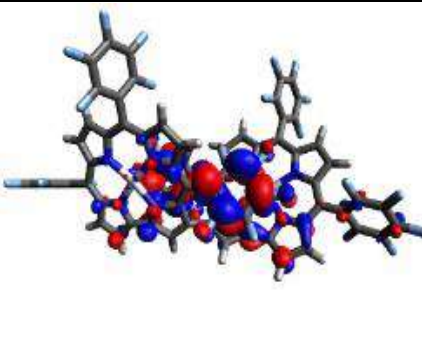
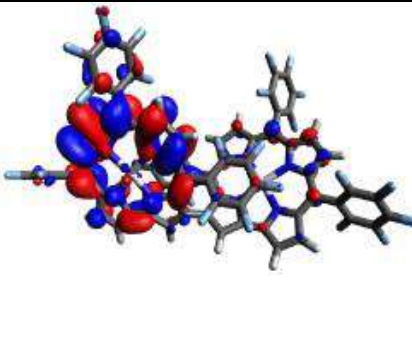
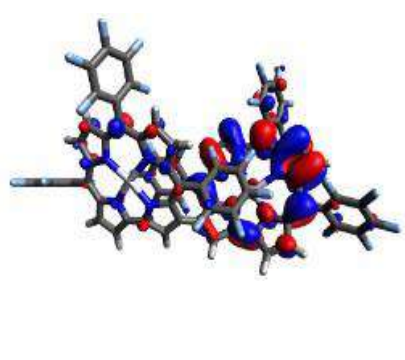
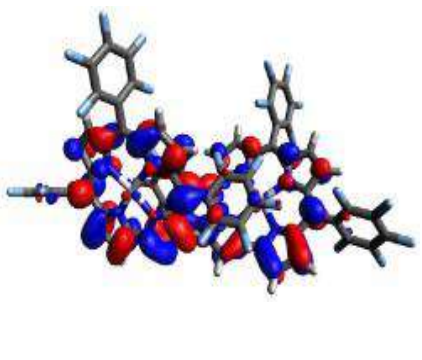
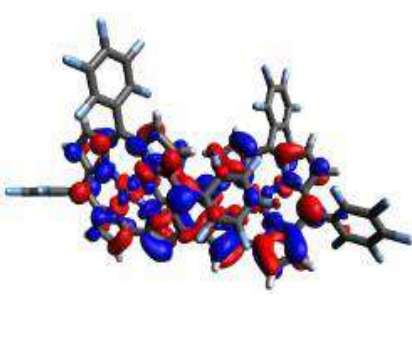
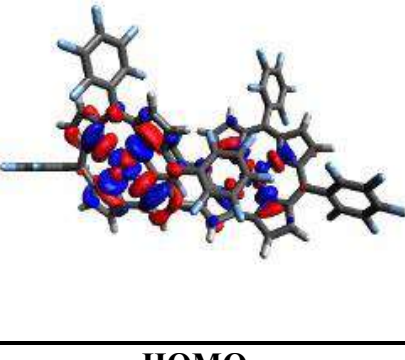
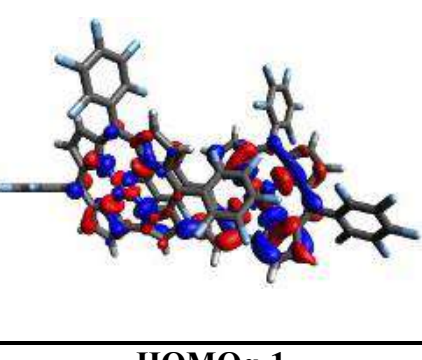
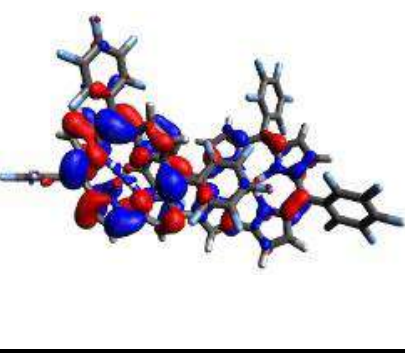
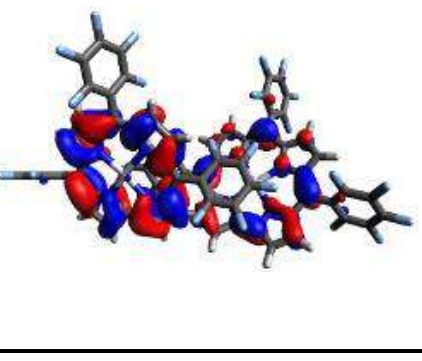
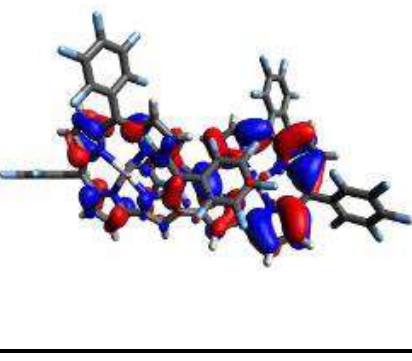
Spin up Orbitals alpha				Spin down orbitals beta			
Orbital No.	Orbital	Energy (Eh)	Energy (eV)	Orbital No.	Orbital	Energy (Eh)	Energy (eV)
445	LUMO α +6	-0.065361	-1.7786	445	LUMO β +7	-0.064450	-1.7538
444	LUMO α +5	-0.116782	-3.1778	444	LUMO β +6	-0.110936	-3.0187
443	LUMO α +4	-0.119803	-3.2600	443	LUMO β +5	-0.112787	-3.0691
442	LUMO α +3	-0.131146	-3.5687	442	LUMO β +4	-0.123745	-3.3673
441	LUMO α +2	-0.136925	-3.7259	441	LUMO β +3	-0.133285	-3.6269
440	LUMO α +1	-0.142875	-3.8878	440	LUMO β +2	-0.142532	-3.8785
439	LUMO α	-0.148440	-4.0393	439	LUMO β +1	-0.146945	-3.9986
438	HOMO α	-0.231316	-6.2944	438	LUMO β	-0.199664	-5.4331
437	HOMO α -1	-0.231699	-6.3049	437	HOMO β	-0.224665	-6.1134

436	HOMO α -2	-0.234701	-6.3865	436	HOMO β -1	-0.232457	-6.3255
435	HOMO α -3	-0.238313	-6.4848	435	HOMO β -2	-0.235648	-6.4123
434	HOMO α -4	-0.273221	-7.4347	434	HOMO β -3	-0.270819	-7.3694
433	HOMO α -5	-0.282150	-7.6777	433	HOMO β -4	-0.281928	-7.6717
432	HOMO α -6	-0.282314	-7.6822	432	HOMO β -5	-0.282090	-7.6761
431	HOMO α -7	-0.283128	-7.7043	431	HOMO β -6	-0.282211	-7.6793
430	HOMO α -8	-0.283207	-7.7064	430	HOMO β -7	-0.282931	-7.6989
429	HOMO α -9	-0.284154	-7.7322	429	HOMO β -8	-0.282963	-7.6998
428	HOMO α -10	-0.285823	-7.7776	428	HOMO β -9	-0.284547	-7.7429
427	HOMO α -1	-0.286814	-7.8046	427	HOMO β -10	-0.285972	-7.7817
426	HOMO α -12	-0.287471	-7.8225	426	HOMO β -11	-0.286100	-7.7852
425	HOMO α -13	-0.288715	-7.8563	425	HOMO β -12	-0.286929	-7.8077
424	HOMO α -14	-0.290059	-7.8929	424	HOMO β -13	-0.287924	-7.8348
423	HOMO α -15	-0.290719	-7.9109	423	HOMO β -14	-0.289982	-7.8908
422	HOMO α -16	-0.292220	-7.9517	422	HOMO β -15	-0.290842	-7.9142
421	HOMO α -17	-0.293030	-7.9738	421	HOMO β -16	-0.291715	-7.9380
420	HOMO α -18	-0.293774	-7.9940	420	HOMO β -17	-0.292501	-7.9593
419	HOMO α -19	-0.296073	-8.0566	419	HOMO β -18	-0.295070	-8.0293
418	HOMO α -20	-0.298532	-8.1235	418	HOMO β -19	-0.296994	-8.0816
417	HOMO α -21	-0.304650	-8.2900	417	HOMO β -20	-0.302994	-8.2449
416	HOMO α -22	-0.310877	-8.4594	416	HOMO β -21	-0.309422	-8.4198
415	HOMO α -23	-0.314796	-8.5660	415	HOMO β -22	-0.312884	-8.5140

5.7.2.2 Molecular orbitals and orbital energies for (1)⁺⁺:

Table 5.11: Composition of all specific molecular orbitals with alpha spin for (1)⁺⁺

	LUMO α +9	LUMO α +8
		
LUMO α +7	LUMO α +6	LUMO α +5

		
LUMOα+4	LUMOα+3	LUMOα+2
		
LUMOα+1	LUMOα	
		
HOMOα	HOMOα-1	HOMOα-2
		
HOMOα-3	HOMOα-4	HOMOα-5

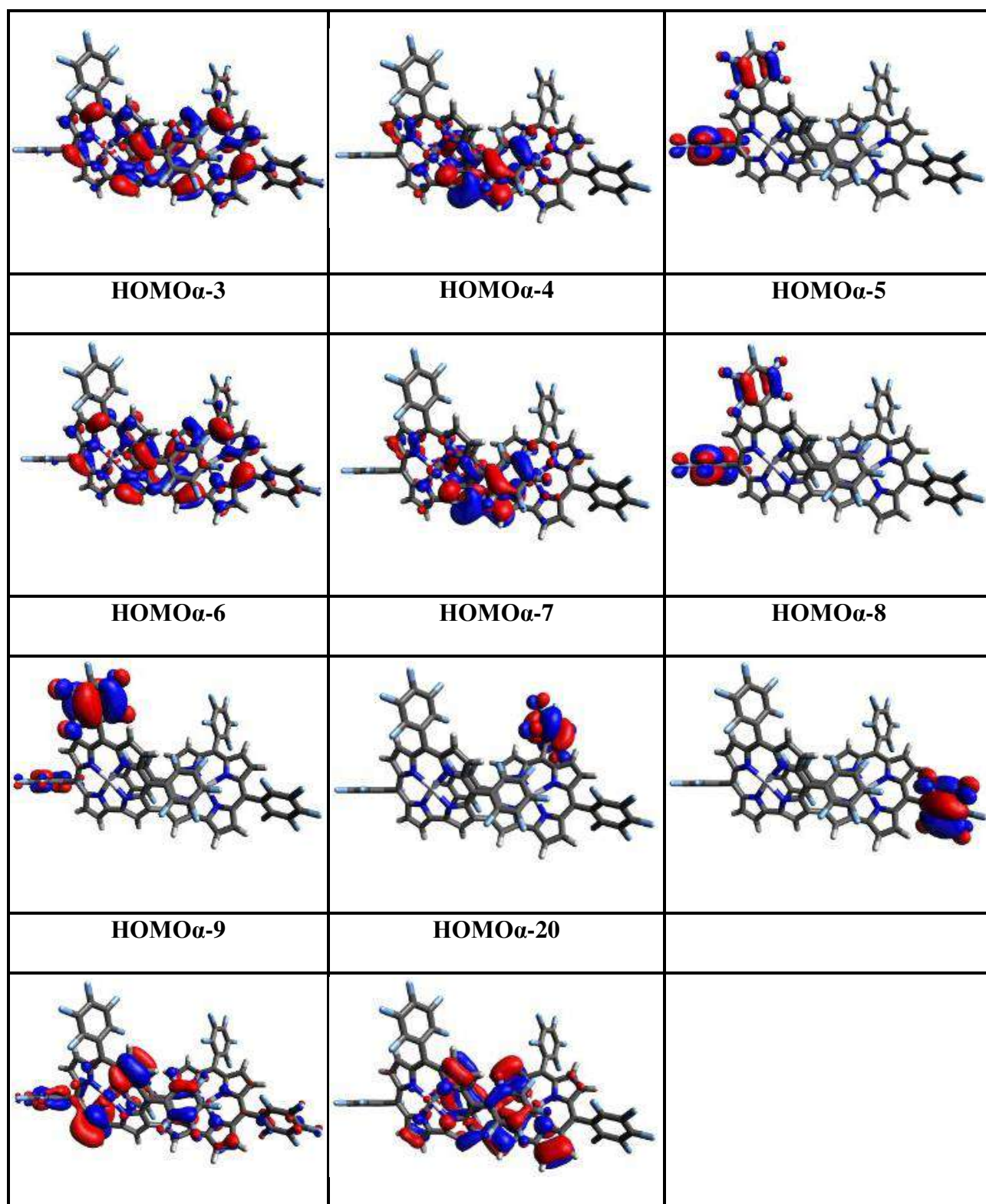
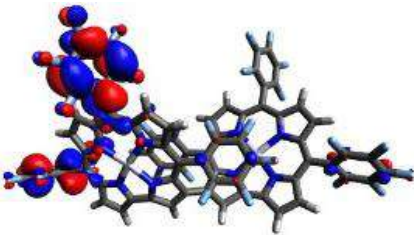
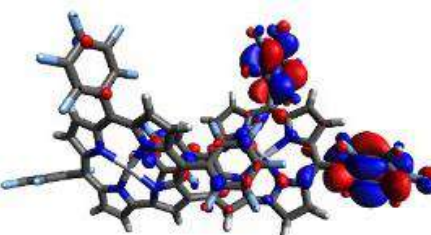
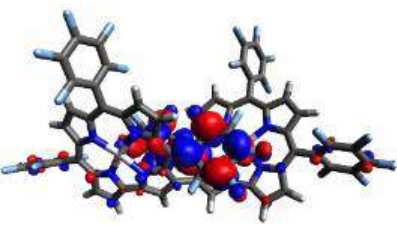
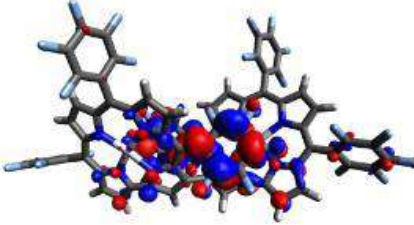
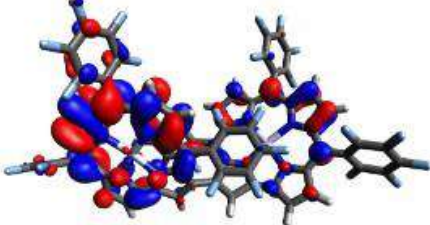
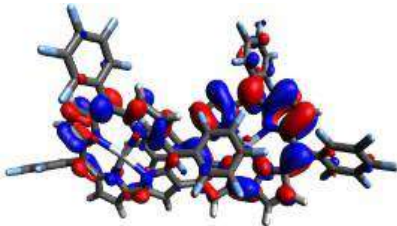
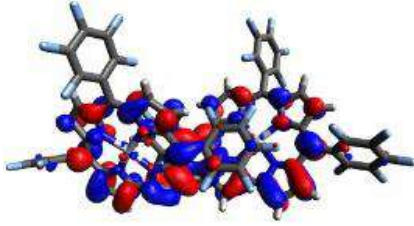
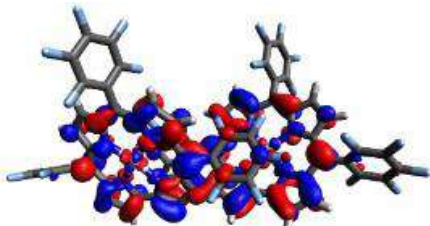
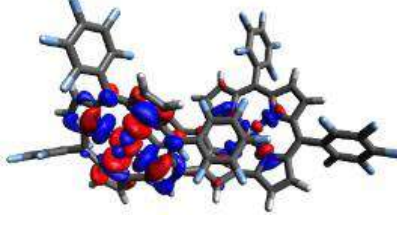
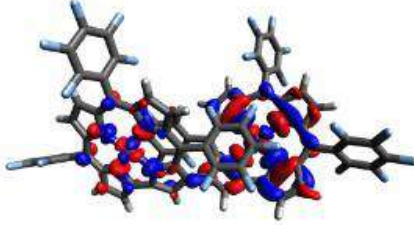
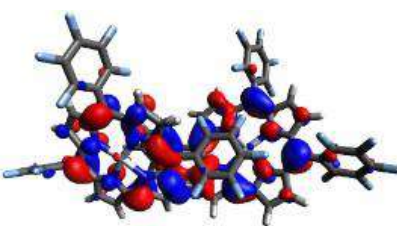
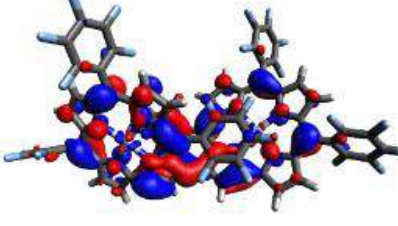
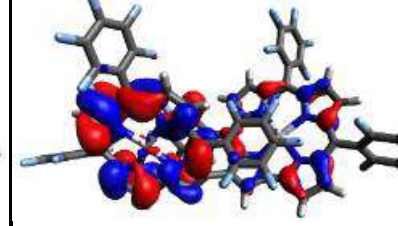
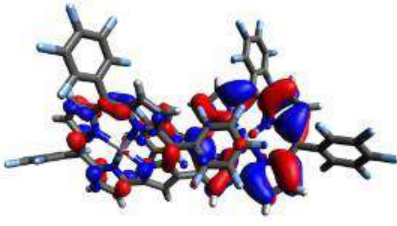
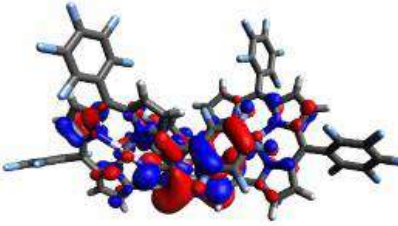
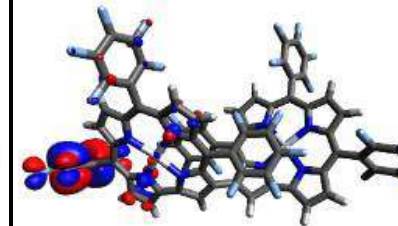
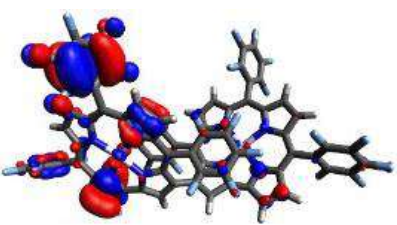
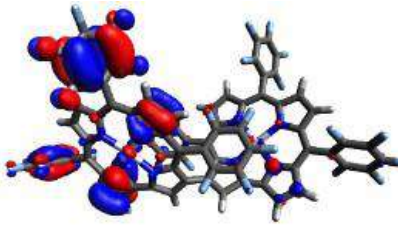
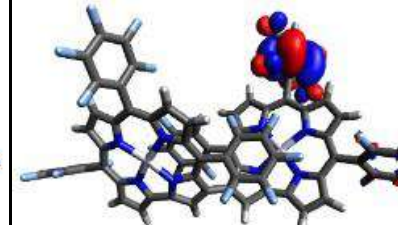
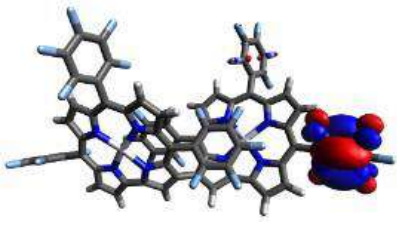
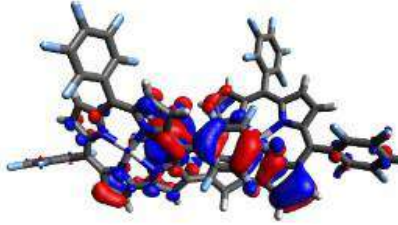
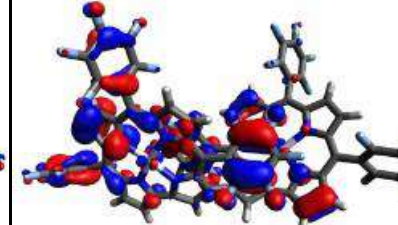
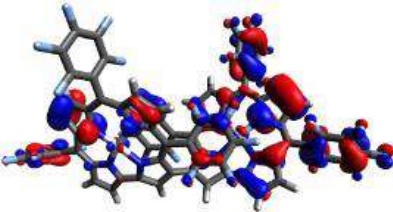
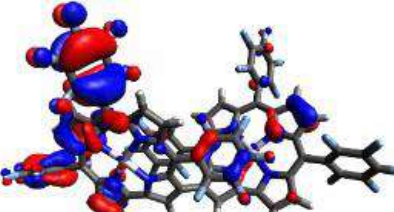
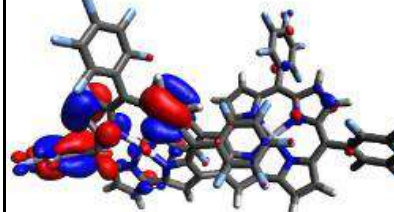
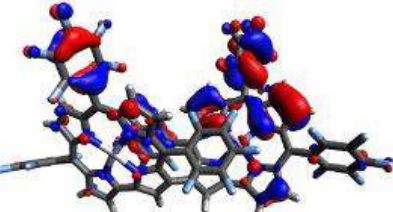
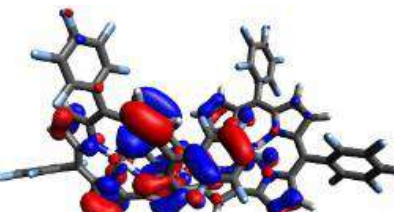
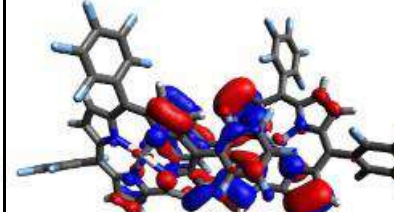
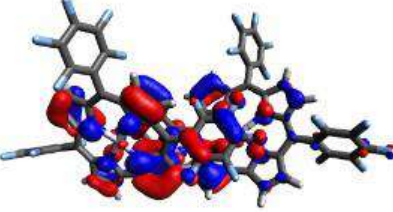


Table 5.12: Composition of selected molecular orbitals with beta spin of (1)⁺⁺.

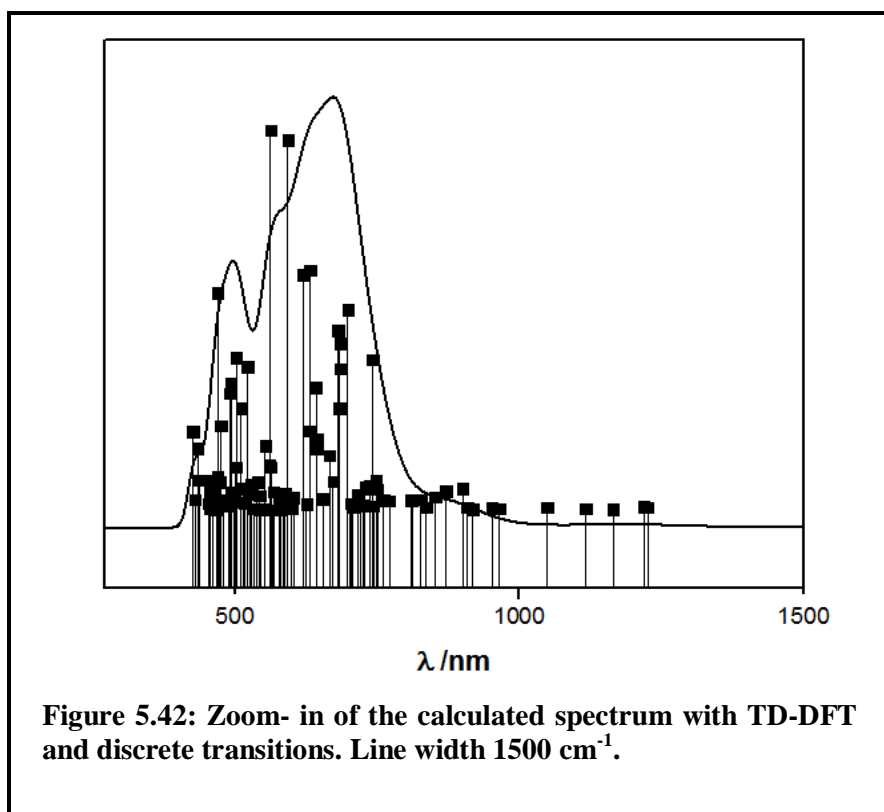
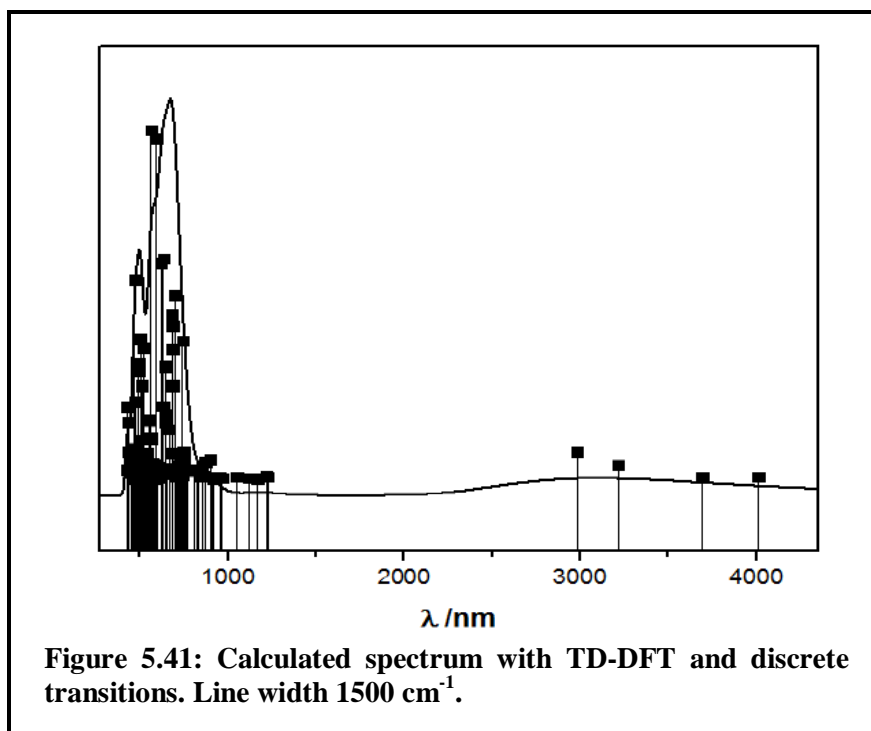
	LUMO β +9	LUMO β +8
		
LUMO β +7	LUMO β +6	LUMO β +5
		
LUMO β +4	LUMO β +3	LUMO β +2
		
LUMO β +1	LUMO β	
		
HOMO β	HOMO β -1	HOMO β -2

		
HOMOB-3	HOMOB-4	HOMOB-5
		
HOMOB-6	HOMOB-7	HOMOB-8
		
HOMOB-9	HOMOB-12	HOMOB-13
		
HOMOB-14	HOMOB-15	HOMOB-16

		
HOMOB-17	HOMOB-19	HOMOB-20
		
HOMOB-22		
		

5.7.3 TD-DFT Calculations for 1^{2+} (Triplet):

5.7.3.1 Calculated spectra, Comparison with Experimental spectrum and TD-DFT Transitions of 1^{2+}



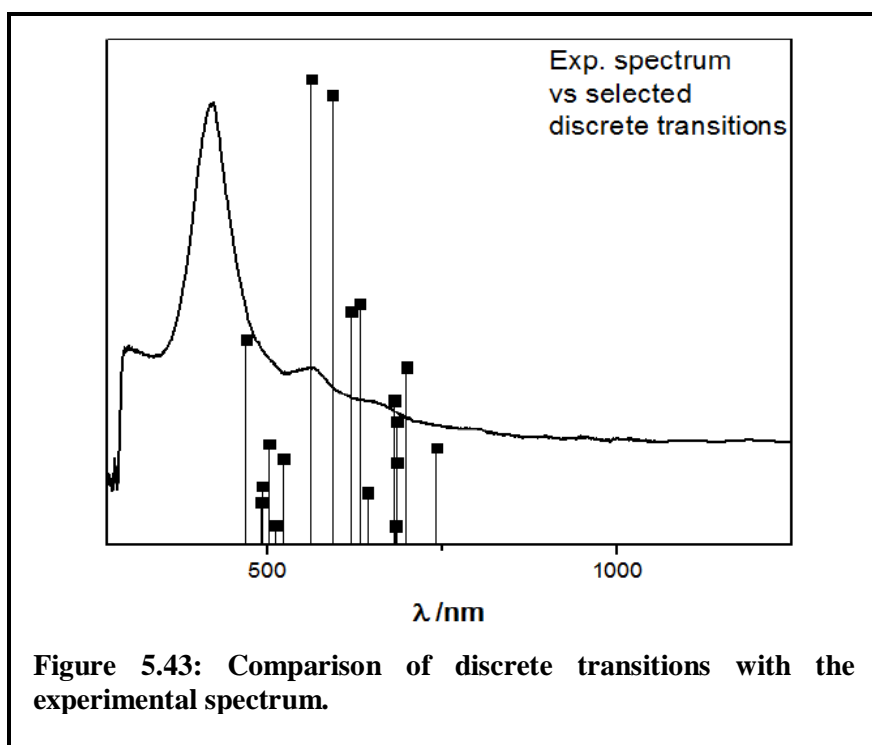


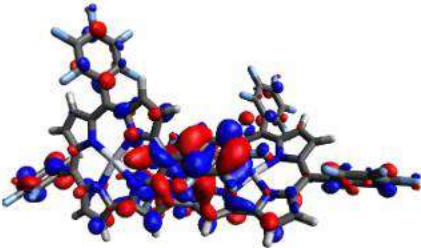
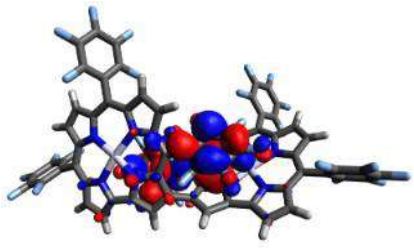
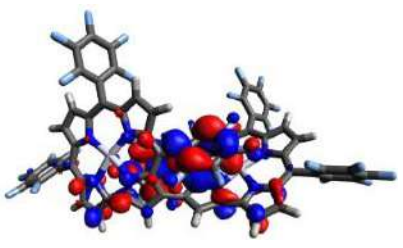
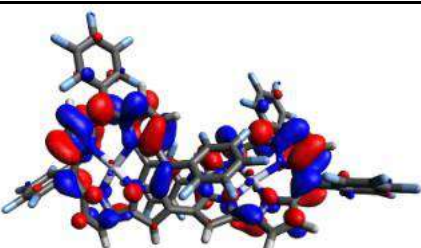
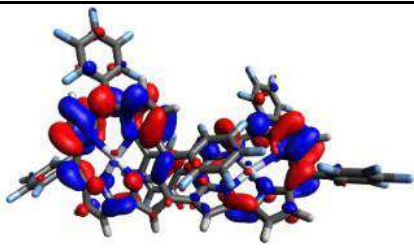
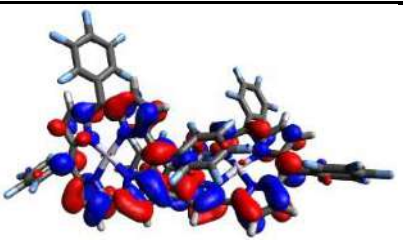
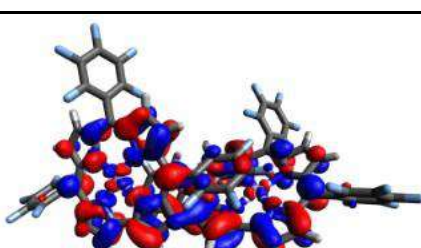
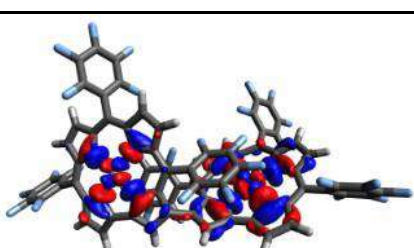
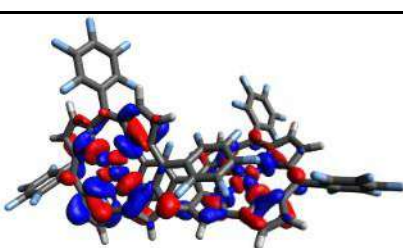
Table 5.13: TD-DFT calculated electronic transitions of (1)²⁺. (Including raw data)

State	Transition	Transition HOMO LUMO	Calculated Transition energy	Oscillator strength	Experimental transition energy	Molar absorption coefficient 10 ³
78	415b → 438b (0.37)	HOMOβ-21 → LUMOβ+1 (0.37)	468.9	0.048	422	101.6
53	437a → 444a (0.10) 438a → 443a (0.21)	HOMOα-1 → LUMOα+5 (0.10) HOMOα → LUMOα+4 (0.21)	562.0	0.083		
47	435a → 440a (0.13) 436a → 441a (0.19) 437a → 441a (0.12) 419b → 437b (0.10)	HOMOα-3 → LUMOα+1 (0.13) HOMOα-2 → LUMOα+2 (0.19) HOMOα-1 → LUMOα+2 (0.12) HOMOβ-17 → LUMOβ (0.10)	592.3	0.081		
37	435a → 440a (0.19) Mixed	HOMOα-3 → LUMOα+1 (0.19) mixed	631.6	0.053	563	22.5
41	418b → 437b (0.23) Mixed	HOMOβ-18 → LUMOβ (0.23) mixed	619.2	0.051		
----- -	-----	-----	-----	-----	653	12.5
17	431b → 437b (0.37) 431b → 438b (0.30)	HOMOβ-5 → LUMOβ (0.37) HOMOβ-5 → LUMOβ+1 (0.30)	908.0	0.001	900-1400	1.3
28	431b → 437b (0.43) 431b → 438b (0.51)	HOMOβ-5 → LUMOβ (0.43) HOMOβ-5 → LUMOβ+1 (0.51)	1225.5	0.001		
30	432b → 437b (0.46) 432b → 438b (0.46)	HOMOβ-4 → LUMOβ (0.46) HOMOβ-4 → LUMOβ+1 (0.46)	1218.2	0.001		
34	433b → 437b (0.17) 433b → 438b (0.62)	HOMOβ-3 → LUMOβ (0.17) HOMOβ-3 → LUMOβ+1 (0.62)	1048.4	0.001		

3	435b \rightarrow 437b (0.19) 435b \rightarrow 438b (0.34) 436b \rightarrow 437b (0.31) 436b \rightarrow 438b (0.12)	HOMO β -1 \rightarrow LUMO β (0.19) HOMO β -1 \rightarrow LUMO β +1 (0.34) HOMO β \rightarrow LUMO β (0.31) HOMO β \rightarrow LUMO β +1 (0.12)	3214.2	0.003	2000-2400+	
4	435b \rightarrow 437b (0.23) 435b \rightarrow 438b (0.30) 436b \rightarrow 438b (0.41)	HOMO β -1 \rightarrow LUMO β (0.23) HOMO β -1 \rightarrow LUMO β +1 (0.30) HOMO β \rightarrow LUMO β +1 (0.41)	2981.6	0.006		
1	435b \rightarrow 437b (0.36) 435b \rightarrow 438b (0.11) 436b \rightarrow 437b (0.37) 436b \rightarrow 438b (0.13)	HOMO β -1 \rightarrow LUMO β (0.36) HOMO β -1 \rightarrow LUMO β +1 (0.11) HOMO β \rightarrow LUMO β (0.37) HOMO β \rightarrow LUMO β +1 (0.13)	4011.5	0.001		
2	435b \rightarrow 437b (0.19) 435b \rightarrow 438b (0.22) 436b \rightarrow 437b (0.25) 436b \rightarrow 438b (0.31)	HOMO β -1 \rightarrow LUMO β (0.19) HOMO β -1 \rightarrow LUMO β +1 (0.22) HOMO β \rightarrow LUMO β (0.25) HOMO β \rightarrow LUMO β +1 (0.31)	3689.6	0.00049		

5.7.3.2 Molecular and orbital energies of 1^{2+} :

Table 5.14: Composition of selected molecular orbitals with alpha spin of $(1)^{2+}$.

LUMO α +9	LUMO α +8	LUMO α +7
		
LUMO α +6	LUMO α +5	LUMO α +4
		
LUMO α +3	LUMO α +2	LUMO α +1
		
LUMO α		

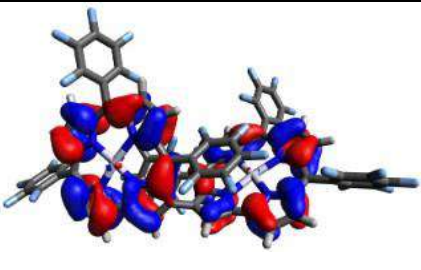
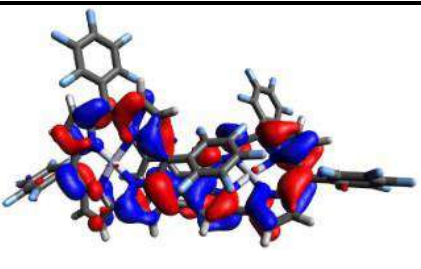
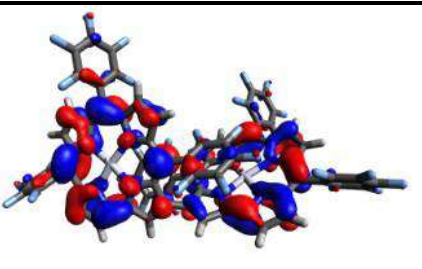
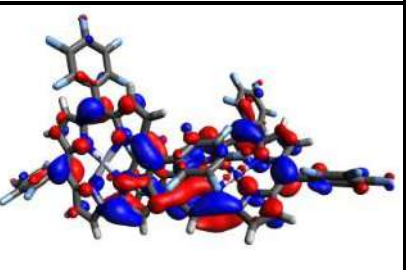
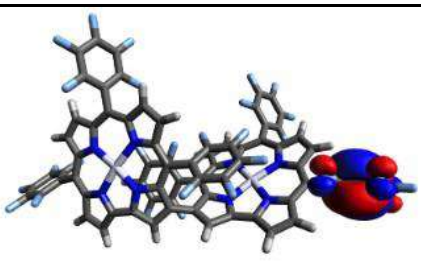
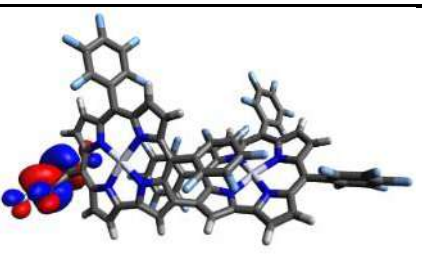
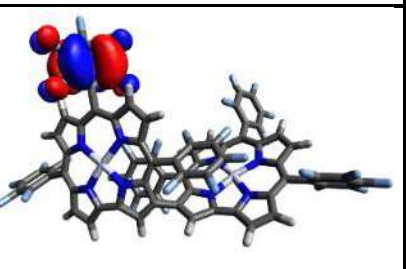
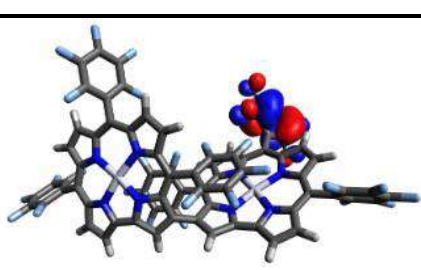
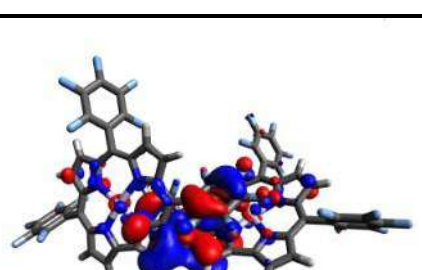
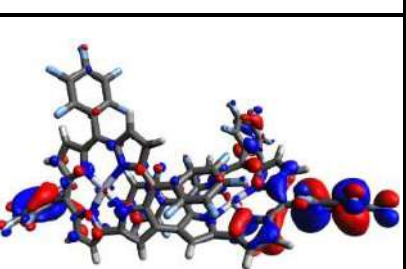
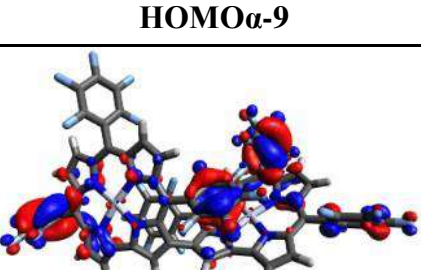
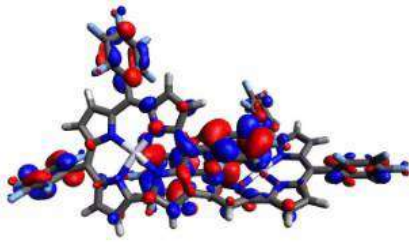
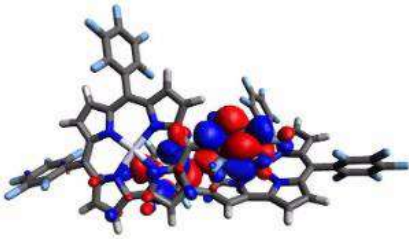
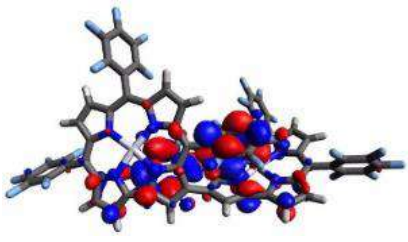
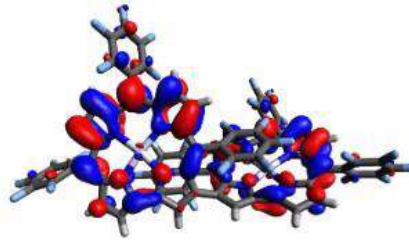
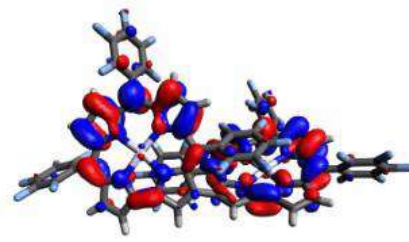
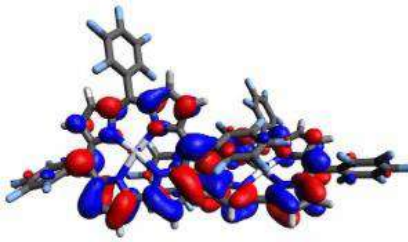
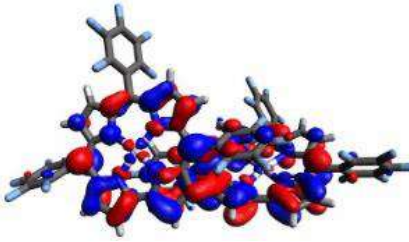
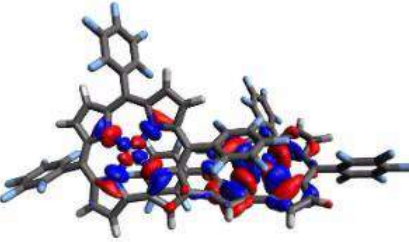
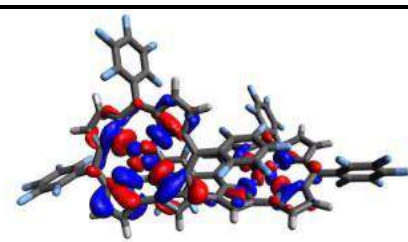
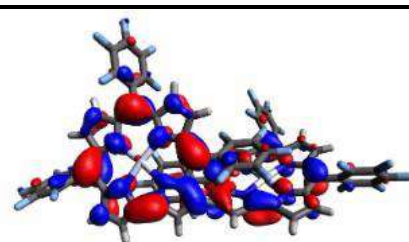
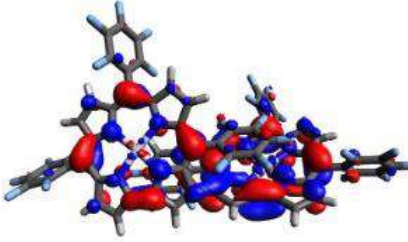
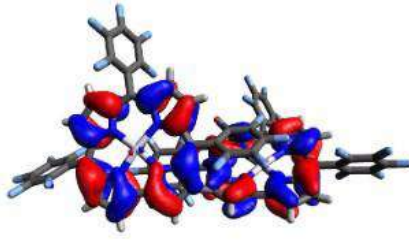
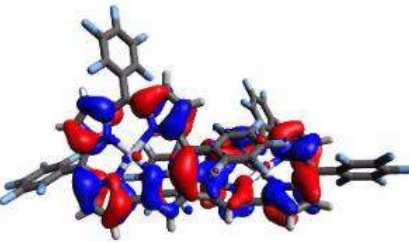
		
HOMOα	HOMOα-1	HOMOα-2
		
HOMOα-3	HOMOα-4	HOMOα-5
		
HOMOα-6	HOMOα-7	HOMOα-8
		
HOMOα-9		
		

Table 5.15: Composition of selected molecular orbitals with beta spin of (1)²⁺.

	LUMOβ+9	LUMOβ+8
		
LUMOβ+7	LUMOβ+6	LUMOβ+5
		
LUMOβ+4	LUMOβ+3	LUMOβ+2
		
LUMOβ+1	LUMOβ	
		
HOMOβ	HOMOβ-1	HOMOβ-2
		
HOMOβ -3	HOMOβ-4	HOMOβ-5

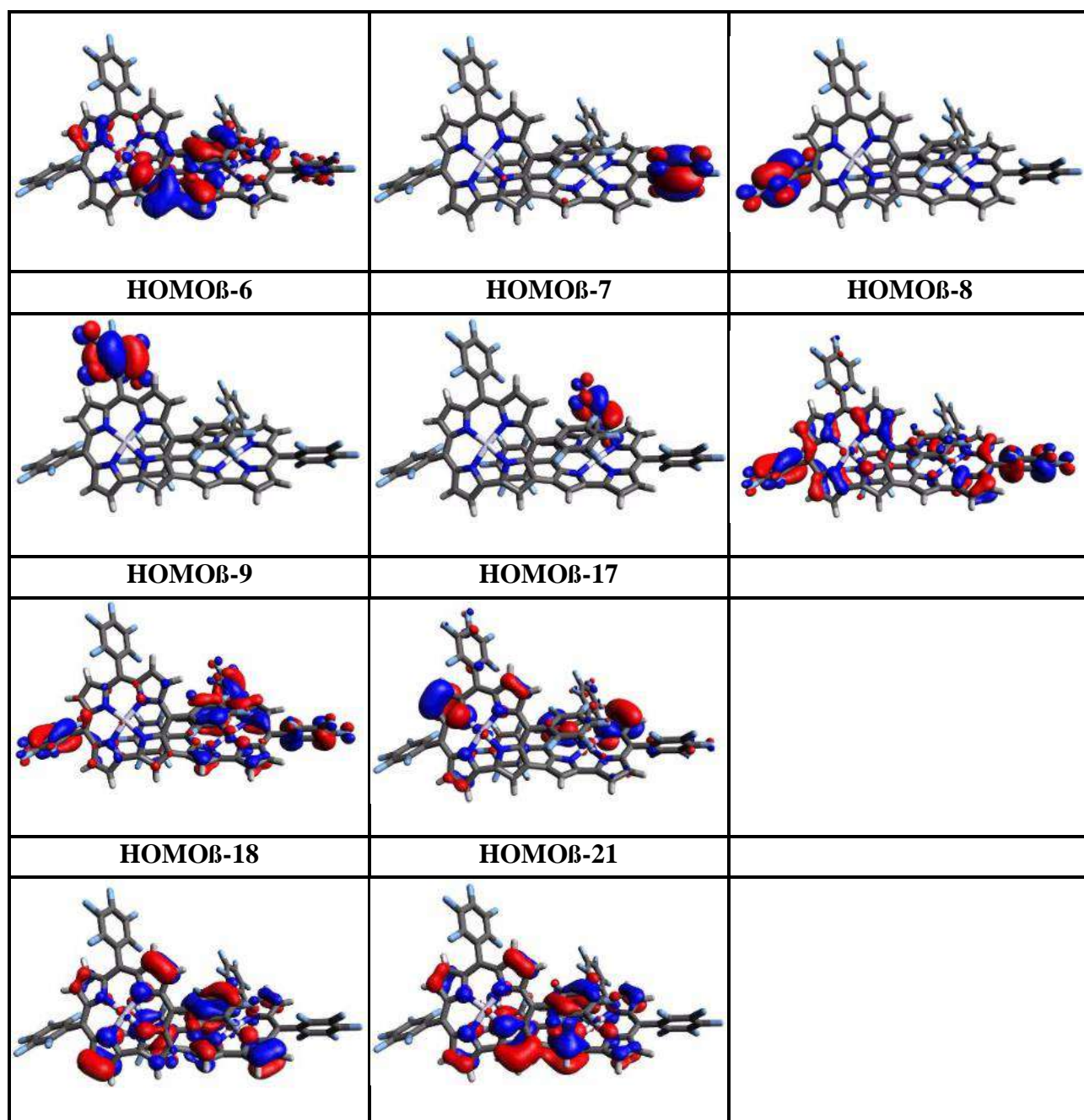
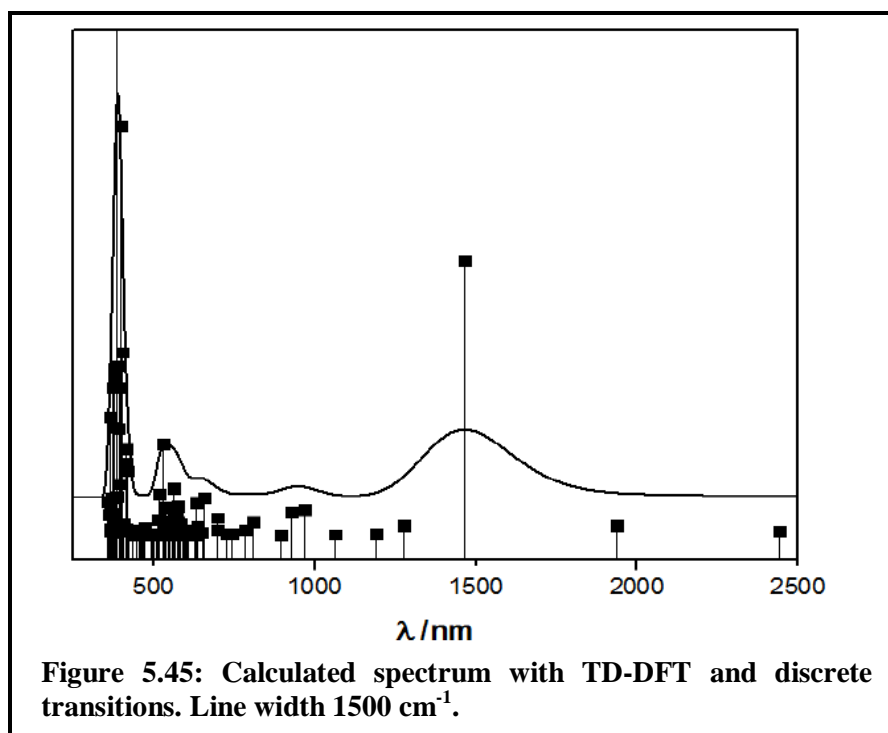
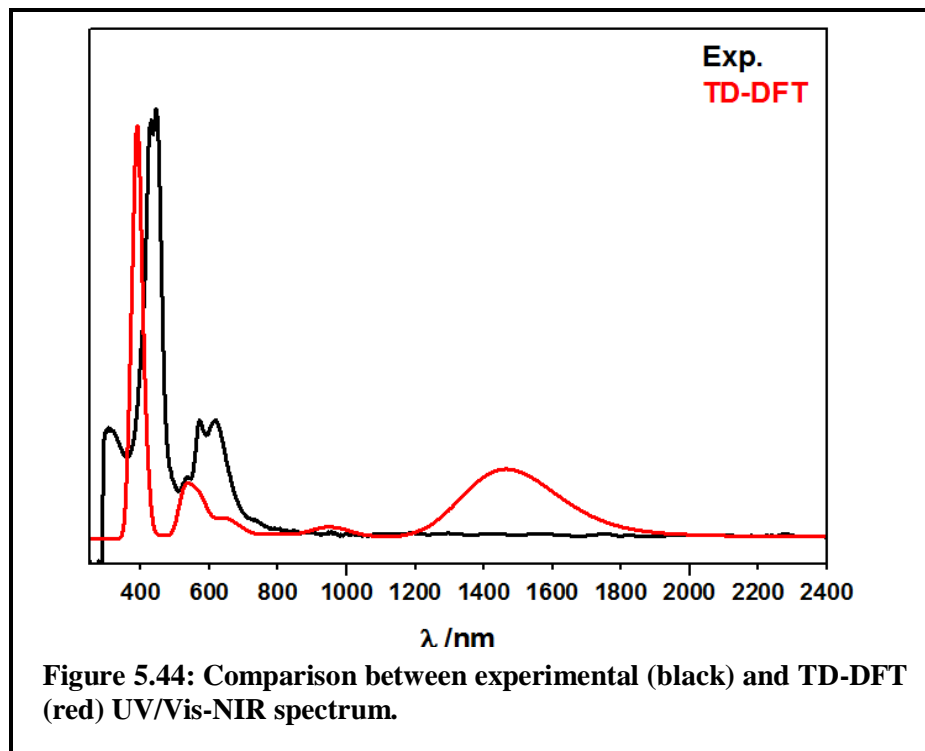


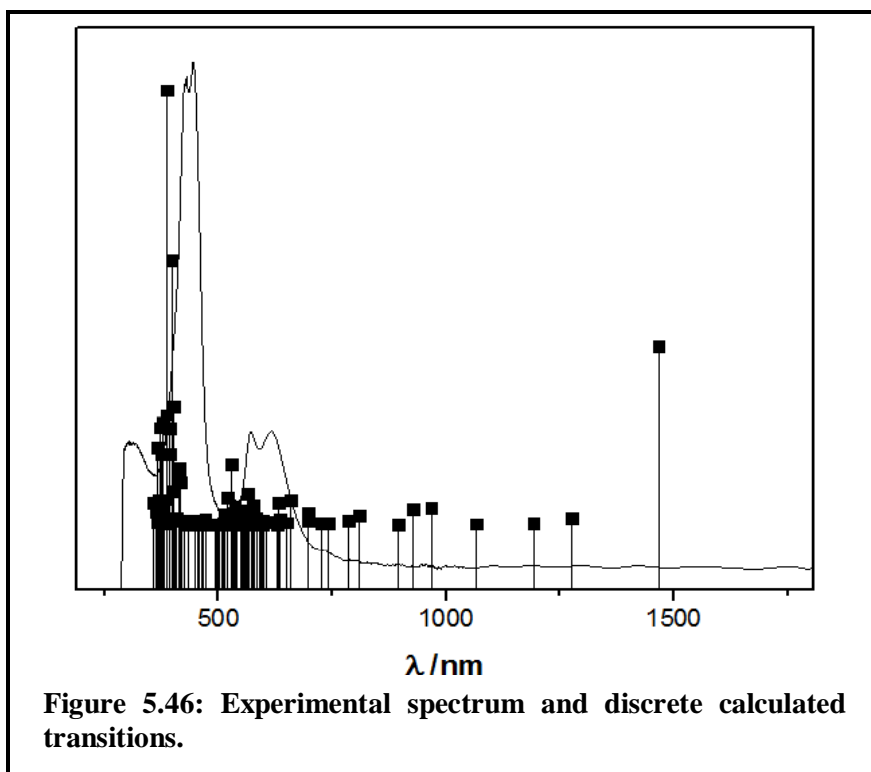
Table 5.16: Orbital energies of (1)²⁺ from DFT-calculation.

Spin up Orbitals alpha				Spin down orbitals beta			
Orbital No.	Orbital	Energy (Eh)	Energy (eV)	Orbital No.	Orbital	Energy (Eh)	Energy (eV)
450	LUMO α +11	-0.071765	-1.9528	450	LUMO β +13	-0.070514	-1.9188
449	LUMO α +10	-0.072618	-1.9760	449	LUMO β +12	-0.071505	-1.9458
448	LUMO α +9	-0.073926	-2.0116	448	LUMO β +11	-0.072508	-1.9731
447	LUMO α +8	-0.077664	-2.1133	447	LUMO β +10	-0.075415	-2.0522
446	LUMO α +7	-0.086485	-2.3534	446	LUMO β +9	-0.085058	-2.3146
445	LUMO α +6	-0.088444	-2.4067	445	LUMO β +8	-0.086227	-2.3464
444	LUMO α +5	-0.143713	-3.9106	444	LUMO β +7	-0.131137	-3.5684
443	LUMO α +4	-0.145729	-3.9655	443	LUMO β +6	-0.132815	-3.6141
442	LUMO α +3	-0.157741	-4.2923	442	LUMO β +5	-0.144418	-3.9298
441	LUMO α +2	-0.162808	-4.4302	441	LUMO β +4	-0.151086	-4.1112
440	LUMO α +1	-0.171354	-4.6628	440	LUMO β +3	-0.168883	-4.5955
439	LUMO α	-0.176087	-4.7916	439	LUMO β +2	-0.172999	-4.7075
438	HOMO α	-0.256306	-6.9744	438	LUMO β +1	-0.215445	-5.8626
437	HOMO α -1	-0.257544	-7.0081	437	LUMO β	-0.219258	-5.9663
436	HOMO α -2	-0.260858	-7.0983	436	HOMO β	-0.258400	-7.0314
435	HOMO α -3	-0.263207	-7.1622	435	HOMO β -1	-0.259655	-7.0656
434	HOMO α -4	-0.296005	-8.0547	434	HOMO β -2	-0.294681	-8.0187
433	HOMO α -5	-0.296525	-8.0689	433	HOMO β -3	-0.295596	-8.0436
432	HOMO α -6	-0.296891	-8.0788	432	HOMO β -4	-0.296030	-8.0554
431	HOMO α -7	-0.297111	-8.0848	431	HOMO β -5	-0.296409	-8.0657
430	HOMO α -8	-0.297674	-8.1001	430	HOMO β -6	-0.296627	-8.0716
429	HOMO α -9	-0.303879	-8.2690	429	HOMO β -7	-0.301226	-8.1968
428	HOMO α -10	-0.304838	-8.2951	428	HOMO β -8	-0.302668	-8.2360
427	HOMO α -1	-0.305380	-8.3098	427	HOMO β -9	-0.303291	-8.2530
426	HOMO α -12	-0.307000	-8.3539	426	HOMO β -10	-0.304190	-8.2774
425	HOMO α -13	-0.307828	-8.3764	425	HOMO β -11	-0.306469	-8.3394
424	HOMO α -14	-0.309509	-8.4222	424	HOMO β -12	-0.307417	-8.3652
423	HOMO α -15	-0.311305	-8.4711	423	HOMO β -13	-0.307645	-8.3714
422	HOMO α -16	-0.313039	-8.5182	422	HOMO β -14	-0.309325	-8.4172
421	HOMO α -17	-0.314360	-8.5542	421	HOMO β -15	-0.310152	-8.4397
420	HOMO α -18	-0.314763	-8.5651	420	HOMO β -16	-0.310415	-8.4468
419	HOMO α -19	-0.320019	-8.7082	419	HOMO β -17	-0.316935	-8.6242
418	HOMO α -20	-0.321167	-8.7394	418	HOMO β -18	-0.317648	-8.6437
417	HOMO α -21	-0.327313	-8.9067	417	HOMO β -19	-0.322607	-8.7786
416	HOMO α -22	-0.334104	-9.0914	416	HOMO β -20	-0.330423	-8.9913
415	HOMO α -23	-0.338443	-9.2095	415	HOMO β -21	-0.333686	-9.0801

5.7.4 TD-DFT Calculations of (1)⁻ (doublet):

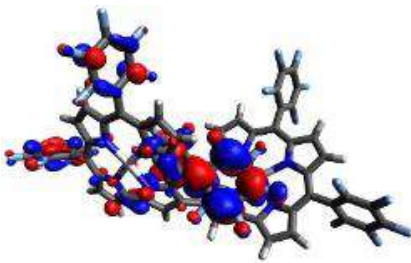
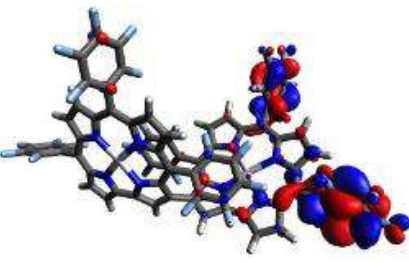
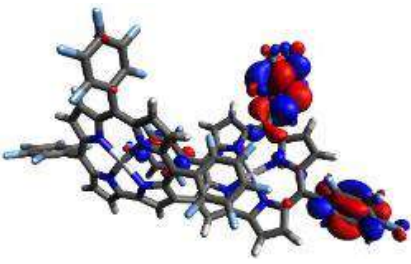
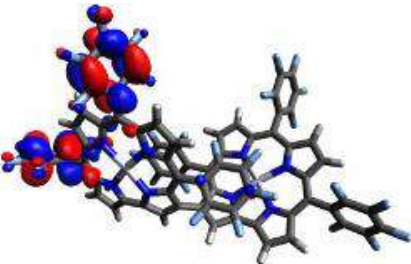
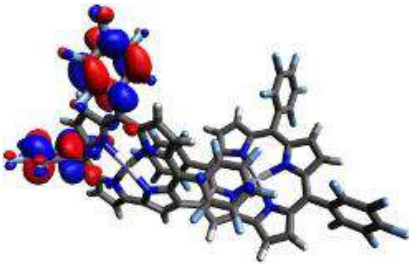
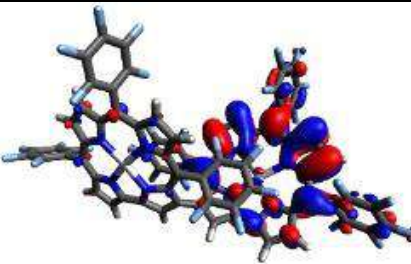
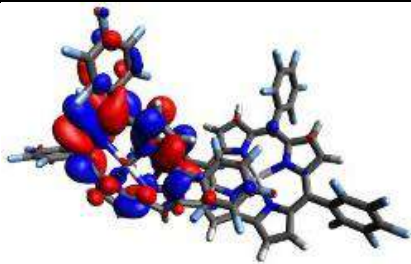
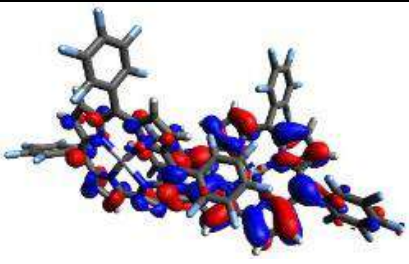
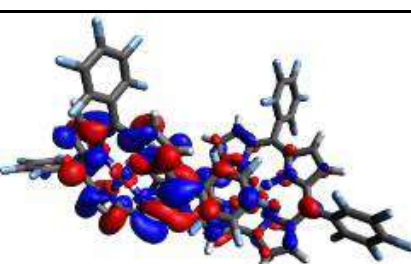
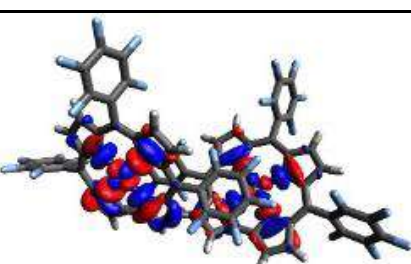
5.7.4.1 Calculated spectra, Comparison with Experimental spectrum and TD-DFT Transitions of (1)⁻:



Table 5.17: TD-DFT calculated electronic transitions of (1)⁺. (Including raw data)

State	Transition	Transition HOMO LUMO	Calculated Transition energy	Oscillator strength	Experimental transition energy	Molar absorption coefficient 10^3
3	439a → 440a (0.61)	HOMOα → LUMOα (0.61)	1466.9	0.372	1100	
	439a → 442a (0.16)	HOMOα → LUMOα+2 (0.16)				
7	437a → 440a (0.71)	HOMOα-2 → LUMOα (0.71)	967.5	0.033		
8	435a → 440a (0.16)	HOMOα-4 → LUMOα (0.16)	929.0	0.031		
	436a → 440a (0.67)	HOMOα-3 → LUMOα (0.67)				
15	438b → 439b (0.31)	HOMOβ → LUMOβ (0.31)	657.7	0.050	616	
	438b → 444b (0.23)	HOMOβ → LUMOβ+5 (0.23)				
25	436a → 441a (0.27)	HOMOα-3 → LUMOα+1 (0.27)	563.8	0.063	571	
	438b → 441b (0.12)	HOMOβ → LUMOβ+2 (0.12)				
34	436a → 442a (0.24)	HOMOα-3 → LUMOα+2 (0.24)	529.4	0.123		
	436b → 440b (0.15)	HOMOβ-2 → LUMOβ+1 (0.15)				
77	427a → 440a (0.11)	HOMOα-12 → LUMOα (0.11)	402.2	0.247	430	
	429a → 440a (0.13)	HOMOα-10 → LUMOα (0.13)				
83	434a → 442a (0.18)	HOMOα-5 → LUMOα+2 (0.18)	386.8	0.228		
89	425a → 440a (0.37)	HOMOα-14 → LUMOα (0.37)	377.8	0.212		
92	434b → 444b (0.13)	HOMOβ-4 → LUMOβ+5 (0.13)	372.5	0.200		

5.7.4.2 Orbital plots Molecular and orbital energies for (1)^{•-}:Table 5.18: Composition of selected molecular orbitals with alpha spin of (1)^{•-}.

	LUMO α +9	LUMO α +8
		
LUMO α +7	LUMO α +6	LUMO α +5
		
LUMO α +4	LUMO α +3	LUMO α +2
		
LUMO α +1	LUMO α	
		
HOMO α	HOMO α -1	HOMO α -2

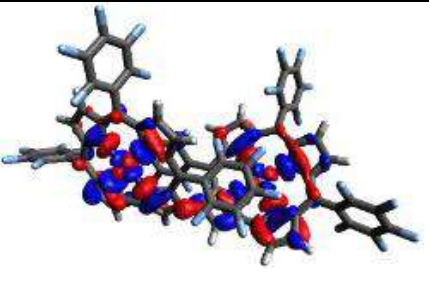
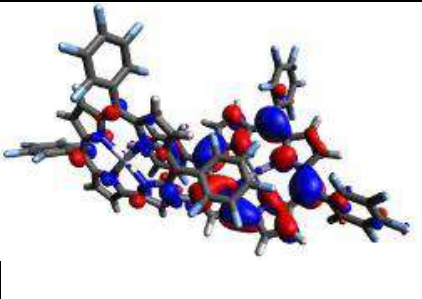
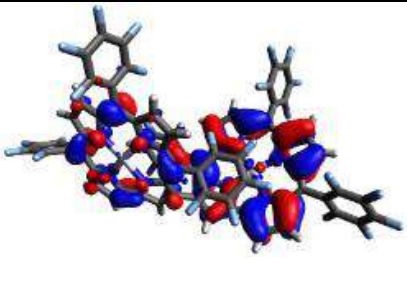
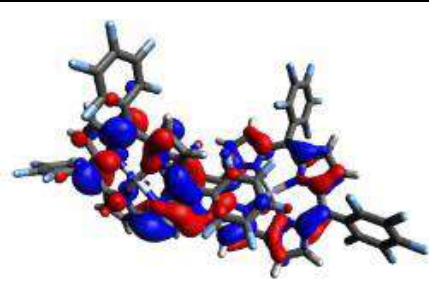
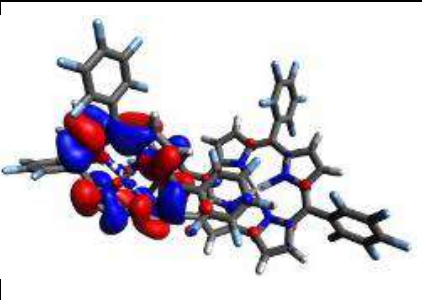
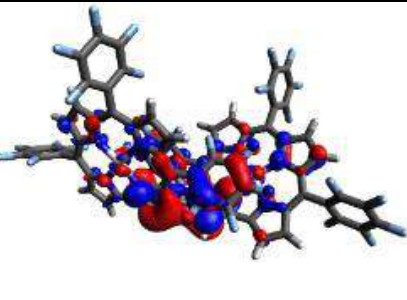
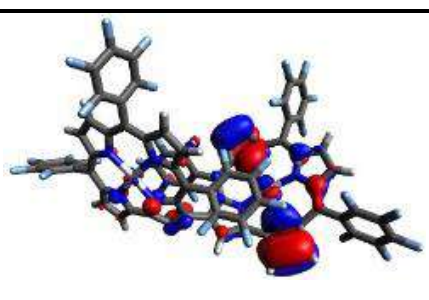
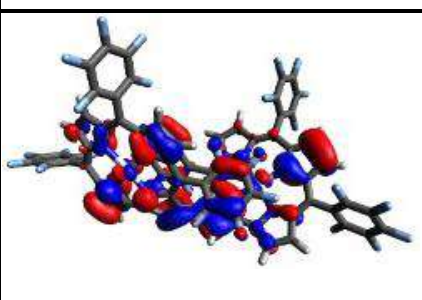
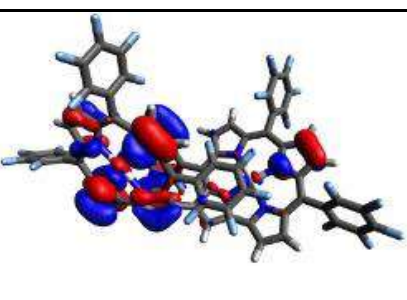
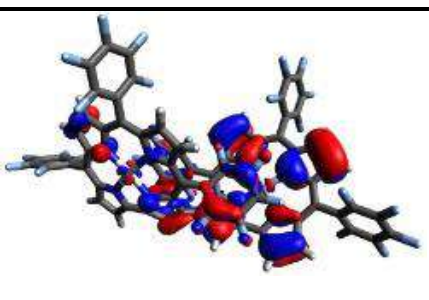
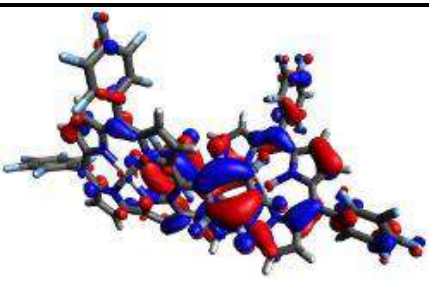
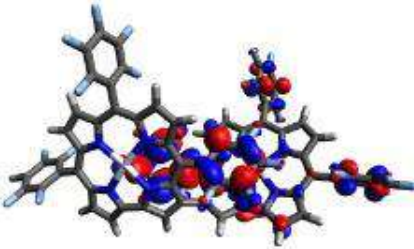
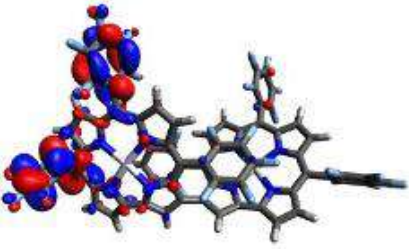
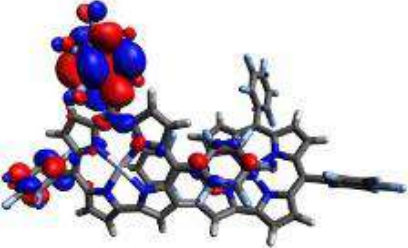
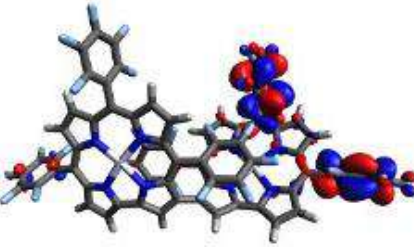
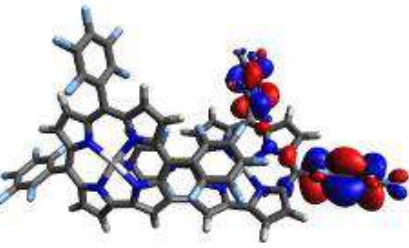
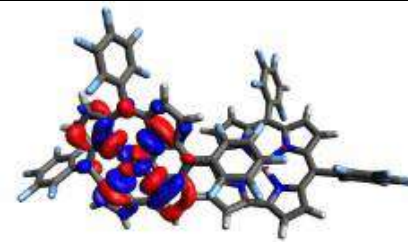
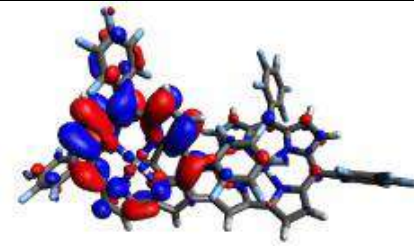
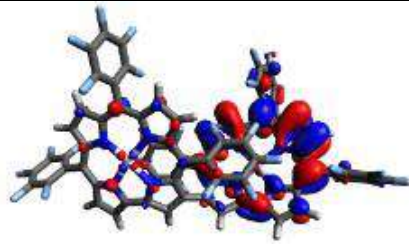
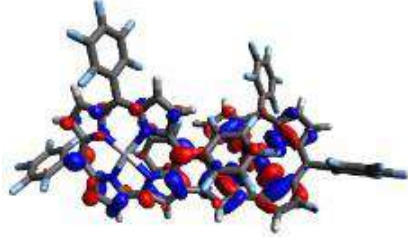
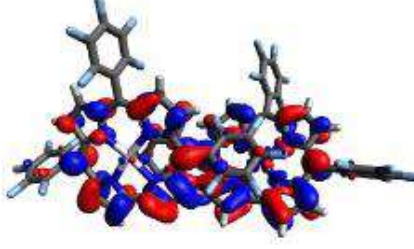
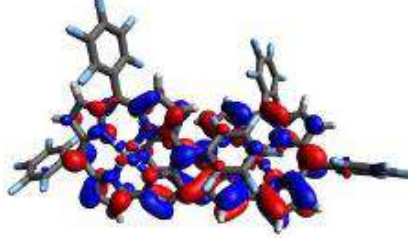
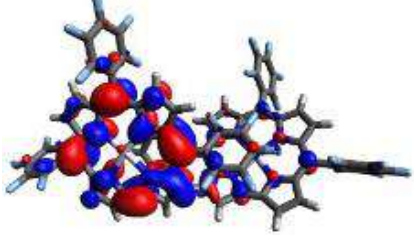
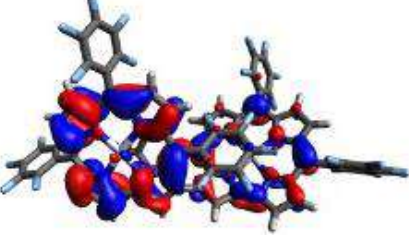
		
HOMOα-3	HOMOα-4	HOMOα-5
		
HOMOα-6	HOMOα-7	HOMOα-8
		
HOMOα-9	HOMOα-10	HOMOα-12
		
HOMOα-14		
		

Table 5.19: Composition of selected molecular orbitals with beta spin of (1)⁺.

	LUMOB+9	LUMOB+8
		
LUMOB+7	LUMOB+6	LUMOB+5
		
LUMOB+4	LUMOB+3	LUMOB+2
		
LUMOB+1	LUMOB	
		
HOMOB	HOMOB-1	HOMOB-2
		
HOMOB-3	HOMOB-4	HOMOB-5

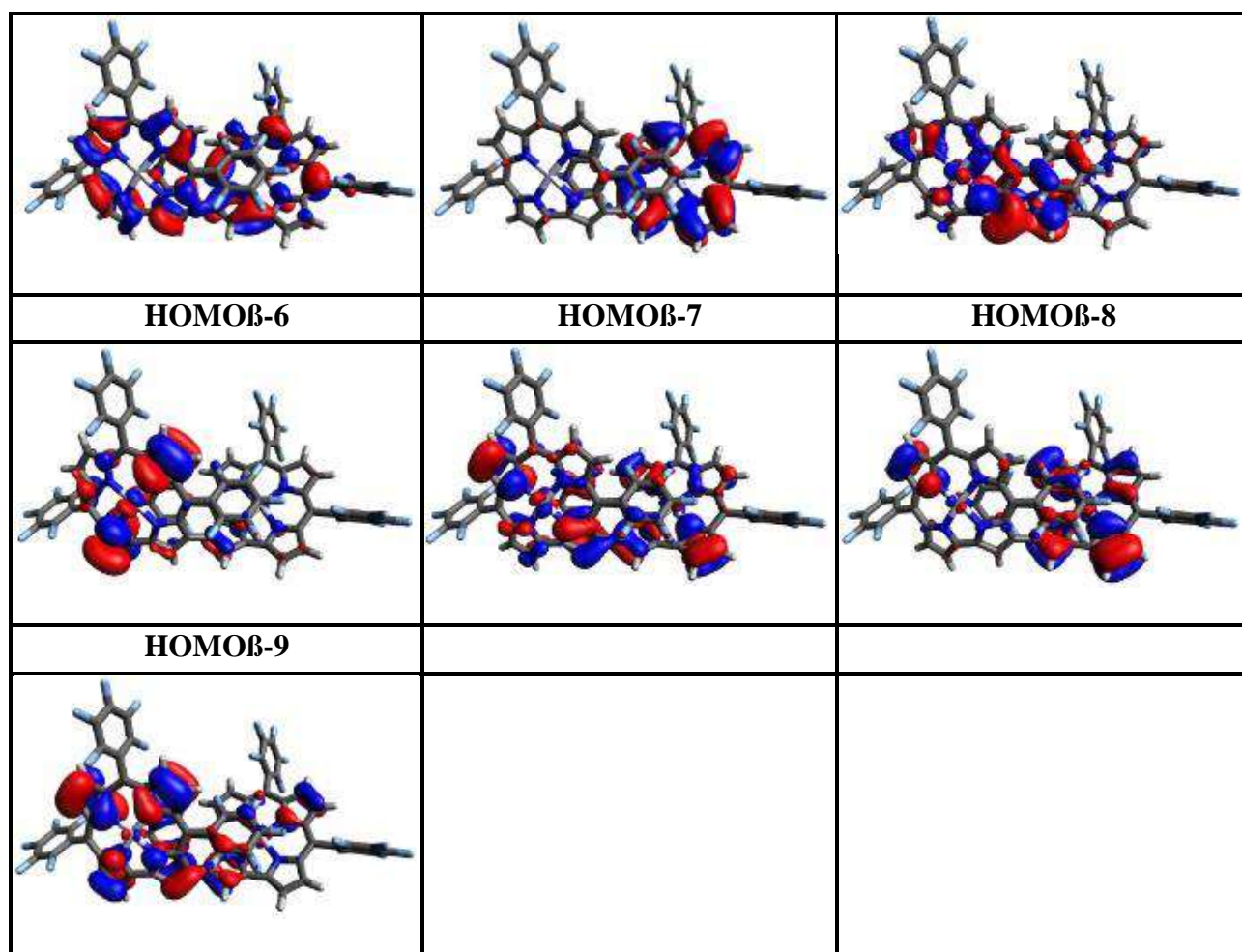


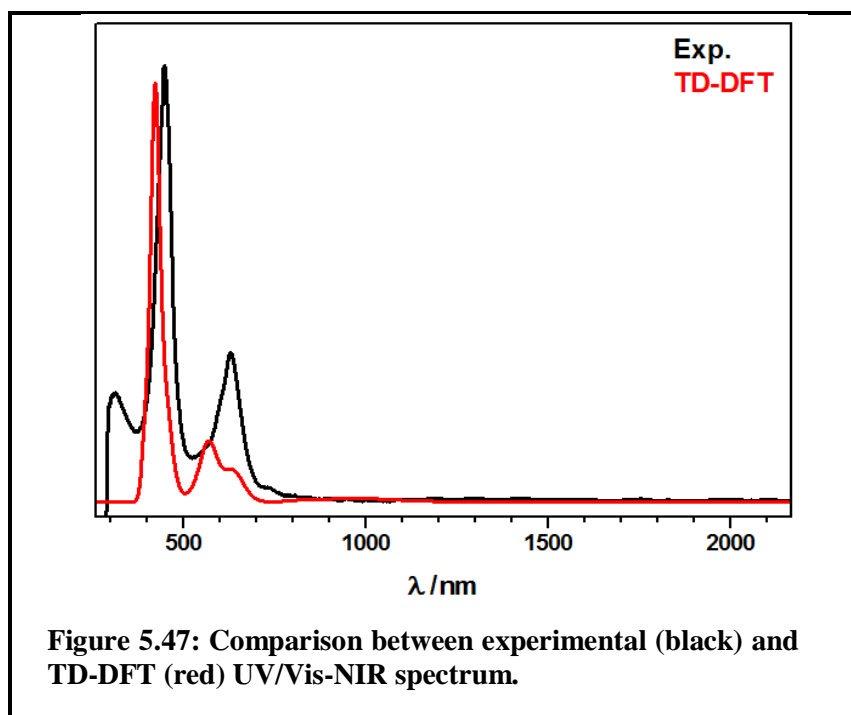
Table 5.20: Orbital energies of (1)^{•-} from DFT-calculation.

Spin up Orbitals alpha				Spin down orbitals beta			
Orbital No.	Orbital	Energy (Eh)	Energy (eV)	Orbital No.	Orbital	Energy (Eh)	Energy (eV)
450	LUMOα+10	-0.020495	-0.5577	450	LUMOβ+11	-0.020287	-0.5520
449	LUMOα+9	-0.021705	-0.5906	449	LUMOβ+10	-0.021580	-0.5872
448	LUMOα+8	-0.025762	-0.7010	448	LUMOβ+9	-0.025630	-0.6974
447	LUMOα+7	-0.026140	-0.7113	447	LUMOβ+8	-0.026064	-0.7092
446	LUMOα+6	-0.026991	-0.7345	446	LUMOβ+7	-0.026907	-0.7322
445	LUMOα+5	-0.029153	-0.7933	445	LUMOβ+6	-0.029086	-0.7915
444	LUMOα+4	-0.067314	-1.8317	444	LUMOβ+5	-0.065858	-1.7921
443	LUMOα+3	-0.070981	-1.9315	443	LUMOβ+4	-0.066844	-1.8189
442	LUMOα+2	-0.082015	-2.2317	442	LUMOβ+3	-0.070477	-1.9178
441	LUMOα+1	-0.087167	-2.3719	441	LUMOβ+2	-0.078219	-2.1285
440	LUMOα	-0.109412	-2.9773	440	LUMOβ+1	-0.081412	-2.2153
439	HOMOα	-0.129645	-3.5278	439	LUMOβ	-0.090233	-2.4554
438	HOMOα-1	-0.176794	-4.8108	438	HOMOβ	-0.175399	-4.7729
437	HOMOα-2	-0.180402	-4.9090	437	HOMOβ-1	-0.178822	-4.8660

436	HOMO α -3	-0.183283	-4.9874	436	HOMO β -2	-0.182207	-4.9581
435	HOMO α -4	-0.185985	-5.0609	435	HOMO β -3	-0.184995	-5.0340
434	HOMO α -5	-0.222459	-6.0534	434	HOMO β -4	-0.221175	-6.0185
433	HOMO α -6	-0.233233	-6.3466	433	HOMO β -5	-0.231284	-6.2936
432	HOMO α -7	-0.236084	-6.4242	432	HOMO β -6	-0.234535	-6.3820
431	HOMO α -8	-0.238283	-6.4840	431	HOMO β -7	-0.237017	-6.4496
430	HOMO α -9	-0.241331	-6.5669	430	HOMO β -8	-0.239921	-6.5286
429	HOMO α -10	-0.243824	-6.6348	429	HOMO β -9	-0.243088	-6.6148
428	HOMO α -11	-0.245233	-6.6731	428	HOMO β -10	-0.244082	-6.6418
427	HOMO α -12	-0.246644	-6.7115	427	HOMO β -11	-0.245961	-6.6929
426	HOMO α -13	-0.250305	-6.8111	426	HOMO β -12	-0.249611	-6.7923
425	HOMO α -14	-0.251758	-6.8507	425	HOMO β -13	-0.251447	-6.8422
424	HOMO α -15	-0.256041	-6.9672	424	HOMO β -14	-0.256002	-6.9662
423	HOMO α -16	-0.256340	-6.9754	423	HOMO β -15	-0.256315	-6.9747
422	HOMO α -17	-0.257298	-7.0014	422	HOMO β -16	-0.257255	-7.0003
421	HOMO α -18	-0.257696	-7.0123	421	HOMO β -17	-0.257611	-7.0100
420	HOMO α -19	-0.258297	-7.0286	420	HOMO β -18	-0.258088	-7.0229

5.7.5 TD-DFT Calculations of 1^2 (Triplet):

5.7.5.1 Calculated spectra, Comparison with Experimental spectrum and TD-DFT Transitions of 1^2 :



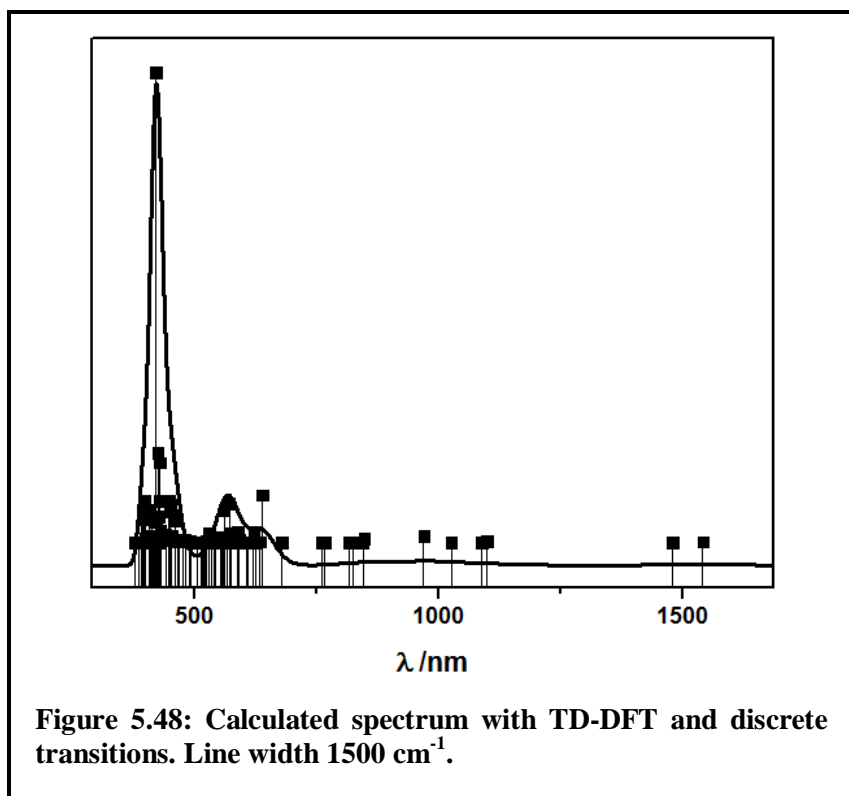


Table 5.21: TD-DFT calculated electronic transitions for (1)²⁻. (Including raw data)

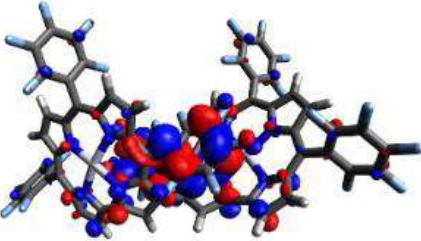
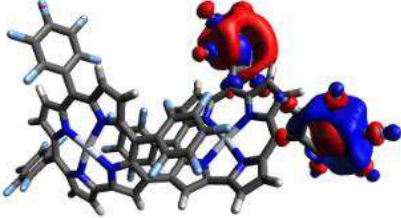
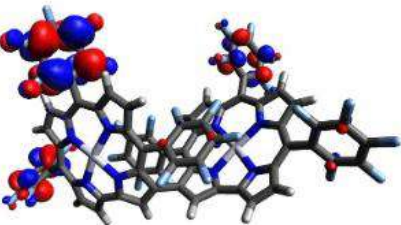
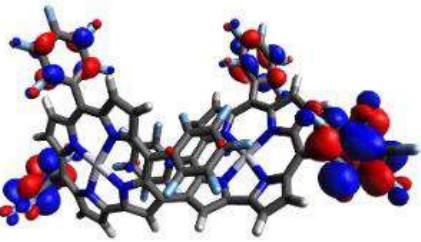
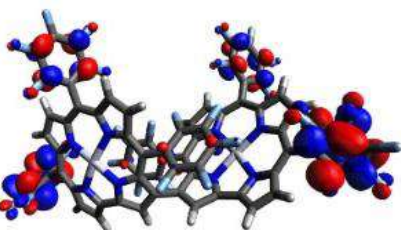
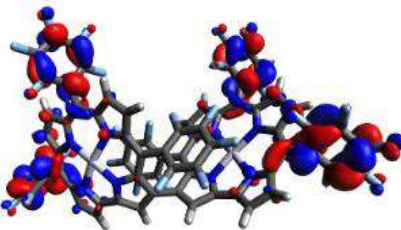
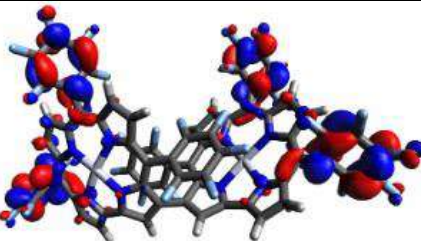
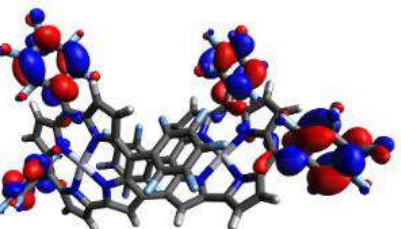
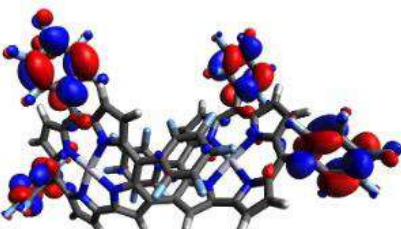
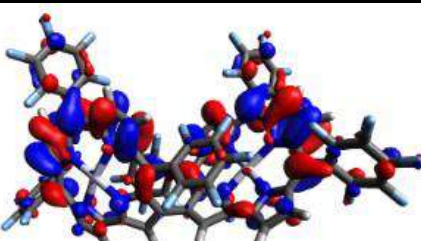
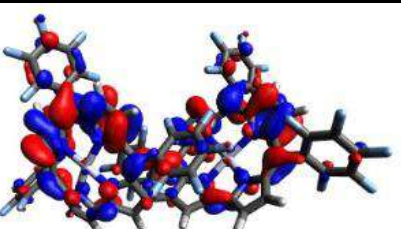
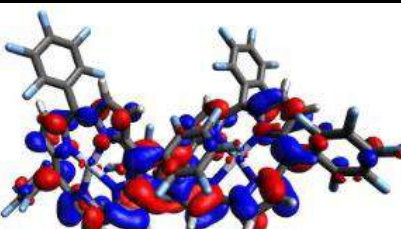
State	Transition	Transition HOMO LUMO	Calculated Transition energy	Oscillator strength	Experimental transition energy	Molar absorption coefficient 10 ³
	Not distinguishable	Not distinguishable			311	35.4
58	434a → 441a (0.17) mixed	HOMOα-6 → LUMOα (0.17) mixed	447.8	0.107	466	146.0
64	437b → 443b (0.20) 438b → 444b (0.21)	HOMOβ-1 → LUMOβ+4 (0.20) HOMOβ → LUMOβ+5 (0.21)	427.6	0.201		
66	437b → 444b (0.25) 438b → 443b (0.26)	HOMOβ-1 → LUMOβ+5(0.25) HOMOβ → LUMOβ+4 (0.26)	424.3	0.227		
69	439a → 449a (0.11) 440a → 459a (0.18)	HOMOα-1 → LUMOα+8 (0.11) HOMOα → LUMOα+18 (0.18)	428.8	0.105		
71	437b → 444b (0.10) mixed	HOMOβ-1 → LUMOβ+5 (0.10) mixed	420.2	1.186		
73	439a → 450a (0.27) 439a → 451a (0.11) 439a → 452a (0.12) 439a → 457a (0.18)	HOMOα-1 → LUMOα+9 (0.27) HOMOα-1 → LUMOα+10 (0.11) HOMOα-1 → LUMOα+11 (0.12) HOMOα-1 → LUMOα+16 (0.18)	450.1	0.096		

96	434a \rightarrow 442a (0.11) 437a \rightarrow 448a (0.17) 438a \rightarrow 447a (0.20) 438b \rightarrow 447b (0.11)	HOMO α -6 \rightarrow LUMO α +1 (0.11) HOMO α -4 \rightarrow LUMO α +7 (0.17) HOMO α -2 \rightarrow LUMO α +6 (0.20) HOMO β \rightarrow LUMO β +8 (0.11)	397.7	0.105		
43	435a \rightarrow 443a (0.19) 435a \rightarrow 444a (0.25) 436a \rightarrow 443a (0.26) 436a \rightarrow 444a (0.17)	HOMO α -5 \rightarrow LUMO α +2 (0.19) HOMO α -5 \rightarrow LUMO α +3 (0.25) HOMO α -4 \rightarrow LUMO α +2 (0.26) HOMO α -4 \rightarrow LUMO α +3 (0.17)	575.2	0.023	628	49.1
25	435a \rightarrow 441a (0.40) 436a \rightarrow 442a (0.10) 436a \rightarrow 443a (0.10) 437b \rightarrow 440b (0.14)	HOMO α -5 \rightarrow LUMO α (0.40) HOMO α -4 \rightarrow LUMO α +1 (0.10) HOMO α -4 \rightarrow LUMO α +2 (0.10) HOMO β -1 \rightarrow LUMO β +1 (0.14)	560.0	0.080		
23	435a \rightarrow 441a (0.15) 437a \rightarrow 442a (0.28) 436b \rightarrow 440b (0.16)	HOMO α -5 \rightarrow LUMO α (0.15) HOMO α -4 \rightarrow LUMO α +1 (0.28) HOMO β -2 \rightarrow LUMO β +1 (0.16)	571.2	0.099		
22	435b \rightarrow 439b (0.44) 437b \rightarrow 440b (0.10)	HOMO β -3 \rightarrow LUMO β (0.44) HOMO β -1 \rightarrow LUMO β +1 (0.10)	587.6	0.029		
15	438a \rightarrow 441a (0.22) 437b \rightarrow 440b (0.14) 438b \rightarrow 439b (0.48)	HOMO α -2 \rightarrow LUMO α (0.22) HOMO β -1 \rightarrow LUMO β +1 (0.14) HOMO β \rightarrow LUMO β (0.48)	638.3	0.121		

Table 5.22: Orbital energies of (1)²⁻ from DFT-calculation.

Spin up Orbitals alpha				Spin down orbitals beta			
Orbital No.	Orbital	Energy (Eh)	Energy (eV)	Orbital No.	Orbital	Energy (Eh)	Energy (eV)
460	LUMO α +19	0.010162	0.2765	460	LUMO β +21	0.010374	0.2823
459	LUMO α +18	0.009178	0.2497	459	LUMO β +20	0.009259	0.2519
458	LUMO α +17	0.002873	0.0782	458	LUMO β +19	0.003765	0.1024
457	LUMO α +16	0.001110	0.0302	457	LUMO β +18	0.001370	0.0373
456	LUMO α +15	0.000621	0.0169	456	LUMO β +17	0.000632	0.0172
455	LUMO α +14	0.000597	0.0162	455	LUMO β +16	0.000609	0.0166
454	LUMO α +13	-0.000499	-0.0136	454	LUMO β +15	-0.000448	-0.0122
453	LUMO α +12	-0.000697	-0.0190	453	LUMO β +14	-0.000637	-0.0173
452	LUMO α +11	-0.004448	-0.1210	452	LUMO β +13	-0.004422	-0.1203
451	LUMO α +10	-0.004528	-0.1232	451	LUMO β +12	-0.004500	-0.1225
450	LUMO α +9	-0.005281	-0.1437	450	LUMO β +11	-0.005220	-0.1420
449	LUMO α +8	-0.005514	-0.1500	449	LUMO β +10	-0.005453	-0.1484
448	LUMO α +7	-0.010982	-0.2988	448	LUMO β +9	-0.010560	-0.2873
447	LUMO α +6	-0.011435	-0.3112	447	LUMO β +8	-0.010984	-0.2989
446	LUMO α +5	-0.012162	-0.3309	446	LUMO β +7	-0.012036	-0.3275
445	LUMO α +4	-0.012440	-0.3385	445	LUMO β +6	-0.012315	-0.3351
444	LUMO α +3	-0.047732	-1.2989	444	LUMO β +5	-0.027037	-0.7357
443	LUMO α +2	-0.048681	-1.3247	443	LUMO β +4	-0.030308	-0.8247
442	LUMO α +1	-0.060063	-1.6344	442	LUMO β +3	-0.047208	-1.2846
441	LUMO α	-0.063930	-1.7396	441	LUMO β +2	-0.048438	-1.3181
440	HOMO α	-0.120143	-3.2693	440	LUMO β +1	-0.059151	-1.6096
439	HOMO α -1	-0.125687	-3.4201	439	LUMO β	-0.065702	-1.7878
438	HOMO α -2	-0.151710	-4.1282	438	HOMO β	-0.149855	-4.0778
437	HOMO α -3	-0.153318	-4.1720	437	HOMO β -1	-0.150760	-4.1024
436	HOMO α -4	-0.157092	-4.2747	436	HOMO β -2	-0.155871	-4.2415
435	HOMO α -5	-0.159593	-4.3428	435	HOMO β -3	-0.157078	-4.2743
434	HOMO α -6	-0.196902	-5.3580	434	HOMO β -4	-0.193028	-5.2526
433	HOMO α -7	-0.207427	-5.6444	433	HOMO β -5	-0.203549	-5.5389
432	HOMO α -8	-0.209449	-5.6994	432	HOMO β -6	-0.205909	-5.6031
431	HOMO α -9	-0.210191	-5.7196	431	HOMO β -7	-0.207084	-5.6350
430	HOMO α -10	-0.216657	-5.8955	430	HOMO β -8	-0.214046	-5.8245

5.7.5.2 Molecular and orbital energies for (1)²⁻:Table 5.23: Composition of selected molecular orbitals with alpha spin of (1)²⁻

LUMO α +18	LUMO α +16	LUMO α +11
		
LUMO α +10	LUMO α +9	LUMO α +8
		
LUMO α +7	LUMO α +6	LUMO α +5
		
LUMO α +4	LUMO α +3	LUMO α +2
		
LUMO α +1	LUMO α	

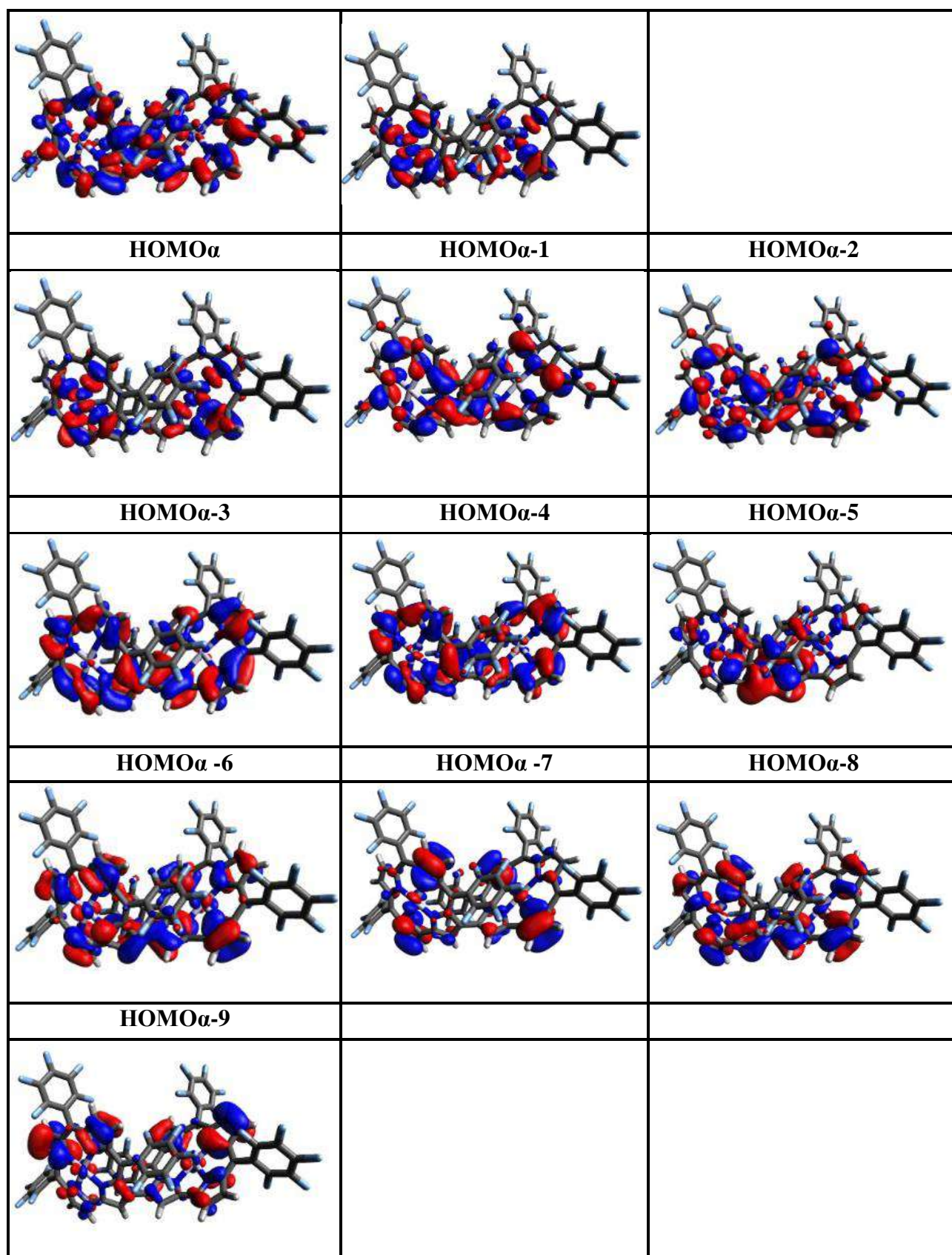
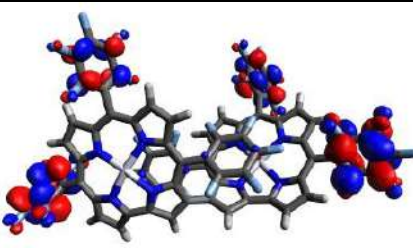
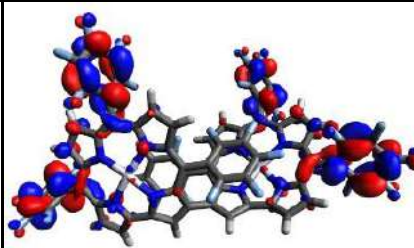
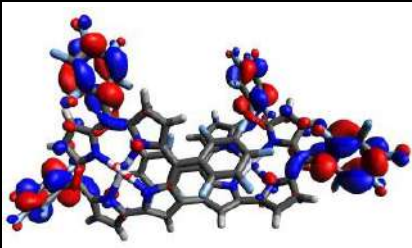
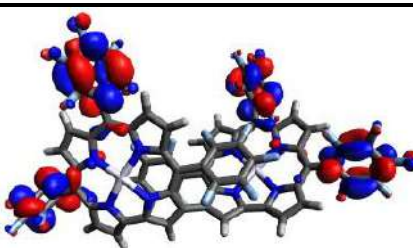
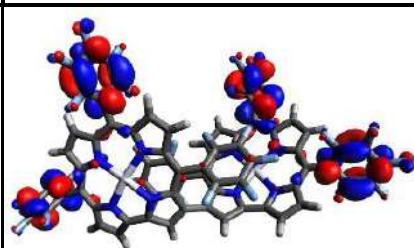
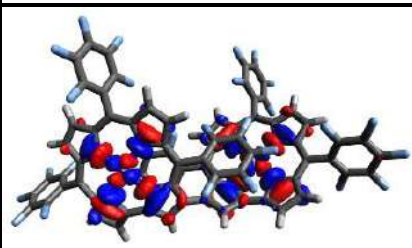
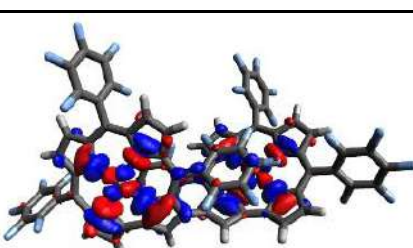
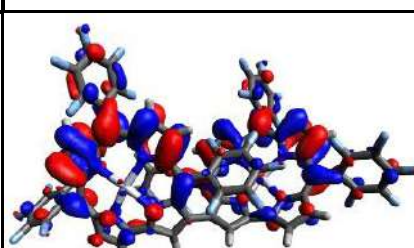
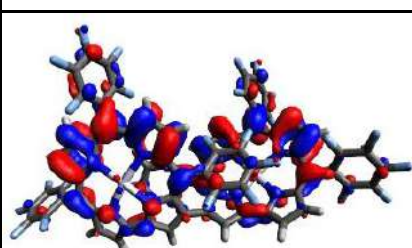
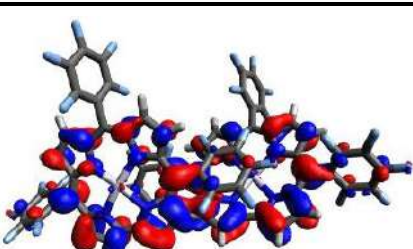
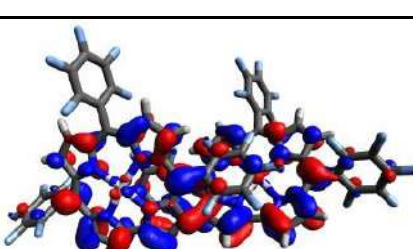
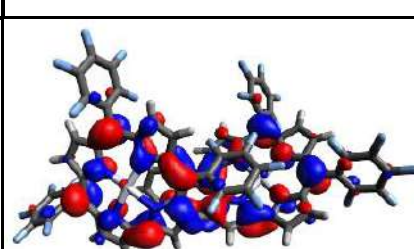
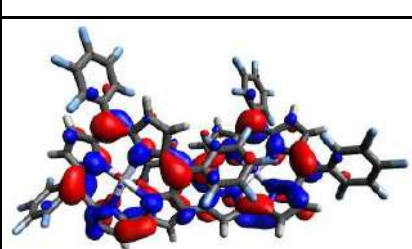
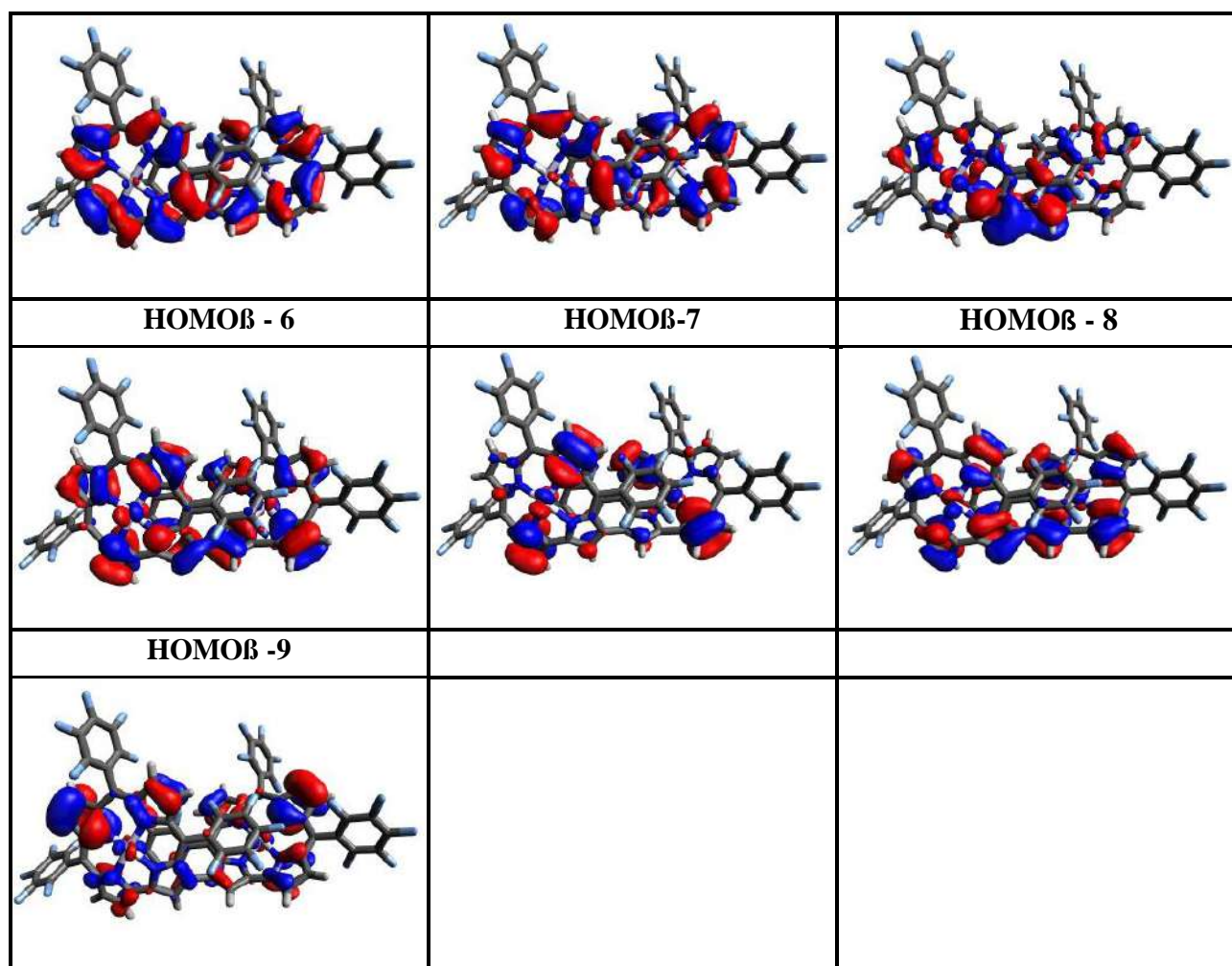


Table 5.24: Composition of selected molecular orbitals with beta spin of (1)²⁻.

LUMOβ+9	LUMOβ + 8	LUMOβ + 7
		
LUMOβ + 6	LUMOβ + 5	LUMOβ + 4
		
LUMOβ +3	LUMOβ +2	LUMOβ +1
		
LUMOβ		
		
HOMOβ	HOMOβ -1	HOMOβ -2
		
HOMOβ - 3	HOMOβ - 4	HOMOβ - 5



5.8 Gouterman Orbitals for the Monomer and Dimer:

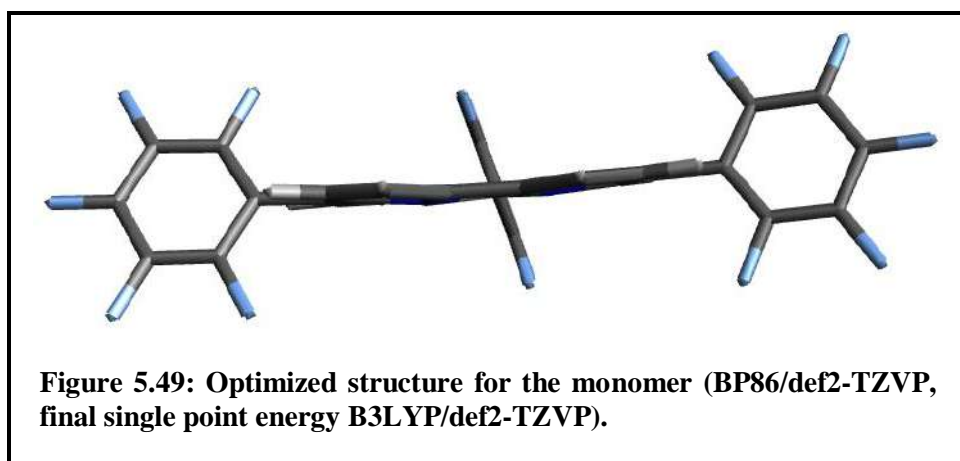
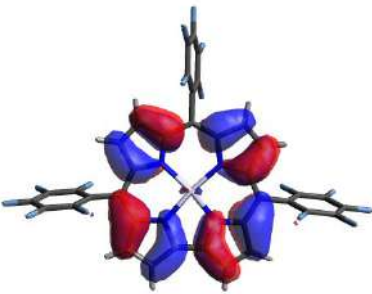
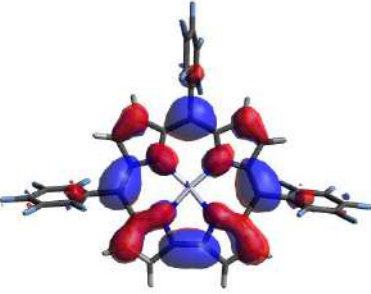
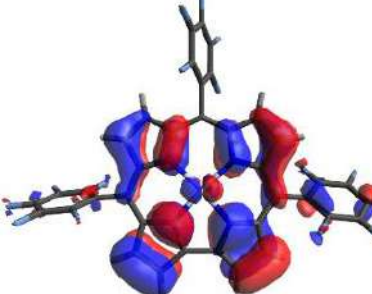
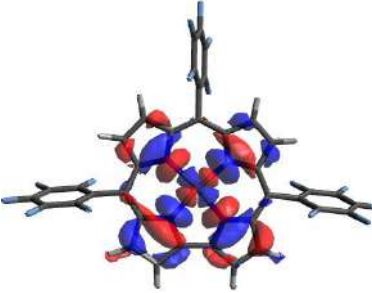
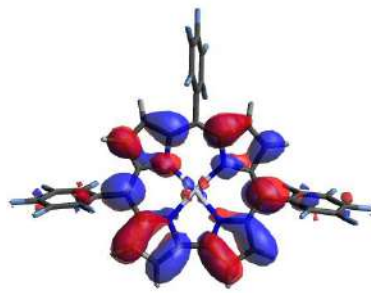
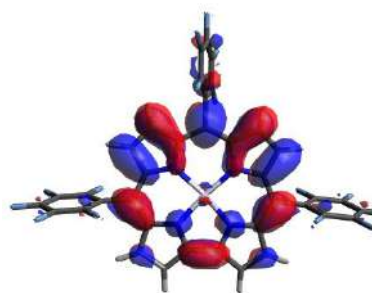


Table 5.25: Gouterman orbitals for the optimized monomer.

		
HOMO-1	HOMO	HOMO-2
a	s	
-5.65 eV	-5.56 eV	
$\Delta\text{HOMO} = 0.09 \text{ eV}$		
		
LUMO	LUMO+1	LUMO+2
	-a	-s
-3.09 eV	-2.83 eV	-2.43
	$\Delta\text{LUMO} = 0.40 \text{ eV}$	

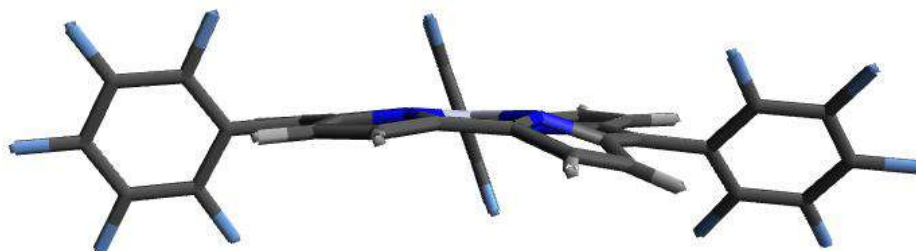


Figure 5.50: Monomer with distorted pyrrole ring, geometry taken directly from the optimized dimer from the dimer (final single point energy B3LYP/def2-TZVP).

Table 5.26: Gouterman orbitals for the distorted monomer.

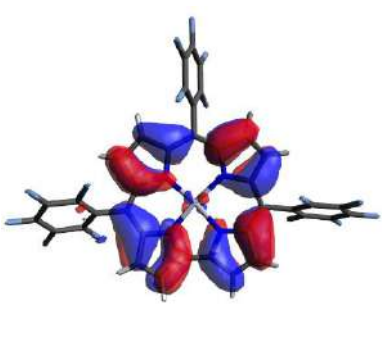
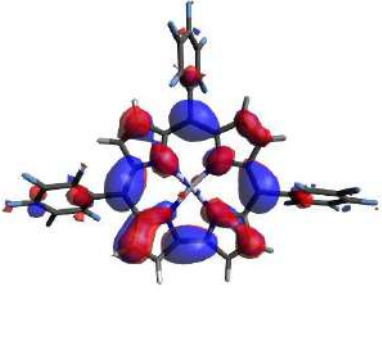
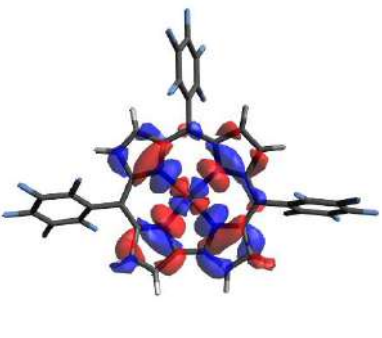
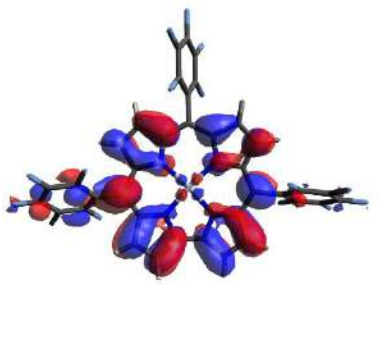
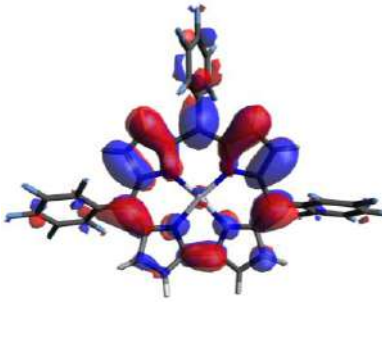
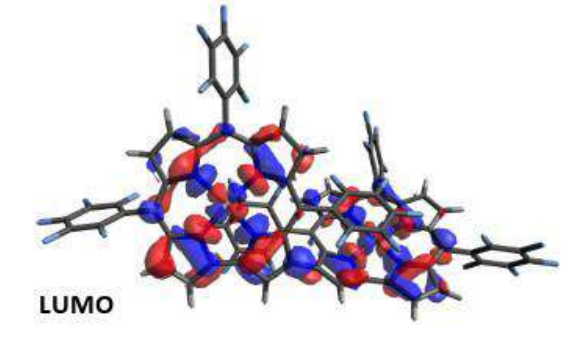
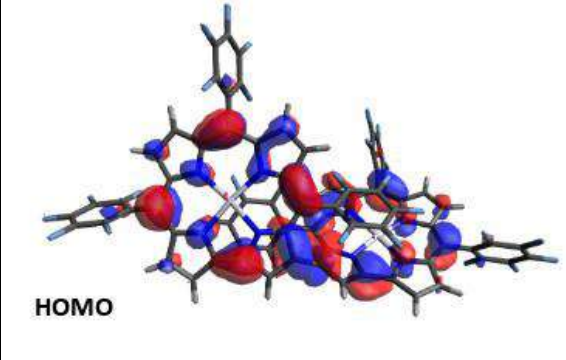
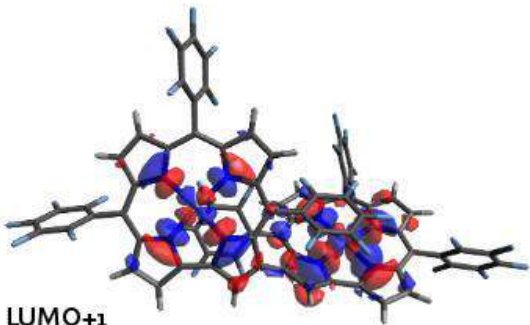
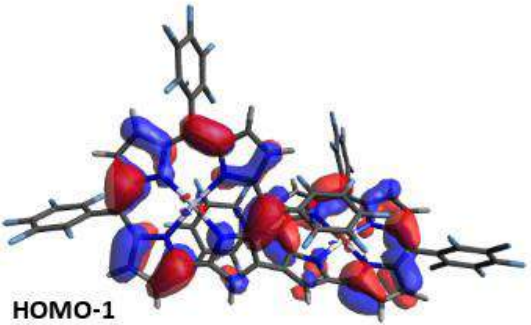
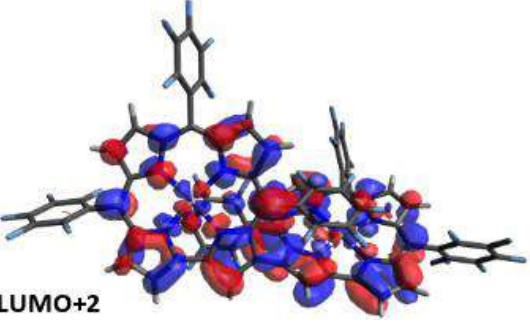
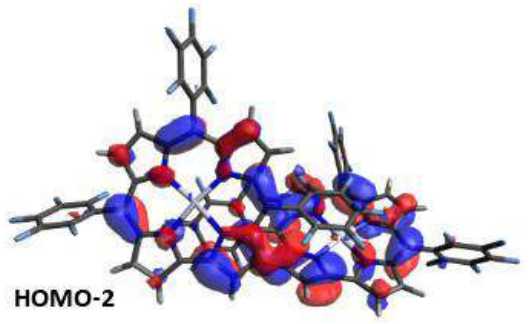
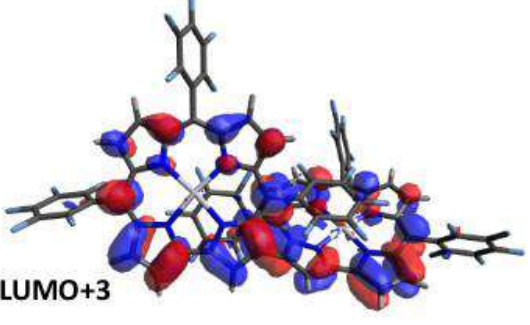
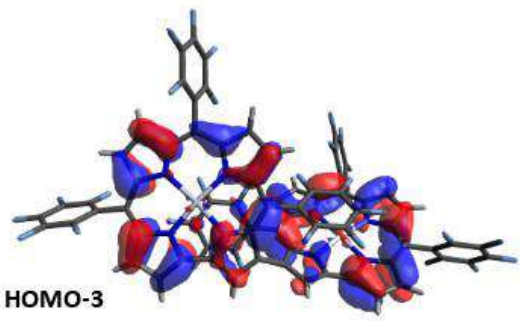
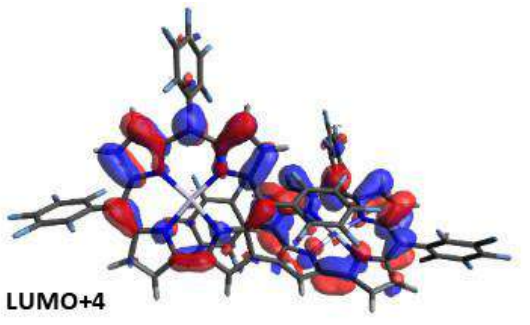
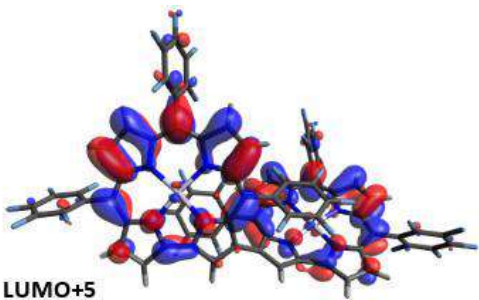
		
HOMO-1	HOMO	
a	S	
-5.62 eV	-5.55 eV	
$\Delta\text{HOMO} = 0.07 \text{ eV}$		
		
LUMO	LUMO+1	LUMO+2
	-a	-s
-3.18 eV	-2.87 eV	-2.44 eV
	$\Delta\text{LUMO} = 0.43 \text{ eV}$	
$ \Delta\text{HOMO}-\Delta\text{LUMO} = 0.37 \text{ eV}$		

Table 5.27: Gouterman orbitals for the dimer 1.

	
LUMO	HOMO
-3.29 eV	-5.53 eV

 LUMO+1	 HOMO-1
-3.17 eV	-5.62 eV
 LUMO+2	 HOMO-2
-2.99 eV	-5.68 eV
 LUMO+3	 HOMO-3
-2.84 eV	-5.71 eV
 LUMO+4	
-2.52 eV	

 <p>LUMO+5</p>	
-2.46 eV	
$\Delta(\text{LUMO}+2-\text{LUMO}+5) = 0.53 \text{ eV}$	$\Delta(\text{HOMO}-\text{HOMO}-3) = 0.18 \text{ eV}$
$ \Delta\text{HOMO}-\Delta\text{LUMO} = 0.35 \text{ eV}$	

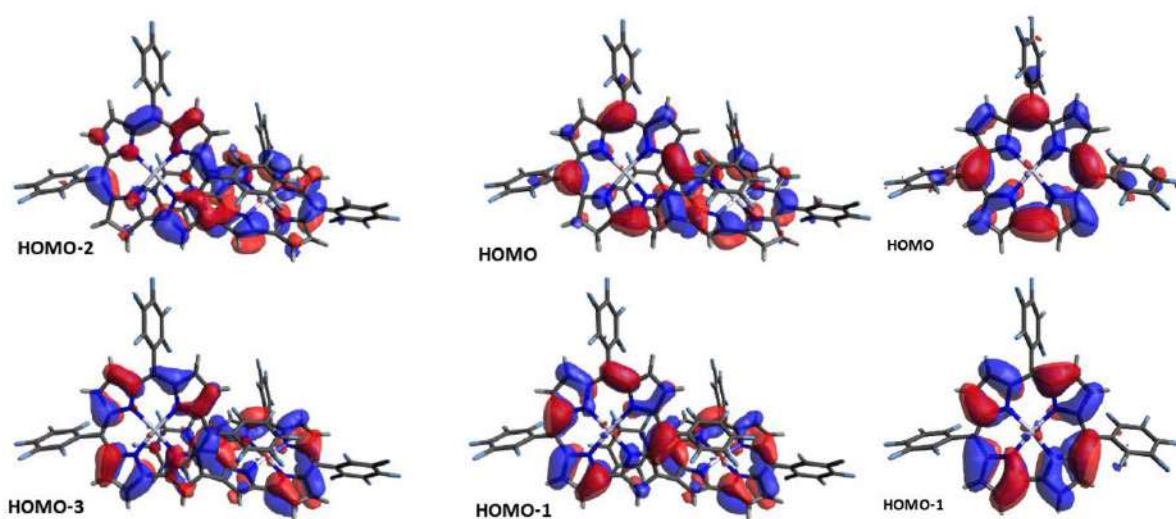
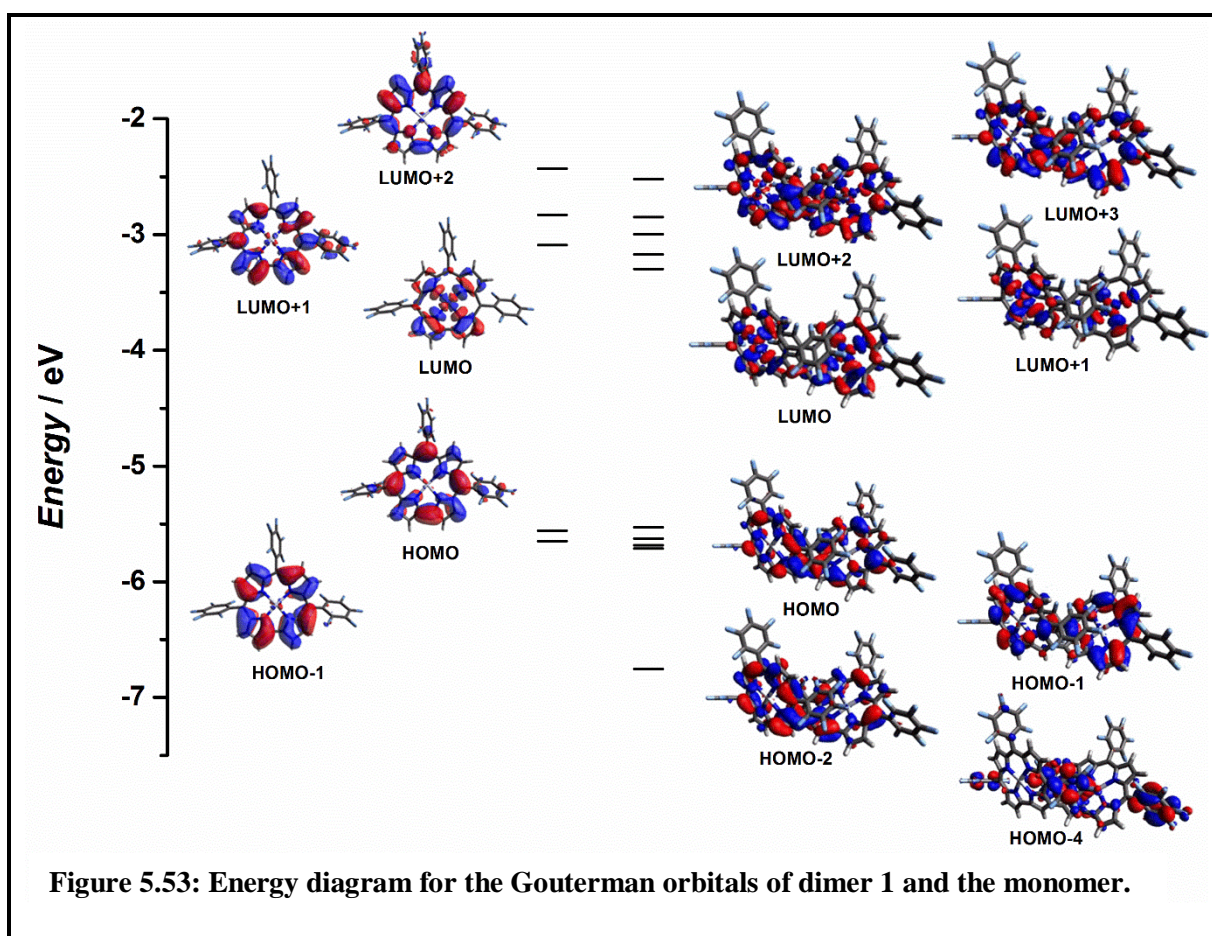
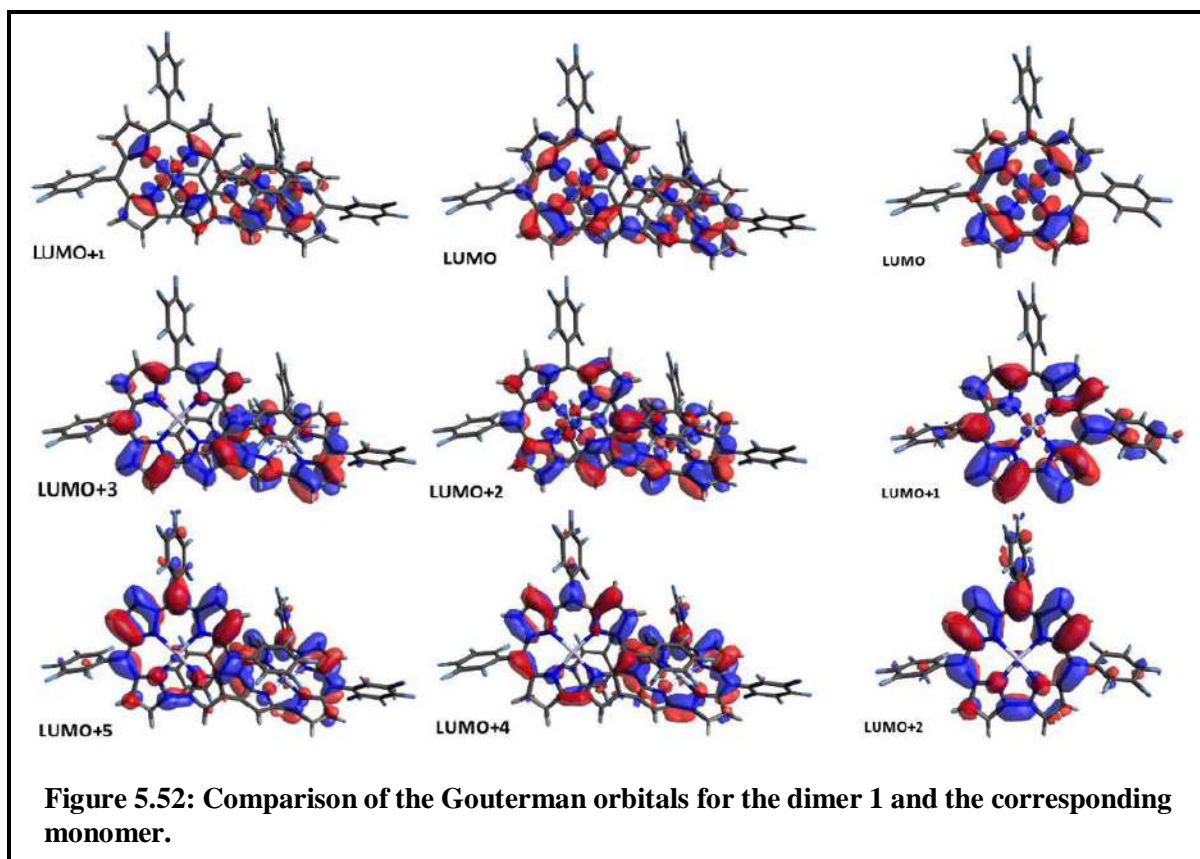


Figure 5.51: Comparison of the Gouterman orbitals for the dimer 1 and the corresponding monomer.



Reference:

1. A. R. Battersby, C. Fookes, G. Matcham, E. McDonald, *Nature*. **1980**, 285, 17-21.
2. K. M. Kadish, Smith, K. M.; Guillard, R.; Editors, *The Porphyrin Handbook; Volume 2, Heteroporphyrins, Expanded Porphyrins and Related Macrocycles*. Academic Press: **2000**.
3. J. M. Berg, S. Lippard, *Principles of bioinorganic chemistry*. Mill Valley, 411s.ed.; University Science Books: **1994**.
4. W. Küster, Hoppe-Seyler's *Z. Physiol. Chem.* **1912**, 82, 463.
5. J. L. Sessler, S. J. Weghorn, *Expanded, contracted & isomeric porphyrins*. Elsevier: **1997**; Vol. 15.
6. V. J. Bauer, L. J. C. Derrick, D. Dolphin, J. B. Paine, F. L. Harris, M. M. King, J. Loder, S. W. C. Wang, R. B. Woodward, *J. Am. Chem. Soc.* **1983**, 105, 6429-6436.
7. H. Rexhausen, A. Gossauer, *J. CHEM. SOC., CHEM. COMMUN.* **1983**.
8. B. Franck, A. Nonn, *Angew. Chem. Int. Ed. Engl.* **1995**, 34, 1795-1811.
9. C. Weiss, *J. Mol. Spectrosc.* **1972**, 44, 37-80.
10. J.-L. Soret, *Compt. Rend.* **1883**, 97, 1269-1273.
11. M. O. Senge, K. M. Smith, *Photochem. Photobiol.* **1991**, 54, 841-846.
12. K. M. Smith, D. A. Goff, R. J. Abraham, *Org. Magn. Resonance*. **1984**, 22, 779-783.
13. K. M. Kadish, K. M. Smith, R. Guillard, Editors, *The Porphyrin Handbook; Volume 1, Synthesis and Organic Chemistry*. Academic Press: **2000**.
14. S. Saito, A. Osuka, *Angew. Chem. Int. Ed.* **2011**, 50, 4342 – 4373.
15. T. K. Chandrashekar, S. Venkatraman, *Acc. Chem. Res.* **2003**, 36, 676-691.
16. Z. S. Yoon, D. G. Cho, K. S. Kim, J. L. Sessler, D. Kim, *J. Am. Chem. Soc.* **2008**, 130, 6930–6931.
17. J. L. Sessler, D. Seidel, A. E. Vivian, V. Lynch, B. L. Scott, D. W. Keogh, *Angew. Chem. Int. Ed.* **2001**, 40, No. 3.
18. J. L. Sessler, T. Murai, G. Hemmi, *Inorganic Chemistry*. Vol. 28, No. 17, **1989** 3391.

-
19. D. C. Hodgkin, J. Kamper, J. Lindsey, M. MacKay, J. Pickworth, J. Robertson, C. B. Shoemaker, J. White, R. Prosen, K. Trueblood, *Proc. R. Soc. Lond. A.* **1957**, 242, 228-263.
 20. A. Johnson, A. Todd, *Vitam. Horm.* **1957**, 15, 1.
 21. R. Bonnett, *Chem. Rev.* **1963**, 63, 573-605.
 22. A. R. Battersby, *J. Nat. Prod.* **1988**, 51, 629-642.
 23. B. Kräutler, B. T. Golding, D. A. J. Wiley & Sons, *Science*. **2008**, 559.
 24. A. Johnson, R. Price, *J. Chem. Soc.* **1960**, 1649-1653.
 25. A. Johnson, I. Kay, *J. Chem. Soc.* **1965**, 1620-1629.
 26. A. Meller, A. Ossko, *Monatsh. Chem.* **1972**, 103, 150-155.
 27. C. G. Claessens, D. G. Rodríguez, and T. Torres, *Chem. Rev.* **2002**, 102, 835–853.
 28. C. G. Claessens, D. G. Rodríguez, M. S. Rodríguez-Morgade, A. Medina, T. Torres, *Chem. Rev.* **2014**, 114, 2192–2277.
 29. S. Nardis, G. Pomarico, F. R. Fronczek, M. Grac, H. Vicente, R. Paolessea, *Tetrahedron Letters*. **2007**, 48, 8643–8646.
 30. M. Bröring, S. Khler, C. Kleeberg, *Angew. Chem. Int. Ed.* **2008**, 47, 5658 –5660.
 31. T. Ito, Y. Hayashi, S. Shimizu, J. Y. Shin, N. Kobayashi, H. Shinokubo, *Angew. Chem. Int. Ed.* **2012**, 51, 8542 –8545.
 32. Y. Inokuma, A. Osuka, *Dalton Trans.* **2008**, 2517–2526.
 33. H. R. Harrison, J. R. Hodder, D. C. Hodgkin, *J. Chem. SOC. (B)*, **1971**.
 34. A. Ghosh, K. Jynge, *Chem. Eur. J.* **1997**, 3, 823-833.
 35. Z. Gross, N. Galili, L. Simkhovich, I. Saltsman, M. Botoshansky, D. Bla1ser, R. Boese, I. Goldberg, *Org. Lett. Vol. 1*, No. 4, **1999**.
 36. I. A. Harel, Z. Gross, *Chem. Eur. J.* **2009**, 15, 8382 – 8394.
 37. R. Paolesse, F. Sagone, A. Macagnano, T. Boschi, L. Prodi, M. Montalti, N. Zaccheroni, F. Bolletta, K. M. Smith, *J. Porphyrins Phthalocyanines*. **1999**, 3, 364-370.

-
38. Y. S. Balazs, I. Saltsman, A. Mahammed, E. Tkachenko, G. Golubkov, J. Levine, Z. Gross, *Magn. Reson. Chem.* **2004**, *42*, 624–635.
39. E. Vogel, S. Will, A. S. Tilling, L. Neumann, J. Lex, E. Bill, A. X. Trautwein, K. Wieghardt, *Angew. Chem., Int. Ed. Engl.* **1994**, *33*, 731–735.
40. R. Orłowski, D. Gryko, D. T. Gryko, *Chem. Rev.* **2017**, *117*, 3102–3137.
41. R. Paolesse, E. Tassoni, S. Licoccia, M. Paci, T. Boschi, *Inorganica Chimica Acta* **241** (1996) 55-60.
42. M. Conlon, A. W. Johnson, W. R. Overend, D. Rajapaksa, C. M. Elson, *J. Chem. Soc. Perkin Trans. 1.* **1973**, 2281–2288.
43. Z. Gross, N. Galili, L. Simkhovich, I. Saltsman, M. Botoshansky, D. Blaeser, R. Boese, I. Goldberg, *Org. Lett.* **1999**, *1*, 599-602.
44. R. Paolesse, L. Jaquinod, D. J. Nurco, S. Mini, F. Sagone, T. Boschi, K. M. Smith, *Chem. Commun.* **1999**, 1307–1308.
45. B. Koszarna, D. T. Gryko, *J. Org. Chem.* **2006**, *71*, 3707-17.
46. V. Král, P. Vašek, B. Dolensky, *Collect. Czech. Chem. Commun.* **2004**, *69*, 1126-1136.
47. J. F. B. Barata, M. G. P. M. S. Neves, M. A. F. Faustino, A. C. Tomé, J. A. S. Cavaleiro, *Chem. Rev.* **2017**, *117*, 3192–3253.
48. S. Will, J. Lex, E. Vogel, H. Schmickler, J.-P. Gisselbrecht, C. Haubtmann, M. Bernard, M. Gorss, *Angew. Chem. Int. Ed. Engl.* **1997**, *36*, 357-361.
49. K. M. Kadish, C. Erben, Z. Ou, V. A. Adamian, S. Will, E. Vogel, *Inorg. Chem.* **2000**, *39*, 3312-3319.
50. K. E. Thomas, A. B. Alemayehu, J. Conradie, C. Beavers, A. Ghosh, *Inorg. Chem.* **2011**, *50*, 12844-12851.
51. C. Brückner, R. P. Briñas, J. A. Krause Bauer, *Inorg. Chem.* **2003**, *42*, 4495-4497.
52. S. Licoccia, R. Paolesse, E. Tassoni, F. Polizio, T. Boschi, *J. Chem. Soc., Dalton Trans.* **1995**, 3617-21.

-
53. Z. Gross, *J. Biol. Inorg. Chem.* **2001**, 6, 733-738.
54. L. Simkhovich, A. Mahammed, I. Goldberg, Z. Gross, *Chem. Eur. J.* **2001**, 7, 1041-55.
55. W. Sinha, N. Deibel, H. Agarwala, A. Garai, D. Schweinfurth, C. S. Purohit, G. K. Lahiri, B. Sarkar, S. Kar, *Inorg. Chem.* **2014**, 53, 1417-1429.
56. J. H. Palmer, M. W. Day, A. D. Wilson, L. M. Henling, Z. Gross, H. B. Gray, *J. Am. Chem. Soc.* **2008**, 130, 7786-7787.
57. A. Mahammed, I. Giladi, I. Goldberg, Z. Gross, *Chem. Eur. J.* **2001**, 7, 4259-65.
58. J. Bendix, I. J. Dmochowski, H. B. Gray, A. Mahammed, L. Simkhovich, Z. Gross, *Angew. Chem. Int. Ed.* **2000**, 39, 4048-4051.
59. A. Mahammed, Z. Gross, *J. Inorg. Biochem.* **2002**, 88, 305-309.
60. K. J. Barnham, C. L. Masters, A. I. Bush, *Nat. Rev. Drug Discov.* **2004**, 3, 205-214.
61. A. Mahammed, Z. Gross, *Angew. Chem.* **2006**, 118, 6694 –6697.
62. A. Mahammed, Z. Gross, *J. Am. Chem. Soc.* **2005**, 127, 2883.
63. J. S. Beckman, *Chem. Res. Toxicol.* **1996**, 9, 836-44.
64. G. Merenyi, J. Lind, S. Goldstein, G. Czapski, *Chem. Res. Toxicol.* **1998**, 11, 712-3.
65. R. Bryk, P. Griffin, C. Nathan, *Nature.* **2000**, 407, 211-215.
66. W. Nam, *Acc. Chem. Res.* **2007**, 40, 465.
67. L. Que, Jr. *J. Biol. Inorg. Chem.* **2017**, 22, 171.
68. W. Nam, *Acc. Chem. Res.* **2015**, 48, 2415.
69. K. Ray, F. F. Pfaff, B. Wang, W. Nam, *J. Am. Chem. Soc.* **2014**, 136, 13942.
70. M. Oszajca, A. Franke, M. Brindell, G. Stochel, R. van Eldik, *Coord. Chem. Rev.* **2016**, 306, 483.
71. X. Huang, J. T. Groves, *J. Biol. Inorg. Chem.* **2017**, 22, 185.
72. X. Engelmann, I. Monte-Pérez, K. Ray, *Angew. Chem., Int. Ed.* **2016**, 55, 7632.
73. D. G. Nocera, *Acc. Chem. Res.* **2012**, 45, 767.

-
74. S. Bang, Y.-M. Lee, S. Hong, K.-B. Cho, Y. Nishida, M. S. Seo, R. Sarangi, S. Fukuzumi, W. Nam, *Nat. Chem.* **2014**, *6*, 934.
75. K. J. Young, B. J. Brennan, R. Tagore, G. W. Brudvig, *Acc. Chem. Res.* **2015**, *48*, 567.
76. S. Sahu, D. P. Goldberg, *J. Am. Chem. Soc.* **2016**, *138*, 11410.
77. Hong, S.; Lee, Y.-M.; Ray, K.; Nam, W. *Coord. Chem. Rev.* **2017**, *334*, 25.
78. G. Yin, *Acc. Chem. Res.* **2013**, *46*, 483.
79. H. M. Neu, R. A. Baglia, D. P. Goldberg, *Acc. Chem. Res.* **2015**, *48*, 2754.
80. A. S. Borovik, *Acc. Chem. Res.* **2005**, *38*, 54.
81. M. Guo, Y. M. Lee, R. Gupta, M. S. Seo, T. Ohta, H. H. Wang, H. Y. Liu, S. N. Dhuri, R. Sarangi, S. Fukuzumi, W. Nam, *J. Am. Chem. Soc.* **2017**, *139*, 15858–15867.
82. H. Agadjanian, J. Weaver, A. Mahammed, A. Rentsendorj, S. Bass, J. Kim, I. Dmochowski, R. Margalit, H. B. Gray, Z. Gross, *Pharm. Res.* **2006**, *23*, 367–377.
83. D. E. J. G. J. Dolmans, D. Fukumura, R. K. Jain, *Nat. Rev. Cancer.* **2003**, *3*, 380–387.
84. L. Simkhovich, I. Goldberg, Z. Gross, *Journal of Inorganic Biochemistry.* **2000**, *80*, 235–238.
85. D. Aviezer, S. Cotton, M. David, A. Segev, N. Khaselev, N. Galili, Z. Gross, A. Yayon, *Cancer Res.* **2000**, *60* (11), 2973–2980.
86. A. Mahammed, H. B. Gray, J. J. Weaver, K. Sorasaene, Z. Gross, *Bioconjugate Chem.* **2004**, *15*, 738–746.
87. R. D. Teo, J. Y. Hwang, J. Termini, Z. Gross, H. B. Gray, *Chem. Rev.* **2017**, *117*, 2711–2729.
88. R. Guillard, F. Jérôme, J. M. Barbe, C. P. Gros, Z. Ou, J. Shao, J. Fischer, R. Weiss, K. M. Kadish, *Inorg. Chem.* **2001**, *40*, 4856–4865.
89. R. Guillard, C. P. Gros, F. Bolze, F. Jérôme, Z. Ou, J. Shao, J. Fischer, R. Weiss, K. M. Kadish, *Inorg. Chem.* **2001**, *40*, 4845–4855.
90. K. M. Kadish, Z. Ou, J. Shao, C. P. Gros, J. M. Barbe, F. Jérôme, F. Bolze, F. Burdet, R. Guillard, *Inorganic Chemistry.* **2002**, *Vol. 41*, No. 15.

-
91. J. M. Barbe, G. Canard, S. Brandès, F. Jérôme, G. Dubois, R. Guillard, *Dalton Trans.* **2004**, 1208 – 1214.
92. J. P. Coliman, R. R. Gagne, C. A. Reed, T. R. Halbert, G. Lang, W. T. Robinson, *Journal of the American Chemical Society.* / 97:6 / March 19, **1975**.
93. Y. Fang, Z. Ou and K. M. Kadish, *Chem. Rev.* **2017**, 117, 3377–3419.
94. W. Sinha, M. G. Sommer, L. Hettmanczyk, B. Patra, V. Filippou, B. Sarkar, S. Kar, *Chem. Eur. J.* **2017**, 23, 2396–2404.
95. W. Sinha, M. G. Sommer, N. Deibel, F. Ehret, M. Bauer, B. Sarkar, S. Kar, *Angew. Chem. Int. Ed.* **2015**, 54, 13769–13774.
96. W. Sinha, M. G. Sommer, N. Deibel, F. Ehret, B. Sarkar, S. Kar, *Chem. Eur. J.* **2014**, 20, 15920–15932.
97. W. Sinha, N. Deibel, H. Agarwala, A. Garai, D. Schweinfurth, C. S. Purohit, G. K. Lahiri, B. Sarkar, S. Kar, *Inorg. Chem.* **2014**, 53, 1417–1429.
98. B. Brizet, N. Desbois, A. Bonnot, A. Langlois, A. Dubois, J.-M. Barbe, C. P. Gros, C. Goze, F. Denat, P. D. Harvey, *Inorg. Chem.* **2014**, 53, 3392–3403.
99. K. E. Thomas, A. B. Alemayehu, J. Conradie, C. M. Beavers, A. Ghosh, *Acc. Chem. Res.* **2012**, 45, 1203–1214.
100. M. Autret, S. Will, E. V. Caemelbecke, J. Lex, J.-P. Gisselbrecht, M. Gross, E. Vogel, K. M. Kadish, *J. Am. Chem. Soc.* **1994**, 116, 9141–9149.
101. D. K. Dogutan, R. McGuire Jr., D. G. Nocera, *J. Am. Chem. Soc.* **2011**, 133, 9178–9180.
102. S. H. Kim, H. Park, M. S. Seo, M. Kubo, T. Ogura, J. Klajn, D. T. Gryko, J. S. Valentine, W. Nam, *J. Am. Chem. Soc.* **2010**, 132, 14030–14032.
103. A. J. McGown, W. D. Kerber, H. Fujii, D. P. Goldberg, *J. Am. Chem. Soc.* **2009**, 131, 8040–8048.
104. H.-Y. Liu, T.-S. Lai, L.-L. Yeung, C. K. Chang, *Org. Lett.* **2003**, 5, 617–620.

-
105. A. Mahammed, B. Mondal, A. Rana, A. Dey, Z. Gross, *Chem. Commun.* **2014**, 50, 2725–2727.
106. Z. Ou, A. Lu, D. Meng, S. Huang, Y. Fang, G. Lu, K. M. Kadish, *Inorg. Chem.* **2012**, 51, 8890–8896.
107. K. M. Kadish, L. Fremond, J. Shen, P. Chen, K. Ohkubo, S. Fukuzumi, M. E. Ojaimi, C. P. Gros, J.-M. Barbe, R. Guillard, *Inorg. Chem.* **2009**, 48, 2571–2582.
108. M. J. Zdilla, M. M. Abu-Omar, *J. Am. Chem. Soc.* **2006**, 128, 16971–16979.
109. C. I. M. Santos, E. Oliveira, J. F. B. Barata, M. A. F. Faustino, J. A. S. Cavaleiro, M. G. P. M. S. Neves, C. Lodeiro, *J. Mater. Chem.* **2012**, 22, 13811–13819.
110. E. Rabinovich, I. Goldberg, Z. Gross, *Chem. Eur. J.* **2011**, 17, 12294–12301.
111. R. D. Teo, J. Y. Hwang, J. Termini, Z. Gross, H. B. Gray, *Chem. Rev.* **2017**, 117, 2711–2729.
112. I. Aviv, Z. Gross, *Chem. Commun.* **2007**, 1987–1999.
113. J. Sankar, H. Rath, V. Prabhuraja, S. Gokulnath, T. K. Chandrashekar, C. S. Purohit, S. Verma, *Chem. Eur. J.* **2007**, 13, 105–114.
114. Z. Gershman, I. Goldberg, Z. Gross, *Angew. Chem. Int. Ed.* **2007**, 46, 4320–4324; *Angew. Chem.* **2007**, 119, 4398.
115. J. Capar, S. Berg, K. E. Thomas, C. M. Beavers, K. J. Gagnon, A. Ghosh, *J. Inorg. Biochem.* **2015**, 153, 162–166.
116. L. M. Reith, M. Koenig, C. Schwarzsinger, W. Schoefberger, *Eur. J. Inorg. Chem.* **2012**, 4342–4349.
117. T. H. Ngo, F. Nastasi, F. Puntoriero, S. Campagna, W. Dehaen, W. Maes, *Eur. J. Org. Chem.* **2012**, 5605–5617.
118. D. Gao, G. Canard, M. Giorgi, T. S. Balaban, *Eur. J. Inorg. Chem.* **2012**, 5915–5920.
119. G. Pomarico, S. Nardis, R. Paolesse, O. C. Ongayi, B. H. Courtney, F. R. Fronczek, M. G. H. Vicente, *J. Org. Chem.* **2011**, 76, 3765–3773.

-
120. T. H. Ngo, F. Puntoriero, F. Nastasi, K. Robeyns, L. Van Meervelt, S. Campagna, W. Dehaen, W. Maes, *Chem. Eur. J.* **2010**, *16*, 5691–5705.
121. M. Stefanelli, J. Shen, W. Zhu, M. Mastroianni, F. Mandoj, S. Nardis, Z. Ou, K. M. Kadish, F. R. Fronczek, K. M. Smith, R. Paolesse, *Inorg. Chem.* **2009**, *48*, 6879–6887.
122. T. H. Ngo, W. Van Rossom, W. Dehaen, W. Maes, *Org. Biomol. Chem.* **2009**, *7*, 439–443.
123. H. Y. Liu, L. Chen, F. Yam, H. Y. Zhan, X. Ying, X. L. Wang, H. F. Jiang, C. K. Chang, *Chin. Chem. Lett.* **2008**, *19*, 1000–1003.
124. T. Ishizuka, H. Yamasaki, A. Osuka, H. Furuta, *Tetrahedron*. **2007**, *63*, 5137–5147.
125. M. Broring, C. Hell, *Chem. Commun.* **2001**, 2336–2337.
126. W. Sinha, S. Kar, *Organometallics*. **2014**, *33*, 6550–6556.
127. K. Murakami, Y. Yamamoto, H. Yorimitsu, A. Osuka, *Chem. Eur. J.* **2013**, *19*, 9123–9126.
128. R. Orłowski, D. Gryko, D. T. Gryko, *Chem. Rev.* **2017**, *117*, 3102–3137.
129. J. F. B. Barata, M. Graca, P. M. S. Neves, M. A. F. Faustino, A. C. Tome, J. A. S. Cavaleiro, *Chem. Rev.* **2017**, *117*, 3192–3253.
130. J.-i. Setsune, A. Tsukajima, N. Okazaki, *J. Porphyrins Phthalocyanines*. **2009**, *13*, 256–265.
131. J. K. Kochi, M. Tamura, *J. Am. Chem. Soc.* **1971**, *93*, 1483–1485.
132. C. Bruckner, C. A. Barta, R. P. Brinas, J. A. Krause Bauer, *Inorg. Chem.* **2003**, *42*, 1673–1680.
133. D. T. Gryko, B. Koszarna, *Org. Biomol. Chem.* **2003**, *1*, 350–357.
134. G. M. Sheldrick, *Acta Crystallogr., Sect. A: Found. Crystallogr.* **2008**, *64*, 112–122.
135. P. Van der Sluis, A. Spek, *Acta Crystallogr., Sect. A: Found. Crystallogr.* **1990**, *46*, 194–201.
136. B. Koszarna, D. T. Gryko, *J. Org. Chem.* **2006**, *71*, 3707–3717.
137. S. Will, A. Rahbar, H. Schmickler, J. Lex, E. Vogel, *Angew. Chem., Int. Ed.* **1990**, *29*, 1390–1393.
138. M. Tse, Z. Zhang, T. C. W. Mak, K. Chan, *Chem. Commun.* **1998**, 1199–1200.
139. C. Jeandon, R. Ruppert, H. J. Callot, *Chem. Commun.* **2004**, 1090–1091.

-
140. C. Jeandon, R. Ruppert, H. J. Callot, *J. Org. Chem.* **2006**, *71*, 3111–3120.
141. B. Ramdhanie, C. L. Stern and D. P. Goldberg, *J. Am. Chem. Soc.* **2001**, *123*, 9447–9448.
142. J. Skonieczny, L. Latos-Grażyński, L. Szterenberga, *Chem. Eur. J.* **2008**, *14*, 4861–4874.
143. M. Fujiki, H. Tabei, K. Isa, *J. Am. Chem. Soc.* **1986**, *108*, 1532–1536;
144. E. Vogel, M. Michels, L. Zander, J. Lex, N. S. Tuzun, K. N. Houk, *Angew. Chem., Int. Ed.* **2003**, *42*, 2857–2862.
145. A. R. Battersby, *Acc. Chem. Res.* **1993**, *26*, 15–21.
146. D. Thibaut, L. Debussche, F. Blanche, *Proc. Natl. Acad. Sci. U. S. A.* **1990**, *87*, 8795–8799.
147. A. R. Battersby, M. J. Bushell, C. Jones, N. G. Lewis, A. Pfenninger, *Proc. Natl. Acad. Sci. U. S. A.*, **1981**, *78*, 13–15.
148. A. I. Scott, A. J. Irwin, L. M. Siegel, J. Shoolery, *J. Am. Chem. Soc.* **1978**, *100*, 7987–7994.
149. V. V. Roznyatovskiy, C.-H. Lee, J. L. Sessler, *Chem. Soc. Rev.* **2013**, *42*, 1921–1933.
150. Z. Gross, *J. Biol. Inorg. Chem.* **2001**, *6*, 733–738.
151. R. Paolesse, S. Nardis, M. Stefanelli, F. R. Fronczek, M. G. H. Vicente, *Angew. Chem., Int. Ed.* **2005**, *44*, 3047–3050.
152. R. S. Czernuszewicz, V. Mody, A. Czader, M. Galezowski, D. T. Gryko, *J. Am. Chem. Soc.* **2009**, *131*, 14214–14215.
153. P. J. Brothers, *Chem. Commun.* **2008**, 2090–2102.
154. J. H. Palmer, A. C. Durrell, Z. Gross, J. R. Winkler, H. B. Gray, *J. Am. Chem. Soc.* **2010**, *132*, 9230–9231.
155. H.-Y. Liu, Y. Fei, Y.-T. Xie, X.-Y. Li, C. K. Chang, *J. Am. Chem. Soc.* **2009**, *131*, 12890–12891.
156. B. Brizet, N. Desbois, A. Bonnot, A. Langlois, A. Dubois, J.-M. Barbe, C. P. Gros, C. Goze, F. Denat, P. D. Harvey, *Inorg. Chem.* **2014**, *53*, 3392–3403.
157. S. Kuck, G. Hoffmann, M. Bröring, M. Fechtel, M. Funk, R. Wiesendanger, *J. Am. Chem. Soc.* **2008**, *130*, 14072–14073.

-
158. K. E. Thomas, H. Vazquez-Lima, Y. Fang, Y. Song, K. J. Gajnon, C. M. Beavers, K. M. Kadish, A. Ghosh, *Chem. Eur. J.* **2015**, *21*, 16839–16847.
159. M. Bröring, F. Bregier, E. Cónsul Tejero, C. Hell, M. C. Holthausen, *Angew. Chem. Int. Ed.* **2007**, *46*, 445–448.
160. A. Ghosh, *Chem. Rev.* **2017**, *117*, 3798–3881.
161. R. Orłowski, D. Gryko, D. T. Gryko, *Chem. Rev.* **2017**, *117*, 3102–3137.
162. Y. Fang, Z. Ou, K. M. Kadish, *Chem. Rev.* **2017**, *117*, 3377–3419.
163. K. Fujino, Y. Hirata, Y. Kawabe, T. Morimoto, A. Srinivasan, M. Toganoh, Y. Miseki, A. Kudo, H. Furuta, *Angew. Chem., Int. Ed.* **2011**, *50*, 6855–6859.
164. B. Patra, S. Sobottka, W. Sinha, B. Sarkar, S. Kar, *Chem. Eur. J.* **2017**, *23*, 13858–13863.
165. S. K. Patra, K. Sahu, B. Patra, D. K. Sahoo, S. Mondal, P. Mukherjee, H. S. Biswal, S. Kar, *Green Chem.* **2017**, *19*, 5772–5776.
166. P. Zhu, P. Ma, Y. Wang, Q. Wang, X. Zhao, X. Zhang, *Eur. J. Inorg. Chem.*, **2011**, 4241–4247.
167. M. Gouterman, *Optical Spectra and Electronic Structure of Porphyrins and Related Rings. in The Porphyrins*, ed. D. Dolphin, Academic Press, New York, **1978**, vol. III, Part A, pp. 1–165.
168. J. Mack, *Chem. Rev.* **2017**, *117*, 3444–3478.
169. L. Latos-Grazynski, K. M. Kadish, K. M. Smith, R. Guillard, *Academic Press, San Diego, CA.* **2000**, vol. 2, p. 361.
170. M. Stefanelli, M. Mastroianni, S. Nardis, S. Licoccia, F.R. Fronczek, K. M. Smith, W. Zhu, Z. Ou, K. M. Kadish, R. Paolesse, *Inorg. Chem.* **2007**, *46*, 10791–10799.
171. E. Pacholska, E. Espinosa, R. Guillard, *Dalton Trans.* **2004**, 3181–3183.
172. J. Rochford, A. D. Rooney, M. T. Pryce, *Inorg. Chem.* **2007**, *46*, 7247–7249.
173. D. Sahoo, S. P. Rath, *J. Chem. Sci.* **2015**, *127*, 327–335.
174. C. H. Devillers, A. Milet, J.-C. Moutet, J. Pécaut, G. Royal, E. Saint-Aman, C. Bucher, *Dalton Trans.* **2013**, *42*, 1196–1209.

-
175. A. Burrell, W. Campbell, G. Jameson, D. Officer, P. W. Boyd, P. Cocks, K. Gordon, *Chem. Commun.* **1999**, 637–638.
176. C. Clark, C. Poole Jr, H. Farach, *J. Phys. C: Solid State Phys.* **1978**, *11*, 769.
177. P. Hakansson, T. Nguyen, P. B. Nair, R. Edge, E. Stulz, *Phys. Chem. Chem. Phys.* **2013**, *15*, 10930–10941.
178. K. M. Kadish, K. M. Smith, R. Guilard, *The Porphyrin Handbook*, ed. Academic Press, New York, vol. 1–20, 1959–2003.
179. N. Aratani, D. Kim, A. Osuka, *Acc. Chem. Res.* **2009**, *42*, 1922–1934.
180. W. Liu, X. Huang, M.-J. Cheng, R. J. Nielsen, W. A. Goddard, J. T. Groves, *Science*. **2012**, *337*, 1322–1325.
181. B. Morandi, E. M. Carreira, *Science*. **2012**, *335*, 1471–1474.
182. R. Breslow, Y. Huang, X. Zhang, J. Yang, *Proc. Natl. Acad. Sci. USA*. **1997**, *94*, 11156–11158.
183. K. Suda, T. Kikkawa, S.-i. Nakajima, T. Takanami, *J. Am. Chem. Soc.* **2004**, *126*, 9554–9555.
184. J. Chen, C. M. Che, *Angew. Chem. Int. Ed.* **2004**, *43*, 4950–4954; *Angew. Chem.* **2004**, *116*, 5058–5062.
185. J. A. Schmidt, E. B. Lobkovsky, G. W. Coates, *J. Am. Chem. Soc.* **2005**, *127*, 11426–11435.
186. C.-Y. Zhou, P. W. H. Chan, C.-M. Che, *Org. Lett.* **2006**, *8*, 325–328.
187. C.-M. Che, J.-S. Huang, F.-W. Lee, Y. Li, T.-S. Lai, H.-L. Kwong, P.-F. Teng, W.-S. Lee, W.-C. Lo, S.-M. Peng, *J. Am. Chem. Soc.* **2001**, *123*, 4119–4129.
188. W.-C. Lo, C.-M. Che, K.-F. Cheng, T. C. W. Mak, *Chem. Commun.* **1997**, 1205–1206.
189. J.-L. Zhang, C.-M. Che, *Org. Lett.* **2002**, *4*, 1911–1914.
190. S.-L. Zheng, W.-Y. Yu, C.-M. Che, *Org. Lett.* **2002**, *4*, 889–892.
191. Y. Li, J.-S. Huang, Z.-Y. Zhou, C.-M. Che, *J. Am. Chem. Soc.* **2001**, *123*, 4843–4844.
192. C.-Y. Zhou, W.-Y. Yu, C.-M. Che, *Org. Lett.* **2002**, *4*, 3235–3238.
193. J. P. Collman, H. J. Arnold, *Acc. Chem. Res.* **1993**, *26*, 586–592.

-
194. J. P. Collman, C. E. Barnes, T. J. Collins, P. J. Brothers, J. Gallucci, J. A. Ibers, *J. Am. Chem. Soc.* **1981**, *103*, 7030–7032.
195. F. R. Hopf, T. P. O'Brien, W. R. Scheidt, D. G. Whitten, *J. Am. Chem. Soc.* **1975**, *97*, 277–281.
196. J. P. Collman, P. Brothers, L. McElwee-White, E. Rose, L. Wright, *J. Am. Chem. Soc.* **1985**, *107*, 4570–4571.
197. J. P. Collman, H. J. Arnold, J. P. Fitzgerald, K. J. Weissman, *J. Am. Chem. Soc.* **1993**, *115*, 9309–9310.
198. F. Cotton, N. Curtis, C. Harris, B. Johnson, S. Lippard, J. Mague, W. Robinson, J. Wood, *Science*. **1964**, *145*, 1305–1307.
199. F. Cotton, *Inorg. Chem.* **1965**, *4*, 334–336.
200. J. P. Collman, C. E. Barnes, P. N. Swebston, J. A. Ibers, *J. Am. Chem. Soc.* **1984**, *106*, 3500–3510.
201. R. Guillard, F. Burdet, J.-M. Barbe, C. P. Gros, E. Espinosa, J. Shao, Z. Ou, R. Zhan, K. M. Kadish, *Inorg. Chem.* **2005**, *44*, 3972–3983.
202. C. M. Blumenfeld, R. H. Grubbs, R. A. Moats, H. B. Gray, K. Sorasane, *Inorg. Chem.* **2013**, *52*, 4774–4776.
203. I. Niguel-Etinger, I. Goldberg, Z. Gross, *Inorg. Chem.* **2012**, *51*, 1983–1985.
204. M. M. Abu-Omar, *Dalton Trans.* **2011**, *40*, 3435–3444.
205. B. R. Gisk, F. Brégier, R. A. Krüger, M. Bröring, N. Frankenberg-Dinkel, *Biochemistry*. **2010**, *49*, 10042–10044.
206. M. El Ojaimi, C. P. Gros, J.-M. Barbe, *Eur. J. Inorg. Chem.* **2008**, 1181–1186.
207. S. Nardis, D. O. Cicero, S. Licoccia, G. Pomarico, B. Berionni Berna, M. Sette, G. Ricciardi, A. Rosa, F. R. Fronczek, K. M. Smith, *Inorg. Chem.* **2014**, *53*, 4215–4227.
208. C. I. Santos, E. Oliveira, J. Fernández-Lodeiro, J. F. Barata, S. R. M. Santos, M. A. F. Faustino, J. A. Cavaleiro, M. G. P. Neves, C. Lodeiro, *Inorg. Chem.* **2013**, *52*, 8564–8572.

-
209. M. Stefanelli, G. Pomarico, L. Tortora, S. Nardis, F. R. Fronczek, G. T. McCandless, K. M. Smith, M. Manowong, Y. Fang, P. Chen, *Inorg. Chem.* **2012**, *51*, 6928–6942.
210. H. L. Buckley, W. A. Chomitz, B. Koszarna, M. Tasior, D. T. Gryko, P. J. Brothers, J. Arnold, *Chem. Commun.* **2012**, *48*, 10766–10768.
211. D. K. Dogutan, S. A. Stoian, R. McGuire Jr., M. Schwalbe, T. S. Teets, D. G. Nocera, *J. Am. Chem. Soc.* **2011**, *133*, 131–140.
212. S. Hiroto, I. Hisaki, H. Shinokubo, A. Osuka, *Angew. Chem. Int. Ed.* **2005**, *44*, 6763–6766; *Angew. Chem.* **2005**, *117*, 6921–6924.
213. H. Furuta, H. Maeda, A. Osuka, *Chem. Commun.* **2002**, 1795–1804.
214. L. Yun, H. Vazquez-Lima, H. Fang, Z. Yao, G. Geisberger, C. Dietl, A. Ghosh, P. J. Brothers, X. Fu, *Inorg. Chem.* **2014**, *53*, 7047 – 7054.
215. A. M. Albrett, K. E. Thomas, S. Maslek, A. Młodzianowska, J. Conradie, C. M. Beavers, A. Ghosh, P. J. Brothers, *Inorg. Chem.* **2014**, *53*, 5486–5493.
216. C. I. Santos, E. Oliveira, J. F. Barata, M. A. F. Faustino, J. A. Cavaleiro, M. G. P. Neves, C. Lodeiro, *J. Mater. Chem.* **2012**, *22*, 13811–13819.
217. P. Leeladee, G. N. Jameson, M. A. Siegler, D. Kumar, S. P. de Visser, D. P. Goldberg, *Inorg. Chem.* **2013**, *52*, 4668–4682.
218. H. L. Buckley, L. K. Rubin, M. Chromiński, B. J. McNicholas, K. H. Tsen, D. T. Gryko, J. Arnold, *Inorg. Chem.* **2014**, *53*, 7941–7950.
219. H. Zhao, K. Pierloot, E. H. Langner, J. C. Swarts, J. Conradie, A. Ghosh, *Inorg. Chem.* **2012**, *51*, 4002–4006.
220. D. Dolphin, *The Porphyrins, Vols. I – VII*, Academic Press, New York, **1979**.
221. M. Gouterman, P. M. Rentzepis, K. D. Straub, *Porphyrins: Excited States and Dynamics*, ACS. **1986**.
222. B. M. Hoffman, J. A. Ibers, *Acc. Chem. Res.* **1983**, *16*, 15–21.

-
223. K. M. Kadish, F. Burdet, F. Jérôme, J.-M. Barbe, Z. Ou, J. Shao, R. Guillard, *J. Organomet. Chem.* **2002**, 652, 69–76.
224. F. Jérôme, B. Billier, J. M. Barbe, E. Espinosa, S. Dahaoui, C. Lecomte, R. Guillard, *Angew. Chem. Int. Ed.* **2000**, 39, 4051–4053; *Angew. Chem.* **2000**, 112, 4217–4219.
225. L. Simkhovich, I. Luobeznova, I. Goldberg, Z. Gross, *Chem. Eur. J.* **2003**, 9, 201–208.
226. J. P. Collman, S. T. Harford, *Inorg. Chem.* **1998**, 37, 4152–4153.
227. S. Patra, T. A. Miller, B. Sarkar, M. Niemeyer, M. D. Ward, G. K. Lahiri, *Inorg. Chem.* **2003**, 42, 4707–4713.
228. W. Kaim, G. K. Lahiri, *Angew. Chem. Int. Ed.* **2007**, 46, 1778–1796; *Angew. Chem.* **2007**, 119, 1808–1828.
229. R. F. Winter, *Organometallics.* **2014**, 33, 4517–4536.
230. J. R. Reimers, N. S. Hush, *J. Am. Chem. Soc.* **1995**, 117, 1302–1308.
231. M. Krejčík, M. Danek, F. Hartl, *J. Electroanal. Chem. Interfacial Electrochem.* **1991**, 317, 179–187.
232. G. M. Sheldrick, *Acta Crystallogr. Sect. A.* **2008**, 64, 112–122.
233. F. Neese, *Wiley Interdiscip. Rev.: Comput. Mol. Sci.* **2012**, 2, 73–78.
234. A. D. Becke, *J. Chem. Phys.* **1993**, 98, 5648–5652.
235. A. D. Becke, *Phys. Rev. Sect. A.* **1988**, 38, 3098–3100.
236. C. Lee, W. Yang, R. G. Parr, *Phys. Rev. Sect. B.* **1988**, 37, 785–789.
237. S. Grimme, J. Antony, S. Ehrlich, H. Krieg, *J. Chem. Phys.* **2010**, 132, 154104.
238. C. van Wellen, *J. Chem. Phys.* **1998**, 109, 392–399.
239. D. A. Pantazis, X.-Y. Chen, C. R. Landis, F. Neese, *J. Chem. Theory Comput.* **2008**, 4, 908–919.
240. F. Neese, *J. Comput. Chem.* **2003**, 24, 1740–1747.
241. F. Neese, F. Wennmohs, A. Hansen, U. Becker, *Chem. Phys.* **2009**, 356, 98–109.
242. O. Vahtras, J. Almlöf, M. W. Feyereisen, *Chem. Phys. Lett.* **1993**, 213, 514–518.

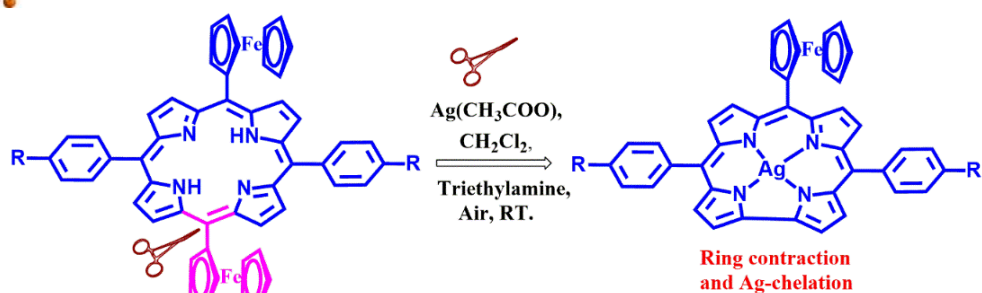
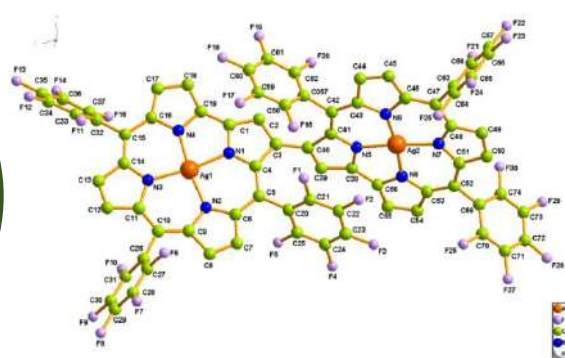
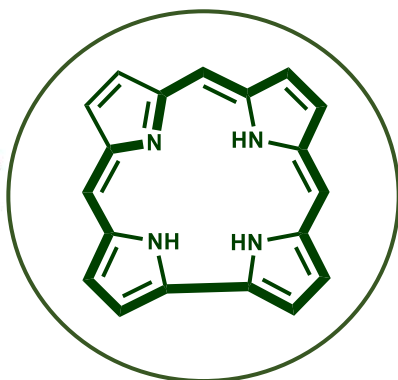
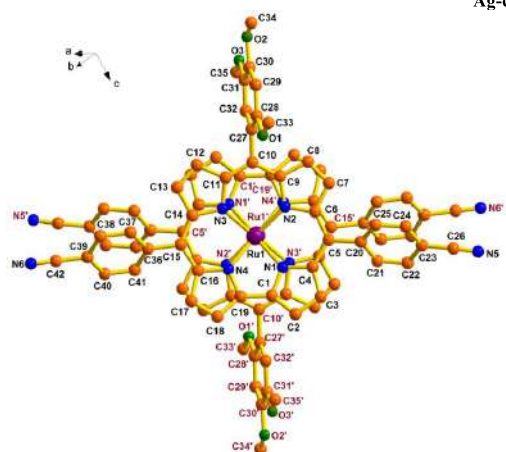
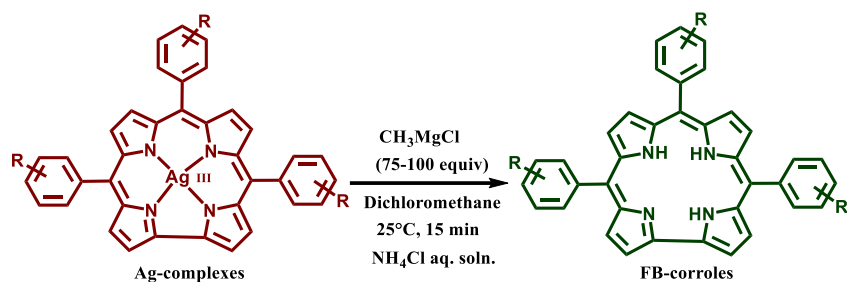
-
243. J. L. Whitten, *J. Chem. Phys.* **1973**, 58, 4496–4501.
244. A. Klamt, G. Scheermann, *J. Chem. Soc. Perkin Trans. 2.* **1993**, 799–805.
245. S. Sinnecker, A. Rajendran, A. Klamt, M. Diedenhofen, F. Neese, *J. Phys. Chem. A.* **2006**, 110, 2235–2245.
246. P. O. Löwdin, *J. Chem. Phys.* **1950**, 18, 365–375.
247. S. Portmann, *CSCS/UNI Geneva: Geneva, Switzerland.* **2009**.
248. W. Sinha, M. G. Sommer, M. van der Meer, S. Plebst, B. Sarkar, S. Kar, *Dalton Trans.* **2016**, 45, 2914–2923.
249. W. Sinha, L. Ravotto, P. Ceroni, S. Kar, *Dalton Trans.* **2015**, 44, 17767–17773.
250. W. Sinha, M. Kumar, A. Garai, C. S. Purohit, T. Som, S. Kar, *Dalton Trans.* **2014**, 43, 12564–12573.
251. M.-H. Baik, R. A. Friesner, *J. Phys. Chem. A.* **2002**, 106, 7407–7412.
252. N. G. Connelly, W. E. Geiger, *Chem. Rev.* **1996**, 96, 877–910.
253. K. D. Demadis, C. M. Hartshorn, T. J. Meyer, *Chem. Rev.* **2001**, 101, 2655–2686.
254. W. Kaim, A. Klein, M. Glöckle, *Acc. Chem. Res.* **2000**, 33, 755–763.
255. W. Kaim, B. Sarkar, *Coord. Chem. Rev.* **2007**, 251, 584–594.
256. D. E. Richardson, H. Taube, *Coord. Chem. Rev.* **1984**, 60, 107–129.
257. T. J. Meyer, *Acc. Chem. Res.* **1978**, 11, 94–100.
258. N. Sutin, *Acc. Chem. Res.* **1982**, 15, 275–282.
259. J. P. Launay, *Coord. Chem. Rev.* **2013**, 257, 1544–1554.
260. L. E. Darago, M. L. Aubrey, C. J. Yu, M. I. Gonzalez, J. R. Long, *J. Am. Chem. Soc.* **2015**, 137, 15703–15711.
261. C. Saracini, K. Ohkubo, T. Suenobu, G. J. Meyer, K. D. Karlin, S. Fukuzumi, *J. Am. Chem. Soc.* **2015**, 137, 15865–15874.
262. R. Cao, C. Saracini, J. W. Ginsbach, M. T. Kieber-Emmons, M. A. Siegler, E. I. Solomon, S. Fukuzumi, K. D. Karlin, *J. Am. Chem. Soc.* **2016**, 138, 7055–7066.

-
263. P. J. Chmielewski, *Angew. Chem. Int. Ed.* **2005**, *44*, 6417–6420; *Angew. Chem.* **2005**, *117*, 6575–6578.
264. D. Sun, C. F. Yang, H. R. Xu, H. X. Zhao, Z. H. Wei, N. Zhang, L. J. Yu, R. B. Huang, L. S. Zheng, *Chem. Commun.* **2010**, *46*, 8168–8170.
265. S. Ooi, T. Tanaka, A. Osuka, *Inorg. Chem.* **2016**, *55*, 8920–8927.
266. A. K. Singh, F. S. T. Khan, S. P. Rath, *Angew. Chem. Int. Ed.* **2017**, *56*, 8849 – 8854; *Angew. Chem.* **2017**, *129*, 8975–8980.
267. W. Grochala, R. Hoffmann, *Angew. Chem. Int. Ed.* **2001**, *40*, 2742 – 2781; *Angew. Chem.* **2001**, *113*, 2816–2859.
268. B. G. Meller, *Angew. Chem. Int. Ed. Engl.* **1987**, *26*, 1081–1097; *Angew. Chem.* **1987**, *99*, 1120–1135.
269. W. Massa, D. Babel, *Chem. Rev.* **1988**, *88*, 275–296.
270. C. Breckner, *J. Chem. Educ.* **2004**, *81*, 1665–1669.
271. C. Breckner, C. A. Barta, R. P. Brinas, J. A. K. Bauer, *Inorg. Chem.* **2003**, *42*, 1673–1680.
272. A. Osuka, H. Shimidzu, *Angew. Chem. Int. Ed. Engl.* **1997**, *36*, 135–137; *Angew. Chem.* **1997**, *109*, 93–95.
273. T. Ogawa, Y. Nishimoto, N. Yoshida, N. Ono, A. Osuka, *Angew. Chem. Int. Ed.* **1999**, *38*, 176–179; *Angew. Chem.* **1999**, *111*, 140–142.
274. A. Tsuda, Y. Nakamura, A. Osuka, *Chem. Commun.* **2003**, 1096–1097.
275. Y. H. Kim, D. H. Jeong, D. Kim, S. C. Jeoung, H. S. Cho, S. K. Kim, N. Aratani, A. Osuka, *J. Am. Chem. Soc.* **2001**, *123*, 76–86.
276. A. Tsuda, A. Nakano, H. Furuta, H. Yamochi, A. Osuka, *Angew. Chem. Int. Ed.* **2000**, *39*, 558–561; *Angew. Chem.* **2000**, *112*, 572–575.
277. A. Tsuda, A. Osuka, *Adv. Mater.* **2002**, *14*, 75–79.
278. N. Aratani, A. Osuka, Y. H. Kim, D. H. Jeong, D. Kim, *Angew. Chem. Int. Ed.* **2000**, *39*, 1458–1462; *Angew. Chem.* **2000**, *112*, 1517–1521.

-
279. H. Segawa, Y. Senshu, J. Nakazaki, K. Susumu, *J. Am. Chem. Soc.* **2004**, *126*, 1354–1355.
280. H. Segawa, D. Machida, Y. Senshu, J. Nakazaki, K. Hirakawa, F. Wu, *Chem. Commun.* **2002**, 3032–3033.
281. P. J. Chmielewski, L. Latos-Grazynski, K. Rachlewicz, T. Głowiak, *Angew. Chem. Int. Ed. Engl.* **1994**, *33*, 779–781; *Angew. Chem.* **1994**, *106*, 805 – 808.
282. H. Furuta, T. Asano, T. Ogawa, *J. Am. Chem. Soc.* **1994**, *116*, 767 –768.
283. G. R. Geier III, D. M. Haynes, J. S. Lindsey, *Org. Lett.* **1999**, *1*, 1455 –1458.
284. M. G. H. Vicente, L. Jaquinod, K. M. Smith, *Chem. Commun.* **1999**, 1771–1782.
285. A. K. Burrell, D. L. Officer, P. G. Plieger, D. C. W. Reid, *Chem. Rev.* **2001**, *101*, 2751–2796.
286. J. Wojaczyński, L. Latos-Grażyński, *Coord. Chem. Rev.* **2000**, *204*, 113–171.
287. S. Richeter, C. Jeandon, R. Ruppert, H. J. Callot, *Chem. Commun.* **2001**, 91–92.
288. S. Richeter, C. Jeandon, J.-P. Gisselbrecht, R. Ruppert, H. J. Callot, *J. Am. Chem. Soc.* **2002**, *124*, 6168–6179.
289. S. Preiss, J. Melomedov, A. W. von Leupoldt, K. Heinze, *Chem. Sci.* **2016**, *7*, 596–610.
290. E. Vogel, S. Will, A. S. Tilling, L. Neumann, J. Lex, E. Bill, A. X. Trautwein, K. Wieghardt, *Angew. Chem. Int. Ed. Engl.* **1994**, *33*, 731–735; *Angew. Chem.* **1994**, *106*, 771–775.
291. R. Paollesse, S. Nardis, M. Stefanelli, F. R. Fronczek, M. G. H. Vicente, *Angew. Chem.* **2005**, *117*, 3107–3110.
292. K. Fujino, Y. Hirata, Y. Kawabe, T. Morimoto, A. Srinivasan, M. Toganoh, Y. Miseki, A. Kudo, H. Furuta, *Angew. Chem.* **2011**, *123*, 6987–6991.
293. S. Hiroto, K. Furukawa, H. Shinokubo, A. Osuka, *J. Am. Chem. Soc.* **2006**, *128*, 12380–12381.
294. A. Mahammed, I. Giladi, I. Goldberg, Z. Gross, *Chem. Eur. J.* **2001**, *7*, 4259–4265.
295. S. Hirabayashi, M. Omote, N. Aratani, A. Osuka, *Bull. Chem. Soc. Jpn.* **2012**, *85*, 558–562.
296. B. koszarna, D. T. Gryko, *Chem. Commun.* **2007**, 2994–2996.
297. J. P. Perdew, *Phys. Rev. B.* **1986**, *33*, 8822–8824.
298. J. P. Perdew, *Phys. Rev. B.* **1986**, *34*, 7406.

-
299. C. T. Lee, W. T Yang, R. G. Parr, *Phys. Rev. B.* **1988**, 37, 785-789.
300. S. Grimme, S. Ehrlich, L. Goerigk, *J Comput Chem.* **2011**, 32, 1456–1465.
301. S. Grimme, J. Antony, S. Ehrlich, H. Krieg, *J. Chem. Phys.* **2010**, 132, 154104.
302. S. Grimme, *J. Comput. Chem.* **2004**, 25, 1463-1476.
303. S. Grimme, *J. Comput. Chem.* **2006**, 27, 1787-1799.
304. C. Van Wüllen, *J. Chem. Phys.* **1998**, 109, 392-399.
305. F. Neese, *J. Comput. Chem.* **2003**, 24, 1740-1747.
306. F. Neese, F. Wenmohs, A. Hansen, U. Becker, *Chem. Phys.* **2009**, 356, 98-109.
307. R. Izsak, F. Neese, *J. Chem. Phys.* **2011**, 135, 144105.
308. F. Neese, G. Olbrich, *Chem. Phys. Lett.* **2002**, 362, 170-178.
309. T. Petrenko, S. Kossmann, F Neese, *J. Chem. Phys.* **2011**, 134, 054116.
310. K. Eichkorn, F. Weigend, O. Treutler, R. Ahlrichs, *Theor. Chem. Acc.* **1997**, 97, 119-124.
311. K. Eichhorn, O. Treutler, H. Öhm, M. Häser, R. Ahlrichs, *Chem. Phys. Lett.* **1995**, 242, 652-660.
312. M. U. Delgado-Jaime, S. DeBeer, *J. Comput. Chem.* **2012**, 33, 2180– 2185.
313. Avogadro: an open-source molecular builder and visualization tool. Version 1.1.1. modified version with extended ORCA support <http://avogadro.openmolecules.net/> and <https://orcaforum.cec.mpg.de/>.
314. M. D Hanwell, D. E Curtis, D. C Lonie, T. Vandermeersch, E. Zurek, G. R Hutchison, *J. Cheminform.* **2012**, 4, 17.

SUMMARY OF THESIS



Silver Corroles

Grignard Reagent Mediated Demetallation of Silver Corrole Complexes

Bratati Patra,^[a,b] Sajal Kumar Patra,^{[a,b],[‡]} Payel Mukherjee,^{[a,b],[‡]} Yogesh Kumar Maurya,^[a,b] Woormileela Sinha,^[a,b] and Sanjib Kar*^[a,b]

Abstract: In order to study the reactivity of various Grignard reagents with differently substituted A₃- and *trans*-A₂B-corrolato Ag^{III} complexes, we have performed a series of reactions. We have observed that among the various Grignard reagents studied, methylmagnesium chloride is the most potent and re-

sulted in the quantitative demetallation of the corrolato-Ag^{III} complexes and produced the respective free-base corroles exclusively. As expected, we have not observed the formation of any unusual σ -methyl/phenyl derivatives.

Introduction

The chemical modification of corroles, by introducing a series of different functional groups, has been an active area of research in recent times. These systems have widespread applications in chemistry, biology, and in materials science. Structural modifications in the corrole macrocycles at the *meso*- and β -positions can lead to the development of newer varieties of corrole derivatives, which can play an important role in electron-transfer reactions,^[1] oxidation catalysis,^[2] reduction catalysis,^[3] group transfer reactions,^[4] sensors,^[5] cancer diagnostics,^[6] and in treatment purposes.^[7] In porphyrin chemistry, various functionalizations at the *meso*- and β -positions of the macrocycles are often carried out by selective metallation and demetallation reactions. One possible reason is that the metal-porphyrinoid systems are often more robust than the metal-free porphyrinoid systems. Contrary to the porphyrin-based systems, the development of suitable demetallation strategies for corrole chemistry is still in its infancy.^[8] Only a few selected metals ions (Cu,^[8h] Ag,^[8g] Mn,^[8k] Bi,^[8b] and Sn^[9]) can be demetallated from the corrole cavity. In addition to this, there is no generalized protocol for demetallation available in the literature of corrole chemistry. Out of the several methodologies described so far, the most intriguing method for the demetallation of corrolato-silver(III) complexes was reported by Paolesse et al.^[8g] They have shown that DBU in THF solutions is an excellent reagent for the demetallation reactions of Ag-corroles with average yields of 45 % to 62 %. Furuta et al. have reported the demetal-

lation of silver(III) complexes of N-confused porphyrin by using sodium borohydride.^[8j] Dehaen et al. have developed an interesting methodology for demetallation of Cu-corroles by using SnCl₂ (in acidic condition) as a reducing agent.^[8h] Ghosh et al. have described the demetallation strategy of Mn-Corroles by using FeCl₂ and conc. H₂SO₄.^[8a] Bröring et al. have performed the demetallation of Mn-Corroles by using HBr in acetic acid.^[8k] Osuka et al. have reported the use of Grignard reagents (4-methylphenylmagnesium bromide) for the first time for the facile demetallation reactions of Ni-porphyrin to FB (free-base) porphyrin via a Mg-porphyrin.^[10] Our group has also reported the demetallation strategy of Sn^{IV}-corroles by using methylmagnesium chloride.^[9] In search of a generalized protocol for the demetallation of metallo-corrole derivatives, we have chosen corrolato-silver(III) complexes for the present work. One reason for this choice is that the native state electronic configurations of corrolato-silver(III) complexes are square planar (d⁸ configurations) and hence diamagnetic in nature. As a result, these complexes can be monitored by NMR spectroscopy very easily after suitable functionalization at their ligand periphery. A series of substituents having different electronic properties have been inserted into the corrole periphery. These substituents have been chosen keeping in mind that a series of post-metallation organic transformation reactions can be conveniently performed on the metallo-corrole derivatives. In the present work, we have observed that a series of corrolato-silver(III) complexes, upon treatment with methylmagnesium chloride resulted in the formation of FB corroles in excellent yields (Scheme 1). Compared with the previously reported results for other demetallation strategies of corrolato-silver(III) complexes, the present methodology delivers significantly improved isolated yields for the corresponding FB corroles.

A series of corrolato-silver(III) complexes have been synthesized for this purpose, namely, 5,10,15-tris(2-bromo-5-fluorophenyl)corrolato-silver(III) (**1B**); 5,10,15-tris(4-cyanophenyl)corrolato-silver(III) (**2B**);^[1d] 10-(4-Bromophenyl)-5,15-bis(4-cyanophenyl)corrolato-silver(III) (**3B**);^[1d] 10-(2,4,5-Trimethoxyphenyl)-

[a] School of Chemical Sciences, National Institute of Science Education and Research (NISER), Bhubaneswar, Khordha 752050, India
E-mail: sanjib@niser.ac.in
<http://www.niser.ac.in/~sanjib/>

[b] Homi Bhabha National Institute, Training School Complex, Anushakti Nagar, Mumbai 400094, India

[‡] Both authors contributed equally to this manuscript.

Supporting information for this article is available on the WWW under <https://doi.org/10.1002/ejic.201601549>.



Metal coordination induced ring contraction of porphyrin derivatives†

Cite this: *Chem. Commun.*, 2018, 54, 9945

Received 12th June 2018,
Accepted 9th August 2018

DOI: 10.1039/c8cc04670k

rsc.li/chemcomm

Bratati Patra,^{ab} Sebastian Sobottka,^c Sruti Mondal,^{ab} Biprajit Sarkar^{ib}*^c and Sanjib Kar^{ib}*^{ab}

A remarkable rearrangement of a diferrocenylporphyrin to give a silver(III) corrole has been discovered. Compared to the previously reported porphyrin to corrole ring conversions (extremely rare and poor reaction yields), our methodology delivers near quantitative yield for this ring contraction.

The synthesis of a corrole ring *via* ring contraction of a suitable porphyrin derivative has been rarely documented in the literature.¹ Corroles are structurally related to corrins.² However, in contrast to corrins, corroles possess aromaticity.³ Many challenging corrole based systems are under intensive research,³ and thus the ring contraction of porphyrins to corroles (rarely explored but a one-step protocol) has a lot of promise for the future development of porphyrinoid based compounds. Very few research reports indeed highlight the ring contraction methodology that leads to a porphyrin to corrole conversion (only one example of a real such conversion with 9% yield, see ESI,† Scheme S1). Vogel *et al.* had first reported a porphycene–isocorrole rearrangement reaction and compared it with the ring contraction step for the facile synthesis of a corrin ring in association with the biosynthesis of vitamin B₁₂.^{1a} Porphycene and isocorrole can be considered as the related analogous macrocycles of porphyrin and corrole, respectively. In later years, during metalation of a highly electron deficient porphyrin ring by using Re₂(CO)₁₀ at higher temperature, Chan *et al.* have observed the formation of oxorhenium(v) corrolate in 9% yield. It was postulated that the reductive conditions favored the porphyrin to corrole conversions.^{1b} Callot *et al.* have observed that a nickel complex of *meso*-tetraarylporphyrins upon treatment

with benzoic anhydride and SnCl₄ and subsequent exposure to air under a basic medium resulted in the formation of nickel complexes of corroles (divalent form) in 24% yield.^{1c,d} They have further demonstrated that the role of the metal ion is pivotal in this transformation and the same reaction was unsuccessful when copper was used instead of nickel. The size of the metal ion is considered to be a vital factor for this transformation. Goldberg *et al.* have described the synthesis of corrolazine by using a ring contraction methodology and have used porphyrazine as a starting material for this purpose.^{1e} Latos-Grażyński *et al.* have also reported a 21-silaphlorin to iso-carbacorrole transformation in 1% yield.^{1f} Overall, the ring contraction methodology is poorly understood in porphyrin based macrocycles, and no synthetic method with high yield is known.

In the following, we present a modified synthetic protocol for the synthesis of two A₂B₂-type ferrocenyl-porphyrin ligands (one new and one literature reported): 5,15-diferrocenyl-10,20-bis(4-cyanophenyl)porphyrin, **1**, and 5,15-diferrocenyl-10,20-bis(4-nitrophenyl)porphyrin, **2**,⁴ and their relevant novel copper complexes with porphyrinato ligands 5,15-diferrocenyl-10,20-bis(4-cyanophenyl)porphyrinato-Cu(II), **3**, and 5,15-diferrocenyl-10,20-bis(4-nitrophenyl)porphyrinato-Cu(II), **4**, and novel silver complexes with corrolato ligands (formed after ring contraction) 10-ferrocenyl-5,15-bis(4-cyanophenyl)corrolato-Ag(III), **5**, and 10-ferrocenyl-5,15-bis(4-nitrophenyl)corrolato-Ag(III), **6** (Scheme 1).

A combined synthetic, electrochemical, and crystallographic approach has been adopted to establish the reactivity pattern of the different metal precursors with the ferrocenyl-porphyrin derivatives. The two *trans*-A₂B₂-type ferrocenyl-porphyrin free base (FB) ligands, **1** and **2**, were prepared by following a modified synthetic strategy (see the ESI†). The corresponding FB porphyrins, **1** and **2**, were dissolved in excess triethylamine and were stirred with excess copper acetate and silver acetate respectively. These reactions led to the generation of complexes **3**, **4**, **5**, and **6** respectively in good yields. The composition and purity of complexes **1–6** were determined by elemental analyses, ¹H and ¹³C NMR spectroscopy and ESI mass spectrometry (see the ESI,† Fig. S1–S20 and Tables S1, S2). The absorption spectra of **1** and **2**

^a School of Chemical Sciences, National Institute of Science Education and Research (NISER), Bhubaneswar – 751005, India. E-mail: sanjib@niser.ac.in

^b Homi Bhabha National Institute, Training School Complex, Anushakti Nagar, Mumbai, 400 094, India

^c Institut für Chemie und Biochemie, Anorganische Chemie Fabockstraße 34-36, D-14195, Berlin, Germany. E-mail: biprajit.sarkar@fu-berlin.de

† Electronic supplementary information (ESI) available: Experimental section, crystallographic data, ¹H NMR, ESI-MS spectra. CCDC 1842435 and 1842436 contain the supplementary crystallographic data for **3** and **5**. For ESI and crystallographic data in CIF or other electronic format see DOI: 10.1039/c8cc04670k

Bioinorganic Chemistry

Ruthenium–Ruthenium-Bonded [Bis{corrolato-ruthenium(III)}]ⁿ
(*n* = 0, +1, −1) Complexes: Model Compounds for the
Photosynthetic Special PairWoormileela Sinha,^[a] Michael G. Sommer,^[b] Lara Hettmanczyk,^[b] Bratati Patra,^[a]
Vasileios Filippou,^[c] Biprajit Sarkar,^{*,[b]} and Sanjib Kar^{*,[a]}

Abstract: We present herein the synthesis of three new bis-(corrolato-ruthenium(III)) complexes containing unsupported Ru–Ru bonds and their characterization in different redox states. The ¹H NMR spectra of the bis(corrolato-ruthenium(III)) complexes displayed “normal” chemical shifts and the compounds proved to be EPR-silent. Crystallographic characterization of the dimers indicated Ru–Ru distances of 2.175 Å, consistent with a triple bond between the two ruthenium centers. All of the synthesized complexes undergo two successive reversible oxidations and a single reversible reduction. A combination of UV/Vis/NIR/EPR spectroelectrochemical studies and DFT calculations established the redox state distributions in these ruthenium–ruthenium-bonded dimers. Whereas reduction of the dimers is metal-based and leads to metal-metal-bonded mixed-valent Ru^{II}–

Ru^{III} species, one-electron oxidation largely retains the Ru^{III}–Ru^{III} situation with the generation of metal-bound corrolato radicals. The present study thus concerns the first UV/Vis/NIR/EPR spectroelectrochemical characterization and DFT calculations of ruthenium–ruthenium-bonded rotationally ordered corrole dimers. The mean plane separation between the two corrole units in these dimers is around 3.543 Å, which is in close agreement to that in the “special pair” in chlorophyll. Oxidation of these ruthenium–ruthenium-bonded dimers gives rise to two new electronic absorption bands in the NIR region (similar to those of the special pair), which have apparently not been mentioned/observed in earlier reports on ruthenium–ruthenium-bonded corrole dimers. These bands mainly originate from inter-corrole transitions.

Introduction

Porphyrinoids are the most prominent ligands used in metal-complex-mediated organic transformations.^[1] The most common example is cytochrome P450 with iron porphyrin as

its cofactor. In many cases, the use of other ligands is not feasible, and porphyrinoids remain as the only viable choice.^[1] In this context, ruthenium porphyrin complexes are extensively used in a variety of organic transformations, including cyclopropanation,^[2] C–H insertion,^[3] cycloaddition,^[4] and carbenoid transformation reactions.^[2a,3c]

Metalloporphyrin dimers with multiple metal-metal bonds have attracted significant interest in recent years.^[5] The native-state electronic structures of these dimers may be qualitatively described by a model proposed by Cotton et al.^[6] It was indeed observed that the bond order of the metal-metal bond in these metalloporphyrin dimers is solely dependent on the number of valence d electrons on each metal center.^[6] However, systematic tuning of the metal-metal bond order of these metalloporphyrin/corrole dimers still remains a challenging task. One simple way of changing the bond order of the metalloporphyrin dimers is selective oxidation and reduction of the dimeric species. Among the various metalloporphyrin-based dimers, ruthenium(II) porphyrin dimers are of particular interest. [(Ru(octaethylporphyrin))₂] was the first such structurally characterized homodimer of ruthenium.^[5c,7] These homodimers of ruthenium have been found to be broadly applicable in various catalytic reactions.^[5d] Thus, study of the redox state distribution of these dimers in various oxidation states is of great importance.

[a] W. Sinha, B. Patra, Dr. S. Kar
School of Chemical Sciences
National Institute of Science Education and Research (NISER)
Bhubaneswar, Khordha, 752050 (India)
and
Homi Bhabha National Institute, Training School Complex
Anushakti Nagar, Mumbai, 400094 (India)
E-mail: sanjib@niser.ac.in

[b] M. G. Sommer, L. Hettmanczyk, Prof. Dr. B. Sarkar
Institut für Chemie und Biochemie, Anorganische Chemie
Freie Universität Berlin, Fabeckstraße 34–36, 14195 Berlin (Germany)
E-mail: biprajit.sarkar@fu-berlin.de

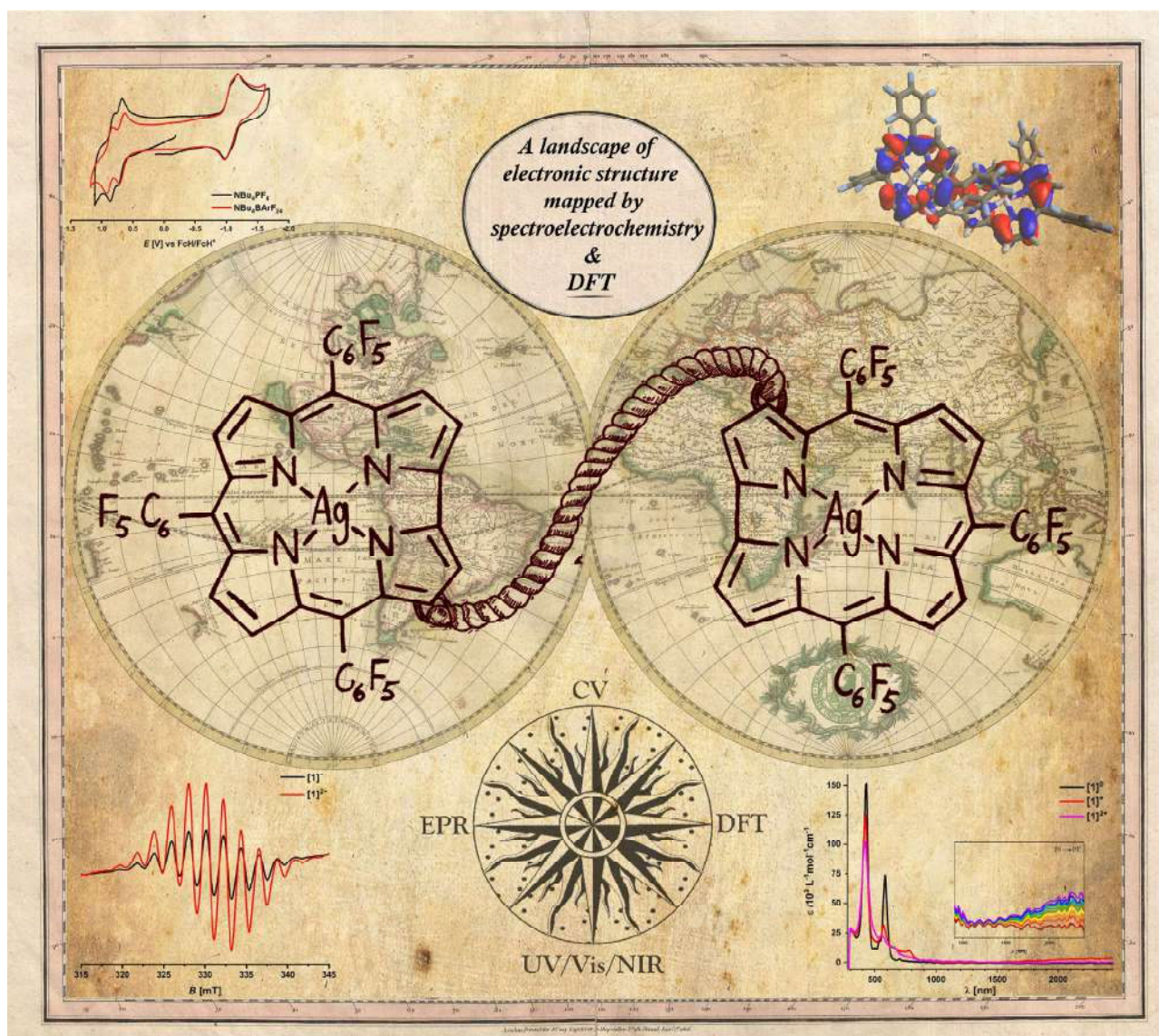
[c] V. Filippou
Institut für Anorganische Chemie, Universität Stuttgart
Pfaffenwaldring 55, 70550 Stuttgart (Germany)

Supporting information for this article can be found under
<http://dx.doi.org/10.1002/chem.201604901>; including ESI mass spectra and
¹H NMR spectra of **1**, **2**, and **3**; packing diagrams of **2**; UV/Vis/NIR and EPR
spectroelectrochemical measurements of **1**, **2**, and **3**. Compositions and en-
ergies of selected molecular orbitals of **1**, **1**⁺, **1**[−], **2**, **2**⁺, and **2**[−]. TD-DFT-cal-
culated electronic transitions for **1**, **1**⁺, **1**[−], **2**, **2**⁺, and **2**[−].

Mixed-Valent Compounds

Isovalent $\text{Ag}^{\text{III}}/\text{Ag}^{\text{III}}$, $\text{Ag}^{\text{II}}/\text{Ag}^{\text{II}}$, Mixed-Valent $\text{Ag}^{\text{II}}/\text{Ag}^{\text{III}}$, and Corrolato-Based Mixed-Valency in β,β' -Linked $[\text{Bis}\{\text{corrolato-silver}\}]^n$ ComplexesBratati Patra^{+, [a, b]} Sebastian Sobottka^{+, [c]} Woormileela Sinha,^[a, b] Biprajit Sarkar,^{*, [c]} and Sanjib Kar^{*, [a, b]}

Dedicated to Professor Pierre Braunstein on the occasion of his 70th birthday



Abstract: Mixed-valent compounds are fascinating entities that are useful as models for investigating electron-transfer reactions, and find use in a host of biologically relevant redox processes. Though the bio-relevant metal copper is well established in mixed-valent chemistry, the $\text{Ag}^{\text{II}}/\text{Ag}^{\text{III}}$ mixed-valent combination of its higher congener in a molecular complex has rarely been reported before. This work reports the synthesis of a new β,β' -linked bis{corrolato-silver(III)} complex and its characterization in five different redox states. A combination of electrochemistry, spectroelectrochemistry, and DFT calculations point to the existence of a mixed-valent $\text{Ag}^{\text{II}}/\text{Ag}^{\text{III}}$ and an isovalent $\text{Ag}^{\text{II}}/\text{Ag}^{\text{II}}$ form. Additionally, characterization of the $\text{Ag}^{\text{III}}/\text{Ag}^{\text{III}}$ form and ligand-based corrolato-centered mixed-valency is presented as well. These results thus open new avenues for bis-corrolato ligands and for mixed-valency in disilver compounds.

Mixed-valent compounds impart intense colors to certain minerals,^[1] are useful for understanding electron-transfer properties in many metallo-proteins,^[2] and are invoked for explaining the high electrical conductivities in certain solids.^[3] As the variable valency is a prerequisite for mixed-valency, most d-block transition elements shows mixed-valency in various coordination complexes and in certain metal salts. In biology, the Cu_A center (mixed-valent dicopper unit) facilitates efficient electron transfer.^[4] In analogy to the mixed-valent dicopper complexes, there are few examples of discrete $\text{Ag}^{\text{II}}/\text{Ag}^{\text{III}}$ species for the higher congener.^[5] There are only few reports on mixed-valent $\text{Ag}^{\text{II}}/\text{Ag}^{\text{III}}$ species and iso-valent $\text{Ag}^{\text{II}}/\text{Ag}^{\text{II}}$ species in discrete coordination complexes.^[6] However, to the best of our knowledge, the spectroscopic nature of such $\text{Ag}^{\text{II}}/\text{Ag}^{\text{III}}$ compounds were never investigated before. In this context, it is worthwhile to mention that the various mixed-valent species in silver complexes are still in their infancy. It has been described earlier that the mixed-valent $\text{Ag}^{\text{II}}/\text{Ag}^{\text{II}}$ and $\text{Ag}^{\text{II}}/\text{Ag}^{\text{III}}$ are indeed very difficult to generate.^[7] Based on theoretical considerations, Hoffmann et al. have reported that $\text{Ag}^{\text{II}}/\text{Ag}^{\text{III}}$ fluoride systems may have applications in superconductors.^[7] Both Ag^{II} and Ag^{III} are known to be potent oxidizing agents in solvated conditions.^[7]

In the solid state, such species are usually stabilized by using fluoro ligands.^[7] It was recently shown that a corrolato core provides a good environment for stabilizing both mononuclear Ag^{III} and mononuclear Ag^{II} in discrete molecular complexes.^[8a,b]

In porphyrinoid chemistry, there has long been widespread research interest in multiple porphyrin-based systems^[9] due to their superior performances in many areas, such as catalysis, photonic devices, and molecular-recognition, and very often they are considered to be superior to their monomeric analogues. Even though the ring-contracted corrole system displays many different properties compared to their porphyrin analogues,^[10] multiple corrole-based systems have been less well explored.^[11] To the best of our knowledge, spectroscopic properties of corrolato-based mixed-valency in bis-corrolato systems have never been investigated before.^[6a] Such investigations are vital for the understanding of electron/hole (de)localization that will play an important role in the future development of molecular electronics. Based on our recent observation that discrete mononuclear Ag^{II} and Ag^{III} complexes can be stabilized within a mono-corrolato framework,^[8a] we have now turned our attention to a bis-corrolato unit. In the following, we present the synthesis of a new $\beta,\beta'(3,3')$ -linked bis{corrolato-silver(III)} complex, **1**, and show that this core is ideal for the stabilization and investigation of the isovalent $\text{Ag}^{\text{III}}/\text{Ag}^{\text{III}}$ and $\text{Ag}^{\text{II}}/\text{Ag}^{\text{II}}$ forms. Additionally, the same core allows us to access the mixed-valent $\text{Ag}^{\text{II}}/\text{Ag}^{\text{III}}$ combination, as well as ligand-centered corrolato-based mixed-valency. Results from a combined synthetic, crystallographic, electrochemical, spectro-electrochemical (UV/Vis-NIR and EPR) and DFT investigation are presented below.

The free base (FB) ligand 3,3'-bis(5,10,15-tris(pentafluorophenyl)corrole), **1A** was prepared by following a synthetic strategy developed earlier by Osuka et al.^[11c] (see the Supporting Information). The $\beta,\beta'(3,3')$ -linked bis{corrolato-silver(III)} complex, **1** (Figure 1), was synthesized by following a general synthetic procedure for the silver metallation.^[8] The corresponding FB corrole (**1A**) was dissolved in excess triethylamine and was stirred with excess silver acetate. This reaction led to the generation of complex **1** in good yield. Composition and purity of complex **1** were determined by elemental analyses, $^1\text{H}/^{19}\text{F}$ -NMR spectroscopy and ESI mass spectrometry (see the Supporting Information). The ^1H NMR spectrum of complex **1** exhibited sharp lines and also a significant deshielding of the β -pyrrolic protons (in comparison to the FB corrole, **1A**) and these observations are in line with the diamagnetic character of the complex **1**.

The molecular structure in the crystal of **1** is shown in Figure 1. The bond lengths and angles in **1** are comparable with the previously reported monomeric corrolato-silver(III) complexes.^[8]

The central silver atoms in **1** fit well into the cavity of the corrolato rings in a slightly distorted square planar geometry with minimal deviations of 0.007 Å (DFT: 0.03 Å) and 0.005 Å (DFT: 0.03 Å) from the respective N4 planes. The distortions in both the rings from the ideal ones are due to slight deviations in the bite angles of N-Ag-N in the ranges of 81.3–96.6° (DFT: 80.6–95.8°) and 80.3–95.1° (DFT: 80.8–95.4°), respectively. As a

[a] B. Patra,* W. Sinha, Dr. S. Kar
School of Chemical Sciences
National Institute of Science Education and Research (NISER)
Bhubaneswar, Khordha, 752050 (India)
E-mail: sanjib@niser.ac.in

[b] B. Patra,* W. Sinha, Dr. S. Kar
Homi Bhabha National Institute, Training School Complex
Anushakti Nagar, Mumbai, 400 094 (India)

[c] S. Sobottka,* Prof. Dr. B. Sarkar
Institut für Chemie und Biochemie, Anorganische Chemie
Freie Universität Berlin, Fabeckstraße 34–36, 14195, Berlin (Germany)
E-mail: biprajit.sarkar@fu-berlin.de

[*] These authors contributed equally to this manuscript.

Supporting information and the ORCID identification number(s) for the author(s) of this article can be found under:
<https://doi.org/10.1002/chem.201703512>.